Characterization of the longitudinal shear strength in composite slabs

Aportació a la caracterització del comportament resistent de les lloses mixtes acer-formigó

UNIVERSITAT POLITÈCNICA DE CATALUNYA
BARCELONA TECH

Departament de Resistència de Materials i Estuctures a l'Enginyeria
ESCOLA TÈCNICA SUPERIOR D'ENGINYERIA INDUSTRIAL DE BARCELONA

A doctoral thesis submitted in the Structural Analysis programme by
Albert Plans Pujolràs

Advisor: Prof. Dr. Frederic Marimon Carvajal
Advisor: Prof. Dr. Miquel Ferrer Ballester

Barcelona, May 2017

per a tu, ***Gemma***
suport, rauxa, paciència,
.... meitat inseparable de tot el que faig

A la ***Núria*** i l’***Abril***,
espontaneïtat, puresa, energia,
... lliçó magistral diària de com ser feliç

A la ***Maria Teresa*** i en ***Joan***
constància, sacrifici, model,
... fonaments i pilars de tot el que sóc

A en ***Marçal***, la ***Neda***, i l’***Adrià***
superació, sacrifici, doctorals,
... tant a prop i tant lluny

I a vosaltres, companys
de feina i estudiants
Sense la vostra ajuda això
tampoc hagués estat possible

Acknowledgements

The doctoral research is always an exciting journey that each student lives in a different way. That journey started for this author back in 2005 when he received a fellowship to perform research at the University of Illinois (UIUC) in United States. For a period of two years, the author was part of a strong group of graduate students in which the passion to develop new ideas, to push some boundaries and at the end, to understand the importance of performing high quality research made a huge impact in him. The author would like to thank professor *Feniosky Peña-Mora* at *Columbia University* in the City of New York for his patience, for infusing high research standards, as well as to promote the co-authoring of several papers in the field of technology supporting emergency responses. Although the author's research focus changed over time, the foundations and the passion were paved back then.

The author also would like to deeply acknowledge professor *Frederic Marimon* at *Universitat Politècnica de Catalunya* (UPC) for almost 15 years of support in multiple areas: from graduate teaching, to doing research, to co-advising this dissertation. It is being a pleasure to learn from his unique experience in structural engineering and together walk the doctoral journey. The author also wants to extend his gratitude to professor *Miquel Ferrer* at *UPC* who has played also an instrumental role co-advising this research with his support in multiple areas, especially finite element modeling. Both professors enabled the access to a rich composite slab database of laboratory tests at the *LERMA* that is one of the foundations of this dissertation.

Lastly but equally important, the author would like to give his appreciativeness to professor David Grau at *Arizona State University*, to David Alamillo at *UPC/Cimpress* and to the Cimpress/Vistaprint company. Professor Grau's expertise in article and dissertation development, combined with David Alamillo's patience and supreme skills in complex finite element programming during the last two years, were the last ingredients to complete this dissertation and conclude the 12-year part-time doctoral journey for this author. The dissertation development was possible due to an extensive support from Cimpress/Vistaprint that enabled the author to take a student leave to complete it and funded some of the cost associated with the PhD program.

Abstract

The concrete-steel composite slabs show a complex structural characterization due to the different behaviours at the two materials. The materials are exposed to different deformations, large deflections and complex stresses with still a limited understanding of their micromechanics. Hence, current building codes rely on expensive and tedious laboratory tests that characterize the composite slab failure and the ultimate resistance. The Finite Element (FE) numerical simulations were introduced more than 25 years ago in composite slab studies as a mechanism to validate new design methods and also as an alternative to reduce laboratory tests requirements. However, the simulations historically observed a significant number of simplifications such as reduced scale models or simplified geometries.

This dissertation introduces initially a novel modeling and simulation methodology that enables new insights in the steel deck and concrete slab response for bending. Distinct full-scale finite element models were generated for four commercial steel deck profiles to simulate the laboratory tests. An intense and systematic optimization process was carried out as the computational costs and the simulation files size associated with the initial FE models were significant. The three-dimensional composite models detailed embossment depth and slope, steel thickness, or tilting angle, among several others. Common limitations and simplifications related to steel-concrete contact, adhesion, and cohesion factors in previous research efforts were addressed. Newton-Raphson was the simulation method and enabled the consideration of geometrical and materials nonlinearities. The proposed methodology was validated by comparison of the results from the bending simulations with the actual maximum loads, midspan deflection and end slip values obtained from laboratory bending tests. Based on the robustness of the bending simulations, parametric and boundary conditions analyses were performed through pull-out simulations.

Micromechanics phenomena that could not be observed during laboratory tests were investigated at the full-scale bending simulations. First, the neutral axes and vertical disconnection representations for the steel deck and concrete slab were characterized and subsequently they proved the existence of partial connection between the materials. Second, a new normal vertical tension parameter σ_{shear} was introduced to describe the vertical stresses at the steel deck and the concrete slab. Third, the longitudinal shear strength τ_u was computed for different midspan deflections, loads and friction coefficients. The longitudinal shear failure is the most common failure phenomenon among open rib steel deck profiles and thus multiple studies were performed. The observation of a constant τ_u value at the shear span of the bending test was novel and indicated that the Eurocode 4 Partial Connection Method was not capable to describe the complex longitudinal shear strength behaviour observed from the simulations.

The dissertation concludes with the introduction of a new characterization parameter $\tau_{u,mechanical}$ to assess the composite slab design efficiency. The parameter is defined as the longitudinal shear strength τ_u computed from the simulations for a null friction coefficient. The new parameter proved to accurately characterize the performance of the different composite slabs studied in this dissertation when compared with the maximum loads from the laboratory tests.

The combiation of the novel modeling and simulation methodology with the $\tau_{u,mechanical}$ computation enabled a new design process for steel deck profiles. The process developed an iterative computer-focused approach with the goal to reduce the reliance in the costly and tedious laboratory tests.

Resum

Les lloses mixtes formades per acer i formigó presenten una caracterització estructural complexa degut al comportament diferent dels seus dos materials constituents. Aquests materials pateixen diferents nivells de deformacions, grans desplaçaments i distribucions d'esforços complexes, i avui en dia encara es desconeixen molts dels aspectes fonamentals de la seva micro-mecànica. En conseqüència, les normatives actuals requereixen la realització d'assajos de laboratori per a cada llosa mixta a través d'un procés costós i llarg. La utilització de les simulacions numèriques basades en elements finits per l'estudi de les lloses mixtes es va introduir fa més de 25 anys com a un mecanisme per validar nous processos de disseny i per reduir els exigents requeriments dels assajos normatius de laboratori. Malgrat això, històricament i fins a dia d'avui les simulacions numèriques han patit simplificacions importants, com la realització de models a escala reduïda o amb geometries simples.

La recerca introdueix inicialment una nova metodologia de modelat i simulació en lloses mixtes que aporta noves dades en el comportament del perfil de xapa nervada i de la llosa de formigó. Es van desenvolupar diferents models d'elements finits per a quatre perfils de xapa comercials per replicar els assajos de laboratori de flexió. Inicialment, es va implementar un procés d'optimització sistemàtic en els models d'elements finits, ja que tant els costos computacionals com la mida de les simulacions eren elevats. Els models tridimensionals van incloure la profunditat i pendent de les emboticions, el gruix de la xapa d'acer i l'angle del nervi, entre molts altres paràmetres geomètrics. Es van millorar simplificacions i limitacions habituals observades en recerca publicada anteriorment sobre la interfície formigó-acer, el factor d'adhesió i els factors de cohesió. Es va implementar el mètode de simulació de Newton-Raphson, que va permetre la consideració de no-linealitats en geometries i materials. La metodologia proposada va ser validada comparant-la amb els resultats experimentals dels assajos de flexió. A partir de la solidesa observada en les simulacions de flexió, es van desenvolupar nous models d'elements finits de l'assaig de pull-out per realitzar un estudi paramètric i de condicions de contorn.

A partir de les simulacions, es van analitzar multitud de fenòmens micro-mecànics que no s'havien pogut detectar directament en el laboratori. Primer, es van caracteritzar les representacions dels eixos neutres i la desconnexió vertical entre el formigó i l'acer, i posteriorment es va demostrar l'existència de connexió parcial entre ambdós materials. Segon, es va definir una nova tensió vertical normal σ_{shear} per descriure les tensions verticals observades entre la xapa d'acer i la llosa de formigó. Tercer, es va calcular l'esforç longitudinal a rasant τ_u per a tota la longitud del nervi i per a diferents càrregues. L'observació d'un segment amb valor constant va validar una de les hipòtesis del Mètode de la Connexió Parcial de l'Eurocodi 4. Així mateix, també va posar de manifest que el model mecànic d'aquest mètode no era capaç de capturar la complexitat observada en les simulacions per l'esforç τ_u.

La recerca conclou amb la introducció d'un nou paràmetre de caracterització de l'eficiència de la llosa mixta anomenat $\tau_{u,mechanical}$. Aquest paràmetre es defineix com l'esforç longitudinal a rasant τ_u obtingut de les simulacions amb fricció nul.la. El nou paràmetre va caracteritzar correctament els diferents perfils comercials modelats quan van ser comparats amb la seva resistència última obtinguda en els assajos de laboratori. La combinació de $\tau_{mechanical}$ i la nova metodologia de modelat i simulació genera un nou procés de disseny per lloses mixtes. A través d'un procés iteratiu centrat en simulacions que optimitzen $\tau_{u,mechanical}$, el procés genera una proposta de disseny final de la xapa d'acer, sense la necessitat de realitzar cap assaig al laboratori.

Contents

List of figures

List of Tables

Glossary

A_p : Nominal steel deck profile area

A_{pe} : Effective area of the steel deck profile in tension

b : Width of the composite slab

b_0 : Average width of the rib

b_c : Average width of concrete compressed zone

$[B]$: Deformation matrix

cg : Distance centroidal axis steel deck profile

d_n : Distance between steel deck ribs

d_p : Distance between the centroidal axis of the steel deck profile and the extreme fiber of the composite slab in compression

d_{pi} : Distance between interior embossments

d_{pe} : Distance between exterior embossments

d_s : Distance between the steel reinforcement in tension to the extreme fiber of the composite slab in compression

E: Young modulus

e,e_n : Distance from the centroidal axis of the steel deck profile to the bottom edge

e_p : Distance from the plastic neutral axis of steel deck profile to the extreme fiber composite slab

eps : Newton – Raphson admissible tolerance

f_{cd} : Nominal strength of concrete

f_{cm} : Mean value of the measured cylinder compressive strength concrete

f_{ct} : Cylinder compressive strength of concrete

f_{yp} : Nominal yield characteristic of steel

f_{ys} : Yield strength of tensioned reinforcement

$F_{u,max}$: Maximum load observed at the pull-out or bending simulations

$[F]$: Forces tensor gradient matrix

h : Overall composite slab depth

h_c : Thickness of the concrete above the main flat surface of the top of the ribs at the steel deck profile

h_p : Overall depth of the steel deck profile excluding embossments

h_t : Overall thickness test specimen

h_1 : Height circular embossments

h_2 : Height long embossments

k : Coefficient k of the m-k method

$[K]$: Jacobian / tangent rigidity matrix

L_{total} : Length of the slab

$L_{bending}$: Length bending span

L_s : Length shear span

L_0 : Length of the rim

L_x : Length of interaction

m : Coefficient m of the m-k method

M_{Ed} : Design maximum moment

M_{pa} : Design value of the plastic resistance moment for the steel deck profile

$M_{pl,Rd}$: Design value plastic resistance moment of composite section with full connection

M_{pr} : Reduced plastic moment of the steel deck profile

$M_{p,Rm}$: Maximum resistance moment of the composite section

M_{Rd} : Design resistance moment

M_{test} : Design resistance moment obtained from laboratory results

N_{cf} : Concrete compression force in the concrete flange with full shear connection

N_c: Concrete compression

N_p : Steel deck profile tension resultant

r : Rounding of the edges of the circular embossments

s : Width of the composite slab pattern at the FE models

$\{s\}$: Vector tensional deviations

$s_{deviation}$: Standard deviation from laboratory results

t : Steel deck profile thickness

T_c : Stiffness multiplier for cracked tensile condition

$T_{student}$: T-Student constant (95%, 3-1 samples)

$\{u\}$: Vector nodal displacements

$V_{l,Rd}$: Design value of longitudinal shear resistance

V_s : Maximum shear strength on the BS-5950 *m-k* method

V_e : Maximum shear strength on the ANSI/AASCE 3-91 *m-k* method

V_t : Maximum shear strength on the PSC method; Vertical reaction at the supports for the bending tests

W_p : Plastic modulus steel deck profile

W_t : Measured failure load

x : Distance neutral axis from composite slab upper fiber

x_{pl} : Depth of the plastic neutral axis

z : Lever arm resultant forces N_c and N_s

Greek symbols

β_t : Transfer coefficient of open crack

$\beta_{c:}$: Transfer coefficient of closed crack

ε : Steel deck unidimensional unitary deformation

ϕ : Embossment slope

γ_{ac} : Partial safety factor for steel

γ_c : Partial safety factor of concrete

γ_{VS} : Partial safety coefficient for the ultimate limit state

$\sigma_{1,2,3}$: Principal stress

$\sigma_{xp,yp,zp}$: Principal stress

σ_c *:* Concrete principal stress

σ_{eq} : von Misses equivalent tension at steel deck

σ_{shear}: Normal vertical stress for composite action

η : Degree of shear connection of the composite slab

τ_0 : Initial Longitudinal shear strength, chemical bond

$\tau_{perfect\_bond}$: Longitudinal shear strength at perfect bond between steel deck and concrete slab

τ_u : Longitudinal shear strength of a composite slab determined from testing

$\tau_{u,bathtub}$: Longitudinal shear strength at the expanded shear span area

$\tau_{u,clamping}$: Longitudinal shear strength contribution from the clamped segment minus $\tau_{u,Ls}$

$\tau_{u,Ls}$: Longitudinal shear strength at the shear span unclamped segment

$\tau_{u,m}$: Mean τ_u longitudinal shear strength from all laboratory results

$\tau_{u,mechanical}$: Longitudinal shear strength for $\mu = 0.0$ at the shear span unclamped segment

$\tau_{u,Rk}$: Characteristic longitudinal shear strength

μ : Friction coefficient

μ_d : Dynamic friction coefficient

μ_s : Static friction coefficient

υ: Poison coefficient

1. Introduction

Composite slabs built by a steel deck and in-situ poured concrete are widely used today in construction. The convenience of a light-weight flooring concept with a flexible integration in different building superstructures make them an efficient solution. Yet, composite slabs mechanical characterization and deformations are complex: the concrete suffers cracking and crushing under different loads and boundary conditions that introduce non-linear behaviors. Equally, the slip between the steel deck and concrete slab creates a set of changing boundary conditions between the materials due to the different deformations among them. All these complexities have directed significant research efforts over the last decades to enhance composite slab design methods.

1.1. Description

The main components of the composite slab are the steel deck and the concrete slab that is poured as part of the construction process. The steel deck is commonly installed on top of a superstructure, becoming a lightweight solution compared with a more traditional solid concrete slab. Additional rebaring is commonly required to enhance fire resistance and also to avoid concrete shrinkage during the curing process.

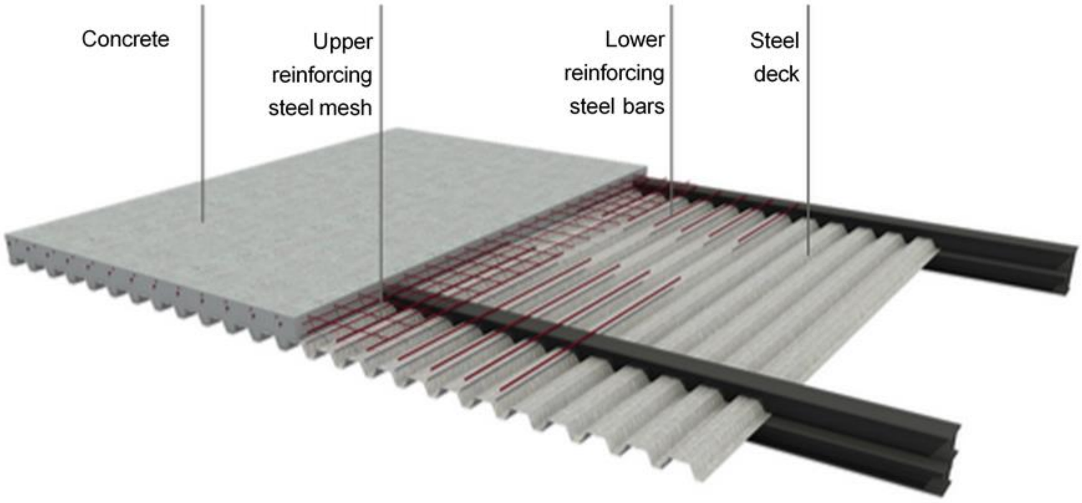

Figure 1.1 *Schematic view for composite slab main components*

The deployment of the composite slab as structural solution was first introduced in 1938 in United States (US) although initially the steel sheet was used only as shuttering for concrete pouring. Gradually, researchers identified the potential benefits to combine the strength of the steel deck as concrete reinforcement. In 1950 a patent was filled in Sant Louis, US, for composite slab design that considered steel strands welded to the steel deck. The steel deck did not include any embossment and therefore additional steel meshes and bars were required to achieve a composite behavior. During the 1960s the first steel deck with embossments was introduced in US while it was not until 1969 that the system was implemented for the first time in Europe. Extensive research performed by Ekberg, Porter and Schuster (Schuster (1970), Porter and Ekberg (1971, 1975a, 1975b)) propelled subsequently the development of the composite slab as structural solution. During 1980s several building codes were issued for composite slab design; for example, the British Standard Institution BS-5950 (1994) and the ASCE ANSI/AASCE 3-91 “Specifications for the design and construction of composite slabs” (1992) that today remain as solid references for the design of composite slabs. Avis techniques developed for multiple structural materials in France in the 1990s, became one of the foundations of the CEN Eurocode 4 (1994) building code that currently is deployed in multiple countries.

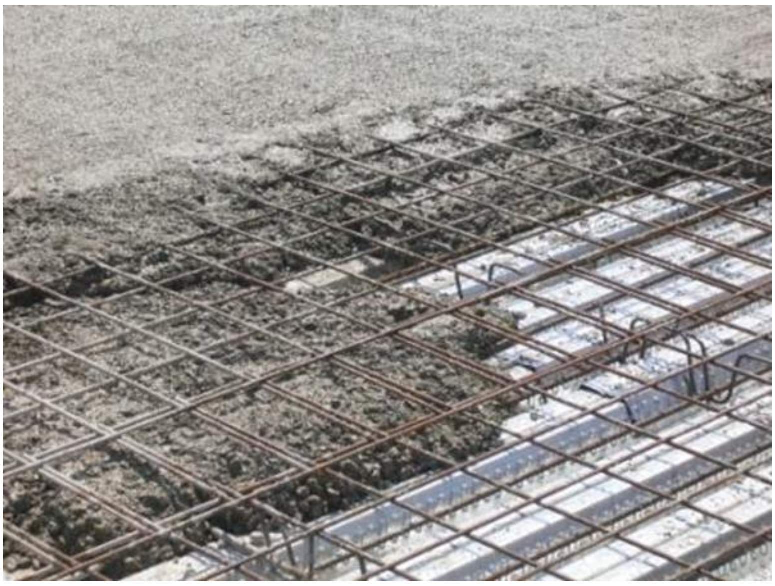

Figure 1.2 *Construction of composite slab*

Among others, the composite slab provides the following advantages:

- The composite action leverages the concrete section for compression stresses while the steel deck is used as a tensile reinforcement. The combined section presents a higher performance with 30-50% less steel weight (Hicks, 2008) and 30% less concrete volume (Nagy, 1998) compared with a more traditional solid concrete slab.
- The steel deck acts as shuttering for the concrete slab pouring hence eliminating the need for expensive and time consuming removable formwork systems. It also acts as a safe working surface for the working crews. This applies for medium span distances and moderate loads, otherwise the steel deck might need to be shored which consequently limits severely most of the composite slab benefits.

- Generally, a less skilled work force in required for the installation of the steel decks and bar reinforcement compared with a more traditional concrete slab.
- Execution speed benefits from the offsite manufacturing process of the steel deck.

On the contrary, the composite slab presents some disadvantages as construction system:

- The steel deck profiles easily adapt to steel and composite superstructures but are less flexible for full concrete solutions.
- The installation of the steel deck units at the construction site requires a given sequence in particular areas as some of the units might be manufactured with specific lengths. That introduces a degree of less flexibility compared with the formwork.
- The performance against fire actions and sound insolation for the composite slabs are significantly below than the equivalent traditional concrete slabs. Additional steel rebaring is added into the composite slab design to improve fire resistance.

A wide range of steel deck profiles, widths and lengths exist today commercially and continue to be developed. The complexity in composite slab design resides in the assurance of the composite action between the two very different materials.

1.2. Problem statement

A composite slab under bending action observes three major modes of failure: flexure, vertical shear and longitudinal shear. However, the longitudinal shear failure is the governing factor for ductile behaviour which is found at the vast majority of open rib steel decks. The longitudinal shear strength also known as shear bond is built by the combination of the initial chemical bond, the steel and concrete friction, and then the mechanical interlock provided primarily by the steel deck embossments. The design purpose of the embossments is to enable an enhanced transmission of the shear forces along the interface of the steel deck and the concrete slab. The understanding of the shear bond behaviour is hence central to most composite slab research: the characterization under different conditions is the basis for all design methods although to date there is limited understanding of its micromechanics.

The Eurocode 4 building code provides design methods for the shear resistance based on semi-empirical methods. The two proposed methods are the *m-k* and the *Partial Connection Method* (PCM) requiring both expensive and time consuming full-scale bending tests to characterize the composite behaviour. The need for those full-scale tests was historically one of the primary motivations for researchers to explore alternative approaches. Reduced laboratory testbeds, Finite Element (FE) numerical simulations and mathematical models were developed during the last decades with a focus in easing the design of composite slabs. Aside of the actual costs to run a large set of tests, the full-scale bending laboratory specimens and the tests preparation require a significant amount of time and face usually variability. Similarly, the specimens for a new steel deck profile need to be produced initially either manually or through a cold rolling process. The industrialized process involved requires a significant up-front investment and provides afterwards limited variance and motivation for future improvements.

The laboratory tests involving smaller specimens, namely pull-out and push-out, provide a much simpler testbed to obtain key parameters for the shear bond behaviour. The reduction in size and the simplicity for the laboratory test enable a more cost efficient approach although those testbeds are not broadly accepted today by building codes. One of the arguments to limit their deployment is the focus in the shear bond behaviour only for one configuration and therefore provides a limited exposure to the composite slab behaviour complexity with different depths and lengths. The full-scale bending tests adopted by the building codes consider specimens of different lengths which are able to capture the shear bond behaviour under different conditions.

Consequently, any advancement in reducing the reliance in full-scale bending laboratory tests and in better understanding the composite slab micromechanics will accelerate and enhance the current design methods.

1.3. Research goals

The FE models simulating the laboratory specimens appeared as a new approach that either in combination with the smaller or directly from full-scale bending testbeds can further simplify the characterization of the composite slab. The development of inexpensive computerized models and the advancements in computational capabilities provide a solid platform to simulate the laboratory tests. The simulations create a flexible testbed for expanded analysis once they are calibrated. However, little research has been reported in open literature on the accurate modeling of the geometrical and physical properties of full-scale bending specimens. Most research based on FE was performed with either simple models that only include a portion of the composite slab such as a pattern/rib or with a significant number of simplifications for the steel – concrete interface. Consequently, the inclusion of the detailed embossments geometry within full-scale FE models sets the foundation for a more comprehensive view of their micromechanics and subsequently, the overall composite slab behavior. The aim of this research is to advance in the characterization of composite slabs through three complementary goals:

Advanced finite element modeling for full-scale composite slab laboratory tests

Development of a novel methodology for the accurate FE modeling of full-scale composite slabs. Based on experimental laboratory results, Eurocode 4 standardized specimens are modelled for four commercial steel deck profiles. The FE models create an opportunity to study the complex characteristics of the composite slabs in non-measurable areas based on the strong agreement with laboratory results. The geometry of embossments is accurately modeled and hence common past simplifications at the steel-concrete interface are no longer necessary. Subsequently, pull-out FE models are developed based on the FE bending models and without the need to perform any laboratory test.

Micromehcanics in composite slabs: enabler of a deeper knowledge of complex stress behaviour

Development of a few new representations for composite slab micromechanics supported by the numerical simulations. Particularly, the longitudinal shear strength τ_u and a newly defined vertical normal stress σ_{shear} between the steel and concrete that frequently define the overall composite slab shear resistance. Furthermore, the steel deck and concrete slab neutral axes position, vertical separation between the two materials and some strains distribution in particular areas for the full-scale bending test. Based on the different micromechanics characterization, this study further develops a parametric analysis among some key steel deck geometry parameters. The accuracy observed at the FE models once compared with the laboratory results enables this new approach to describe complex stresses distributions in composite slabs.

New composite slab characterization parameter: $\tau_{mechanical}$

A new characterization parameter $\tau_{u,mechanical}$ is proposed to characterize the embossment steel deck design efficiency. The parameter, based on the findings from the longitudinal shear behaviour at the simulations, capture the complex three-dimensional phenomena that occurr at the shear resistance. The parameter is defined as the longitudinal shear strength τ_u computed from the simulations with a friction coefficient $\mu = 0.0$. Additionally, a design process for steel deck profiles is proposed that combines the novel finite element methodology and the $\tau_{u,mechanical}$ values. Based on sequential and iterative steps, the computer-focus design process enables an efficient steel deck profile performance while reduces the reliance in the costly and tedious laboratory tests.

1.4. Scope and approach

This research leverages first the extensive composite slab database built at the *Laboratori d'Elasticitat i Resistència de Materials* (LERMA) during the last 15 years. The information available captures dozens of laboratory bending specimens tested for multiple commercial steel deck profiles. Advanced FE models are created that replicate the full-scale bending tests for four commercial steel decks. Common past simplifications are avoided with the introduction of the accurate geometry and material properties for the steel deck and concrete slab. The good agreement observed between the simulations and the tests results enables a first set of preliminary results around the robustness of the simulations. Subsequently, pull-out laboratory simulation are created for one of the commercial steel deck profiles based on the bending specimens without the need to perform any laboratory test.

Second, several characterizations for one of the commercial steel decks studied are performed based on the results from the bending laboratory tests and the implementation of different building codes. The application of the different building codes and design methods, for the same laboratory tests and steel deck profile, highlights some discrepancies among them. The lack of a mechanical model for the codes based on the *m-k* method, or the slightly different interpretations for the PCM method, provides a first sense on the complexity for the composite slab design and reinforces the need to understand its micromechanics.

Third, in-deep analyses are performed in critical sections to characterize the composite behaviour for various load configurations and in different spans for the bending simulations. Several stresses representations, materials separations and deformations generate novel visualizations for composite slab micromechanics. Additionally, comparisons between FE models that include different shear spans and lengths, friction coefficients and loading schemes are created to improve the knowledge for composite slab characterization.

Lastly, the research leverages the findings in micromechanics to discuss areas of improvement for the current design methods. A new shear bond characterization parameter is proposed that captures the complex longitudinal shear strength distribution at the composite slab. The new parameter, named $\tau_{u,mechanical}$ in combination with the novel FE modeling approach, generate a new design process to ensure efficient embossment design at the steel deck with less reliance in laboratory tests.

This research approach differs from other authors as it focuses first on the development and understanding of the composite slab micromechanics to subsequently evaluate macro-behaviors. Past research focused extensively first in the macro-behaviors of the composite slab specimens to subsequently move to FE modeling for some punctual aspects. In order to build this approach, an advanced modeling approach was required. More than 5 Terabytes of data were computed for the approximate 50 simulations developed. All simulations combined exceed a computational time of 8,300 hours with an average duration of 2 days per simulation. The hardware used was a Intel-based Xeon CPU E5-1620 3.60GHz and 8Gb RAM common today in professional engineering environments.

1.5. Structure of this report

This dissertation is organized in 8 chapters. The following chapter 2 provides the reader with a literature review for composite slab design methods and FE modeling approaches. The testbed for the laboratory bending specimens is described in chapter 3. Chapter 4 shows a detailed overview for the FE novel methodology developed. Then, chapter 5 outlines the results from the numerical analyses and simulations. A discussion for current building codes and how the new composite slab micromechanics influence a new characterization parameter follow in chapter 6. Chapter 7 highlights the research conclusions and recommendations. Finally, chapter 8 talks about future research developments

Appendix A includes a detailed description of the FE commands for a simulation so it can be easily replicated. The author plans to share all FE models commands online to further encourage the development of FE tools in composite slab research.

2. Literature review: composite slab design methods

This chapter introduces initially the main components, material properties and the different failure modes for composite slabs. Subsequently, a review of the current design methods included in several building codes is performed. To conclude the chapter, a literature review for composite slab new design methods and FE modeling is conducted.

2.1. Definitions and structural characterization

2.1.1 Composite slab components

The basic components of the composite slab are the steel deck and the concrete slab, commonly accompanied by an upper reinforcing steel mesh and lower reinforcing steel bars. Complementary to the basic components, composite slabs sometimes also include connectors.

Steel deck profile

The steel deck is manufactured offsite from a galvanized steel coil throughout a cold forming process. The base material transits between rollers that gradually conform the final steel deck profile while it is hardened due to the process infused deformations. Embossments are created as part of this cold forming process, in which their shapes, deepness and orientations are transferred to the final product manufactured. Main parameters for the steel deck are summarized below.

- Steel grade (based on EN 10326): S220, S250, S280, S320, S350
- Thickness: t = 0.75 - 1.5 mm
- Depth: h_p = 40 - 120 mm
- Width: b = 700 - 900 mm
- Rib width: d_n = 150 - 300 mm

Concrete

All current building codes allow the use of both regular and lightweight compositions for the concrete slab. Particularly, Eurocodes allow C20/C25 grades for regular and LC20/22 and LC60/66 for lightweight concretes. The deployment of additives is common as the pouring mechanism frequently require the concrete to be pumped.

Additional steel rebaring

Steel rebaring is an important component for the composite slab. Three different types are commonly installed as part of the construction process:

- Upper reinforcing mesh: placed near the upper side rib of the steel deck, it limits concrete shrinkage, cracking and crushing, first as part of the concrete curing process and subsequently under service conditions.
- Upper reinforcing bars: placed at and near composite slab supports to absorb tensile efforts from negative moments.
- Lower reinforcing bars: placed at the bottom side of the steel deck rib, the bars provide enhanced performance under fire action. Exceptionally, they also provide additional steel section for tensile efforts under composite action in case that the steel deck has insufficient capacity in partial connection.

End anchorage connectors

The connection between the steel deck and the supporting superstructure is commonly performed through high-pressure metallic nails. However, for more complex distributions, end anchorages are also common which enable a higher degree of interaction between the composite slab and the superstructure. The end anchorages introduce also an enhanced performance between the steel deck and the concrete slab due to an improved mechanism to avoid the relative slip between them. The most common end anchorages are the welded studs named *Nelson* and the thin-profiled components (usually named *Hilti* as the manufacturer that distributes them) both depicted in Figure 2.1.

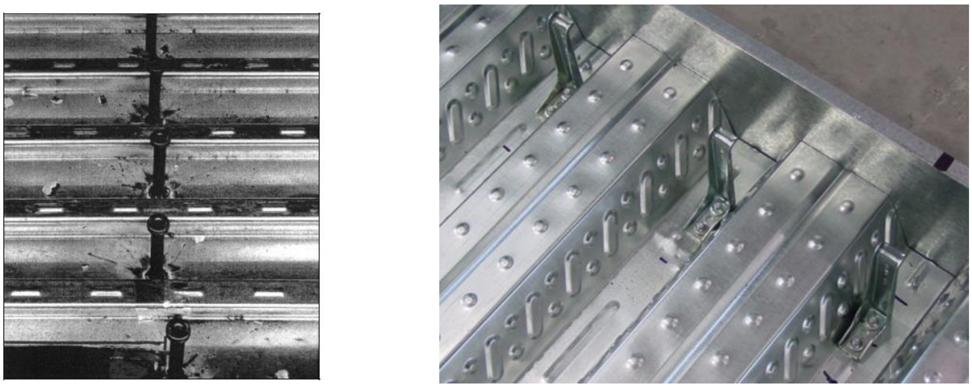

(a) (b)

Figure 2.1 *Composite slab connectors typologies (a) Nelson and (b) Hilti*

2.1.1 Steel deck and concrete slab interaction

The steel deck needs to transmit the longitudinal shear forces at the interface with the concrete slab to ensure a composite behavior. Several mechanisms co-exist to enable that transmission as summarized in Figure 2.2 and below.

- Initial chemical bond between materials.

- Mechanical interlock provided by embossments and indentations.
- Frictional interlock for profiles shaped in re-entrant form.
- End anchorage provided by welded studs or another type of local connector.
- End anchorage by deformation of the ribs at the end of the steel deck.

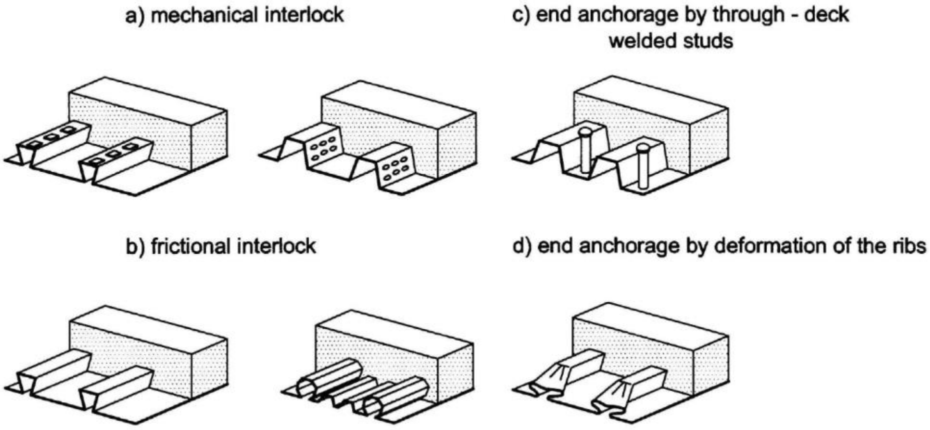

Figure 2.2 *Typical forms of interlock in composite slabs, adapted from Eurocode 4 (1994)*

A composite slab under bending action presents different behaviors depending on the degree of shear strength transmission between materials, namely the connection degree η. The interaction can be categorized in three groups:

- Full connection ($\eta = 1$): no relative slip occurs between the concrete slab and the steel deck. Longitudinal deformations for both materials are considered uniform at the ultimate state and equal and therefore both materials are considered to perform as a unique section in perfect bond.
- Partial connection ($0 < \eta < 1$): certain slip occurs between the concrete slab and the steel deck. Longitudinal shear forces are still transmitted between materials however it cannot be assumed that deformations are continuos between both materials. Steel deck and concrete slab have different neutral axes.
- Null connection ($\eta \approx 0$): no shear forces transmission exists between materials and consequently they are considered as completely independent structural elements. The assembly of the steel deck and concrete slab should not be considered as a composite structural element. The null connection is usually observed once the ultimate resistance load is exceed with large end slips between the steel deck and the concrete slab.

2.2. Failure modes

A composite slab is subjected to three main failure modes at ultimate limit states in the bending laboratory testbeds: flexure, longitudinal shear and vertical shear. Figure 2.3 illustrates the sections that are affected by each failure mode. Complementary, Figure 2.4 depicts a visual representation of the failure modes under different composite slab geometry conditions. The main parameters for failure characterization are the experimental shear force V_t and the shear span length L_s which are obtained as part of the laboratory bending tests. Additional geometrical parameters such as the slab width b, the steel deck centroidal axis distance d_p and the steel deck cross-sectional nominal area A_p among others, characterize the failure mode as detailed herein.

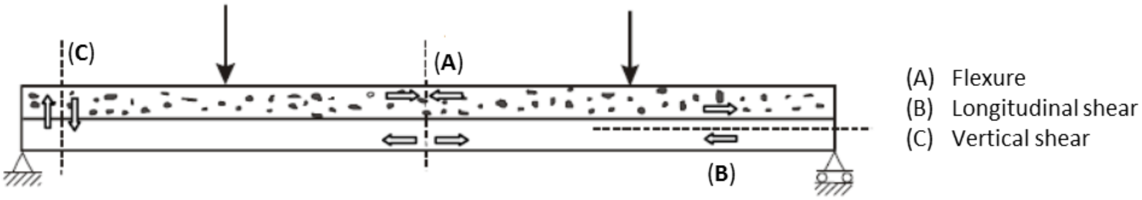

Figure 2.3 *Failure mechanisms and affected cross sections*

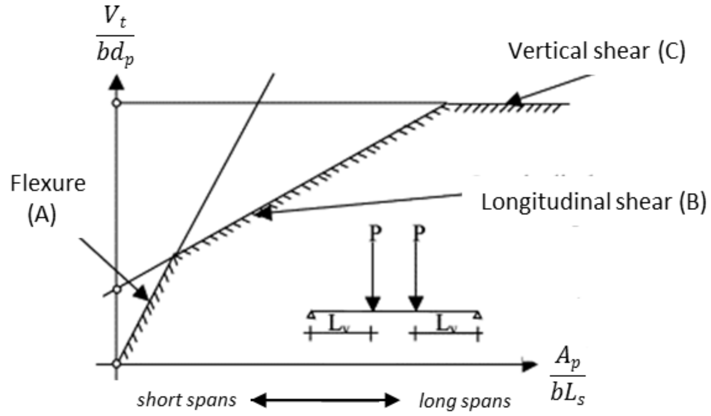

Figure 2.4 *Visual representation failure mechanism for composite slab*

2.2.1 Flexure

Flexure failure occurs in a composite slab presenting full connection $\eta = 1$ and in which the moment M_{Ed} at the center section of the span exceeds the ultimate resistance $M_{pl,Rd}$ of the composite section. Generally, this failure appears in cases with a reduced relationship between shear and flexure efforts, frequently observed in composite slabs with long spans and small depths.

2.2.2 Longitudinal shear

This failure mode is the most common due to the existence of partial connection $0 < \eta < 1$ between the steel deck and concrete slab. The capacity of the different transmission mechanisms for the longitudinal shear (see Figure 2.2) is exceeded and therefore a relative slip between materials exists. Diagonal concrete cracks are usually observed near the section where the load is applied and different end slips at the materials can be identified. The failure mode is caused fundamentally due to four different phenomena that are introduced herein and which are extensively analyzed throughout the simulations performed in this dissertation.

Clamping phenomenon and steel deck longitudinal liberation

The longitudinal slip between the concrete slab and the steel deck is converted into a local transversal bending at the steel deck in a clamping process. Figure 2.5 summarizes schematically the conversion. The newly generated transversal bending has a strong correlation with the amount of shear transmission between steel and concrete that eventually contributes to the overall composite slab performance.

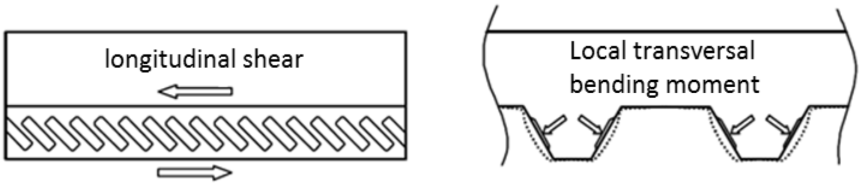

Figure 2.5 *Transversal bending, adapted from Ferrer (2005)*

At the ultimate longitudinal shear resistance, the steel deck deflection and the relative slip are large enough to release the embossments positions from the concrete. The steel deck suffers then a liberation from the concrete slab. The failure mechanism is defined by the transversal bending resistance of the steel deck profile.

Vertical separation

This failure phenomenon is most common for open rib steel sheets such as the one represented in Figure 2.6. The titling angle at the lateral sides of the steel rib generates a vertical force component due to the interaction with the embossments. That component induces a vertical separation between the steel deck and the concrete slab which implies a decrease of their geometrical interaction. As a consequence, the composite slab observes a reduction in shear resistance. The only way to counterbalance the vertical separation is throughtout embossment designs that are capable to develop a certain retention angle.

Vertical separation is commonly studied in combination with the longitudinal unleashing. The actual phenomenon at the composite slab can be characterized by the descomposition in longitudinal and vertical separation. Figure 2.6 shows a composite slab laboratory specimen that featured both phenomena. It is important to note that re-entrant steel deck geometries such as the ones represented in Figure 2.2(b) reduce significantly the presence of this failure.

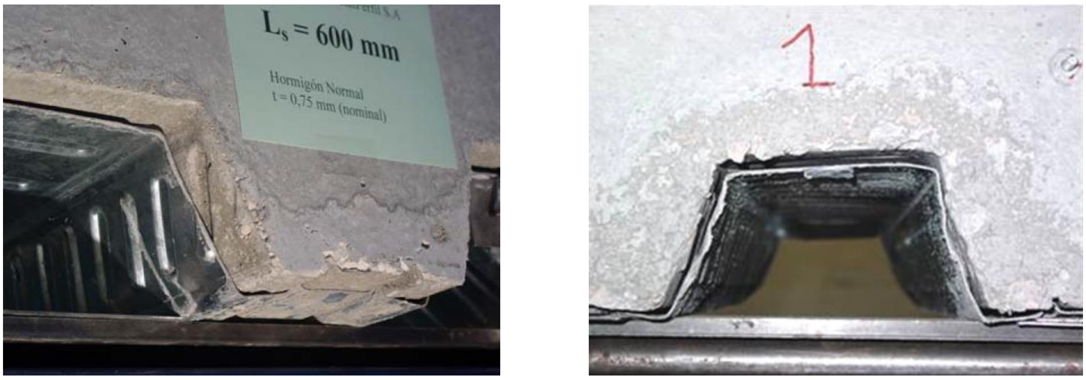

Figure 2.6 *Laboratory specimen end slip and vertical separation, LERMA (2006)*

Local concrete crushing and cracking

Composite slabs with high performance in longitudinal and vertical separations might be exposed to the concrete crushing and cracking phenomena. The concrete slab might deteriorate punctually in areas with high concentration of stresses. To avoid this phenomenon, regular concrete strength as opposed to lightweight concrete and special reinforcement at the affected areas are common practices. The following list summarizes most common forces originating concrete crushing and cracking:

- Vertical tension at the bottom side of the rib for re-entrant steel deck profiles.
- Longitudinal shear at the bottom side of the rib for re-entrant steel deck profiles.
- Concrete shear at the base of the embossments.
- Concrete sections around embossments.
- Local compression at the contact zones.

Embossments flattening

A steel deck shape that includes inward embossments into the concrete slab with reduced slope might observe a normal reaction coming from the clamping phenomenon. The perpendicular effort at the rib lateral sides introduces a significant reaction and therefore can flatten partly or totally the embossment geometry. That softness in embossments geometry reduces also the composite slab capability for shear bond.

2.2.3 Vertical shear

This failure mode appears located at the support areas and it is originated due to a high concentration of shear forces. Among the different failure modes, it is not frequent and commonly only appears for composite slab compact configurations with high thicknesses and short spans.

2.2.4 Punching shear

Similar to vertical shear, the punching shear failure is not common except for special loading configurations in composite slabs. The existence of any significant load concentrated in a reduced area needs to be analyzed individually. Concretely, a critical perimeter of influence needs to be identified to subsequently analyze the steel deck and concrete slab resistance in front on the relevant forces generated.

2.3. Ductile and brittle behaviours

A composite slab can present two different behaviors at longitudinal shear failure. Brittle behavior appears suddenly and generally without important deformations: an excessive rigidity from either one or various steel – concrete transmission mechanisms limits the capability to develop an uniform shear resistance distribution. Oppositely, ductile behavior shows a progressive and predictable path with visible deformations. Both the steel deck and the concrete slab are capable to uniformly distribute the shear resistance and retain their individual performance against relative slip.

Most building codes provide boundary conditions to classify the behavior. For example, Eurocode 4 stipulates as ductile if the failure load exceeds the load causing a recorded end slip of 0.1 mm by more than 10%. Additionally, if the maximum load is reached at a midspan deflection exceeding L/50, the failure load should be taken as the load at the midspan deflection of L/50. The behaviour classification is relevant as design methods differentiate the composite slab characterization based on it.

2.4. Building codes and specifications

The composite slab design method *m-k* is based on the shear bond concept and it is currently implemented at the vast majority of composite slabs building codes ANSI/AASCE 3-91, Canadian Sheet Steel Building Institute CSSBI 12M-96 (1996), BS-5950 and Eurocode 4. The method was initially developed by Schuster (1970) and subsequently improved by Porter and Ekberg (1971, 1975a, 1975b). In order to overcome some of the *m-k* method limitations, namely the lack of a mechanical model, researchers developed the *PCM* based on the plastic analysis of the material sections and the use of stress blocks for the steel deck and concrete slab. The method frames the shear bond behavior of the composite slab throughout the displacements and relative deformations of the steel deck once the concrete slab slips over it. The method was initially developed by Stark (1978) and improved afterwards by Stark and

Brekelmans (1990), Bode and Sauerbon (1992), Bode et al. (1996) and Bode and Dauwel (1999). The method was adopted by the Eurocode 4 code initially as an annex in 1992 and subsequently introduced as a design method.

2.4.1 *m-k*

The method determines the longitudinal shear resistance of composite slabs with mechanical or frictional interlock but not for end anchorages. It requires full-scale bending tests from which the longitudinal shear strength is correlated linearly with the main composite slab geometry parameters. A set of at least two different groups of specimens A and B with different shear spans L_s are required to obtain the *m* (slope) and *k* (initial value). The design relationship is formed by the linear regression of these characteristic values for groups A and B as illustrated in Figure 2.7.

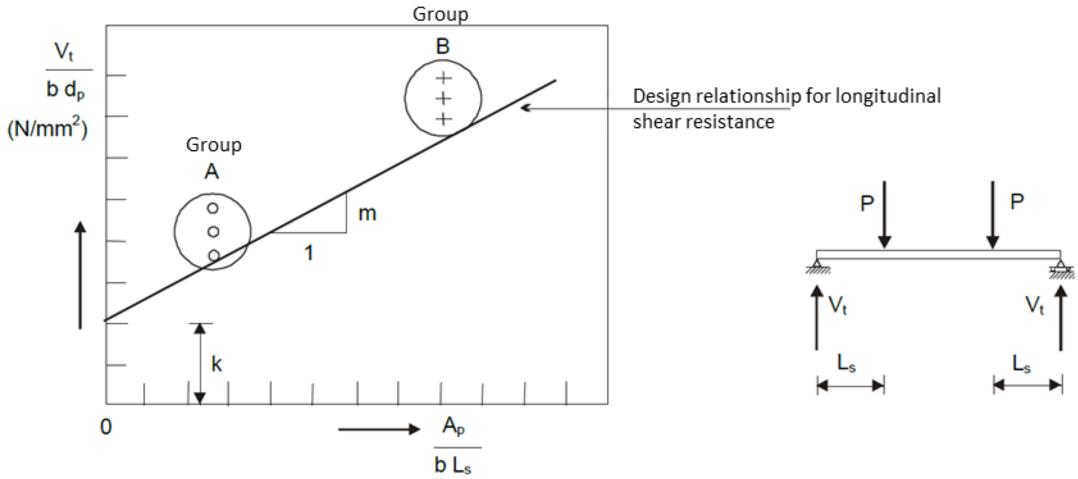

Figure 2.7 *Evaluation of test results and deployment m-k method*

The method can be applied when slab behaviour is either brittle or ductile and the failure is produced due to longitudinal shear. The value of the representative experimental shear force V_t is calculated from the value of the failure load W_t as follows:

$$V_{t,ductile} = 0.5W_t \tag{2.1}$$

$$V_{t,brittle} = 0.8V_{t,ductile} \tag{2.2}$$

The maximum design vertical shear V_{Ed} should not exceed the design shear resistance $V_{t.Rd}$ calculated for a width of slab *b*. Different building codes apply similar relationships but with some small differences between them. Eurocode 4 approach is described in Equation 2.3.

$$V_{Ed} \leq V_{l,Rd} \qquad V_{l,Rd} = \frac{b \cdot d_p \cdot \left(\frac{m \cdot A_p}{b \cdot L_s} + k\right)}{\gamma_{vs}} \tag{2.3}$$

where,

$V_{l,Rd}$ design value of the resistance to shear

A_p nominal cross-section area of the steel deck profile

L_s shear span; defined as:

- $L/4$ for uniformly distributed loads along the total span
- Distance between the applied load and the nearest support for two symmetric loads
- Distance based on observation from full scale tests

γ_{VS} partial factor for design shear resistance

The building code ANSI/AASCE 3-91 proposes Equation 2.4. The formulation is complemented by Equation 2.5 that provides the characterization for cases in between the span lengths tested in laboratory.

$$\frac{V_e}{b \cdot d_p \cdot \sqrt{f_{ct}}} = \frac{m \cdot A_p \cdot d_p}{L_s \cdot \sqrt{f_{ct}} \cdot b \cdot d_p} + k \tag{2.4}$$

where,

f_{ct} Concrete cylinder resistance

$$\Phi V_n = \Phi[b \cdot d \left(\frac{m \cdot \rho \cdot d}{l'_i} + k \cdot \sqrt{f'_c}\right) + \frac{\gamma \cdot W_s \cdot l_f}{2}] \tag{2.5}$$

Similarly, the building code BS-5950 proposes Equation 2.6:

$$V_s = b \cdot d_p \left(\frac{m_r \cdot A_p}{b \cdot L_s} + k_r \cdot \sqrt{\frac{f_{ck}}{0{,}8}}\right) \tag{2.6}$$

Several authors researched the benefits and limitations of the *m-k* method implementation. Particularly, Bode and Suerborn, and Hicks highlighted the lack of a mechanical model reaching a few conclusions:

- The method lacks a mechanical model and hence does not allow to extract the shear bond contribution from each shear transmission mechanism.
- The contribution from additional steel rebaring cannot be quantified without the execution of new laboratory tests.
- The testbed is the same for both brittle and ductile behaviours and therefore is not possible to isolate that influence in the composite slab characterization. However, the method enables both type of behaviours as opposed to others that are limited to only ductile behaviours.

In a similar framework, Seleim and Schuster (1985), Daniels (1988) and Bode and Suerborn performed studies that highlighted the limited influence from the concrete compressive strength for the most common typologies in composite slabs. That finding was captured by Eurocode 4 which eliminated concrete influence at the formulation and it is nowadays the main difference with ANSI/AASCE 3-91 in composite slab design.

2.4.2 Partial Connection Method

The method is based on the concept of a uniform longitudinal shear strength τ_u between the steel sheet and concrete slab at the shear span L_s. The maximum bending moment from the laboratory test M_{test}, in combination with the theoretical ultimate limit states from each material between null $\eta = 0$ to full $\eta = 1$ connection, enables the definition of the characterization curve depicted in Figure 2.8. The method is based on the hypothesis that the concrete slab and the steel deck have relative slip and that generates a uniform longitudinal shear strength τ_u as defined in Equation 2.7. The mechanical model mirrors the principles realized in the shear connection characterization in composite beams with flexible connectors. This hypothesis is extensively analyzed and some findings developed as part of this dissertation.

$$\tau_u = \frac{\eta \cdot N_{cf} \cdot}{b \cdot (L_s + L_o)} \tag{2.7}$$

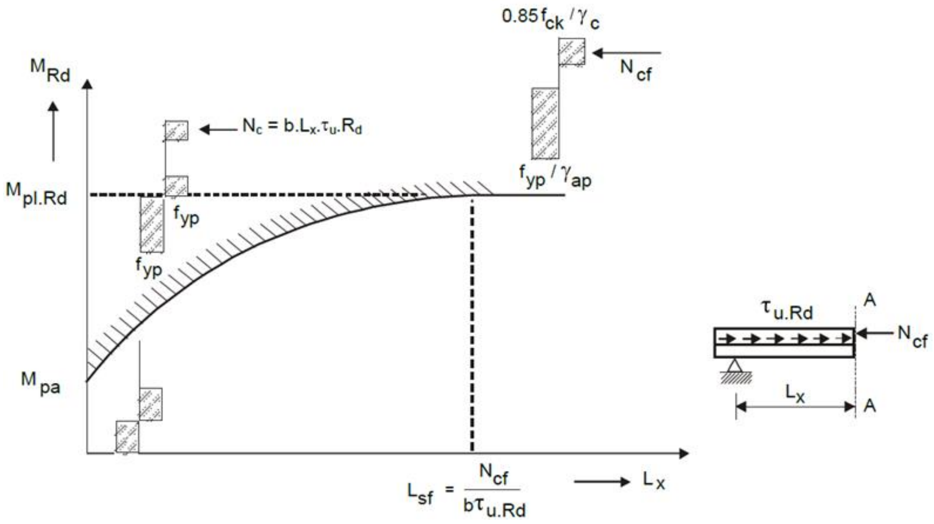

Figure 2.8 *PCM – characterization of degree of shear connection from M_{test}*

where,

f_{cm}	mean value of the measured cylinder compressive strength concrete
f_{yp}	yield strength of structural steel
M_{pa}	plastic resistance moment of the effective cross-section of the steel deck
$M_{p,Rm}$	maximum resistance moment of the composite section
N_{cf}	compressive normal force in the concrete flange with full shear connection

The method deployment is restricted to composite slabs with ductile behavior. However, opposed to the *m-k* method, PCM allows the isolation of the contribution of some of the shear bond transmission mechanisms such as the additional rebaring or connectors. Some other elements though are not possible to isolate as the contribution from the clamping phenomenon or the friction generated at the supports.

2.5. New and enhanced design methods

Based on the limitations from the *m-k* and PCM methods, several authors explored over the last four decades different approaches for composite slab characterization. Some of the new developments also included the development of innovative FE models which are reviewed separately at the next section 2.6.

Researchers from the West Virginia University developed and empiric model to characterize de bending moment resistance for composite slabs (Luttrell and Davidson (1973); Luttrell and Prasannan (1984); Luttrell (1986)). The method assumed that the ultimate resistance was achieved once, at the steel deck, the lower side of the rib reached the yield strength of the structural steel. Through the measurement of parameters at the laboratory tests, the authors proposed a new set of equations though were limited to certain steel deck profiles. Seleim and Schuster presented a new design approach for the longitudinal shear failure that was incorporated into the CSSBI building code. The method was based on a multivariant regression analysis and considered as a key component the fact that there is relative slip between the concrete slab and the steel deck prior the ultimate resistance is achieved.

Patrick and Bridge (1994) developed in parallel both a new design method based on the *PCM* and a simplified laboratory testbed named *slip block* test. The parameters of shear strength and support friction were obtained from the laboratory specimens which were input into a new formulation for the maximum moment resistance. Veljkovic (1996a, 1996b) developed a new design method named *Three Parameters Partial Connection Strength Method (3P PCSM)* based on FE models. The author leveraged three elemental testbeds -(1) *push-out,* (2) *slip block* and (3) *tension-push-* to characterize the initial shear resistance, the friction parameters and a reduction function of steel deck mechanical yield in a method that resembled the *m-k* method. The same author Veljkovic (1998, 2000) published subsequently an enhancement of the *3P PCSM* method as he realized that the longitudinal shear strength increased with more uniform load distributions.

An (1993) introduced an equilibrium forces method to characterize the shear resistance – end slip mechanism throughout a simplified testbed. Based on several laboratory tests, the author identified the most critical parameters for the longitudinal shear failure. Subsequently, Crisinel and Marimon

(2004) developed a design method named *New Simplified Method* based in the combination of results from standard full-scale bending and pull-out tests. The simple calculation model described a moment–curvature relationship at the critical cross-section of a composite slab. The method modelled the steel deck as an inverted I-shaped steel beam, while the concrete was modelled as rectangular block. Figure 2.9 summarizes visually the design method.

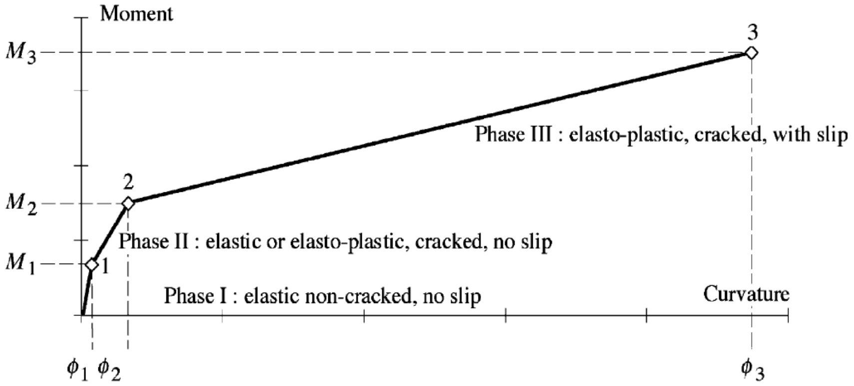

Figure 2.9 *New Simplified Method, adapted from Crisinel and Marimon (2004)*

Bode and Sauerborn and Johnson (2004) reached a similar conclusion in regards the relative slip between the concrete slab and the steel deck: the end slip values were significantly high and hence supported the PCM hypothesis of a uniform and constant longitudinal shear strength τ_u. In parallel, research performed by Abdullah (2004) and Abdullah and Easterling (2009) highlighted some of the limitations of the PCM. Concretely, the PCM provided a better characterization for configurations in which the geometries and the loads for the composite slab were similar to the laboratory specimens tested. In that framework, Abdullah proposed a design method based on a variance of the equilibrium forces approach previously proposed by An. The curvatures from the concrete slab and the steel deck were assumed equal under bending efforts and subsequently an equation for the maximum bending moment resistance developed. Subsequently, Abdullah and Easterling incorporated the slenderness as a key parameter to define the shear bond for composite slabs. Figure 2.10 illustrates the stresses distribution assumed that enabled the authors the characterization of the composite slab behaviour.

Researchers Patrick and Bridge , and Calixto et al (1998) also leveraged a constant longitudinal shear strength τ_u as a pillar for new developments in the composite slab design methods although could directly neither measure nor visualize it.

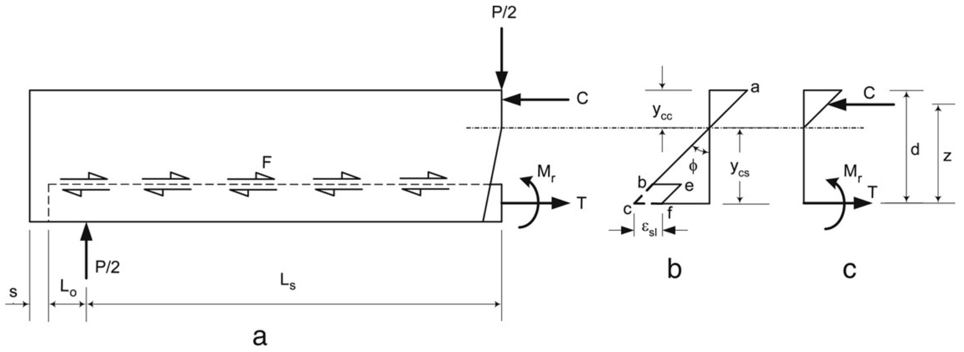

Figure 2.10 *Visual representation τ_u, adapted from Abdullah and Easterling (2009)*

Vainiunas et al. (2006) proposed a new methodology for the interface steel – concrete based on the theory of built-up bars. The proposed method evaluated the influence of both plastic deformations of the concrete layer and cracks in the concrete on the rigidity of this layer and of the whole slab as well. Similarly, Tsalkatidis and Avdelas (2009) and Tzaros et al (2010) developed also complex mathematical models for the steel-concrete contact problem. Nonmonotone material laws with hemivariational inequalities and nonconvex-nonsmooth optimization simulations for unilateral contact problems with friction were developed respectively. Although the mathematical models did not introduce a new design method per se, they did contribute in the understanding of the complex longitudinal shear strength characterization.

2.6. Finite element modeling

Both *m-k* and *PCM* design methods are semi-empirical and therefore require full-scale bending laboratory tests to define the composite slab structural behaviour. The dependency on costly laboratory tests incentivized researchers to develop new simplified design methods and to propose enhancements to the existing ones as described in previous section 2.5. FE models became a key component for some new developments as they created a solid framework to test multiple configurations in advance. They also enabled concurrently the expansion from initial results to more complex configurations without the need of additional full-scale tests. The computational nature at the FE models allowed to test virtually almost any steel deck profile and configuration. The steel deck profile as a cold formed structural component could be modified at the computer model to achieve incremental improvements and therefore avoid the production of costly manufacturing components for the cold roll forming process.

Materials definition as non-linear for both the steel deck and concrete slab, as well concrete elements with the capacity of cracking and crushing became more common as the computational cost decreased. However, either the lack of geometrical embossments definition, a set of simplified contact surface assumptions, or a reduced scale modeling report a solid but simplistic view for composite slabs micromechanics to date in FE models.

Daniels and Crisinel (1993) introduced a first FE concept to validate a new simplified design method for composite slabs based on a reduced scale test. The FE model included material non-linearity and it was based on a simplification of the mechanical model found in reinforced concrete beams. Experimental data was based on pull-out specimens and the FE models allowed the analysis of both single and multiple spans configurations. Researcher An analyzed the characterization of the composite slabs through two-dimensional FE models using ABAQUS software for the design method based on the equilibrium forces reviewed in section 2.5. Both the steel deck and the concrete slab were modelled as simple 2-node beam elements, while their interaction was introduced as a spring element with an array of equations as boundary conditions.

Veljkovic introduced for the first time the three-dimensional FE models at the composite slab behaviour analysis for the *3P PCSM* design method validation. The steel – concrete interface was characterized by a special nodal contact element at the DIANA software with experimental data obtained from push-out tests while the geometries were simplified without embossments. Widjaja (1997) also deployed FE to validate two new analytical models for composite slabs design. The models were built replicating a simple supported beam scheme in which a single rib pattern was modelled and the steel-concrete interface was introduced as a spring. Adjacent rib patterns were introduced as spring boundary conditions.

Abdullah in 2004 proposed the modeling of a complete composite slab rib leveraging experimental data from pull-out tests. The ABAQUS software was deployed with three-dimensional non-linear FE components while the steel-concrete contact was implemented through radial-thrust connector elements. The vertical interaction between the steel deck and the concrete slab was not implement as it was implicitly assumed at the connector element for the shear bond property. Subsequently, Abdullah and Easterling deployed FE models for the development of the design method reviewed in section 2.5 that introduced the slenderness as key parameter for the composite slabs. The main parameters for the shear resistance behaviour were obtained from bending tests and captured as shear bond stress – slip curves. The curves were introduced subsequently into the FE analyses to model the steel-concrete contact and therefore again the need to introduce the materials accurate geometries was avoided.

Lòpez et al (2007) and Seres (2012) developed FE models for the analysis of the steel deck cold forming process. In order to get the embossments into the deck, the steel deck goes through a rolling process that hardeners the material. The researches proved some sensitiveness at the steel yield which enabled some parametric analysis for the minimum distance between embossments and the physical limitations of the overall rolling process for common steel deck thicknesses. Although the studies were not focused on composite slabs, the models captured the accurate geometry of the steel deck components and leveraged the FE to complement the laboratory tests.

Ferrer (2005) developed FE models for one composite slab pattern to visualize its structural micromechanics. Figure 2.11 highlights the approach for the modeling. That new approach based on the composite slab micromechanics, even though for a small portion of the rib, allowed a parametric analysis for main geometrical parameters at the steel deck such as the embossments shape, height and density. Based on the findings in one pattern, the author expanded them to a complete pull-out composite slab geometry and suggested a new design for a steel deck profile. The accurate FE modeling removed the need to introduce any simplification at the steel – concrete interface for the first time, although the scope was limited to only one pattern.

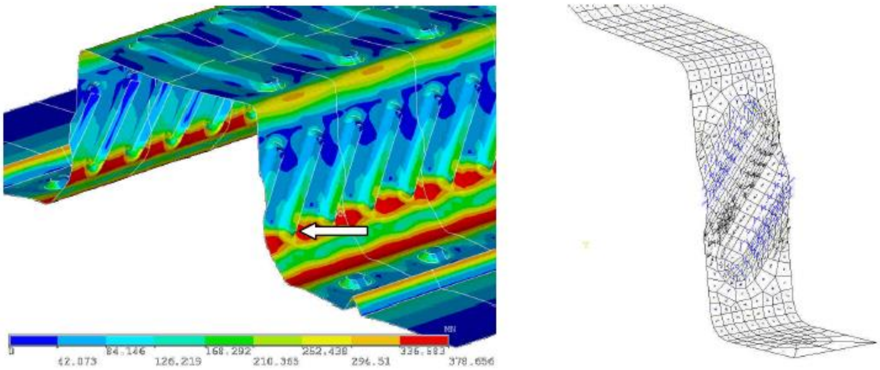

Figure 2.11 *FE geometry accurate modeling for composite slab patterns, Ferrer (2005)*

Chen and Shi (2011) created FE models for the full-scale bending laboratory tests. The authors proposed the modeling of the longitudinal shear strength as a contact problem, introducing the adhesion and friction as a Coulomb theory behaviour. Chen and Shi argued that the three-dimensional FE models developed constituted a universal FE model capable of capturing any composite slab profile once the right contact parameters from experimental bending and pull-out tests were input. The authors leveraged the laboratory tests previously performed by Widjaja and Abdullah and Easterling to validate the robustness of the simulations. The need to introduce the detailed geometry of the steel sheet and concrete slab was removed using contact and adhesion parameters. Figure 2.12 illustrates the modelling approach implemented at the steel-concrete interface.

Gholamhoseini et al (2014) analyzed four steel deck profiles common in Australia. As part of the analyses, three-dimensional FE models build with the ATENA 3D software were deployed. The author divided the overall simulation in several steps and for each one, specific FE parameters and boundary conditions were implemented to better represent the actual composite slab behaviour. The contact between the steel deck and concrete slab was modelled throughout a contact element based on the Mohr-Coulomb criterion with tension cut off.

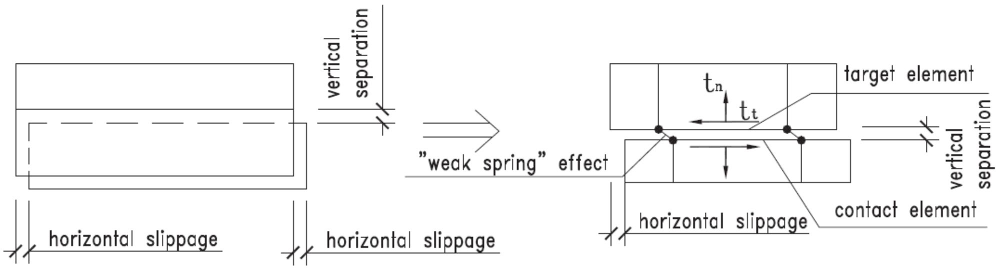

Figure 2.12 *Proposed steel-concrete interfac, Chen and Shi (2011)*

Alvarez-Rabanal et al (2016) explored the simulation of composite slabs in ANSYS for light-weight concrete configurations. The FE models included a full-scale geometry of the 4-point bending test experiments with a focus in the concrete material behaviour under different loading conditions. Different concrete strain-stress curves were implemented and multilinear isotropic hardening laws for the materials were input based on a combination of pull-out and laboratory tests. The FE models were leveraged to discuss the influence of the concrete plasticity and composition in composite slab failure.

Despite all these successful research efforts from new design methods and FE modeling, most of the complex micromechanics that occur at the composite slabs are still unknown. The three-dimensional distribution of stresses at the two very different materials steel and concrete resulted historically in significant simplifications and interpretations for the composite slab design methods as described.

The approach of accurate FE modeling for full-scale laboratory tests developed in this dissertation enables the analysis of the composite slab structural micromechanics and continues to consolidate the numerical simulations as key platform for future development of design methods. Particularly, the micromechanics amplify the knowledge in some areas such as the longitudinal shear strength τ_u, the steel sheet and concrete slab neutral axes behaviour, the influence of embossments geometries and the steel and concrete materials vertical separation. These parameters are key constituents of the composite slab characterization.

3. Laboratory specimens

Eurocode 4 prescribes the testbed to perform the full-scale bending laboratory test that supports both the *m-k* and the *PCM* design methods. This research leveraged an existing database of laboratory tests available at the LERMA from the *Escola Tècnica Superior d'Enginyeria Industrial de Barcelona* (ETSEIB) and hence no new tests were performed. This chapter details the tested parameters and introduces the 28 laboratory specimens studied in this dissertation.

Pull-out laboratory specimens were also modelled in FE as part of this dissertation. The models were created from the initial FE bending models without performing any laboratory test. Consequently, the laboratory specimens and testbed descriptions are introduced in chapter 4 as part of the modeling discussion.

3.1. Bending test

The goal of the laboratory test was to determine the longitudinal shear strength between the steel deck and concrete slab for any composite slab. In order to quantify it, the composite slab must be subjected to longitudinal shear failure (see Figure 2.3) which in practice is translated into a relative slip between the concrete slab and the steel deck. Figure 3.1 shows the standard testbed that included two equal concentrated line loads, placed symmetrically at *L/4* and *3L/4*.

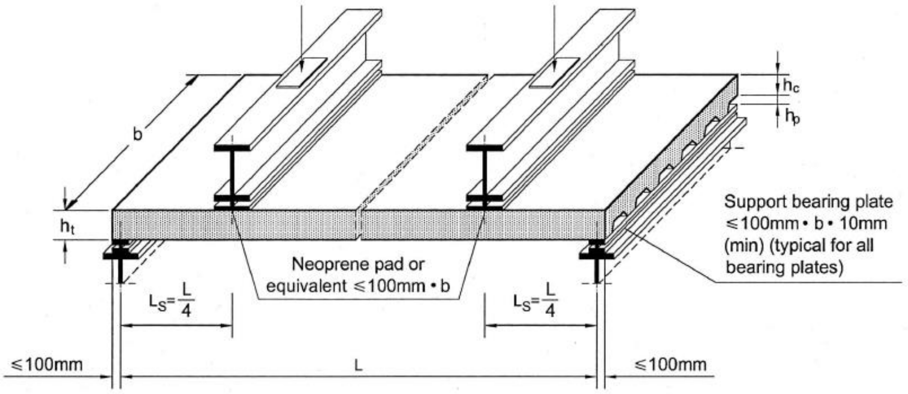

Figure 3.1 *Bending testbed, adapted from Eurocode 4 (1994)*

Eurocode 4 requires to test two groups of either three laboratory specimens with two different span lengths *L* or alternatively three groups with two specimens each to characterize the *m-k* parameters. The *Laboratori d'Elasticitat i Resistència de Materials* database (LERMA (2004), LERMA (2005), LERMA(2006), SAFSS (2013)) included mainly the first option, with group A short span total length range of *L*= 2,600 - 2,800 mm and group B long span total length range of *L*= 4,800 - 5,200 mm. Figure 3.2 summarizes the different dimensions.

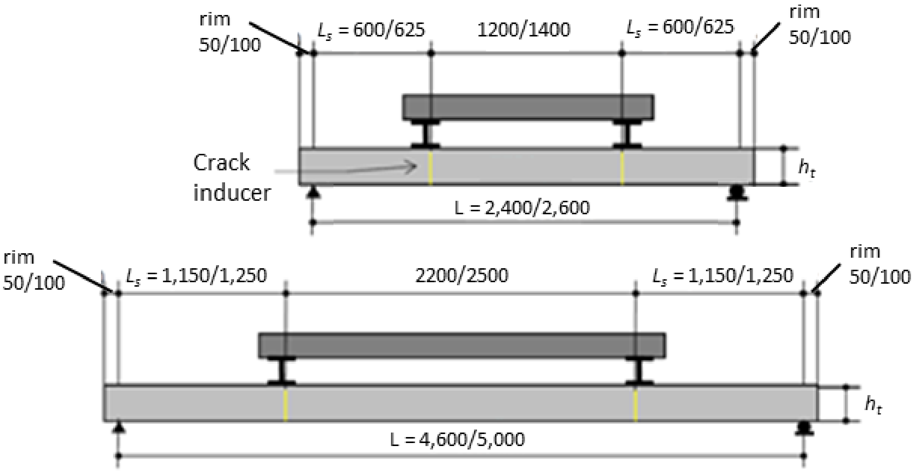

Figure 3.2 *Definition of short and long spans laboratory specimens, all dimensions in [mm]*

The preparation of the laboratory specimens required the inclusion of a crack inducer across its full width near the point load section. Figure 3.3 shows an example of the installation of the inducer during and prior the concrete pouring. Crack inducers were placed to better define the shear span length L_s and to eliminate the tensile strength contribution of concrete. The impact of the crack inducer is explored in detail in this dissertation as it notably influenced the behaviour of the composite slab in early loading stages for the simulations.

Figure 3.3 *Crack inducer inclusion as part of the preparation of the laboratory specimen*

Figure 3.4(a) shows an actual picture of the testbed that highlights some of its main parameters. First, one support of the specimen was a fixed joint, while the other was a rolling pin to ensure a constant moment and shear efforts between the point loads and the supports as represented in Figure 3.4(b). Second, the loads were applied through a hydraulic cylinder that distributed it evenly through two HEB100 steel beams. The rigidity of these steel beams, combined with a neoprene pad under them, ensured a uniform load linear distribution at the laboratory specimen.

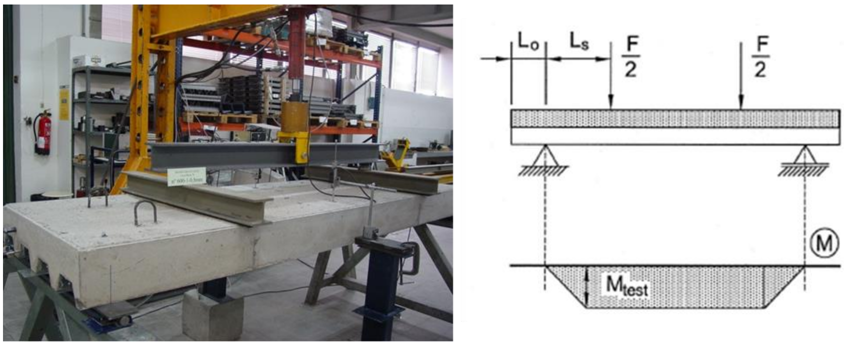
(a) (b)

Figure 3.4 *Full-scale bending testbed (a) laboratory picture, (b) moment and shear distributions*

The laboratory test measurements were based on the constant recording of the force applied at the hydraulic cylinder, the generated displacement at the midspan and the relative slip at the end of the specimen. Linear displacement sensors *d1* and *d2* were placed at the center of the laboratory specimen to measure the midspan deflection. Additionally, two more sensors *d3* and *d4* were fixed to the concrete slab at each end of the specimen to measure the relative end slip with the steel deck. See Figures 3.5 and Figure 3.6. Specifically, for the study of the long span specimens group, an additional *d5* sensor was added to monitor the central curvature of the steel deck. The information captured by *d5* helped to characterize the initial concrete cracking under flexure.

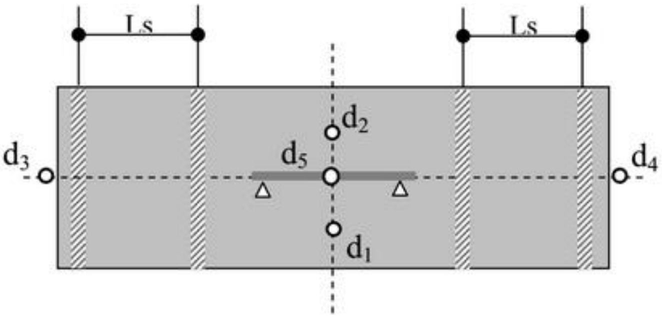

Figure 3.5 *Sensors distribution at the full-scale bending testbed*

Figure 3.6 *Examples of midspan and end slip displacement sensors*

Additionally to the *d1* to *d5* sensors, one set of laboratory results included micro-deformations gauges measurements. The characterization of local deformations based on the readings of the strain gauges allowed a much detailed micromechanics characterization in identified areas. Figure 3.7(a) illustrates the distribution of the *g1* to *g32* strain gauges along the external side of the rib for the laboratory specimen. Figure 3.7(b) highlights the split of strain gauges distribution to measure different types of stresses. The measurements from the strain gauges were directly compared with the micro-deformation results of the FE simulations and hence contributed to validate their robustness.

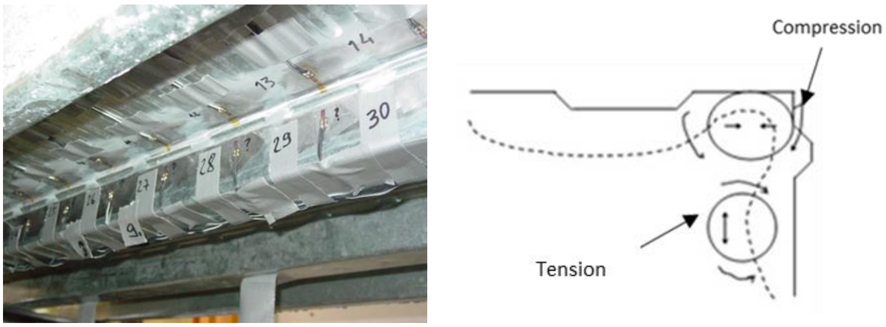

(a) (b)

Figure 3.7 *Strain gauges in laboratory specimens (a) actual distribution, (b) micro-deformation measurements*

3.2. Composite slabs analyzed

Four steel deck profiles named INCO70, C60, QL60 and T80 were analyzed from the LERMA database. The main parameters for the full-scale bending laboratory test carried out are described herein.

For all the steel deck profiles nominal and actual geometrical dimensions were provided. The actual dimensions were measured from a steel deck sample of 0.5 square meters while the commercial values were incorporated from manufacturers catalogues. The use of the actual values was relevant as some geometry parameters introduced a significant variance at the FE simulations.

Figure 3.8 *Concrete cylinders and steel coupons for material characterization*

Similarly, steel coupons and concrete standard cylinders were tested for each laboratory specimen to obtain materials properties. Figure 3.8 illustrates a set of typical samples: the steel coupons measured approximately 24 mm wide and 200 mm long and the concrete cylinders had a diameter of 150 mm. The averaged values from the different specimens in each short and long span groups were reported and subsequently implemented at the FE models.

3.2.1 INCO70

The steel deck geometry was based on an open rib trapezoidal profile with non-symmetrical and inclined vertical embossments. The profile also included circular embossments at the rib lateral and upper sides as shown schematically in Figure 3.9. The steel deck was manufactured by Incoperfil under the INCO 70.4 name. The complete set of laboratory tests was performed at the LERMA on March 2006. Eight full-scale tests were developed, three units for the short span L_s = 600 mm / L = 2,800 mm and three for long span L_s = 1.250 mm / L = 5,200 mm configurations all of them with a composite slab depth of h_t = 180 mm and a steel deck thickness t = 0.8 mm. Exceptionally, and beyond the Eurocode minimal testing requirements, one short span and one long span laboratory specimens were tested with a steel deck thickness of t = 1.2 mm. The steel deck profile width measured b = 840 mm and it was profiled originally from a steel coil 1,250 mm width.

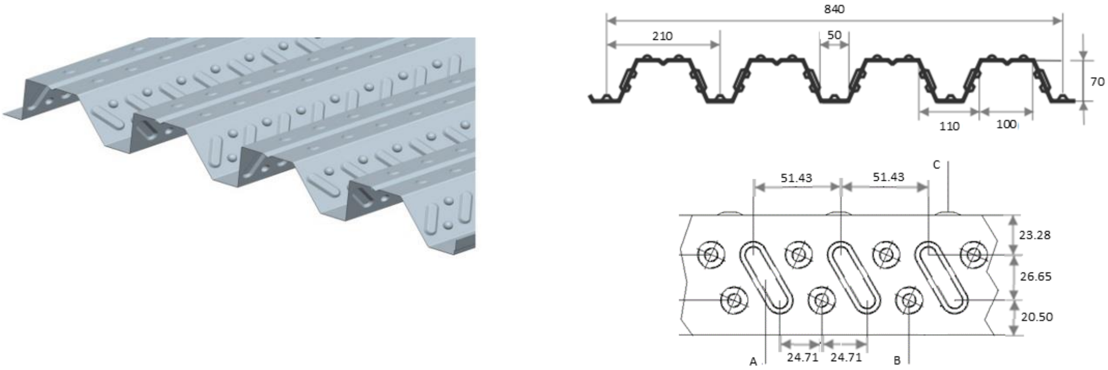

Figure 3.9 *INCO70 steel deck, all dimensions in [mm]*

Table 3.1 shows the comparison between the nominal and measured dimensions for the steel deck. Additionally, steel coupons and concrete standard cylinders were tested for each laboratory specimen to obtain materials properties. The mean values among the samples for the steel deck yield was f_{yp} = 342 N/mm^2. The mean value of the compressive strength of concrete was f_{ck} = 26.90 N/mm^2. All tested composite slab specimens presented ductile behavior.

	Nominal	Measured
Top circular embossment diameter [mm]	-	17.0
Top circular embossment depth [mm]	4	2.8
Top circular embossment slope [º]	45º	Variable
Lateral longitudinal embossment depth [mm]	3.0	2.2
Lateral longitudinal embossment length [mm]	-	47.0
Lateral longitudinal embossment slope [º]	45º	Variable
Separation between patterns [mm]	51.4	51
Profiled angle [º]	66.8º	66.0º

Table 3.1 *INCO70 steel deck geometrical nominal and measured dimensions*

3.2.2 C60

The steel deck geometry was based on an open rib trapezoidal profile with a simple non-symmetrical and inclined vertical embossment as shown in Figure 3.10. The steel deck was manufactured by ArcelorMittal under the COFRAPLUS 60 name. The complete set of laboratory tests was performed at the LERMA on June 2013. Six full-scale bending tests were developed, three units for the short span L_s = 625 mm / L = 2,500 mm configuration with a composite slab depth h_t = 100 mm and three for long span L_s = 1,075 mm / L = 4,300 mm configuration with h_t = 180mm. All laboratory specimens deployed a steel deck thickness of t = 0.8 mm. The steel deck profile width measured b = 1,035 mm.

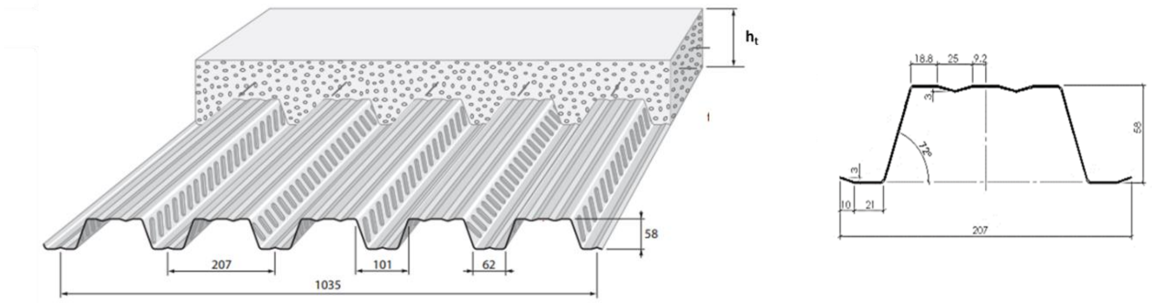

Figure 3.10 *C60 steel deck, deck, all dimensions in [mm]*

Table 3.2 shows the comparison between the nominal and measured dimensions of the steel deck profile. Steel coupons and concrete standard cylinders were tested for each laboratory specimen to obtain materials properties. The mean values among the samples for the steel deck yield was f_{yp} = 326 N/mm^2. The mean value of the compressive strength of concrete was f_{ck} = 26.86 N/mm^2. All tested composite slab specimens presented ductile behavior.

	Nominal	Measured
Lateral longitudinal embossment depth [mm]	3.0	2.4
Lateral longitudinal embossment length [mm]	31.0	29.5
Lateral longitudinal embossment slope [º]	45º	48º
Separation between embossments [mm]	37.5	33.0
Separation between patterns [mm]	207.0	206.0
Profiled angle [º]	71.4º	72.0º

Table 3.2 *Steel deck C60 geometrical nominal and measured dimensions*

3.2.3 QL60

The steel deck geometry was based on a 90-degree vertical rib profile with two simple symmetrical embossments. The first type of embossments was longitudinal and it was located at the lateral side of the rib while the second type was transversal and it was located at the upper side as shown in Figure 3.11. The steel deck profile also included small circular embossments at the bottom side of the rib. This steel deck could be categorized in between the open and re-entrant ribs due to its geometry, although its deformation under service conditions suggested to categorize it as a re-entrant profile. The steel deck was manufactured by British Robertson SL under the QL60 name. The complete set of laboratory tests was performed at the LERMA on September 2004. Seven full-scale tests were developed, four units for the short span $L_s = 600$ mm / $L = 2{,}600$ mm and three for long spans $L_s = 1{,}150$ mm / $L = 4{,}800$ mm. All laboratory specimens deployed a depth of $h_t = 180$mm and a steel deck thickness $t = 0.8$ mm.

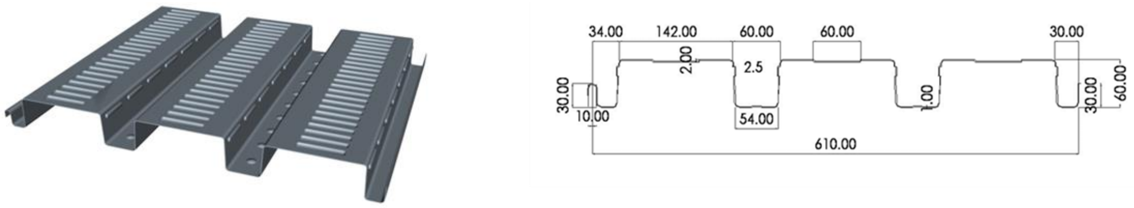

Figure 3.11 *QL60 steel deck, deck, all dimensions in [mm]*

Table 3.3 shows the comparison between the nominal and measured dimensions of the steel deck profile. Steel coupons and concrete standard cylinders were tested for each slab to obtain materials properties. The mean values among the samples for the steel deck yield was $f_{yp} = 336$ N/mm^2. The mean value of the compressive strength of concrete was $f_{ck} = 24.9$ N/mm^2. All tested composite slab specimens presented ductile behavior.

	Nominal	Measured
Bottom circular embossment depth [mm]	1.0	0.7
Side longitudinal embossment depth [mm]	2.5	2.1
Side longitudinal embossment length [mm]	65.0	52.5
Upper transversal embossment depth [mm]	2.0	1.5
Upper transversal embossment length [mm]	60.5	55.0
Separation between embossments [mm]	-	35.0

Table 3.3 *Steel deck QL60 geometrical nominal and measured dimensions*

3.2.4 T80

The steel deck geometry was based on an open rib trapezoidal profile with non-symmetrical and inclined lateral embossments. The vertical embossments were cold-formed throughout a sequence of inward - outward alternate distribution. The steel deck profile also included transversal embossments at the upper side of the rib and longitudinal embossments at the bottom of the rib as shown schematically in Figure 3.12. The steel deck was manufactured by Metalperfil under the Acercol 80 name. The complete set of laboratory tests was performed at the LERMA on May 2005. Seven full-scale tests were developed, three units for the short span L_s = 600 mm / L = 2,600 mm configuration and three for long span L_s = 1.200mm / L = 5,000 mm configuration all of them with a composite slab depth of h_t = 180 mm and a steel deck thickness t = 0.8 mm. An additional intermediate specimen with L_s = 800 mm / L = 3,400 mm was also investigated although not included as part of this dissertation scope. The steel deck profile width measured b = 840 mm and it is profiled originally from a steel coil 1,250 mm width.

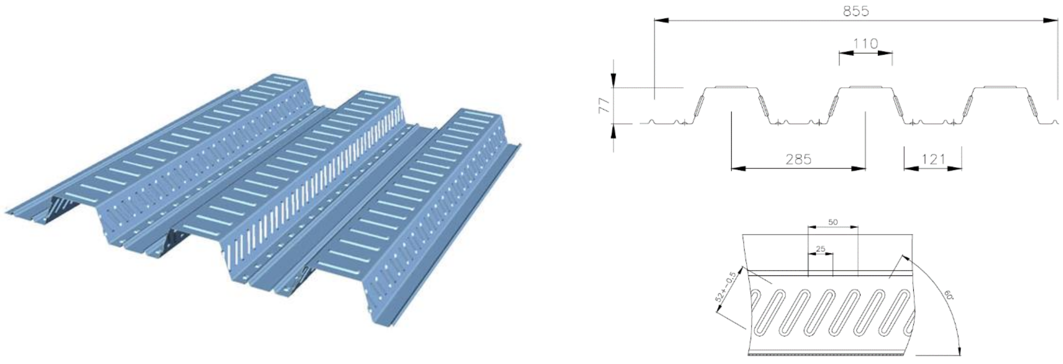

Figure 3.12 *T80 steel deck, deck, all dimensions in [mm]*

Table 3.4 shows the comparison between the nominal and measured dimensions of the steel deck profile. Steel coupons and concrete standard cylinders were tested for each slab to obtain materials properties. The mean values among the samples for the steel deck yield was f_{yp}=313 N/mm^2. The mean value of the compressive strength of concrete was f_{ck}=30.75 N/mm^2. All tested composite slab specimens presented ductile behavior.

	Nominal	Measured
Depth embossment - maximum value [mm]	3.3	2.9
Depth embossment - minimum value [mm]	2.7	2.2
Depth of embossment - average value [mm]	3.0	2.5
Length upper embossments - average value [mm]	80.0	79.8
Length lateral embossments - average value [mm]	52.0	52.4
Slope of embossments - average value	45º	40 º
Embossments patterns separation [mm]	50.0	52.5
Profiled angle [º]	70º	70º

Table 3.4 *Steel deck T80 geometrical nominal and measured dimensions*

The T80 steel deck profile was proposed by Ferrer as part of his doctoral research in 2005. The design optimized some relevant findings for shear bond as the inclination and the separation between embossments, the inward – outward sequence for vertical embossments and the shape of embossments among others. Figure 3.13 shows some additional steel deck details.

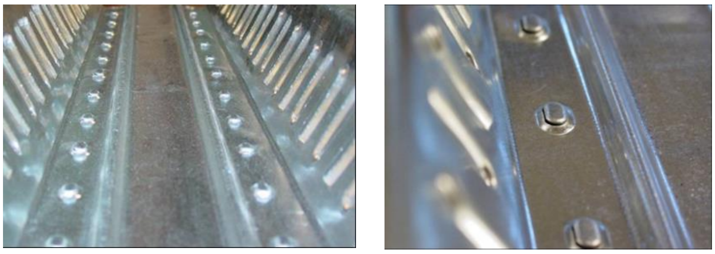

Figure 3.13 *Detailed views for T80 steel deck embossments*

4. Finite element method and analyses

This chapter develops the novel simulation methodology that is based on the inclusion of the accurate geometry of the composite slab and hence the avoidance of simplifications at the steel-concrete interface. The three-dimensional composite models detailed embossment depth and slope, steel thickness, tilting angle, and concrete crack inducers among several others. The FE modeling tool used was Ansys version 13. A brief description of the FE method is introduced: it enabled the capability to simulate models with large deformations, large displacements, stress stiffening and non-linear geometric, material and boundary conditions that are common in composite slabs.

The Newton-Raphson method was applied to evaluate the convergence of the incremental steps at the simulation. It provided an algorithm for finding successively better approximations. The performance of different FE element types to define the steel deck and the concrete slab is also evaluated in combination with the definition of the materials, contact surfaces and penetration tolerances. Further details about the meshing strategy and the iterative process to enhance simulations convergence are also described.

The chapter concludes with preliminary results from the FE models. The results are grouped in two different areas: first, the influence of some elements such as the crack inducers and finite element types was discussed. Second, a comparison of the results from the bending simulations with the actual values obtained from laboratory bending tests is performed.

4.1. Simulation method

The Newton-Raphson is currently one of the more deployed simulation methods for non-linear modeling in composite slab research (Ferrer, Seres, Gholamhoseini et al., Majdi et al. (2014)). The non-linear behaviours are defined as an aggregate of linear equations through an incremental and iterative process in which the Newton-Raphson algorithm evaluates the convergence. Figure 4.1 illustrates graphically the *full* Newton – Raphson method implemented in this dissertation simulations that updated the material stiffness matrix in each iteration. The update in each iteration was required due to the influence from the deformations and displacements. There were other algorithm variations such as the Newton-Raphson *modified* method with a lower update frequency that were disregarded due to a slower convergence. Note that the intermediate iterations could not be equilibrium points and hence could not be located at the equilibrium curve.

Ansys provided some enhanced equation solvers for the deployment of the Newton-Raphson method in case of complex convergence cases. The first one investigated was the *arc-length* that helped to avoid the presence of bifurcation points. The equation solver forced the equilibrium iterations to converge along an *arc* often preventing divergence. It was implemented during the development of the simulations but disregarded due to the limited convergence observed and a computational time required twelve times higher than similar equation solvers. The *Preconditioned Conjugate Gradient* (PCG) iterative equation solver was also investigated since it required less disk file space and presented a faster performance compared with similar solvers for large FE models. The results presented several issues with convergence and the solver was disregarded. Finally, the *Sparse Direct* equation solver was investigated and selected due to its robustness and velocity at the simulations. The solver was specially well suited for non-linear analyses where indefinite matrices were frequently encountered and contact status altered the mesh topology. It required considerable more disk file space than the PCG solver, but it proved to be more stable with strong convergence for all the FE models created.

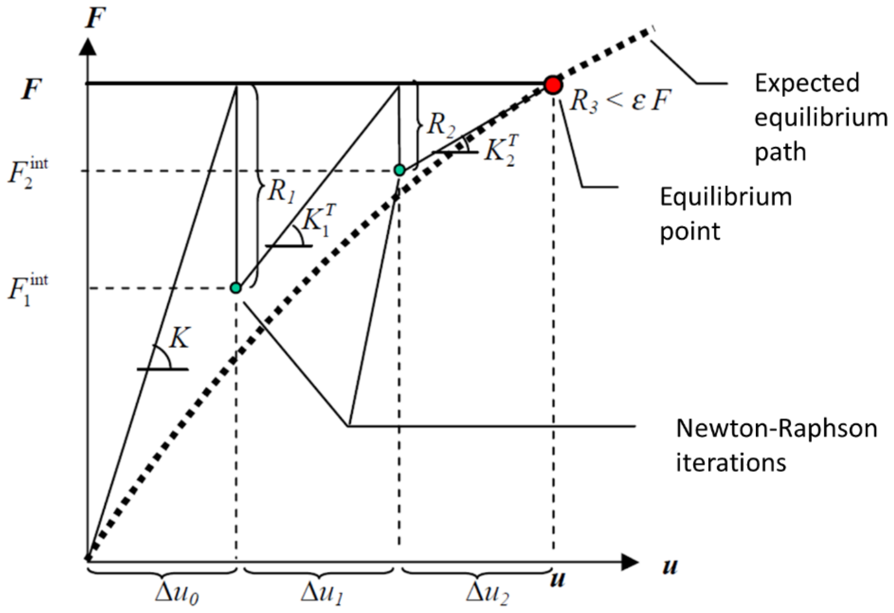

Figure 4.1 *Newton-Raphson method with stiffness matrix [K] update*

4.2. Finite element components

The software Ansys provided an extensive range of tools to characterize both linear and non-linear behaviours in structural analysis. This research developed several preliminary composite slab models. They explored different steel and concrete geometry characterizations, meshing options and the suitability from different FE element types. Only relevant FE models or parameters that influenced the final modeling approach are discussed herein and thus this chapter is not an exhaustive list of all the models developed.

4.2.1 Steel deck

Two different FE element types “shell” were evaluated in detail to mesh the steel deck: *SHELL181* and *SHELL281*. The *SHELL181* element type was previously selected by Ferrer among other options such as *SHELL43, SHELL93* and *SHELL143* from the Ansys software library. Ferrer realized that there was a better performance in *SHELL181* due to the thickness changes experienced as part of the deformation process and the reduced computational costs associated compared with the more elaborated element types. All the element types considered previously by Ferrer and *SHELL281* share a set of common characteristics that enable a solid meshing of the steel deck:

- Suitable for analyzing thin to moderate-thick shell structures.
- Six degrees of freedom in each node (3 displacements and 3 rotations).
- Large displacements were enabled.
- The perpendicular shear stresses τ_{xz} and τ_{yz} were assumed constant within the plate thickness.
- Shear deformations were accounted in the analysis and therefore moderate thick plates can be analyzed.
- Normal perpendicular stress of the plate varied linearly through its thickness.
- The interpolation functions did not provide a stiffness value for the plate perpendicular rotation degree of freedom. Each element provided a different solution to solve it.

SHELL181 presented four nodes with six degrees of freedom at each node: translations in the x, y, and z directions, and rotations about the x, y, and z-axes (UX, UY, UZ, ROTX, ROTY i ROTZ). The element was well-suited for linear, large rotation, and/or large strain non-linear applications. Change in plate thickness was accounted in non-linear analyses. In the element domain, both full and reduced integration schemes were supported. *SHELL181* accounted for load stiffness effects of distributed pressures. The element type formulation was based on true stress measures and logarithmic strain; its kinematics allowed for finite membrane strains. However, the curvature changes within a time increment were assumed to be small which was aligned with the actual composite slab behaviour.

The *SHELL181* element was implemented in early models for this research. Simulations showed a strong convergence and the element type enabled a lot of flexibility for the characterization. However, it was realized that *SHEL281* enabled a better compatibility with the different element types considered for concrete. *SHELL281* shared the same properties introduced previously for *SHELL181* but the element presented eight nodes with also six degrees of freedom at each node. *SHELL281* introduced an additional order of analysis with larger size elements compared with other investigated elements such as *SHELL93*. Consequently, the larger size translated in a faster convergence but required a densification of the geometry meshing in specific areas. Figure 4.2 introduces the SHELL281 element.

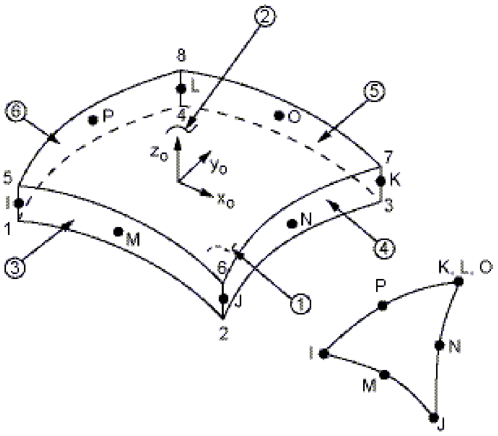

Figure 4.2 *SHELL281 element, Ansys (2013)*

4.2.2 Concrete slab

Similar to the steel deck, several FE element types were evaluated for the concrete slab characterization. The concrete material showed an additional complexity as it might suffer cracking and crushing phenomena under bending forces that was relevant in some structural behaviors. Multiple Ansys element types allowed the introduction of these second order magnitude analysis, but the computational costs associated once deployed in full-scale models were significant. Section 4.4.2 provides a detailed analysis of the three different element types *SOLID65*, *SOLID185* and *SOLID187* studied and the resultant recommendation to deploy *SOLID185*. This section summarizes the main parameters for all element types analyzed.

SOLID65 is currently categorized by Ansys as a legacy element and hence it is recommended to deploy *SOLID185*. However, due to its historical use in concrete modeling, the element type was deployed as part of the scope in some initial FE models. *SOLID65* was a dedicated three-dimensional and isoparametric solid to model non-linear behaviours in brittle materials. The element was defined by eight nodes having three degrees of freedom at each node: translations in the nodal x, y, and z directions (UX, UY, UZ, ROTX, ROTY i ROTZ). The concrete material was assumed to be initially isotropic and the element type enabled cracking in tension and crushing in compression. Figure 4.3 illustrates the main components for the *SOLID65* element. Additional element type characteristics are summarized below from the Ansys user manual (2013):

- The concrete material was capable of directional integration point cracking and crushing besides incorporating plastic and creep behavior. In particular, cracking was permitted in three orthogonal directions at each integration point under tension.

- If cracking occurred at an integration point, the cracking was modeled through an adjustment of material properties which effectively treated the cracking as a “smeared band” of cracks, rather than discrete cracks.
- The concrete reinforcement had uniaxial stiffness only and was assumed to be smeared throughout the element. Directional orientation was accomplished through user specified angles.
- The reinforcement element was assumed to be “smeared” throughout the concrete element.
- In addition to cracking and crushing, the concrete may also undergo plasticity, with the *Drucker-Prager* failure surface being the most commonly used.
- The concrete matrix material was capable of plasticity, creep, cracking and crushing. A material model was also available in Ansys that predicted either elastic behavior, cracking behavior or crushing behavior. If elastic behavior was predicted, the concrete was treated as a linear elastic material. If cracking or crushing behavior was predicted, the elastic, stress-strain matrix was adjusted for each failure mode.
- Cracks were developed at an integration point. They were represented through modification of the stress-strain relations by introducing a plane of weakness in a direction normal to the crack face. An additional shear transfer coefficient was introduced which represented a shear strength reduction factor for those subsequent loads which induced sliding (shear) across the crack face.
- The material was assumed to crush if it failed in uniaxial, biaxial, or triaxial compression at an integration point. For *SOLID65*, the crush effect was defined as a complete deterioration of the structural integrity of the material. Once concrete crush occurred, material strength was assumed to have degraded to an extent such that the contribution to the stiffness of an element at the integration point in question could be ignored.

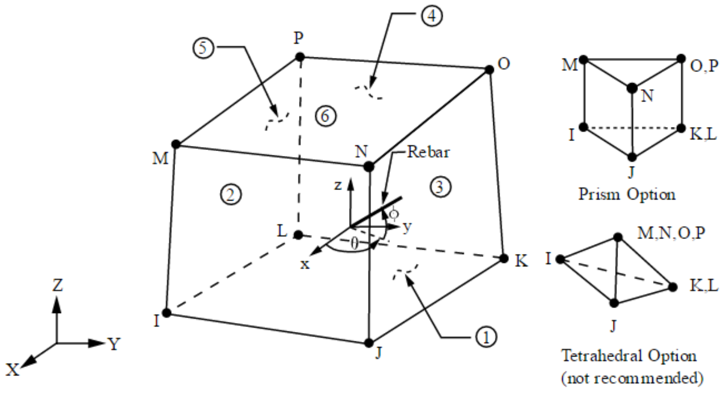

Figure 4.3 *SOLID65 element, Ansys (2013)*

SOLID185 was used for three-dimensional modeling of solid structures. It was defined by eight nodes having three degrees of freedom at each node: translations in the nodal x, y, and z directions. The element had plasticity, hyper elasticity, stress stiffening, creep, large deflection, and large strain capabilities. Figure 4.4 illustrates the main parameters of this element type. Additional element parameters are summarized below from the Ansys user manual:

- The element type included a mixed formulation capability for simulating deformations of nearly incompressible elastoplastic materials, and fully incompressible hyperplastic materials.
- *SOLID185* used a standard method where volumetric strain terms at the *Gauss* integration points were replaced by the average volumetric strain of the elements. This method was also known as the selective reduced integration method. Using this method helped to prevent mesh volumetric locking in nearly incompressible cases.
- The element could exhibit shear locking in bending types of applications. In such situations, the use of a specific definition was recommended, which used uniform reduced integration technique with hourglass stiffness for controlling hourglass modes.

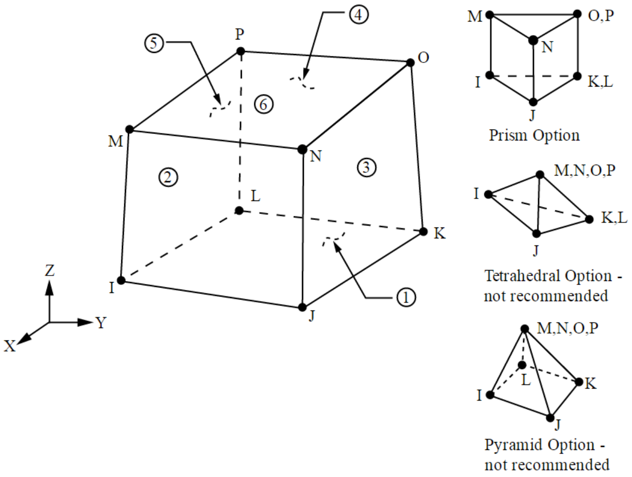

Figure 4.4 *SOLID185 element, Ansys (2013)*

SOLID187 element type was a higher-order 10-node option. The element type featured a quadratic displacement behavior and was better suited for modeling irregular meshes compared with *SOLID185*. The element type was defined by 10 nodes having three degrees of freedom at each node: translations in the nodal x, y, and z directions. *SOLID187* incorporated plasticity, hyper elasticity, creep, stress stiffening, large deflection, and large strain capabilities. It also enabled a mixed formulation capability for simulating deformations of nearly incompressible elastoplastic materials, and fully incompressible hyperplastic materials.

The use of the *SOLID185* element type as the preferred approach was based on the similarity with both *SOLID65* and *SOLID187* capabilities but a much optimized computational time. *SOLID65* provided concrete crushing and cracking capabilities that are proven to have limited impact in the simulations performed (see section 4.4.2). Similarly, the higher-order nature of *SOLID187* proved to be a limiting factor when modeling the groups of long span full-scale laboratory specimens. The FE models required a significant additional running time whilst no enhancement in results was observed.

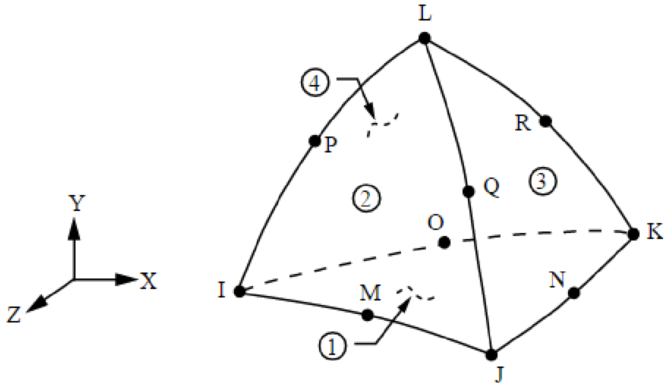

Figure 4.5 *SOLID187 element, Ansys (2013)*

4.2.3 Material characterization

The materials definition was an important input to characterize the actual behaviour of any FE model. Ansys enables the deployment of different approaches based on the representation of the actual material properties through mathematical models. For the composite slab simulations, two different materials were represented.

Steel

The work done by Ferrer, Lopez, and Seres, focused in the steel deck characterization in FE models, suggested the deployment of a bi-linear stress-strain curve. Figure 4.6(a) illustrates an actual case of a bi-linear elastic-perfectly plastic stress-strain curve implemented in the FE models for this research. The initial stresses were modeled through a constant slope for the elastic stage of the material. Once the stress f_{yp} was achieved, the material entered a plastic behavior which was captured with a second flat segment with the same value f_{yp}. It was assumed that the yield stress and the ultimate stress coincided. The input parameters for the material definition were the poison ratio $\upsilon = 0.28$, the Young Modulus $E = 210{,}000$ N/mm^2, and the nominal value for the yield characteristic strength of steel f_{yp}. The f_{yp} value which was obtained in each group of laboratory specimens coupons tests varied within the 313 – 342 N/mm^2 range for the different FE models developed (see section 3.2).

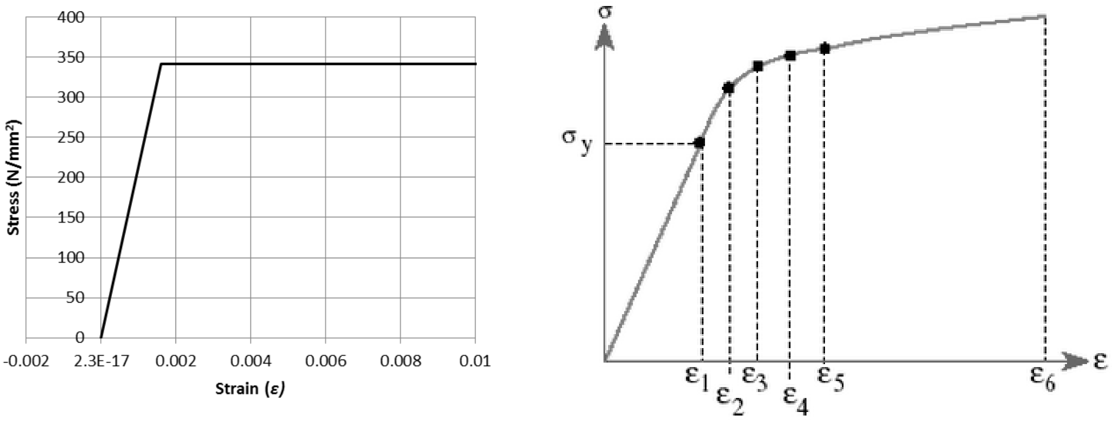

(a) (b)

Figure 4.6 *Stress-strain curve (a) bi-linear model and (b) multi-linear model*

Prior to the selection of a bi-linear stress-strain curve for the material, some FE models were tested with the multi-linear model represented in Figure 4.6(b). Such a stress-strain curve provided a more accurate representation of the actual material specially in the transition between elastic and plastic behaviours. Yet, it increased considerably the complexity at the model and the computational time. The curve required additional characterization parameters with pairs of stress-strain σ_i,- ε_i values in combination with the already required inputs for υ, E and f_{yp} at the more simpler bi-linear model. The models reported no additional enhancements for the simulations and consequently the multi-linear curve approach was disregarded.

The Von Mises criterion was implemented for the steel failure. The material initiated its yielding once the defined yield strength, σ_e it was achieved. The mathematical model was captured in Equations 4.1 and 4.2 and Figure 4.7 depicts a three-dimensional view for the multi-axial stress state. The von Mises stress was used to predict the yielding of materials under any loading condition of simple uniaxial tensile tests results such as the ones implemented in the laboratory tests. The von Mises stress satisfied also the property that two stress states with equal distortion energy had an equal von Mises stress. The criterion was applicable in plastic deformation for ductile materials, such as the steel deck from the composite slab specimens.

$$\sigma_{eq} = \sqrt{\frac{{(\sigma_1-\sigma_2)}^2+{(\sigma_2-\sigma_3)}^2+{(\sigma_3-\sigma_1)}^2}{2}} \tag{4.11}$$

$$\sigma_{eq} = \mathrm{f}(\{\sigma\}) = \sqrt{\frac{3}{2}\ \{s\}^t[M]\ \{s\}} \tag{4.12}$$

where,

$\{s\}$ vector tensional deviations

$$[\mathrm{M}] = \begin{bmatrix} 1 & 0 & 0 & 0 & 0 & 0 \\ 0 & 1 & 0 & 0 & 0 & 0 \\ 0 & 0 & 1 & 0 & 0 & 0 \\ 0 & 0 & 0 & 2 & 0 & 0 \\ 0 & 0 & 0 & 0 & 2 & 0 \\ 0 & 0 & 0 & 0 & 0 & 2 \end{bmatrix}$$

When large displacements were active, the FE analysis accounted for the reduction in cross-sectional area under increased load and the material hardening under plastic deformations. The hardening law described the plastic surface changes in relation with the deformation progression. A symmetric hardening model based on deformation was implemented in which the surface subjected to plastic behavior remained centric in its initial position but increased its size as the deformation progresses and updates the elastic limit uniaxial σ_i.

The material characterization did not incorporate any residual strain induced by the steel deck cold-form manufacturing process. The FE model used the actual geometry and dimensions of the steel deck as free-strain reference case.

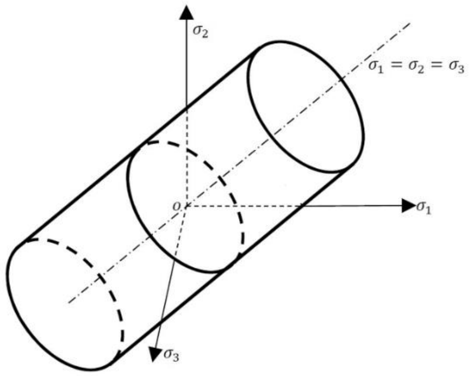

Figure 4.7 *Von Mises yield function in a multi-axial stress state*

Concrete

The concrete was categorized within the FE models as an elastic and isotropic material with different behaviours and properties under tension and compression. The two only parameters introduced were the Poison coefficient $\upsilon = 0.15$ and the elastic modulus $E = 20{,}000$ N/mm^2. The compressive concrete strength resistance f_{cm} was not introduced as its values were almost two order of magnitude apart than the steel deck material. This approach was also captured at the Eurocode 4 building code which does not include f_{cm} in the formulation for its composite slab design methods.

Among the different FE meshing implemented for concrete modeling, *SOLID65* included the capability of crushing and cracking. The mathematical model implemented in some initial FE models was the *William-Warnke* yield criterion that provided a function capable to predict when failure would occur in concrete. Figure 4.8(a) illustrates the three-dimensional view for the failure surface. The presence of a crack was represented through modification of the stress-strain relations by introducing a plane of weakness in a direction normal to the crack face. Hence, for concrete to crack due to tension at least $\boldsymbol{\sigma}_{zp}$ must be positive and the fissure would appear in the perpendicular direction of that principal stress. If none of the principal stresses was positive, then the concrete experienced crushing.

Figure 4.8(b) shows a bi-axial representation of a tension state. For this modeling, additional parameters were required: the transfer coefficients of open and closed crack β_t and β_c were introduced. The factor T_c that is the stiffness multiplier for cracked tensile condition was also introduced, in this case the Ansys default value 0.6 was considered as it provided better performance in simulations convergence after some cases evaluation.

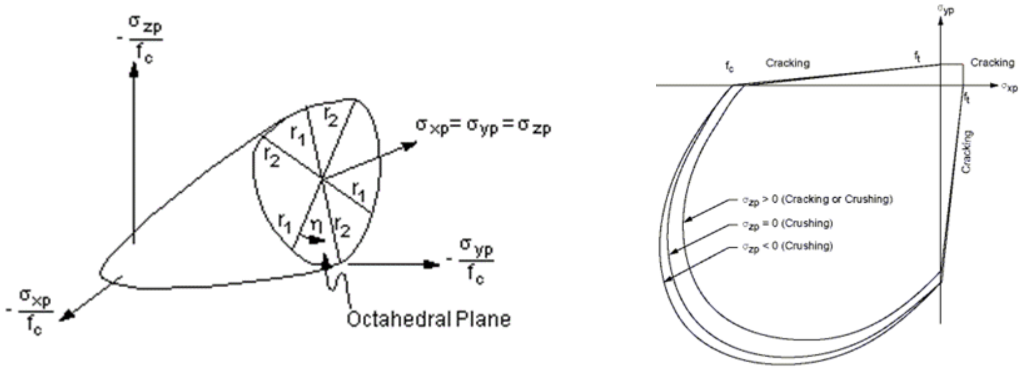

Figure 4.8 *William-Warnke criterion (a) three-dimensional surface failure, (b) bi-axial state of tensions*

For the crushing failure, the material failed in uniaxial, biaxial, or triaxial compression. *SOLID65* defined crushing as a complete deterioration of the structural integrity of the material. Consequently, the material strength was assumed to have degraded to an extent such that the contribution to the stiffness of an element could be ignored.

4.2.4 Concrete slab crack inducer

The Eurocode 4 bending testbed requires a crack inducer mechanism at the point load section L_s (see Figure 3.3) with the purpose to remove the tensile contribution of the concrete and also to artificially define two different spans for composite behaviour.

The modeling of such crack inducer could be accomplished with different solutions and its existence eased significantly the FE modeling of the composite slab specimens. The crack inducer introduced two different concrete slab blocks from the beginning of the simulation which enabled the failure characterization for the composite slab. See Figure 4.9(a). The FE definition was characterized by a set of unique nodes shared in both blocks consequently coupled along the rib width that enabled a relative rotation. Figure 4.9(b) illustrates the solution implemented.

Each concrete slab section was meshed separately and an iterative process implemented to refine the density of nodes at the crack inducer sections for the steel deck. A high density of nodes introduced a significant computational cost. The solution required to deploy a more refined mesh only at the embossment areas. The introduction of additional surface-surface contact parameters between the concrete sections was also necessary to characterize the behavior.

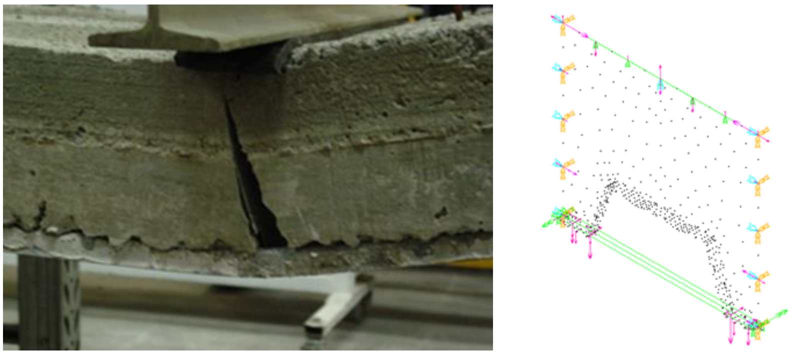

(a) (b)

Figure 4.9 *Crack inducer (a) actual impact in composite slab tests, (b) FE modelling*

4.2.5 Contact, friction, initial adherence and additional modeling parameters

Normal contact forces

The modeling of the normal contact forces was achieved with the implementation of a penalty method with Lagrange multipliers. The Lagrange multiplier algorithm, also known as augmented Lagrangian method, was an iterative series of penalty methods. The penalty method was the default approach in Ansys for surface-to-surface contact elements.

Particularly for the simulations, the algorithm incremented the contact forces in case of excessive penetration during the equilibrium iteration so the final penetration was smaller than a defined parameter *FTOLN*. The amount of penetration between contact and target surfaces depended on the normal stiffness which was also defined with the *PKN* parameter. High values for *PKN* combined with low values in *FTLON* decreased the impact from penetration, but could lead to complex global stiffness matrices with difficulties in convergence. Oppositely, low values in *PKN* and high values for *FTLON* could allow penetration into the material but generated an inaccurate solution. Several tests for *FTLON* and *PKN* values were performed at the FE models. The sensitiveness observed, combined with the particularities of the simulations recommended the values *FTLON* = 0.2 and *FKN* = 0.1 for all models developed in this research. *FKN* = 0.1 was recommended by the Ansys user manual for models in which bending is a predominant factor.

Friction

The friction characterization at the FE models was implemented though the Coulomb theory. The Coulomb mathematical model stipulated that two different surfaces in contact were capable to resist a shear tension without any slip until a certain threshold τ_{max}. If the threshold was overcome, then slip initiated between surfaces. The threshold was proportional to the normal contact force, except for values exceeding the absolute value τ_{max}. Figure 4.10 illustrates the main characteristics considered for the FE models developed. A common and valid approximation to the τ_{max} value was $\sigma_y/\sqrt{3}$. The parameter σ_y characterized the von Mises equivalent for the yield strength of the structural steel.

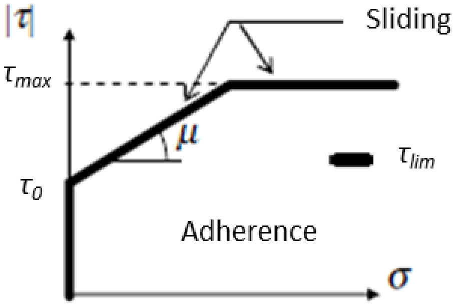

Figure 4.10 *Coulomb friction model*

The option to implement a more elaborated friction model that combined dynamic, rigid and elastic frictions was explored. The model considered an initial adherence τ_0 that once overcome could differentiate static and dynamic friction functions. The Coulomb Friction model was deployed selecting a friction coefficient μ with values between 0.0-0.5 and a static to dynamic friction ratio μ_s/μ_d = 1,25. The simulations computed showed a significant increase in complexity based on the more elaborated analysis required. It was concluded that the rigid and more simple Coulomb friction model was capable to accurately reproduce the quasi-static behaviour for the simulations. The selected modeling reduced significantly the computational time compared with the more elaborated model and there were minimal enhancements in the results. Consequently, the rigid friction model was implemented in the FE models developed.

Based on the friction model defined, this dissertation includes multiple analysis of laboratory specimens with different friction values. Some FE models were simulated with $\mu = 0.3$, $\mu = 0.5$, $\mu = 0.8$ and $\mu = 0$ to replicate ideal cases with no friction based on previous research. Chen and Shi, and Abdullah proposed friction values between 0.3 and 0.6. Burnet and Oehlers (2001) proposed values between 0 and 0.6 and Tsalkatidis and Avdelas deployed a value of 0.3. The results of those simulations can be observed in chapter 6.

Chemical bond – initial adherence

The chemical bond, also known as initial adherence between the steel deck and the concrete slab, is defined as the longitudinal strength at the first slip. It represented a behavior that needed to be characterized for the composite slab at the FE models.

The chemical-physic phenomenon generally reported a significant lower scale effect than the other physical components of the composite slab failure. Additionally, building codes such Eurocode 4 in its test arrangements ensured the removal of the effect based on cyclic loading procedures. Two different approaches were explored to model the chemical bond. First, some simulations were developed with the introduction of an initial friction τ_0 parameter which reproduced an initial static friction. The results showed a strong reliance in laboratory tests results and required a tedious calibration process at the FE models. The intrinsic variance observed in the actual laboratory tests consequently introduced another complexity for the modeling

As an alternate approach, the creation of two different FE models for the same laboratory specimen was proposed. One of the FE models did not include the crack inducer and captured better the early steps of the simulation in which the chemical bond is the main resistance component. A detailed definition of the approach is developed in section 4.4.4.

Contact elements

The Ansys software included three different types of pair contact elements: surface-surface, point-surface and point-point. For all of them, a "*target*" and a "*contact*" components needed to be defined. The surface-surface pair modeling enabled a better characterization for the simulations developed in this research compared with the other two types. The *TARGE170* was deployed initially to represent three-dimensional target surfaces with the associated elements *CONTA173*, *CONTA174*, *CONTA175*, *CONTA176* and *CONTA177*. The contact element overlaid solid, shell and line components describing the boundary of a deformable body. The three-dimensional elements *CONTA173* (4 nodes), *CONTA174* (8 nodes) were selected finally as the most capable for the composite slab behaviour. The Figure 4.11 graphically depicts the concept for the contact elements. Among others, the selected elements provided the following advantages.

- Enabled the implementation of second order surfaces, mostly developed from intermediate contact nodes.
- Enabled the efficient analyses of large deformations with significant slips and could adopt complex friction mathematical models.
- Provided no restrictions from surface shapes.

- Presented less amount of modeling elements that enhanced the computational costs of the simulations.
- Enabled movement control for rigid surfaces from an unique master node.
- Enabled more simple element modeling (compared with equivalent contact elements option.

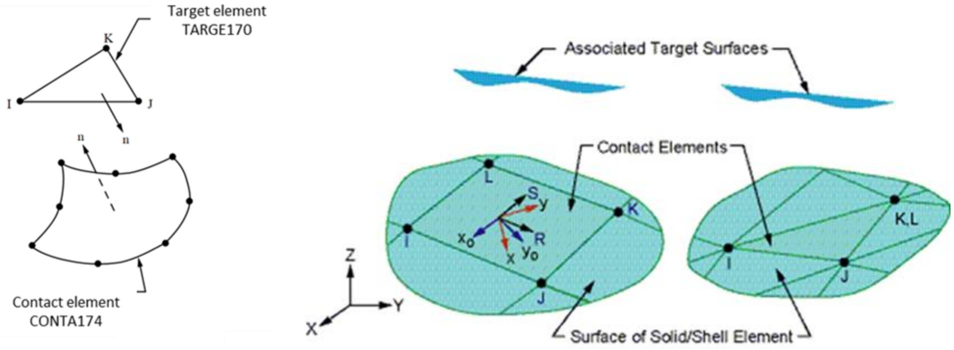

(a) (b)

Figure 4.11 *Contact pair contacts TARGE170 and CONTA174, Ansys (2013)*

Elements to mesh

An additional element *MESH200* element was deployed as part of the creation of the FE models. The element did not affect in the analyses but supported specific needs for meshing complex surfaces and materials. Particularly, the *MESH200* was implemented to support the modeling of the concrete surfaces between the different discrete units (patterns) in which the full-scale models were divided. The element ensured that the nodes and the three-dimensional spaces with triangles, quadrilaterals and bricks were uniform between different FE patterns. Once the meshing process was completed, the *MESH200* element was deleted.

Geometry idealizations

The accurate geometry of the steel deck and concrete slab was modeled for the full-scale FE models developed. Due to the generous manufacturing tolerances observed at the different steel deck profiles, the geometries introduced were based on actual measurements of the steel deck laboratory coupons. Chapter 5 provides a parametric analysis for the steel deck embossments dimensions in which the sensitiveness of some geometric parameters is discussed.

Equally, the concrete superficial erosion effect at the embossments edges and some rounding dimensions at the steel deck shape were not included for the characterization. This phenomenon introduced a more elaborated analysis and hence required a significant additional computational time. The effects from the superficial erosion were assumed to be partially embed at the definition of the friction coefficient μ.

Loading conditions

The simulations were based on incremental vertical displacement steps at the point load that replicated the vertical load applied at the laboratory testbeds. The point load section presented a singular FE definition as its nodes were coupled to ensure an uniform transmission of the displacement across the full width. The deployment of incremental prescribed displacements in composite slabs simulation was broadly implemented in FE modeling (Ferrer, Abdullah, Abdullah and Easterling, Chen and Shi) as it ensures a more stable convergence of the simulations.

Discretization and mesh optimization

The main physical phenomenon to replicate in the simulations was the longitudinal slip between materials that defined the shear resistance and therefore a significant effort was directed to its characterization. With the goal to simulate full-scale models within reasonable computational times, and especially for the long span laboratory specimens with a large size, multiple iterations with the FE models were performed. Distinct meshing sizes and schemes combined with detailed geometries were simulated for the most sensible areas. For example, areas surrounding embossments were more densely meshed to accurately simulate the strains, deformations and displacements that occurred there.

Similarly, the selection of the steel deck FE element type *SHELL281* with reduced integration and a regular element size was an output of the optimization process. Section 4.4.2 provides a detailed overview in the selection of the concrete type *SOLID185*.

4.3. Full-scale finite element models

This section introduces the different models developed to simulate the laboratory specimens. Three main groups of FE models are discussed.

- Full-scale bending simulations: a detailed description was provided for the modeling parameters deployed. First, as part of the construction of the model, different parameters performance were discussed to shape a final modeling recommendation. Second, the FE models for short and long span specimens for each steel deck profile INCO70, C60, QL60 and T80 were presented and compared with laboratory results.
- Simplified pull-out simulations: the pull-out laboratory testbed is introduced and followed subsequently by a detailed description of a simplified one-pattern FE model. A parametric analysis for the main geometric properties was performed to

identify the most influential parameters for the longitudinal shear resistance. The INCO70 steel deck profile was selected for the analysis

- Full-geometry pull-out simulations: a detailed description of the modeling parameters is provided. The FE models were created in Ansys without the support of any laboratory results and based on the bending models. Different geometric parameters are analyzed to discuss the robustness of the simulations. The INCO70 steel profile was selected for the analysis.

4.3.1 Bending

The FE models replicated the Eurocode 4 testbed described in section 3.1. Both short and long spans configurations were replicated. Due to symmetries, only one eight of the full-scale composite slab specimen was necessary to enable the bending simulations. See Figure 4.12.

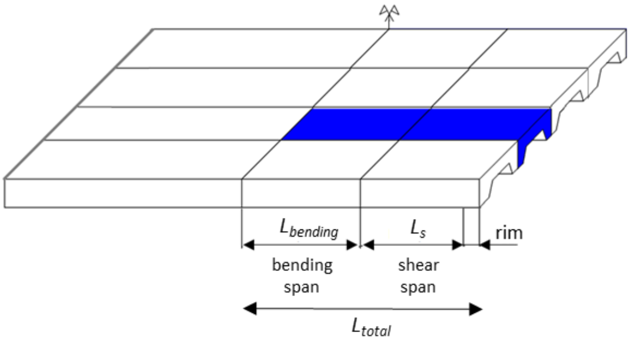

Figure 4.12 *FE bending simulation model. Definition bending and shear spans*

The central rib for each steel profile was built as the combination of multiple half patterns with a predefined *s* width. Figure 4.13 illustrates the INCO70 steel deck profile pattern. The pattern width varied between different steel deck profiles as it represented the minimum length to capture all geometrical elements that were repetitive. Both the profile steel sheet and concrete elements were modeled in a geometrical and physical form: embossments depth and slope, sheet thickness, titling angle, length and width and spacing of embossments, and profiling angle of the rib shape for all the simulations.

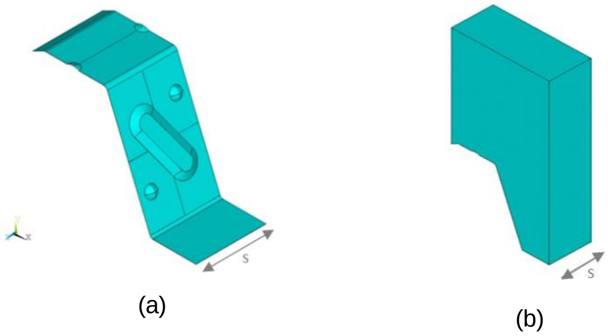

Figure 4.13 *Modeling of a composite slab pattern (a) steel deck and (b) concrete slab*

Based on the initial half pattern, a first mirror symmetry was applied to complete the full pattern rib. The concrete slab included an inversed geometry from the steel deck embossments. The simulations performed to optimize the elements meshing gradually reported a higher density of nodes and smaller element type size near the embossments. Figure 4.14 summarizes the steel deck profiles and concrete slab patterns developed for the INCO70, C60, QL60 and T80 composite slabs.

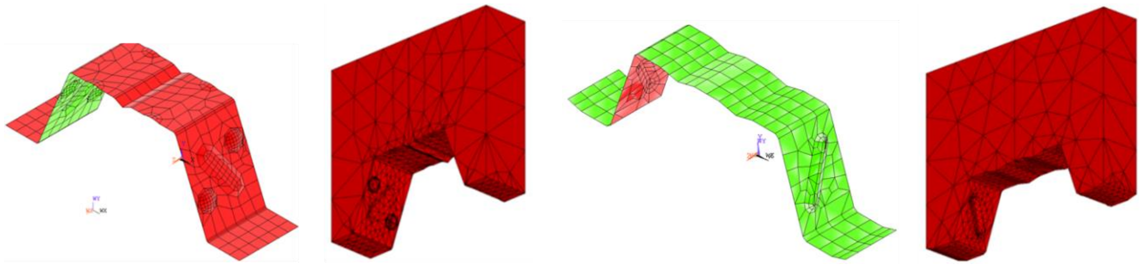

INCO70 (*s* = 53 mm) C60 (*s* = 38 mm)

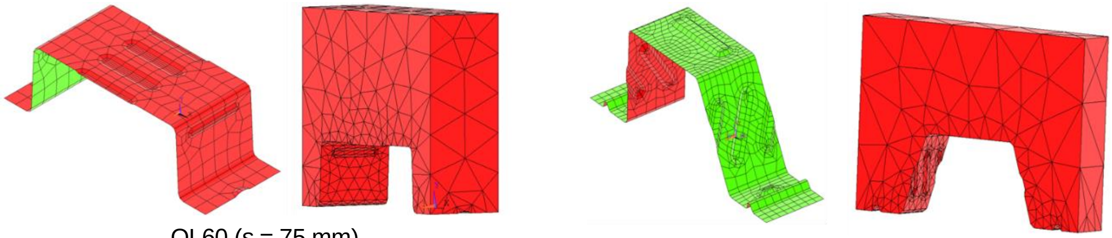

QL60 (*s* = 75 mm) T80 (*s* = 50 mm)

Figure 4.14 *FE full pattern characterization for the concrete slab and steel deck*

Subsequently, a discrete number of full patterns were combined linearly to represent the L_{total} length of the composite slab. Tables 4.1 and 4.2 summarize the number of patterns for short and long spans respectively. The FE model represented half of the actual laboratory specimen due to symmetries as introduced in Figure 4.12. The modeling required occasionally that the lengths of the FE models and the laboratory specimens were not exactly the same due to some concessions to optimize the meshing and computational time. Yet, the FE models always ensured that the shear span lengths L_s were equal and the variance was captured preferably at either the bending span $L_{bending}$ or at the rim.

	Number patterns	*s* width pattern [mm]	FE model length L_{total} [mm]	Actual lab. specimen 50% length (LERMA) [mm]	FE model equivalent total length [mm]
INCO70	27	53	1,431	1,400	2,862
C60	35	38	1,330	1,300	2,660
QL60	17	75	1,275	1,300	2,550
T80	26	50	1,300	1,400	2,600

Table 4.1 *Geometry properties summary for short span FE models*

Figure 4.15 depicts some initial views for the three-dimensional model. Some modeling features description follows. Nodes at the edges of the steel deck were coupled and symmetry conditions imposed at concrete slab lateral surfaces for each pattern. Vertical displacements were restricted in the Y axis at the support pattern. The right end of the rib was cantilevered to simulate the specimen rim. An additional steel deck pattern, without neither concrete slab nor embossments, was introduced at the end of the rim area to enable a smooth convergence of the simulations; it eased the end slip of the concrete over a surface and it did not influence the overall results.

	Number patterns	*s* width pattern [mm]	FE model length L_{total} [mm]	Actual lab. specimen 50% length (LERMA) [mm]	FE model equivalent total length [mm]
INCO70	44	53	2,385	2,650	4,770
C60	62	38	2,356	2,250	4,712
QL60	32	75	2,400	2,400	4,800
T80	47	50	2,350	2,500	4,700

Table 4.2 *Geometry properties summary for long span FE models*

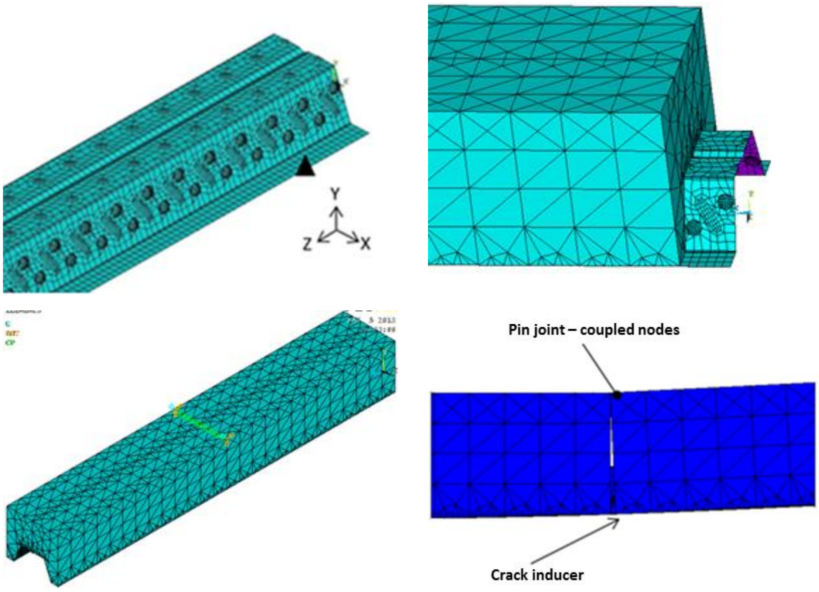

Figure 4.15 *Initial three-dimensional views for the FE model*

Eurocode 4 testbed required a crack inducer mechanism at the point load section L_S. The first span embraced the length L_s between the point load and the support, plus the rim, and predominantly observed simple bending and shear forces. The subsequent span between the point load and the middle of the actual specimen $L_{bending}$ observed pure bending moments. See Figure 4.12. Tables 4.3 and Table

4.4 introduce the lengths for the FE models developed. A few optimization features were introduced at the FE models: the concrete slab meshing decreased its density and sizes at the bending span as most of the shear bond phenomena occurred in the shear span. Oppositely, an increased meshing was deployed at the crack inducer area as it represented a singular area for the simulation. After the meshing, iterative optimization processes, the FE model included a significant lower number of elements. Tables 4.3 and 4.4 summarize the number of FE element types and nodes for each FE model developed.

	FE model equivalent length [mm]	L_s [mm]	$L_{bending}$ [mm]	rim [mm]	h_t [mm]	FE number of element types	FE number of nodes	Computational time per simulation [hr]
INCO70	2,862	600	700	100	180	174,640	209,030	23
C60	2,660	625	625	50	100	241,766	64,445	27
QL60	2,550	600	600	100	180	133,417	180,379	30
T80	2,600	600	700	100	180	221,598	60,697	28

Table 4.3 *Definition short span lengths and number of FE elements and nodes*

	FE model equivalent length [mm]	L_s [mm]	$L_{bending}$ [mm]	rim [mm]	h_t [mm]	FE number of element types	FE number of nodes	Computational time per simulation [hr]
INCO70	4,770	1,250	1,250	100	180	302,866	173,826	48
C60	4,712	1,075	1,075	50	180	267,362	166,047	30
QL60	4,800	1,150	1,150	100	180	211,045	79,492	48
T80	4,700	1,200	1,200	100	180	351,954	96,889	45

Table 4.4 *Definition long span lengths and number of FE elements and nodes*

4.3.2 Pull-out: simplified approach

Based on the robustness of the bending simulations, no pull-out laboratory tests were conducted but rather FE models developed for that reduced testbed. Concretely, pull-out specimen geometries, materials definition and laboratory test conditions were modeled leveraging the steel deck and concrete slab properties from the bending simulations, and adapting them to the specifics of actual pull-out laboratory testbed. Such testbed consisted of two confronted composite slab ribs separated by a rigid steel sheet that provided the shear resistance. The two concrete blocks were pressed with lateral forces originated from springs in order to reproduce the actual laboratory configuration. The testbed corrugated bars were located at the inner of the concrete block and were replaced at the FE model by point that gradually introduced a relative displacement as the mechanism to characterize the shear resistance. Figure 4.16 illustrates the configuration for the pull-out specimen and its testbed.

For the simplified pull-out simulation, a half pattern of the steel deck and concrete block was modeled as depicted in Figure 4.17. Nodes at the steel deck edges were coupled to ensure a uniform behavior under test conditions in each pattern. A mesh refinement on both circular and long embossments was implemented. In order to simulate the laboratory test, an imposed displacement was applied at a master node located in one of the pattern edges. Displacements were restricted at the steel deck bottom line in all directions except in the Z axis.

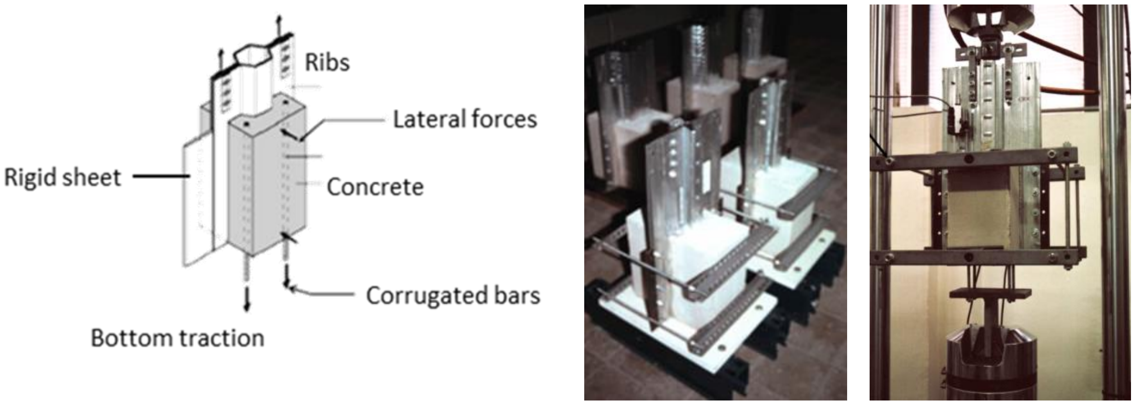

Figure 4.16 *Pull-out laboratory specimens and testbed*

Figure 4.17 also illustrates the inclusion of springs to reproduce the self-weight of the concrete block. Displacements for the concrete block were restricted in all directions except in the Y axis to simulate the laboratory test conditions. The steel deck could slip along the Z axis while the concrete block remained static in the Z and X axes. A mirror condition was applied at the middle section symmetry plane for both the steel deck and the concrete block to enable a complete composite slab pattern simulation based on the initial half pattern modeled.

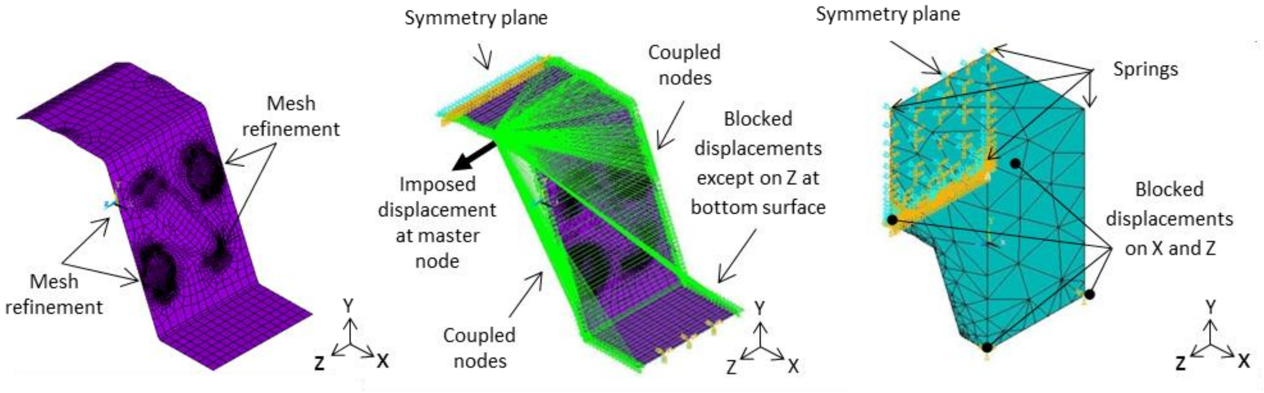

Figure 4.17 *Pull-out simplified FE model for INCO70, adapted from Ferrer (2005)*

After the meshing optimization iterative process, the FE model included 24,464 element types and 32,986 nodes of which 10,356 were at the steel deck, 22,630 were at the concretes slab. The computational time varied between 4 to 6 hours depending on the geometrical and micromechanic parameters that were analyzed.

4.3.3 Pull-out: full geometry

The pull-out complete simulation was generated from the simplified model. Initially, seven simplified models were consecutively layout and united followed by a double symmetry sequentially along the YX and ZY axes as illustrated in Figure 4.18. Nodes located at the edge line of the steel deck were coupled in the Z direction to enable a uniform behavior once the imposed horizontal displacement was applied. Two patterns were added additionally at the edge towards the horizontal displacement direction to allow the concrete block to slip over the steel deck. Four springs were applied on the four top corners of the concrete block to model testbed lateral forces. The springs were modeled with the Ansys element type *COMBIN14* as uniaxial tension-compression elements.

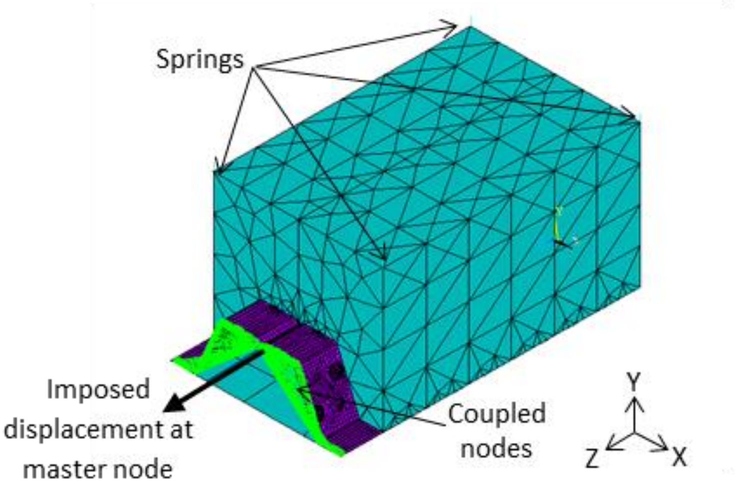

Figure 4.18 *Pull-out full-scale FE model for INCO70*

After the meshing optimization iterative process, the FE model included 52,296 nodes of which 36,747 were at the steel deck, 31,640 were at the concretes slab. The springs modeling required 8 additional nodes and 4 Ansys type elements. The computational time varied between 12 and 14 hours depending on the geometrical and micromechanics parameters that were analyzed.

4.4. Simulations optimization

Once the geometries and the FE model definition was completed an iterative process to optimize the simulations was implemented. The initial full-scale bending models without any enhancement were significantly instable for convergence and required more than 180 hours of computational time. The optimization process sought the following goals:

- Ensure alignment with the actual behavior observed at the laboratory tests.
    - Benchmarked midspan and end slip curves as numerical indicators for performance of the FE model compared with actual laboratory specimens.
    - Benchmarked composite slab macro-behaviours as qualitatively indicators: steel deck localized deformations, crack inducer opening, concrete peeling and concrete traces.
- Ensure critical areas for composite slab characterization were properly modeled.
    - Avoided simplifications and “light” meshing in areas that were relevant for composite slab failure.
    - Focused in phenomena that were novel and had a significant relevance in composite slab characterization: clamping phenomenon, concrete-steel vertical separation and longitudinal shear strength.
- Optimize the computational time.
    - Found the right balance for order of analysis and quality of results. If needed, prioritized components that were critical for composite slab failure characterization.
    - Explored the option to deploy different Ansys element types depending on the numerical analysis requirements.
    - Leveraged meshing optimization to increase and decrease density in correspondence with expected composite slab behavior.

The different aspects developed to optimize the simulations are described herein. The description is not exhaustive of all the actions performed but captures the most relevant aspects for full scale three-dimensional composite slab modeling. Concretely, the aspects analyzed are:

- Initial calibration and preliminary simulations performance
- Influence in steel deck measured dimensions
- Influence in concrete modeling: solid, crush and crack
- Influence in concrete crack inducer modeling
- Modeling laboratory test with two distinct FE models

4.4.1 Bending full-scale simulations: initial optimization process and calibration

The first full-scale models were developed with the steel deck INCO70 and replicated the short span laboratory specimens. The short span model was smaller in size compared with the equivalent long span model and hence eased the process to iteratively optimize the simulations. Figure 4.19 shows the initial load-midspan curve computed from the FE model and the actual laboratory test.

For this initial simulation, the maximum load observed $F_{u,max}$ at the FE model was 47.14 kN and produced a midspan deflection of 16.42 mm. The actual laboratory specimen reported a maximum load V_t = 60.21 kN at 19,15 mm midspan deflection that represented 21.7% and 14.3% deviations respectively for $F_{u,max}$ and midspan deflection compared with the simulation. Yet, the curve behavior from the simulation represented accurately the laboratory specimen progression under the incremental test loads. At the segment identified with (1), the simulation represented a lineal and elastic behavior for the composite slab, in line with the laboratory test. At the maximum load $F_{u,max}$ point (2), the simulation replicated the behaviour of a slow reduction in loading bearing capacity seen at the laboratory test. At the end of the simulation, point [3], the simulation equalized the values found at the laboratory test for $F_{u,max}$ and the midspan deflection.

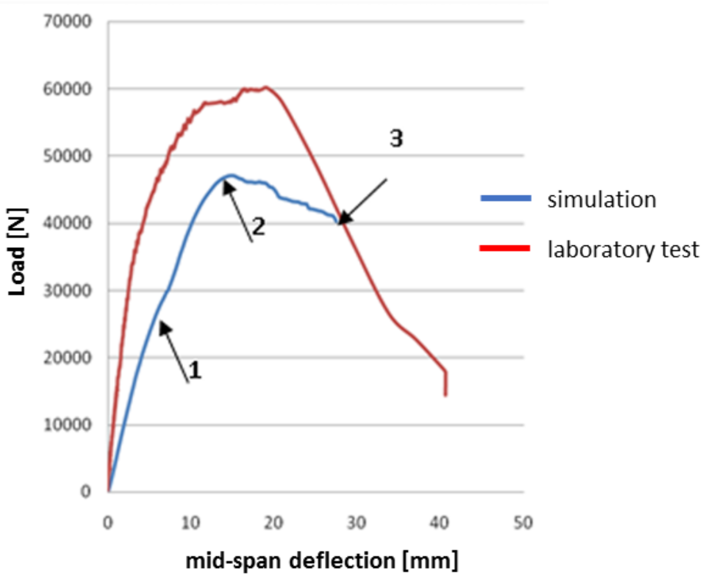

Figure 4.19 *Preliminary load – midspan curve in FE model*

Figure 4.20 introduces the end slip representation for the simulation and the laboratory specimen. At $F_{u,max}$ when the maximum value was observed, both the simulation at the laboratory specimen reported the largest end slips and similar values. The laboratory specimen recorded 3,74 mm and 1,55 mm for the left and right displacement sensors respectively -averaged value of 2.64 mm- while the laboratory specimen recorded 2,51 mm which indicated a 4.9% deviation.

The differences observed between the laboratory specimen and the simulation were initially attributed to a set of identified sources:

- The actual embossments dimensions were significantly different from the steel deck manufacturers nominal measures. Manufacturers catalogues represented ideal dimensions from the cold-forming process that were not achieved in none of the steel deck profiles tested. Additionally, circular embossments were not actually perfectly circular.
- The FE model included a crack inducer that actively influenced the composite slab behavior from the initial steps of the simulation. In the laboratory specimens, the crack inducer existed as a constituent element but it did not generated any concreted crack initially.
- No chemical bond was modeled.
- Friction coefficient was input initially as μ = 0.3 based on the literature review performed from other authors that recommended a value between 0.3 and 0.6.
- No steel reinforced bars were modeled due to complexity infused in the FE models. However, some initial FE models were created to conclude that reinforced bars had an was extremely limited influence.
- The support was modeled as a line support when in reality it was surface.

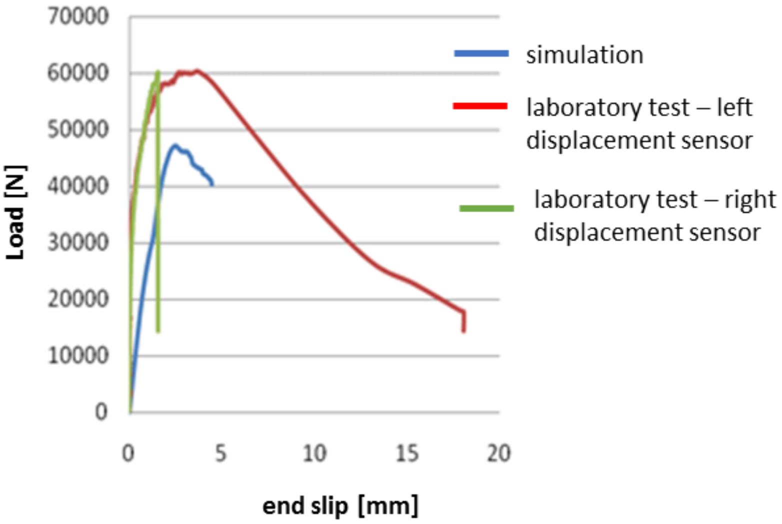

Figure 4.20 *Preliminary load - end slip curves*

Although the differences identified, multiple behaviours observed at the laboratory test were replicated at the numerical simulations that verified their robustness. Figure 4.21 illustrates the steel deck deformations along the span for three different midspan deflection cases: 7mm, 16.42mm when $F_{u,max}$ was achieved, and 19.15 mm. The deformation scheme observed replicated the ones observed in the laboratory tests.

The FE model observed different behaviours in the shear and bending spans. Figure 4.22(a) reproduces, in a 20x augmented scale, the steel deck deformation experienced within the shear span L_s

under the maximum load. The steel deck was subjected to a local transversal bending moment from the clamping phenomenon due to the slip between the materials. The new moment had a strong correlation with the amount of shear connection between steel and concrete as introduced inward deformations into the steel deck lateral sides. The clamping phenomenon is developed in more detail in chapter 6. Similarly, Figure 4.22(b) reproduces, in a 20x augmented scale, the deformation under the same conditions for a section located at the pure bending zone $L_{bending}$. Clearly the steel deck deformation presented a different intensity due to the different reactions from the concrete slab and exterior loads.

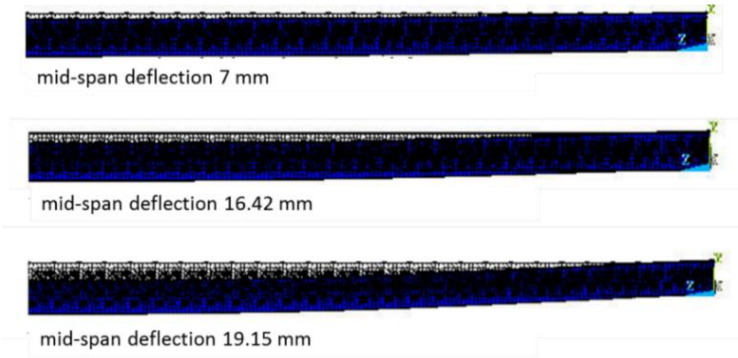

Figure 4.21 *Steel deck deformation under different midspan deflections*

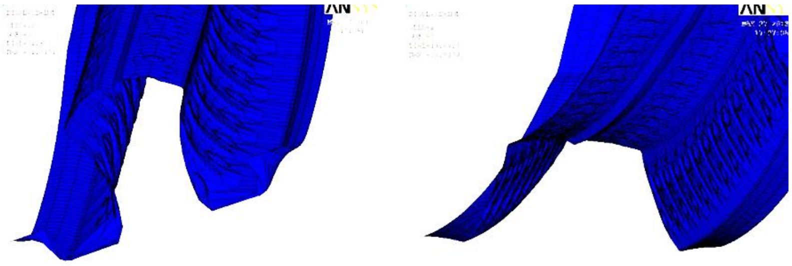
(a) (b)

Figure 4.22 *Steel deck sections deformation at shear and bending spans (20x)*

Figure 4.23 illustrates, again under a 20x augmented representation, the inflection area under the point load and with the presence of the crack inducer in which the steel deck sections transitioned between the shear and bending spans. The maximum steel deck transversal deformation was coincident with the largest loading value $F_{u,max}$ achieved at the simulation and preceded the vertical separation between the steel deck and the concrete slab.

The representation also showed a local deformation caused for the presence of the loading mechanism: the upper side of the steel deck presented a singular inward deformation which was opposed to any other deformation along the rib, caused by the load introduction at that point. The deformation at the inducer crack area, combined with the longitudinal inflection point observed were aligned with the expected clamping phenomenon from the concrete slab reaction. The modeling of the crack inducer and the subsequent development of two different concrete blocks capable to slip over the steel deck, introduced the different behavior in the shear L_s and pure bending $L_{bending}$ spans.

The concrete slab displacements presented two different components: horizontal slip and vertical separation. Figure 4.24 illustrates the correlation between the simulation results and the actual laboratory specimens when replicating both displacements.

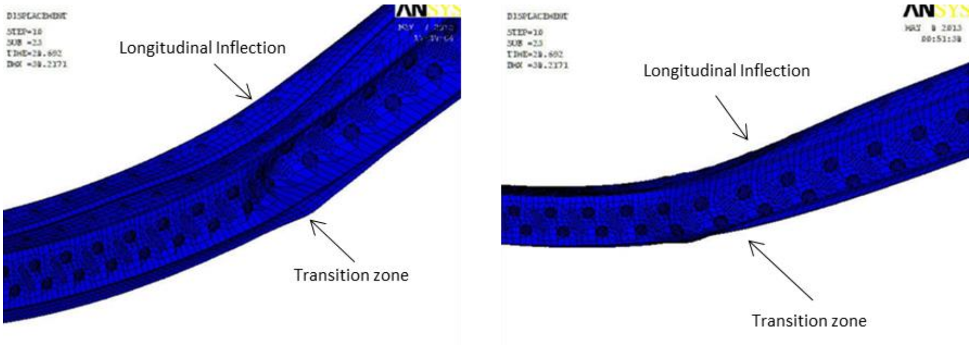

Figure 4.23 *Steel deck deformation (20x) between shear and bending spans*

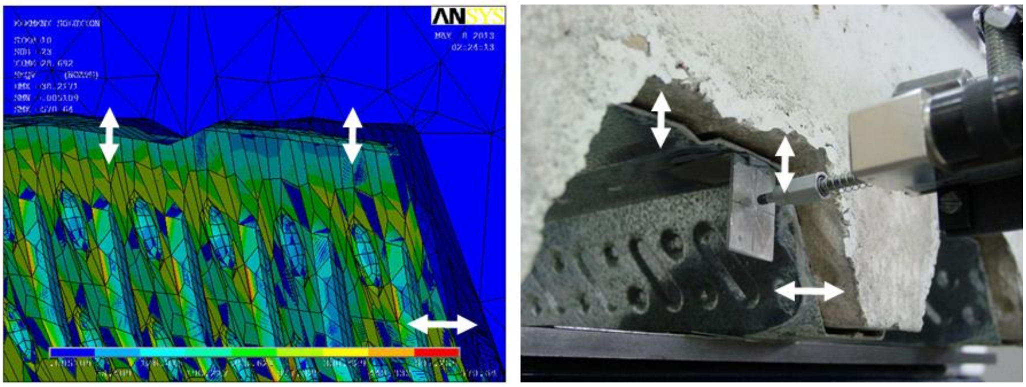

Figure 4.24 *Concrete slab and steel deck relative slip and vertical separation*

The relative slip of the concrete slab at the shear span L_s gradually abraded the embossment indentations at the concrete contact surfaces. Even though the FE definition of the concrete element type did not allow crack or crush phenomena initially, Figure 4.25 shows how the FE model was capable to capture concrete punctual areas under tensile stresses surrounding the embossments at the steel deck.

Another important area of focus for the simulation was the modeling of the crack inducer. The early simulations reported a strong agreement with laboratory specimens as shown in Figure 4.26. The FE model was capable to replicate not only the midspan deflection but also the descent introduced by the load at the crack inducer section at the end of the laboratory test. The pin joint defined at the FE model at the upper line replicated accurately the actual behavior observed.

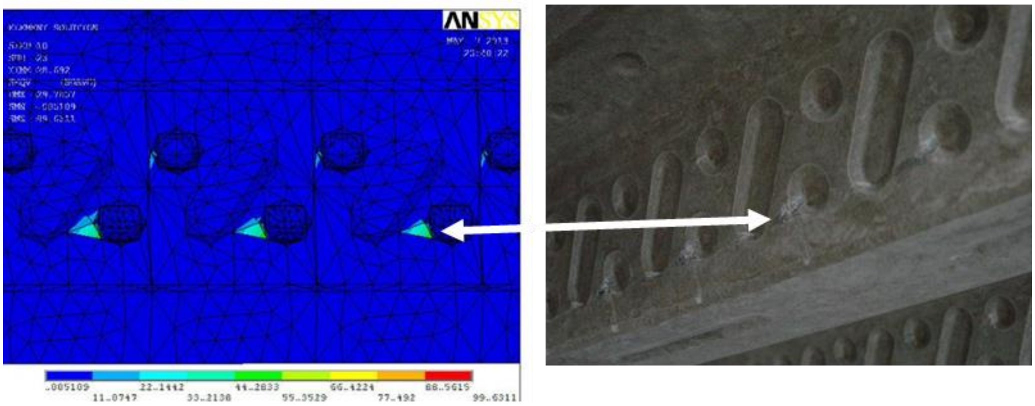

Figure 4.25 *Tensile stresses FE model and actual laboratory test*

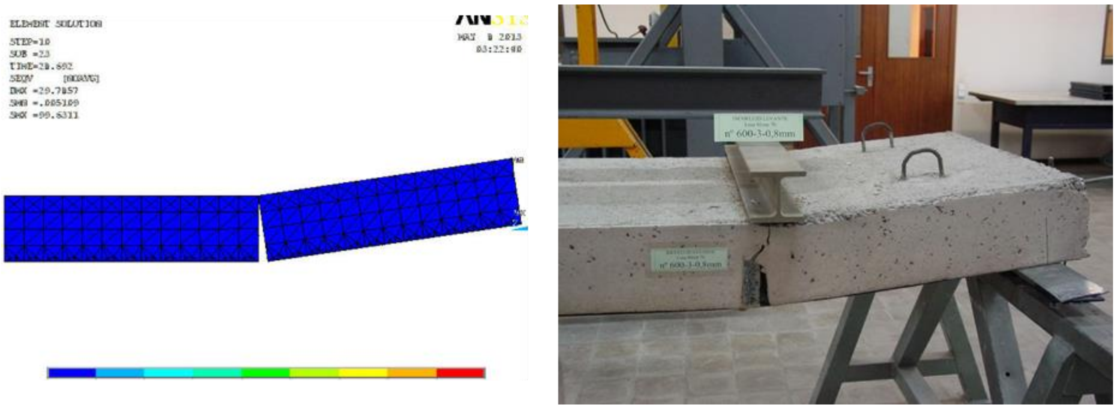

Figure 4.26 *Concrete crack inducer comparison FE model and actual laboratory test*

Additional studies were performed considering the capability to report nodal reactions for any Ansys element type at any simulation step. The understanding of the concentrated stresses allowed a detailed initial review of the performance from different FE element type selected (e.g. *SOLID185*, *SOLID187*) and also it was relevant for the optimization process to enhance the elements meshing. For example, Figure 4.27(a) depicts the nodal reactions computed at the pure bending span while Figure 4.27(b) shows the reactions at the shear span. For larger midspan displacements, the nodal reactions absolute values were significantly larger than early simulation steps. See Figure 4.28. In both cases, the reactions were concentrated at the surroundings of the embossments and the values varied depending on the exterior load applied.

The nodal reactions showed a consistent behaviour under different midspan defection cases:

- Both circular and longitudinal embossments reported larger values at the shear span compared with the pure bending span.
- Reactions concentrations were observed at the circular embossments and in less degree at the longitudinal embossments.

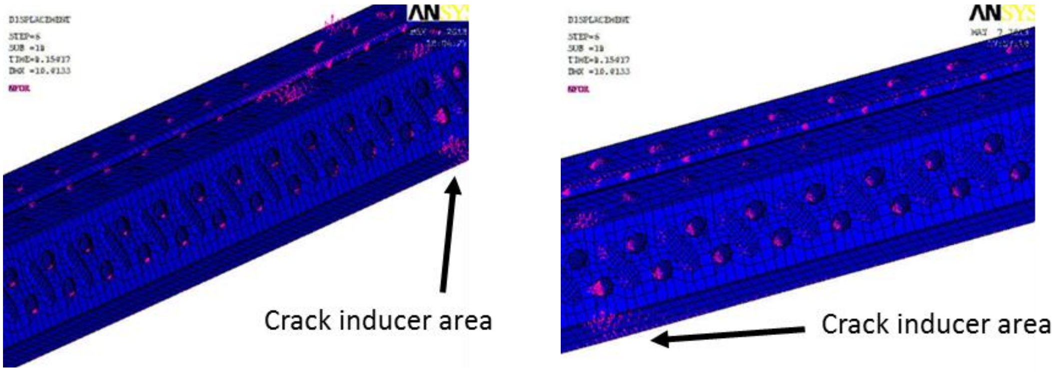

(a) (b)

Figure 4.27 *Nodal reactions at 7 mm midspan (a) bending span; (b) shear span*

The transition area between the shear and bending spans near the crack inducer concentrated the largest nodal reactions. The values observed increased as the midspan displacement increased.

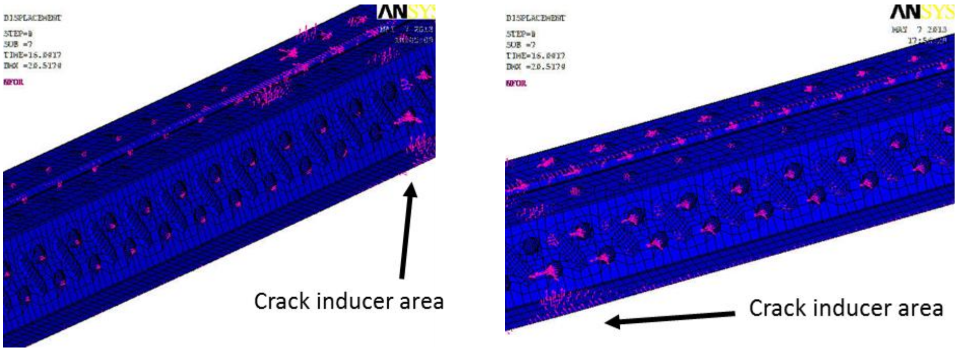

(a) (b)

Figure 4.28 *Nodal reactions at 16.42 mm midspan (a) bending span; (b) shear span*

The von Mises stresses were also investigated along the rib. Figures 4.29 and 4.30 depict a clear behaviour differentiation firstly at the shear and bending spans and secondly for the different midspan deflection cases. The steel deck observed larger stress values at the shear span and particularly at the crack inducer and support sections. The stresses also increased for larger midspan deflections as the composite slab observed larger loads such as in the laboratory experiment.

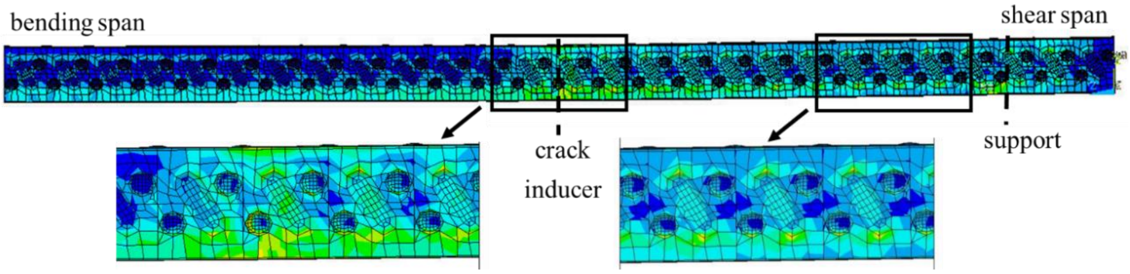

Figure 4.29 *Von Mises stress distribution, 7 mm midspan*

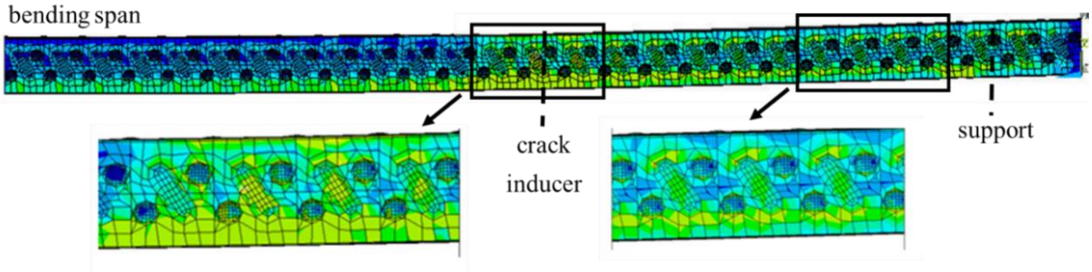

Figure 4.30 *Von Mises stress distribution, 16.42 mm midspan*

In all computed midspan deflection cases, the two circular embossments at the lateral sides of the steel deck near the concrete inducer always reported the highest concentration of stresses. A move towards either the pure bending or the shear spans from the crack inducer section, reported a gradual decrease in embossments stresses and ultimately a constant stress configuration in each section. The FE model also highlighted sections at the steel deck with plastic deformations due to the slip at the concrete inducer section. In those areas, the steel stresses observed different values before and after the separation occurred. The only other singular area observed was the support section where another stress concentration was observed.

An additional study was performed at the FE models for the principal stresses analyses. Figures 4.31 and 4.32 illustrate the representation computed when considered the upper fiber of the steel deck for the midspan deflection cases 7 mm and 16.42 mm respectively. The principal stresses vector representation allowed to identify the principal directions and magnitudes of the strains at the model. The two augmented representations in Figure 4.31 at the shear span highlighted again the concentration surrounding the circular embossments and, in a different degree, the longitudinal embossments. A dome effect was observed at the circular embossments and also a stress concentration at the front and punctual contact between the concrete slab and the steel deck. The direction of the vectors, namely tensions or compressions, did not change between different midspan deflection cases although values incremented for larger midspan deflections.

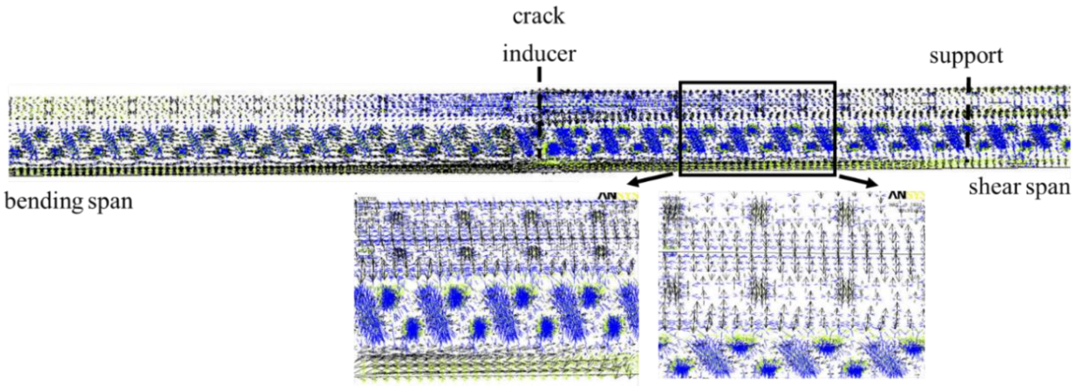

Figure 4.31 *Principal stresses vectors, 7 mm midspan*

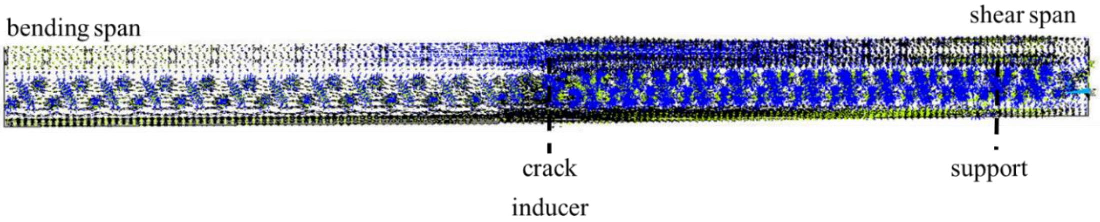

Figure 4.32 *Principal stresses vectors, 16.42 mm midspan*

The steel deck at the shear span concentrated larger stress values as it was exposed to two different phenomena: longitudinal bending and the local transversal bending from the longitudinal slip. The transversal bending was observed due to the compression found at the circular embossments and the tractions at the steel deck upper side. The longitudinal bending was observed at the rib lower surface in where the black colored vectors indicated tension and the blue colored vectors indicated longitudinal compression.

4.4.2 Concrete and crack inducer finite elements interaction and definition

Three different finite element types were proposed as candidates for concrete modeling: *SOLID185* as an 8-node linear elastic hexahedron element, *SOLID187* as a 10- node multi-linear elastic tetrahedron and *SOLID65* as an 8-node linear elastic tetrahedron element. *SOLID65* was initially implemented in early FE models due to its historic background in modeling concrete across multiple disciplines. Those preliminary models reported difficulties in convergence due to a large increase on computational requirements and other complexities such as high penetrations identified at the concrete areas surrounding the embossments. Furthermore, Ansys classifies today *SOLID65* as a legacy element and hence it discouraged its deployment as a preferred FE element type.

Consequently, only two different FE models named C60_185 and C60_187 were developed with *SOLID185* and *SOLID187* concrete type elements to study the suitability for the composite slab simulations. Table 4.5 summarizes the parameters of the initial FE models created. All FE models were based on the C60 steel deck profile and replicated the short span 2,600 mm bending laboratory tests. Nominal dimensions for the steel deck and materials properties presented in section 3.3.2 were implemented.

Initially, both C60_185 and C_187 models included the concrete capability for crushing and cracking. The models required a significant computational time that exceeded 300 hours per simulation and reported significant issues with convergence. Collaterally, the modeling approach experienced a broader challenge when the long span 5,000 mm laboratory specimens were modeled: the computational time required exceed 450 hours. The need to run a more elaborated analysis in such long full-scale models, combined with a strong alignment with the laboratory results from early FE models without the cracking and crushing capabilities, encouraged to simplify the concrete element type.

FE model code	FE concrete element	Crack inducer	Special modeling elements
C60_185	SOLID185	Yes	-
C60_187	SOLID187	Yes	-
C60_185_1CF	SOLID185/ SOLID65	Yes	One concrete pattern cracking and crushing
C60_185_2CF	SOLID185/ SOLID 65	Yes	Two concrete patterns cracking and crushing
C60_185_F	SOLID185	Yes	Second crack inducer

Table 4.5 *Concrete element types and crack inducer modeling optimization*

Figure 4.33 illustrates the load-midspan deflection curves for the C60_185 and C60_187 FE models. Both curves correlated well with the test specimen (see Figure 4.38) and showed minimal discrepancies for the overall composite slab behavior. Based on the results similarity, the *SOLID185* was the recommended element type for the concrete FE modeling: its computational time requirements were half compared with *SOLID187*.

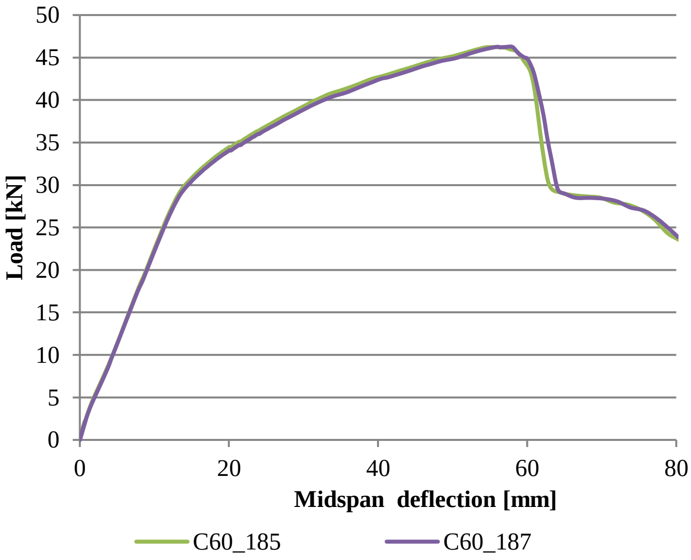

Figure 4.33 *Load-midspan curves SOLID185 and SOLID187*

Although the inclusion of the cracking and crushing capabilities for the complete concrete block was initially disregarded, two new models were developed with the inclusion of those capabilities in specific sections at the bending span. The C60_185_1CF and C60_185_2CF models included either one or two concrete patterns defined with *SOLID65* and the capability to crush and crack. The goal of the

FE models was to add concrete capabilities in areas where concrete behaviour was known to be singular based on laboratory test observation. The first new pattern, common for both models, was located at 1,100 mm from the support. The second new pattern, only defined at the C60_185_2CF model, was located at a distance of 750 mm from the support. Figure 4.34(a) depicts conceptually the location of the new patterns. The 8 mm-wide *SOLID65* new patterns were placed strategically between embossments to avoid the high penetration during calculation steps observed on initial FE models. The new material parameters used for concrete were: $\beta_t = 0.2$ and $\beta_c = 0.6$ for the coefficients of open and closed crack respectively. These parameters were introduced following previous modeling cases developed by Palerm (2011) and Chen and Shi. The new FE concrete patterns were merged to the rest of *SOLID185* elements with the prisms option.

Additionally, a third C60_185_F model included the addition of a second crack inducer, with the same properties such as the one defined near the loading point. The new crack inducer at the bending zone was modelled at a distance of 1,100 mm from the support at the bending span and proposed to extend the concrete block deformations replicating the behavior observed in some laboratory tests when concrete showed cracking. Figure 4.34(b) depicts conceptually the location of the new elements.

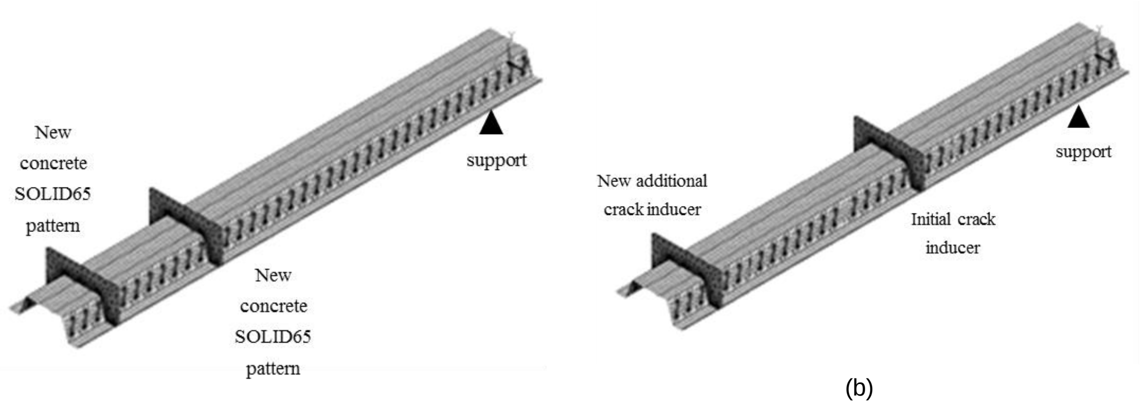

(a)

(b)

Figure 4.34 *FE models with additional concrete and crack inducer capabilities*

All the three new simulations reported additional computational time but not to the scale observed with the models that included the concrete cracking and crushing capabilities at the complete FE model. Figure 4.35 captures the load-midspan curves for the different models computed. The curves showed minimal deviation across FE models except for the C60_185_F model. Results depicted similar behaviours between models C60_185_CF, C60_185_2CF and C60_185 with the first two FE models including concrete cracking patterns. The 185_F model created 3 different areas bounded by the location of the two crack inducers which were different from the common shear and bending spans observed at both the test laboratory specimens and the rest of the FE models.

Figure 4.36 highlights a cross-section at the *SOLID65* pattern for a 16,42 mm midspan deflection in which the maximum load $F_{u,max}$ was achieved. The patterns presented cracking at the concrete areas in contact with the steel deck. However, the influence of the concrete cracking did not modify the overall modeling as both C60_185_CF and C60_185_2CF showed a similar load-midspan behavior than the C60_185 model.

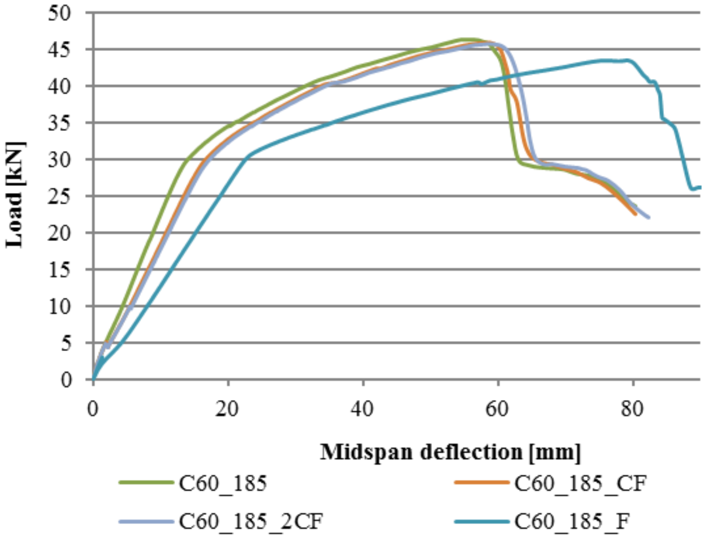

Figure 4.35 *New FE models additional parameters for concrete and crack inducer modeling*

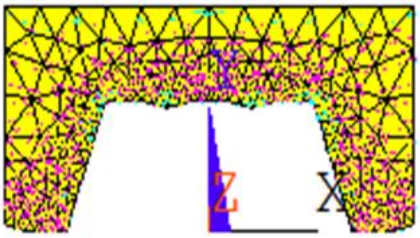

Figure 4.36 *Concrete slab section with cracking phenomenon*

Consequently, the modeling with the SOLID185 element type without the inclusion of cracking and crushing capabilities was implemented for all the simulations developed in this research.

4.4.3 Influence on steel deck measured dimensions

Parallel to the concrete elements and crack inducer modeling optimization, the dimensions of the embossments affected considerably the composite slab maximum shear bond. An additional FE model C60_185_RM was developed to study the sensitiveness from the embossments geometries and compared subsequently with the C60_185 model. Table 4.6 summarizes the main parameters for both models. The measured dimensions for the C60 steel deck were previously described in Table 3.2 as part of the description of the steel deck profile and are reproduced again below as Table 4.7.

FE model code	FE concrete element	Crack inducer	Geometry
C60_185	SOLID185	Yes	Nominal
C60_185_RM	SOLID185	Yes	Measured

Table 4.6 *FE models embossments geometrical dimensions*

	Nominal	Measured
Lateral longitudinal embossment depth [mm]	3.0	2.4
Lateral longitudinal embossment length [mm]	31.0	29.5
Lateral longitudinal embossment slope [º]	45º	48º
Separation between embossments [mm]	37.5	33.0
Separation between patterns [mm]	207.0	206.0
Profiled angle [º]	71.4º	72.0º

Table 4.7*C60 steel deck profile nominal and measured dimensions*

Figure 4.37 illustrates the main differences among embossment geometries. The theoretical embossment shape is captured in Figure 37(a); the cold-formed process should generate a constant depth and an uniform unit, with a flat surface at the upper side of the embossment. Figure 37(b) shows an actual picture of the real embossment. The base of the embossment at the steel deck surface was wider than the theoretical measure and the upper flat surface was almost non-existent. The slope was consequently lower than the theoretical model. Figure 4.37(c) represents the final embossment geometry implemented at the C60_185_RM FE model.

(a) (b) (c)

Figure 4.37 *Embossment dimensions actual and nominal*

Figure 4.38 illustrates the load-midspan and load-end slip curves for the FE models under study and also the actual laboratory specimen named C60_Laboratory specimen. It can be observed that the C60_185_RM model that implemented the actual embossment dimensions agreed better with both curves. The C60_185 model with the nominal dimensions introduced a larger shear resistance at the composite slab, with a $F_{u,max}$ maximum load resistance of 46.22 kN compared with the 36.05 kN value reported at the laboratory specimen. Table 4.8 compares numerically some of the key values from the simulations and the laboratory specimen. C60_185_RM also represented a more accurate behavior for the midspan and end slip curves for $F_{u,max}$.

	C60_185	C60_185_RM	Laboratory specimen
$F_{u,max}$ [kN]	46. 22	33.02	36.06
Midspan deflection [mm] at $F_{u,max}$	55.57	70.05	75.22
End slip [mm] at $F_{u,max}$	3.34	5.57	5.21

Table 4.8 *Simulation results for $F_{u,max}$ in different embossment geometry modeling*

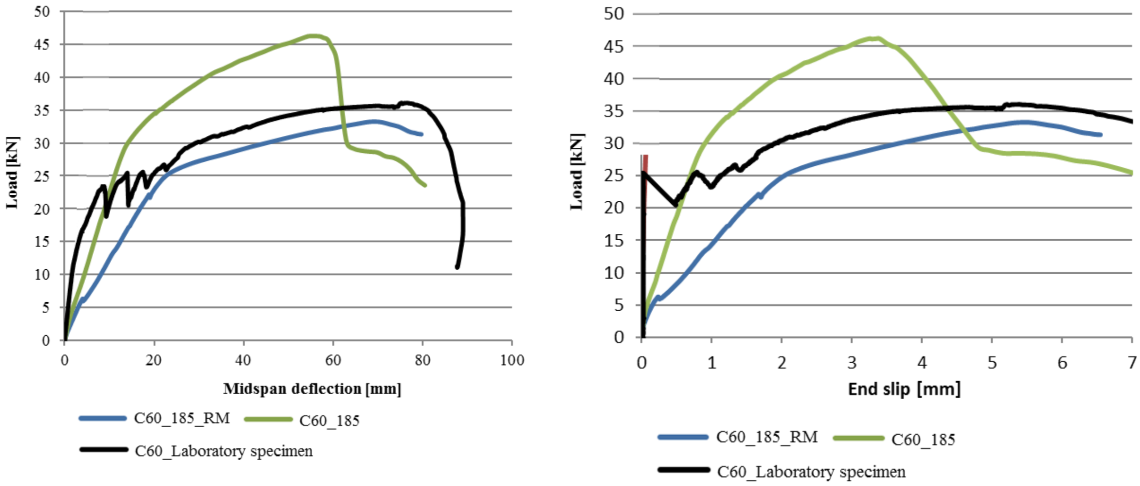

Figure 4.38 *FE models with measured and nominal embossment dimensions*

Similar comparisons were performed with other embossment typologies such as circular shapes found at the INCO70 and the T80 steel deck profiles. The differences in dimensions were captured in Tables 3.1, 3.2, 3.3 and 3.4 previously introduced as part of the steel deck definition. Based on the results, the measured dimensions were implemented for the development of the numerical simulations.

4.4.4 Bending full-scale simulation with two different FE models

During the development of the initial FE models captured in sections 4.4.1 to 4.4.3 it was observed that they were not capable to replicate with accuracy the early loading stages when the concrete crack at the inducer was not yet developed. Simulations discussed in Figures 4.19 and 4.38 were examples in which the load-midspan curve from the FE models presented a different slope prior the initial slip between the steel deck and the concrete slab initiated. The existence of the crack inducer as a joint pin from the early simulation stages was considered to be the main factor.

In order to overcome this limitation, a novel modeling approach was introduced: two different FE models were developed, with and without crack inducers. In early loading stages of the laboratory test, the steel deck and concrete slab share full connection and no slip exist between the materials. Such longitudinal strength contribution from the chemical bond is not exclusively related to any material or geometry property and therefore building codes recommend to disregard it as part of the shear resistance analysis. Consequently, a FE model without the crack inducer was proposed to enhance the simulation delaying the presence of large relative slip between materials. Once the slip exceeded 0.1 mm, a crack inducer could characterize better composite performance as then the shear resistance main components were defined by the embossment mechanical interlock. Table 4.9 summarizes the main parameters for the proposed FE models. The C60_185_AF model was developed with no crack inducer at the point load L_S. The concrete slab included all the concrete element types merged and therefore neither a joint pin nor a crack section existed in the model.

FE model Code	FE concrete element	Crack inducer	Geometry
C60_185_RM	SOLID185	Yes	Measured
C60_185_AF	SOLID185	No	Measured

Table 4.9 *FE models with and without crack inducer*

Figure 4.38 illustrates the load-midspan and load-end slip curves computed for the two FE models. During early loading stages, slope for the C60_185_AF in both curves agreed well with C60_Laboratory specimen curves and differed significantly from the C60_185_RM model. Yet, gradually as the load increased, the C60_185_RM curves correlated more accurately for mid and late stages of the simulation.

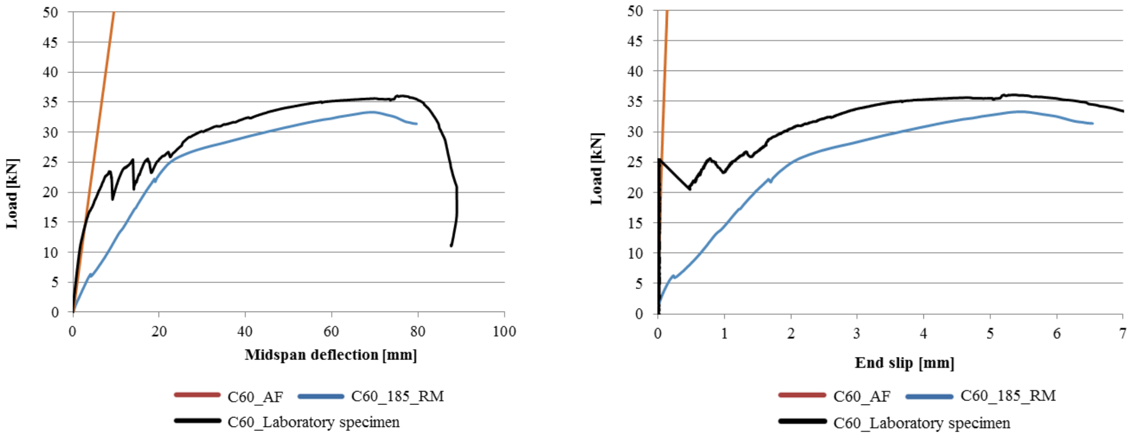

Figure 4.39 *Bending simulation characterization with two different FE models*

The proposed modeling scheme with two different FE models solved two complex behaviours observed in FE modeling in composite slabs: first, the characterization of the initial chemical bond. Some early simulations were developed with the introduction of a friction τ_0 parameter which reproduced an initial static friction. The results showed a strong reliance in laboratory tests results and required a tedious calibration process for each FE model. Alternatively, the FE model without the crack inducer represented a shear perfect bond behaviour in the early loading stages which was proven to mirror accurately the effect from the chemical bond. Second, the avoidance to deploy more elaborated modeling techniques such as point-to-point load-deformation curves or dynamic friction schemes. For example, the introduction of contact point-to-point pairs for the surfaces at the crack inducer was tested in order delay the capability to separate the concrete slab surfaces. Results were similar to the test of an initial τ_0 parameter discussed in section 4.2.5 and therefore presented a strong reliance from the initial calibration with laboratory specimens. The deployment of more elaborated analyses in FE resulted in significant increases in computational time requirements.

The bending full-scale simulations with two FE models for each steel deck profile are described in detail in section 4.5 and were captured as conference proceedings for Eurosteel 2014, Plans et al. (2014).

4.5. Preliminary results

This section summarizes the preliminary results from the FE models developed for the four steel deck profiles INCO70, C60, QL60 and T80. Initially, the load-mid span and load-end slip curves from the bending short and long spans FE models were compared with the laboratory specimens. A in-deep analysis is performed for the INCO70 steel deck as case study: multiple laboratory specimens were analyzed, analytical studies performed and additional FE models created. The same analyses were performed for the rest of the steel deck profiles but are not reported in this section unless a significant different result was observed.

Based on the strong agreement between the FE models and the laboratory specimens, subsequently full scale pull-out models were developed for the INCO70 steel deck profile without the need to perform any laboratory test. Both bending and pull-out FE models included the optimization approaches and techniques described previously.

4.5.1 Full-scale bending

The bending FE models developed replicated the short and long spans laboratory specimens. Table 4.10 summarizes all the simulations and key parameters developed. Most of the LERMA composite slab laboratory tests shared a composite slab overall thickness h_t = 180 mm and a steel deck thickness *t* = 0,8 mm. Otherwise, it was noted as part of the FE model name. The FE models followed the naming convention detailed below:

(S) Short span or (L) Steel deck profile name Long span
Code Name: *(CI) Crack Inducer or (NCI) No Crack Inducer*
Special parameters:

- *(1.2) steel deck (t) thickness in case it is not 0.8 mm*

Example: INCO70_S_CI_1.2 stands for: INCO70 steel deck profile, short span, with crack inducer and steel deck thickness 1.2 mm.

	Short span	Long span	Comments
INCO70	INCO70_S_CI_0.8	INCO70_L_CI	-
	INCO70_S_NCI_0.8	INCO70_L_NCI	-
	INCO70_S_CI_1.2		For the INCO70 short span two different steel deck thicknesses were evaluated: 0.8 and 1.2 mm
	INCO70__S_NCI_1.2		-
C60	C60_S_CI	C60_L_CI	The composite slab depth for the short span was h_t=100 mm
	C60_S_NCI	C60_L_NCI	-
QL60	QL60_S_CI	QL60_L_CI	-
	QL60_S_NCI	QL60_L_NCI	-
T80	T80_S_CI	T80_L_CI	-
	T80_S_NCI	T80_L_NCI	-

Table 4.10 *FE models naming convention*

Not all the FE models shared the same lengths and geometries. As part of the FE modeling process, patterns of *s* width were defined for each steel deck to capture the smallest unit that included all the repetitive features. Tables 4.1, 4.2, 4.3 and 4.4 previously introduced captured the main properties for the full-scale bending FE models.

INCO70 numerical simulations

The INCO70 steel deck profile was leveraged as base case for detailed analyses and in-depth discussions performed between the FE models and the laboratory specimens. For the rest of steel deck profiles, a more summarized approach was performed unless singularities were found. For example, FE models were only compared with a laboratory specimen with the closest behaviour as opposed to the common three tests requested by the building codes.

The INCO70 FE models load-midspan and load-end slip curves for short span were compared with the three laboratory specimens available from LERMA. Two different analyses were performed to study the agreement between the simulations and the laboratory tests: first, the maximum load values

$F_{u,max}$ and V_t for the curves were compared. Secondly, an approach to measure and compare areas under the curves was performed. Exceptionally, an additional FE model was developed to characterize more accurately the influence of the steel deck thickness *t* as laboratory results were available for $t = 1.2$ mm.

Short span

The Newton-Raphson simulation of the bending models resulted in composite slab behaviors very similar to those of the three laboratory specimens in midspan and end slip curves. Figure 4.40 illustrates the similitude in load-midspan deflections between the INCO70_S_CI_0.8 and INCO70_S_NCI_0.8 and the laboratory specimens. Similarly, Figure 4.41 illustrates the similitude in end slip behaviors.

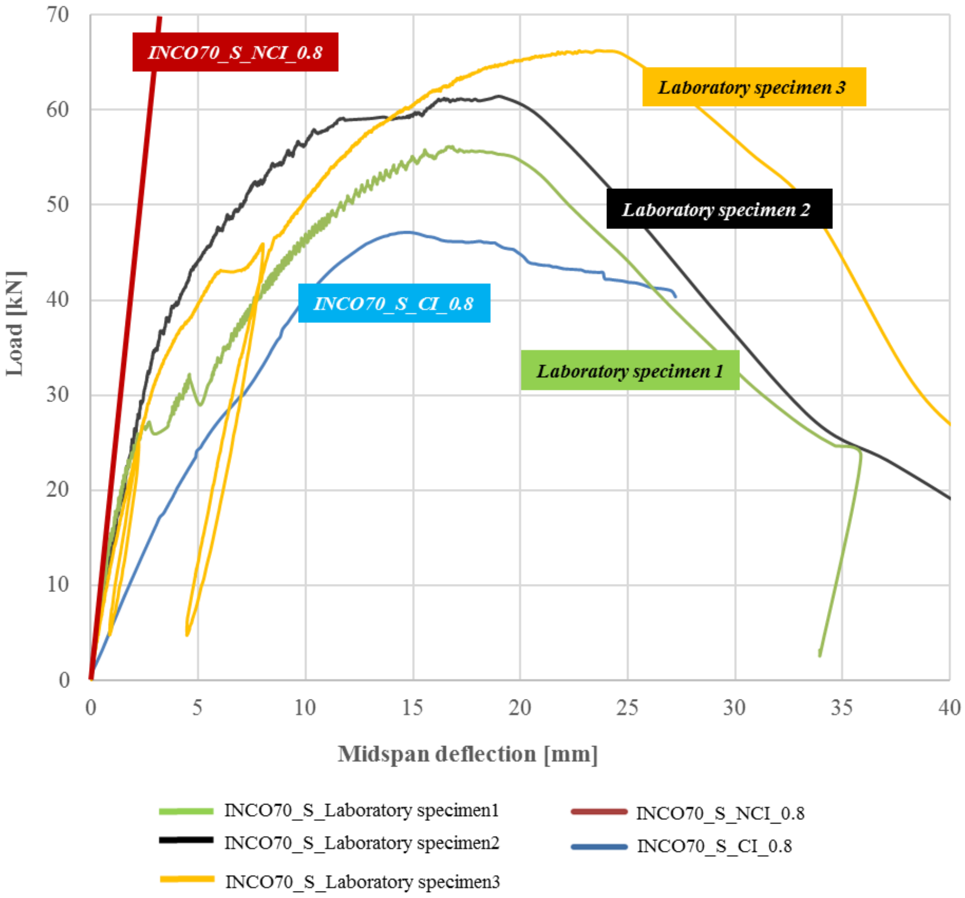

Figure 4.40 *INCO70 load-midspan curves for all laboratory specimens and FE models*

First, midspan and end slip discrete values from the simulations were benchmarked against laboratory tests results. Table 4.11 summarizes eight simulation steps and shows the variance in the load values observed. Indeed, the INCO70_S_NCI_0.8 model characterized better the early stages of bending with an almost linear behavior before the end slip initiated. Compared with the laboratory tests results, the FE model reported a strong alignment with load variances around or below 10% for end slip values up to 0.005 mm. A significant variance was then observed in the range between 0.02 mm and 1.5 mm of end slip, which represented the shear resistance transition to embossments mechanical interlock from the initial chemical bond. The behavior of the INCO70_S_CI_0.8 model evolved in a nonlinear manner of the load-deflection curve and better represented the composite behavior once all chemical bond disappeared. In the last simulation steps, with loads approaching the maximum composite slab shear resistance, load variances were observed below or around 15% for a wide range of slip values when compared to the tests.

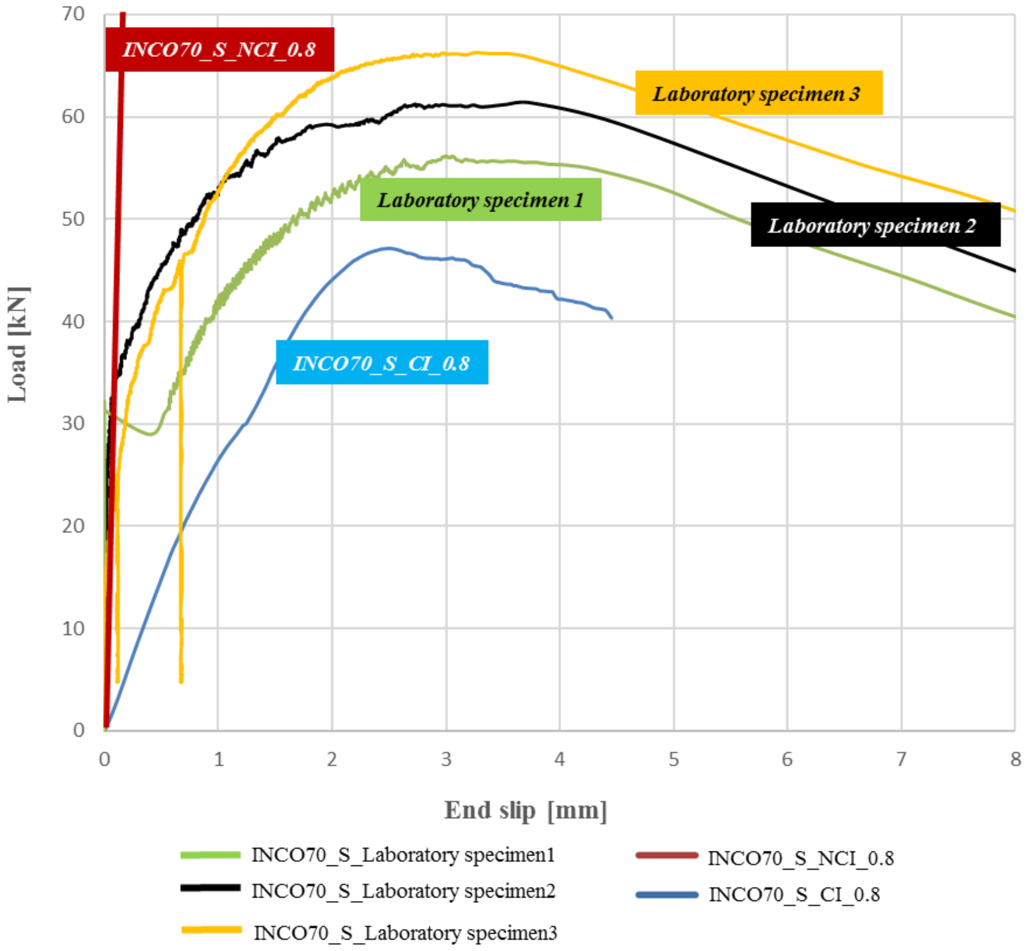

Figure 4.41 *INCO70 load-end slip curve for all laboratory specimens and FE models*

Second, a comparison between the areas under the load-midspan (see Figure 4.40) and load-end slip (see Figure 4.41) curves for the INCO70_S_CI_0.8 model and the laboratory specimens were computed as an additional measure of model reliability. Given that the simulation and test curves resemble, the proportion of the area covered by the simulation in relation to the specimens provide an additional measure of reliability of the computational approach. Reimann method to the calculation of discrete areas was leveraged to compute the total area for the range of midspan and end slip values from the simulations. Subsequently, ratios for the values obtained between the INCO70_S_CI_0.8 and LaboratorySpecimen1 against each laboratory specimen were calculated. See Table 4.12.

	Simulations			Variance *with closest laboratory specimen*	
FE model code	Midspan deflection [mm]	End slip [mm]	Load F [kN]	Load F [kN]	Load F (%)
INCO70_S_NCI_0.8	0.05	0.00	1.18	0.06	5.07
INCO70_S_NCI_0.8	0.10	0.01	2.36	0.28	10.81
INCO70_S_NCI_0.8	0.50	0.02	11.84	3.30	38.57
INCO70_S_NCI_0.8	4.00	0.66	19.24	9.45	32.93
INCO70_S_NCI_0.8	9.00	1.51	35.77	7.34	17.03
INCO70_S_NCI_0.8	14.96	2.46	47.11	6.98	12.90
INCO70_S_NCI_0.8	20.00	3.29	45.35	8.25	15.39
INCO70_S_NCI_0.8	27.47	4.45	40.72	1.56	3.69

Table 4.11 *Load comparison observed simulations and laboratory specimens*

The INCO70_S_CI_0.8 simulation covered 84.61% of the area generated by the midspan deflection in LaboratorySpecimen1, and 78.59% of the area generated by the end slip curve. These values were similar to those observed between laboratory specimens. For example, LaboratorySpecimen1 covered 81.87% and 81.99% with respect to LaboratorySpecimen2 in terms of load-midspan deflection and load-end slip curves respectively. Laboratory tests had intrinsic variance among them and hence the request from different building codes to test multiple specimens to characterize composite slabs.

	Midspan deflection Range: 0 – 27,47 mm		End slip Range: 0 – 4.40 mm	
	INCO70_S_CI_0.8	Lab. Specimen1	INCO70_S_CI_0.8	Lab. Specimen1
Specimen 1	84.61%	-	78.59%	-
Specimen 2	69.27%	81.87%	64.44%	81.99%
Specimen 3	61.88%	73.14%	56.19%	71.50%

Table 4.12 *Area ratios between simulations and laboratory specimens*

Subsequently, two additional models INCO70_S_CI_1.2 and INCO70_S_NCI_1.2 were developed that modeled a steel deck thickness $t = 1.2$ mm. Figure 4.42 illustrates the load-midspan and load-end slip curves for the FE models and the LaboratorySpecimen1 specimen and Table 4.13 summarizes a reduced analysis comparing them. The new FE models also accurately computed the behaviour and coincidently agreed more for the displacement curves. The author hypothesizes, as a source for the better alignment, that the belated yielding of the steel deck material due to a thicker profile enabled a better characterization by the FE models. The extended elastic regime proved to be more predictable.

	INCO70_S_CI_0.8	INCO70_ Lab. specimen	INCO70_S_CI_1.2	INCO70_ Lab. specimen
$F_{u,max}$ [kN]	55.60	55.13	105.25	112.92
Midspan deflection [mm]	17.02	16.64	20.10	21.52
End slip [mm]	3.22	2.99	3.31	3.62

Table 4.13 *FE models comparison at $F_{u,max}$ with laboratory specimens*

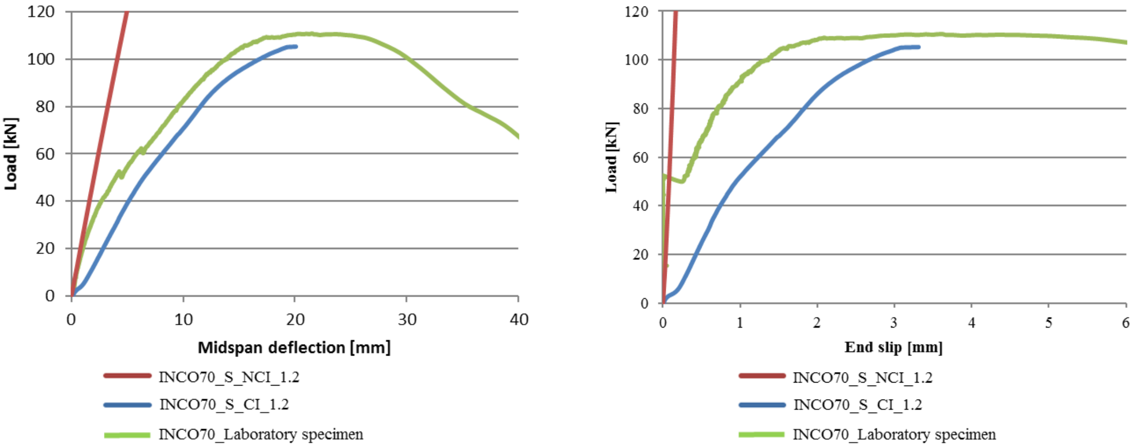

Figure 4.42 *Load-midspan and load-end slip curves, INCO70 t = 1.2 mm, short span*

Long span

Figure 4.43 illustrates the load-midspan deflections and load-end slip between the INCO70_L_NCI and INCO70_L_CI and the closest laboratory specimen. The laboratory specimen selected was the one closest to the FE model behaviour. As observed previously, the first FE model represented accurately the initial simulation steps while the second model better represented the laboratory specimen when the concrete slab – steel deck slip had initiated. Particularly, starting at the 0.4 mm of end slip, the INCO70_S_CI model matched the behaviour. Previously, the INCO70_L_NCI had a similar curve slope of 84° similar to the laboratory specimen. Table 4.14 summarizes eight simulation steps and shows the variance in the load values observed with the laboratory specimen.

Similar to the performance observed in the short span, the FE model without the crack inducer agreed better initially before any slip originated. Subsequently, the FE model with a crack inducer captured more accurately the behaviour with deviations around 1% - 15% at midspan deflections. The analysis for the areas under the midspan and end slip curves was also computed. The INCO_L_CI simulation covered 96.4% of the area generated by the midspan deflection in INCO_LaboratorySpecimen for the values between 0 mm and 55.3 mm. Equally, the area covered by the end slip curve was 92.8% for the values between 0 and 5.33 mm.

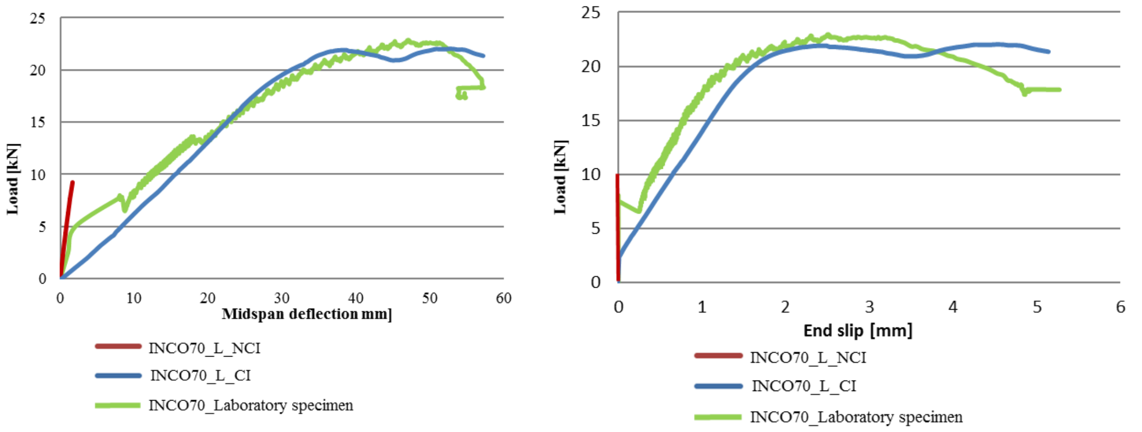

Figure 4.43 *Load-midspan and load-end slip curves, INCO70, long span*

		Simulations		Variance *with the closest laboratory specimen*			
FE model code	Load F [kN]	Midspan deflection [mm]	End slip [mm]	Midspan deflection [mm]	Midspan deflection (%)	End slip [mm]	End slip (%)
INCO70_L_NCI	0.50	0.10	0.00	0.25	60.00	0.00	0.00
INCO70_L_NCI	1.00	0.15	0.00	0.50	70.00	0.00	0.00
INCO70_L_NCI	3.00	0.50	0.00	1.15	56.52	0.00	0.00
INCO70_L_CI	5.00	0.80	0.10	2.00	60.00	0.00	0.00
relative slip starts							
INCO70_L_CI	5.00	8.32	0.22	2.00	75.96	0.00	0.00
INCO70_L_CI	10.00	15.44	0.63	13.23	14.31	0.44	30.16
INCO70_L_CI	15.00	22.85	1.09	22.56	1.27	0.80	26.61
INCO70_L_CI	20.00	31.12	1.60	32.26	3.53	1.40	12.50

Table 4.14 *Summary variations observed between INCO70 FE models and laboratory specimens*

C60 numerical simulation

Table 4.15 captures a reduced summary of the values observed at the simulations and compare them with the laboratory results.

	Short span slab		Long span slab	
	C60_S_CI	C60_Lab. specimen	C60_S_CI	C60_Lab. specimen
$F_{u,max}$ [kN]	33.02	36.06	30.51	26.14
Midspan deflection [mm]	69.31	75.22	26.72	41.25
End slip [mm]	5.57	5.21	2.03	1.97

Table 4.15 *FE models comparison at $F_{u,max}$ with laboratory specimens, C60*

Short span

Figure 4.44 illustrates the load-midspan and load-end slip curves for the FE models and the closest laboratory specimen. The C60 short span simulations were previously deployed to optimize the modeling and thus a detailed description of the shear bond behaviour can be found in section 4.4.

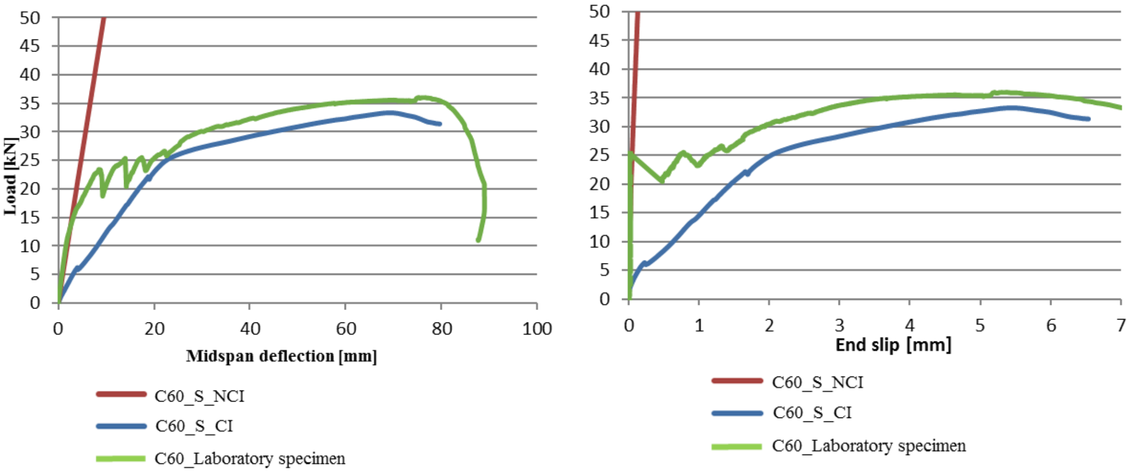

Figure 4.44 *Load-midspan and load-end slip curves, C60, t = 0.8 mm, short span*

Long span

Figure 4.45 illustrates the midspan deflections and end slip curves between the C60_L_NCI, C60_L_CI and the closest laboratory specimen. The C60_L_CI model replicated accurately the initial steps of the laboratory tests until the slip initiated. Particularly, between 10 and 20 mm of midspan deflection, the curve slopes between the FE model was 43º and the laboratory specimen was 56º and showed similarity. Yet, it could be observed that the laboratory specimen curve experienced an abrupt decrease prior to reach $F_{u,max}$ maximum load. For this particular case, the deflection in which the maximum load was observed in the laboratory test was offset from the value observed at the FE model. Table 4.16 summarizes thirteen simulation steps and shows the variance in the load values observed.

Although the curves did not observe the $F_{u,max}$ maximum load at similar midspan deflection cases, the decrease in loading capacity once the maximum load was achieved shared a similar slope with of 27º at the simulation and 20.5º for the laboratory specimen.

The analysis for the areas under the midspan and end slip curves was also computed. The C60_L_CI simulation covered 87.4% of the area generated by the midspan deflection in C60_LaboratorySpecimen for the values between 0 mm and 71.2 mm. Equally, the area covered by the end slip curve was 94.3% for the values between 0 and 2.62 mm.

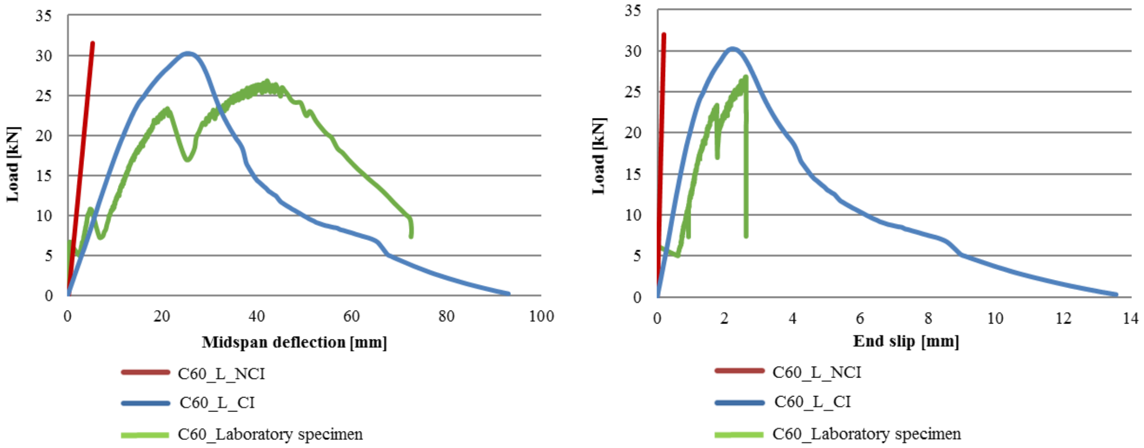

Figure 4.45 *Load-midspan and load-end slip curves, C60, t = 0.8 mm, long span*

		Simulations		Variance *with the closest laboratory specimen*			
FE model code	Load F [kN]	Midspan deflection [mm]	End slip [mm]	Midspan deflection [mm]	Midspan deflection (%)	End slip [mm]	End slip (%)
C60_L_NCI	0.50	0.31	0.00	0.11	67.71	0.00	0.00
C60_L_NCI	1.00	0.60	0.00	0.10	83.37	0.00	0.00
C60_L_NCI	3.00	0.62	0.00	0.22	67.70	0.00	0.00
C60_L_NCI	5.00	0.90	0.00	0.30	66.70	0.00	0.00
relative slip starts							
C60_L_CI	5.00	2.80	0.22	2.50	10.75	0.60	63.30
C60_L_CI	10.00	5.63	0.45	5.20	7.65	0.84	46.40
C60_L_CI	15.00	8.63	0.69	12.32	29.83	1.12	38.43
C60_L_CI	23.00	14.60	1.17	20.50	28.96	1.76	34.54
C60_L_CI	23.00	32.40	3.30	32.21	0.64	2.62	20.68
C60_L_CI	20.00	35.80	3.74	54.60	34.47	2.62	-
C60_L_CI	15.00	38.30	4.55	62.53	37.17	2.62	-
resistance capacity decreases							
C60_L_CI	10.00	50.00	6.25	71.20	29.89	2.62	-

Table 4.16 *Summary variations observed between C60 FE models and laboratory specimens*

QL60 numerical simulation

Table 4.17 captures a reduced summary of the values observed at the simulations and compare them with the laboratory results.

	Short span slab		Long span slab	
	QL60_S_CI	QL60_S_Lab. specimen	QL60_S_CI	QL60_S_Lab. specimen
$F_{u,max}$ [kN]	47.90	50.01	26.19	27.55
Midspan deflection [mm]	18.34	25.60	28.42	78.25
End slip [mm]	2.51	2.93	2.48	2.92

Table 4.17 *FE models comparison at $F_{u,max}$ with laboratory specimens, QL60*

Short span

Figure 4.46 depicts the load-midspan and load-end slip curves for the FE models and the closest laboratory specimen.

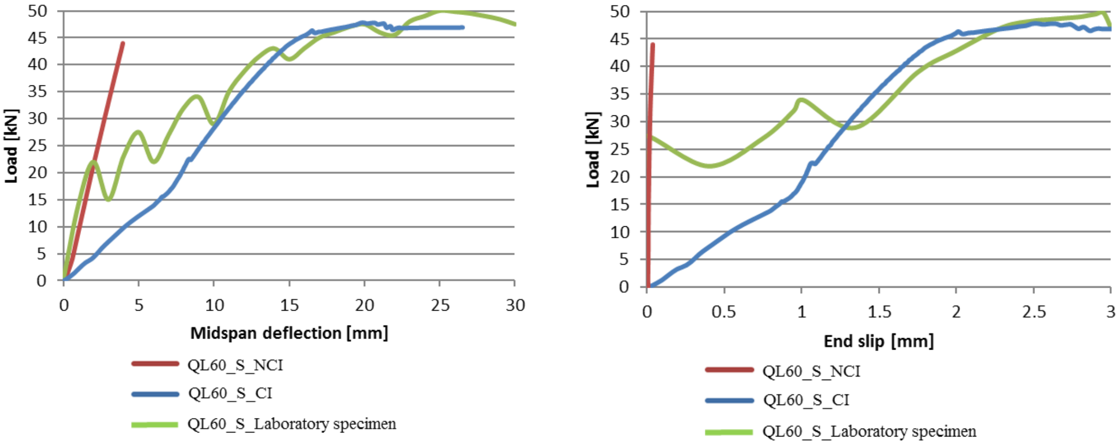

Figure 4.46 *Load-midspan and load-end slip curves, T80, short span*

Long span

Figure 4.47 illustrates the load-midspan deflections and load-end slip curves between the QL60_L_NCI, QL60_L_CI and the laboratory specimen.

The QL60_L_NCI model reported deviations around 3% with the laboratory specimen values observed for both curves prior the relative slip initiated. The QL60_L_CI then replicated subsequently the laboratory specimen behaviour with strong agreement. Concretely, the FE model observed deviations fluctuating between 10% and 40% for the F_u loads but with wide segments of alignment. At the laboratory test, the composite slab observed a load capacity recession around the 50 mm of midspan deflection which was replicated at the QL60_L_CI model. A noticeable difference was observed at the $F_{u.max}$ – midspan deflection pairs, with the laboratory specimen observing the $F_{u.max}$ at a larger deflection. Table 4.18 summarizes ten simulation steps and shows the variance in the load values observed.

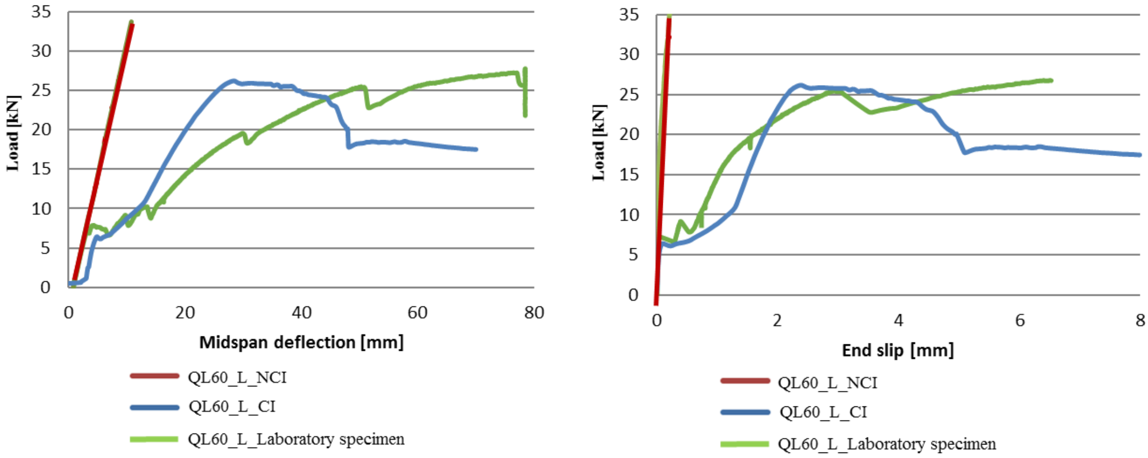

Figure 4.47 *Load-midspan and load-end slip curves, QL60, long span*

		Simulations		Variance *with the closest laboratory specimen*			
FE model code	Load F [kN]	Midspan deflection [mm]	End slip [mm]	Midspan deflection [mm]	Midspan deflection (%)	End slip [mm]	End slip (%)
QL60_L_NCI	0.50	0.94	0.00	0.94	0.00	0.00	0.00
QL60_L_NCI	1.00	1.19	0.00	1.19	0.00	0.00	0.00
QL60_L_NCI	5.00	2.30	0.00	2.31	0.40	0.00	0.00
QL60_L_NCI	7.00	2.90	0.00	2.97	2.35	0.00	0.00
relative slip starts							
QL60_L_CI	7.00	8.05	0.38	7.60	5.60	0.30	21.0
QL60_L_CI	10.00	12.24	1.20	12.41	1.30	0.74	38.3
QL60_L_CI	15.00	16.40	1.68	20.80	21.10	1.04	38.1
QL60_L_CI	20.00	20.40	2.11	33.70	39.55	1.61	23.7
QL60_L_CI	25.00	25.80	2.51	48.50	46.80	2.80	10.3
resistance capacity decreases							
QL60_L_CI	25.00	38.60	5.32	48.60	18.52	4.80	9.7

Table 4.18 *Summary variations observed between QL60 FE models and laboratory specimens*

T80 numerical simulations

Table 4.19 captures a reduced summary of the values observed at the simulations and compare them with the laboratory results.

	Short span slab		Long span slab	
	T80_S_CI	T80 Lab. specimen	T80_S_CI	T80 Lab. specimen
$F_{u,max}$ [kN]	80.92	88.10	44.56	49.50
Midspan deflection [mm]	9.86	10.12	87.53	10.12
End slip [mm]	1.02	1.10	2.99	0.10

Table 4.19 *FE models comparison at $F_{u,max}$ with laboratory specimens, T80*

Short span

Figure 4.48 depicts the load-midspan and load-end slip curves for the FE models and the closest laboratory specimen. Table 4.19 captures a reduced summary of the values observed at the models.

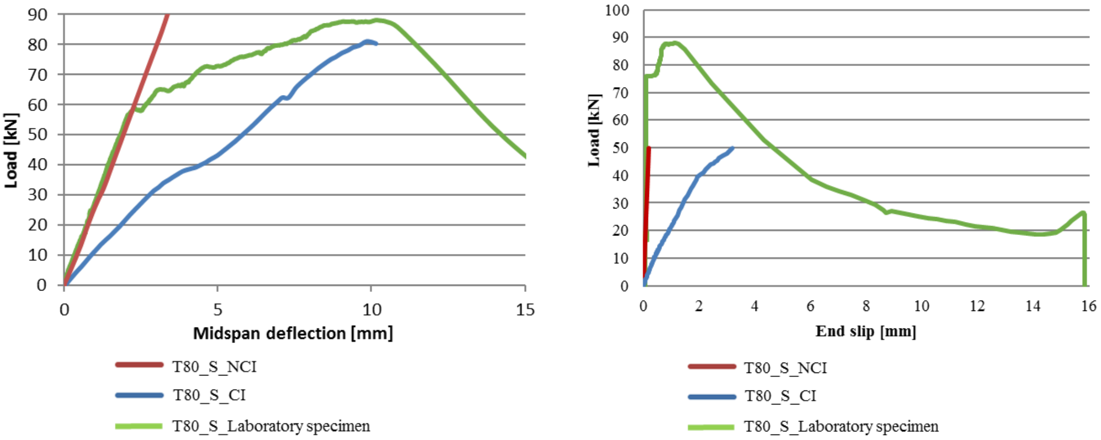

Figure 4.48 *Load-midspan and load-end slip curves, T80, short span*

The T80 steel deck profile presented full connection with the concrete slab and steel material yielding during a significant segment early at the laboratory test. The optimized embossments distribution and the profile shape enabled a significantly better performance than previous steel deck computed. That phenomenon was also observed at the FE models: the T80_S_NCI midspan and end slip curves replicated the laboratory specimen behaviour in a significantly broader simulation segment as opposed to other models. Until the laboratory specimen reached a load of 60 kN, equivalent to 70% of the maximum load $F_{u,max}$, the FE model without the crack inducer perfectly matched the behaviour. In parallel, the INCO_S_CI neglected the initial correspondence with the laboratory specimen but agreed strongly for the $F_{u,max}$ load observed first, and subsequently for the midspan deflection computed.

Long span

Figure 4.49 illustrates the midspan deflections and end slip curves between the T80_L_NCI, T80_L_CI and the laboratory specimen. The T80_L_NCI model accurately replicated the initial steps of the laboratory tests before the slip initiated at the laboratory specimen. Different from previous steel deck profiles, the existence of steel material yielding reported a significant difference at the load-end slip curve. The laboratory specimen did not observe any relative slip until the maximum load 55.52 kN was achieved which in this case, was larger than the actual $F_{u,max}$ = 49.50 kN computed for the composite slab characterization. Eurocode 4 stipulates a maximum midspan deflection of *L/50* for $F_{u,max}$ definition in cases where the rupture load is not observed previously. Once the end slip initiated, a gradual decrease at the shear bond capacity was observed.

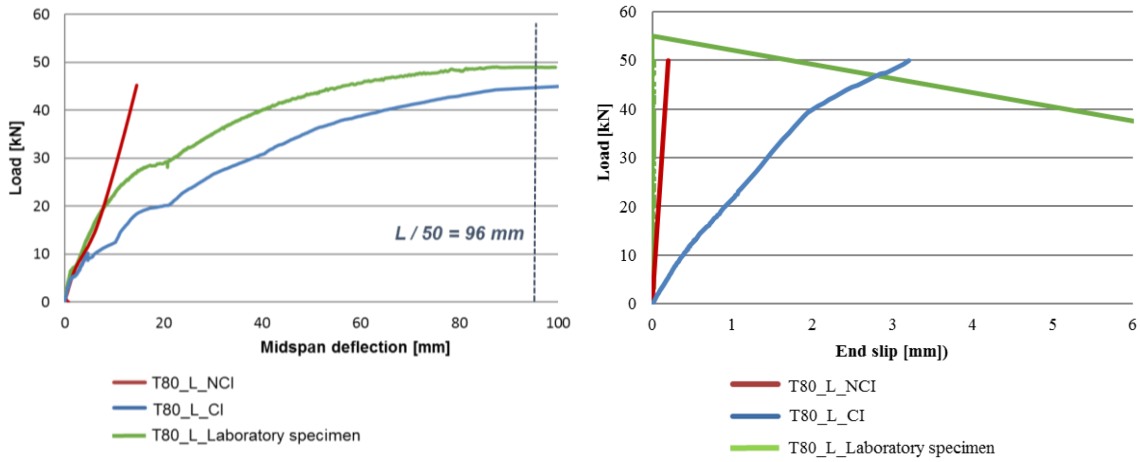

Figure 4.49 *Load-midspan and load-end slip curves, T80, long span*

		Simulations		Variance *with the closest laboratory specimen*			
FE model code	Load F [kN]	Midspan deflection [mm]	End slip [mm]	Midspan deflection [mm]	Midspan deflection (%)	End slip [mm]	End slip (%)
T80_L_NCI	10.00	3.53	0.04	3.35	5.14	0.00	-
T80_L_NCI	20.00	7.99	0.08	8.43	5.22	0.00	-
T80_L_NCI	30.00	11.90	0.15	22.48	47.18	0.00	-
T80_L_CI	30.00	41.35	1.49	22.48	45.67	0.00	-
T80_L_CI	40.00	68.17	2.07	38.21	43.35	0.00	-
T80_L_CI	80.92	78.76	3.21	88.00	9.45	0.00	-

Table 4.20 *Summary variations T80 FE models and laboratory specimens*

Similar to the behaviour observed in the T80 short span case, the T80_L_NCI model explained more accurately a wide segment of the simulation. The existence of material yielding at the steel deck due to the full interaction between the materials, recommended the deployment of the model without the crack inducer until a later simulation step, compared with the prior FE models computed. The existence of the crack inducer from early stages at the T80_L_CI which induced an end slip from early loads, made the model less suitable to characterize that steel deck. Table 4.20 highlights the variances between the FE models and the laboratory test. Yet, the combination of the two FE models ensured a proper characterization of the composite slab laboratory test.

4.5.2 Composite slab macro-behaviors observed

The different FE models developed also proved capable of qualitatively replicate several other composite behaviors that were observed at the laboratory tests. As equally important as $F_{u,max}$ maximum load, midspan deflections and end slips discussed previously, the FE models robustness was also observed in those macro-behaviours. For example, Figure 4.50 illustrates the concrete crack inducer at the point load section L_s at the end of the experimental loading process. The built-in pin joint at the FE model enabled a rotation at the top of the section that characterized the incremental separation between concrete blocks over the course of the laboratory test. In another example, Figure 4.52 illustrates the end slips between steel deck and concrete slab for both laboratory specimen and FE model. Also, Figure 4.51 illustrates that the computed concrete peeling zones were coincident with the concentrated stresses surrounding the steel deck embossments in the FE models.

Traces of concrete were observed at the top of circular embossments after the laboratory test, and were corresponded to equivalent nodal forces in the simulations. See Figure 4.53. The steel deck deformation at the loading point was also observed at the FE models as it captures Figure 4.54. The macro behaviors provided a qualitative assessment of the robustness of the simulations, beyond the quantitative approach captured in previous sections.

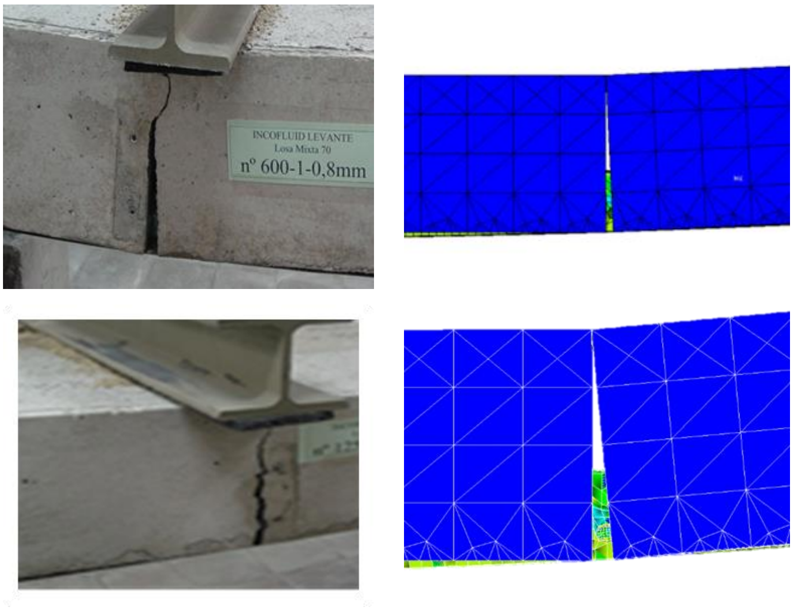

Figure 4.50 *Crack inducer at the concrete block*

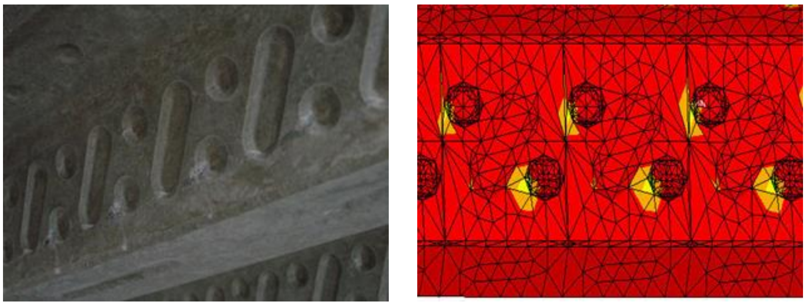

Figure 4.51 *Concrete peeling and stressed elements*

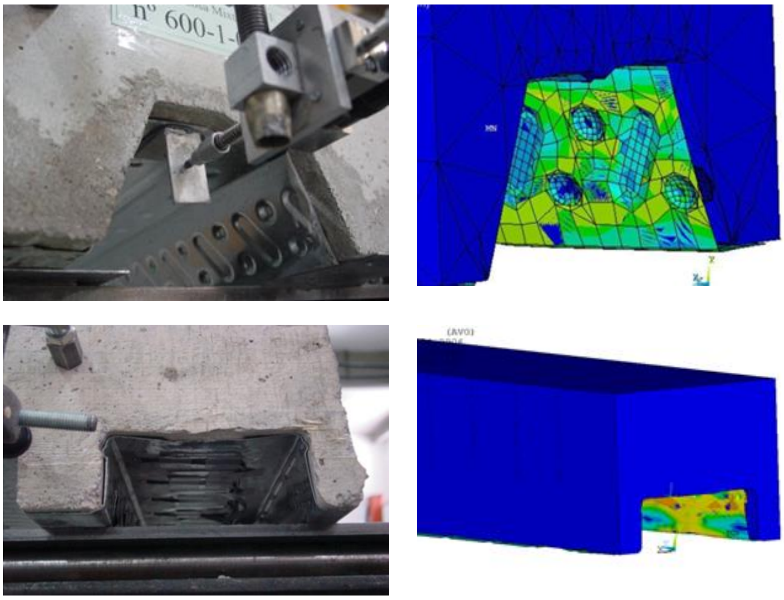

Figure 4.52 *End slip*

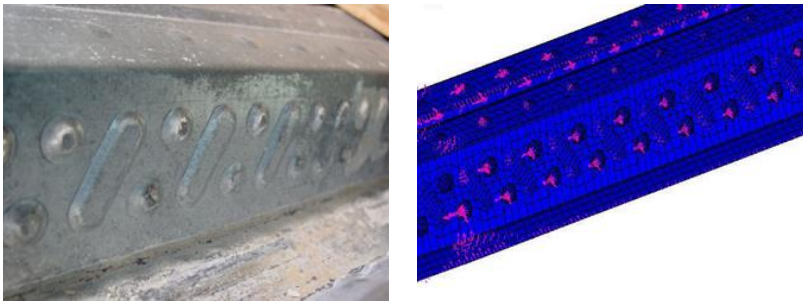

Figure 4.53 *Traces of concrete and nodal forces*

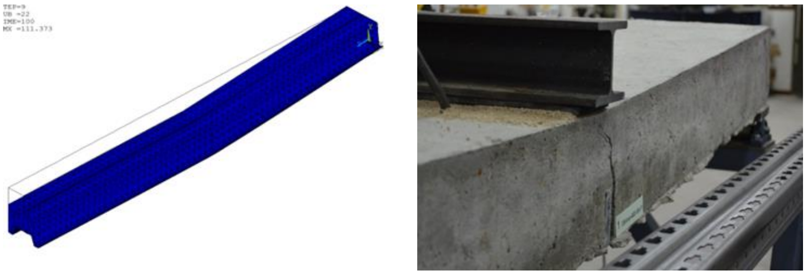

Figure 4.54 *Steel deck deformation at point load*

5. Results

This chapter introduces a comprehensive overview of building codes and composite slab micromechanics that are the foundations in composite slab performance. First, a discussion in the deployment of the current building codes was introduced. An actual characterization for each building code was developed for the INCO70 steel deck that included the process from laboratory results to shear resistance definition. The discussion highlighted how the lack of a mechanical model behind the characterization at most of the building codes generated different results for the same composite slab specimens.

Second, the chapter introduces novel views for composite slab micromechanics. The FE models were leveraged to perform in-depth analyses in both pull-out and bending specimens for characterization parameters such as concrete-steel vertical separation, concrete slab and steel deck neutral axes and the longitudinal shear strength. All the parameters were key constituents to define the shear resistance and ultimately the performance for composite slab.

5.1. Building codes implementation

Laboratory results from the LERMA were leveraged for the building codes verification at ultimate limit states. Eurocode 4 *m-k* method and *Partial Connection Method* (PCM), BS-5950 *m-k* method and ANSI/AASCE 3-91 *m-k* method were computed for the INCO70 steel deck and subsequently a comparison among them performed. The results from each building code deployment were also benchmarked against the actual values observed at the laboratory specimens through the shear force parameter V_t (see Equations 2.1 and 2.2). The comparison required some statistical concessions and formulation approaches already introduced from past researchers performing similar studies. A much more detailed description was provided for the Eurocode 4 PCM due to its reliance in a constant longitudinal shear strength τ_u that subsequently is discussed as an essential part of the composite slab micromechanics. A discussion of the influence from friction coefficient values μ within the different building codes formulae is introduced to finalize the section. The friction coefficient impact is further discussed in detail in chapter 6 as one influential parameter for the composite slab characterization.

5.1.1 Laboratory tests results

Table 5.1 summarizes the laboratory test results for the three short and three long span INCO70 specimens. All the laboratory specimens observed ductile behaviour and hence Equation 2.1 was applied to characterize the shear force V_t from the measured failure load W_t. Based on Eurocode 4 testing arrangements, W_t is the maximum load that produces the composite slab collapse and induces a midspan deflection not greater than $L_{total}/50$. All the laboratory specimens shared the longitudinal shear as the failure mode.

	W_t [kN]	$V_t = \frac{W_t}{2}$ [kN]
Short span	62.92	31.46
	68.03	34.02
	72.82	36.41
Long span	37.08	18.54
	38.73	19.37
	38.61	19.31

Table 5.1 *Laboratory results INCO70 specimens*

5.1.2 Partial Connection Method (PCM) - Eurocode 4

Section 2.4.2 introduced conceptually the design method based on a uniform longitudinal shear strength τ_u (see Equation 2.7) between the steel deck and the concrete slab. A more detailed view is provided herein to enable the actual method calculation.

The degree of shear connection was defined as the relation between the concrete compression force at partial connection N_c and at full connection $N_{c,f}$:

$$\eta = \frac{N_c}{N_{c,f}} = \frac{N_c}{A_{pe} f_{yp,d}} = \frac{\tau_{u,Rd} b L_x}{A_{pe} f_{yp,d}} \tag{5.1}$$

The PCM states that, between the extreme situations corresponding to null connection $\eta = 0$ and full connection $\eta = 1$, the degree of shear connection η can be calculated from the maximum bending moment M_{test} obtained experimentally, assuming that the longitudinal slipping process is ductile enough to drive both materials steel and concrete to their respective maximum stresses. All the INCO70 laboratory specimens reported ductile behaviour: the W_t values exceed 10% from the load observed at 0.1 mm end slip.

The stress diagram corresponding to the partial connection ultimate limit state of the composite section is illustrated in Figure 5.1.

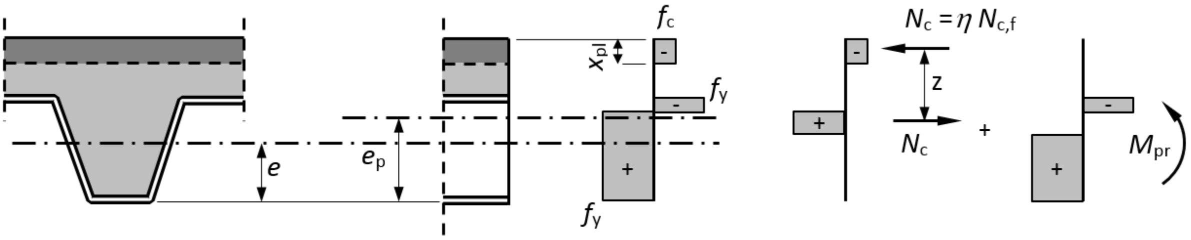

Figure 5.1 *Stress distribution in sagging bending in partial connection, adapted from SAFSS (2013)*

The maximum design bending moment M_{Ed} should not exceed the design resistance M_{Rd}:

$$M_{\mathrm{Ed}} \leq M_{\mathrm{Rd}} = N_c \cdot \mathrm{z} + M_{\mathrm{pr}} = \tau_{\mathrm{u,Rd}} b L_x \cdot \mathrm{z} + M_{\mathrm{pr}} \tag{5.2}$$

The location of the tensile force N_{c} at the steel sheet varies from e (full connection) to e_{p} (near to null connection), as showed in Figure 5.2.

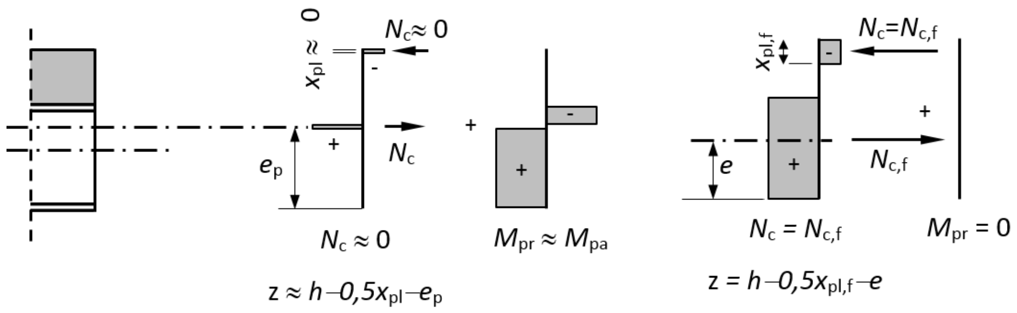

(a) (b)

Figure 5.2 *Stress distributions (a) $\eta \approx 0$ null connection, (b) $\eta = 1$ full connection, adapted from SAFSS (2013)*

Equations 5.3 and 5.4 were assumed for simplicity to calculate the lever arm z.

$$\mathrm{z} = h - 0.5x_{\mathrm{pl}} - e_{\mathrm{p}} + (e_{\mathrm{p}} - e)\eta \tag{5.3}$$

$$M_{\mathrm{pr}} = 1.25 \cdot M_{\mathrm{pa}}(1 - \eta) \leq M_{\mathrm{pa}} \tag{5.4}$$

To obtain the design value of the shear resistance $\tau_{u,Rd}$ for the INCO70 steel deck, the connection degree was calculated from the laboratory tests performed. Eurocode 4 building code establishes that only three slabs of one span length are needed for calculations. Besides, it defines that the span length should be as long as possible, provided that the slab fails due to longitudinal shear. Both short and long span specimens were leveraged for the PCM analysis.

Based on Equations 5.3 and 5.4 and using the mean strength values instead of design values, the partial interaction diagrams were drawn. The partial connection degree η and the ultimate shear stresses $\tau_{u,Rd}$ were obtained for each M_{test} as outlined in Eurocode 4 B.3.6(2) and B.3.6(3):

$$\tau_{\mathrm{u}} = \frac{\eta N_{\mathrm{c,f}} - \mu V_{\mathrm{t}}}{b(L_{\mathrm{x}} + L_0)} \tag{5.5}$$

where,

L_0	length of the rim
μ	default value of friction coefficient (0,5 recommended by Eurocode 4 B.3.6(3))
V_{t}	shear force / reaction at the support (if taken into account)

From the τ_u values, the characteristic $\tau_{u,Rk}$ and the design values $\tau_{\mathrm{u,Rd}}$ were eventually computed according to Eurocode 4 B.3.6 (4) and (5). The characteristic value $\tau_{\mathrm{u,Rk}}$ was based on statistical approach developed in EN 1990 Eurocode 0 (1990) which proposes a 5% fractile from the laboratory tests. The distribution selected for this study was a T-Student as captured in Equation 5.6 .

$$\tau_{u,Rk} = \tau_{um} - T_{student} \cdot s_{deviation} \tag{5.6}$$

where,

τ_{um}	τ_u mean from all laboratory results
$T_{student}$	T-Student constant (95%, 3-1 samples)
$s_{deviation}$	standard deviation from laboratory results

The partial connection degree η could be directly calculated by solving the quadratic equations reflected in Equations 5.7 and 5.8.

$$M_{\mathrm{test}} = \eta N_{\mathrm{c,f}} \cdot \left(h - 0.5\eta x_{\mathrm{pl,f}} - e_{\mathrm{p}} + \left(e_{\mathrm{p}} - e\right)\eta\right) + 1.25M_{\mathrm{pa}}(1-\eta) \tag{5.7}$$

$$\mathrm{A} \cdot \eta^2 + \mathrm{B} \cdot \eta + C = 0 \tag{5.8}$$

where,

$$\mathrm{A} = N_{\mathrm{c,f}}\left(e_{\mathrm{p}} - e - x_{\mathrm{pl,f}}\right) = A_{\mathrm{pe}} f_{\mathrm{yp}} \left(e_{\mathrm{p}} - e - \frac{A_{\mathrm{pe}} f_{\mathrm{yp}}}{b \cdot f_{\mathrm{cm}}}\right) \tag{5.9}$$

$$\mathrm{B} = N_{\mathrm{c,f}}\left(h - e_{\mathrm{p}} + 1.25M_{\mathrm{pa}}\right) = A_{\mathrm{pe}} f_{\mathrm{yp}}\left(h - e_{\mathrm{p}} + 1.25M_{\mathrm{pa}}\right) \tag{5.10}$$

$$\mathrm{C} = 1.25M_{\mathrm{pa}} - M_{\mathrm{test}} \tag{5.11}$$

The INCO70 steel deck analyzed was an open-rib profile, being$\left(e_{\mathrm{p}} - e - x_{\mathrm{pl,f}}\right) > 0$, hence the partial connection curve was concave. Figure 5.3 captures the generic interaction curve calculated for any steel deck once PCM is deployed: the goal for the method was to find the pair values $\eta - (M_{test}/M_{P,Rm})$ at (1), (2) and (3) that enabled the construction of the curve based on the test results.

Table 5.2 summarizes the geometrical and material parameters for the INCO70 steel deck that were required to numerically apply the PCM. The properties were shared for both long and short span specimens with the only difference in the shear span length L_s and the total length L_{total}. Tables 5.3 and 5.4 illustrate the different steps performed to find the $\eta_i - (M_{test}/M_{P,Rm})_{\mathrm{i}}$ pairs for the short and long spans respectively. The computation of the PCM was implemented for the 6 laboratory specimens, 3 short and 3 long span units. A mean value for τ_u for each group was at the end provided as the actual value suggested by Eurocode 4.

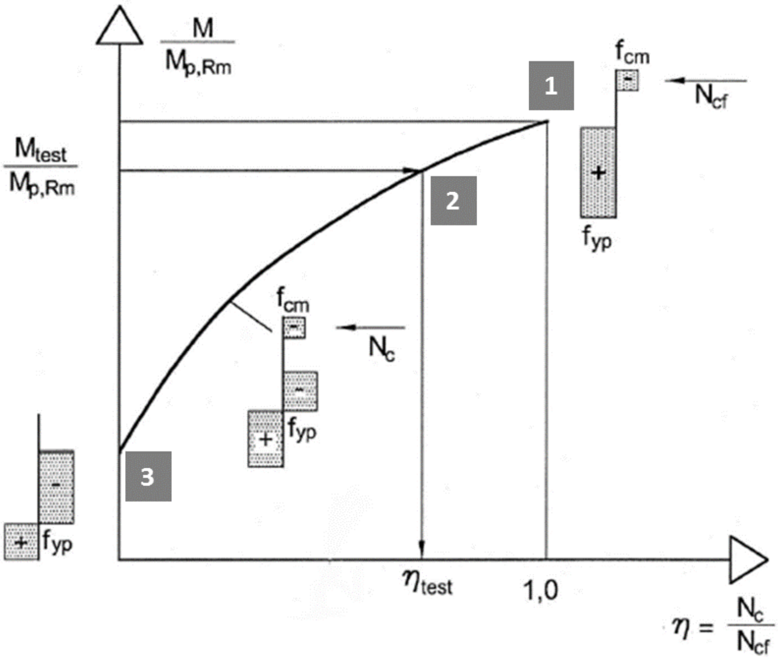

Figure 5.3 *Determination of the degree of shear connection from M_{test}*

The pair values $\eta_2 - (M_{test}/M_{P,Rm})_2$ came from the resolution of Equations 5.6 and 5.7 and are highlighted in bold in Tables 5.3 and 5.4 as core PCM calculations. Pair values $\eta_1 - (M_{test}/M_{P,Rm})_1$ represented full connection for $\eta = 1$ and $\eta_3 - (M_{test}/M_{P,Rm})_3$ represented for null connection $\eta \approx 0$.

Characteristic value of the concrete compressive strength 28 days	f_{ck}	[N/mm²]	33.64
Design value of the yield strength of the steel deck profile	f_{yp}	[N/mm²]	342.00
Thickness of concrete above the main surface of the top steel deck	h_c	[mm]	110.00
Composite slab width	b	[mm]	740.00
Thickness steel deck profile	t	[mm]	0.80
Overall depth of the steel deck profile without embossments	h_p	[mm]	70.00
Distance between steel deck ribs	d_n	[mm]	50.00
Distance between interior embossments	d_{pi}	[mm]	100.00
Distance between exterior embossments	d_{pe}	[mm]	110.00
Cross-sectional area steel deck profile	A_p	[mm²]	967.41
Centroidal axis steel deck profile	x_g	[mm]	40.77
Plastic modulus steel profile	W_p	[mm³]	14,177.66
Distance from the centroidal axis of the steel sheet to the extreme fiber of the composite slab in tension	e	[mm]	39.97
Distance from the plastic neutral axis of the steel sheet to the extreme fiber of the composite slab in tension	e_p	[mm]	45.69
Longitudinal shear span L_s for short / long spans	L_s	[mm]	600 / 1,250

Table 5.2 *INCO70 steel deck profile geometry and material properties*

			Lab. Specimen 1	Lab. Specimen 2	Lab. Specimen 3
Moment force from experimental test	M_{test}	[N.mm]	18,365,769	19,901,769	21,335,769
Compressive normal force in concrete flange with full connection	N_{cf}	[kN]	300.77	300.77	300.77
Depth concrete compressive zone (N_{cf} / N_c)	x	[mm]	14.21	14.21	14.21
Distance between the centroidal axis of the steel deck profile and the extreme fiber of the composite slab in compression	d_p	[mm]	139.23	139.23	139.23
Design value plastic resistance moment of the composite section with full connection	$M_{pl,Rd}$	[N.mm]	39,739,378	39,739,378	39,739,378
Design value plastic resistance moment of the effective cross-section of the steel deck	M_{pa}	[N.mm]	4,407,963	4,407,963	4,407,963
Shear force / support reaction	V_t	[kN]	31.46	34.02	36.41
Slab mass	*Slab mass*	[kN]	7.37	7.37	7.37
Compressive normal force in the concrete flange	N_c	[kN]	111.32	124.69	137.19
Partial connection factor	η_1	-	1	1	1
Ratio $M_{test} / M_{p,Rm}$	y_1	-	1	1	1
Partial connection factor	$\boldsymbol{\eta_2}$	**-**	**0.37013**	**0.41457**	**0.45611**
Ratio $\boldsymbol{M_{test} / M_{p,Rm}}$	$\boldsymbol{y_2}$	**-**	**0.46215**	**0.50080**	**0.5368**
Partial connection factor	η_3	-	0	0	0
Ratio $M_{test} / M_{p,Rm}$	y_3	-	0.11092	0.110921801	0.11092

Table 5.3 *INCO70 short span specimens PCM results*

			Lab. Specimen 1	Lab. Specimen 2	Lab. Specimen 3
Moment force from experimental test	M_{test}	[N.mm]	20,964,062	22,001,562	21,926,562
Compressive normal force in concrete flange with full connection	N_{cf}	[kN]	300.77	300.77	300.77
Depth concrete compressive zone (N_{cf} / N_c)	x	[mm]	14.21	14.21	14.21
Distance between the centroidal axis of the steel deck profile and the extreme fiber of the composite slab in compression	d_p	[mm]	139.23	139.23	139.23
Design value plastic resistance moment of the composite section with full connection	$M_{pl,Rd}$	[N.mm]	39,739,378	39,739,378	39,739,378
Design value plastic resistance moment of the effective cross-section of the steel deck	M_{pa}	[N.mm]	4,407,963	4,407,963	4,407,963
Shear force / support reaction	V_t	[kN]	18.54	19.37	19.31
Slab mass	*Slab mass*	[kN]	14.15	14.15	14.15
Compressive normal force in the concrete flange	N_c	[kN]	133.95	142.99	142.34
Partial connection factor	η_1	-	1	1	1
Ratio $M_{test} / M_{p,Rm}$	y_1	-	1	1	1
Partial connection factor	$\boldsymbol{\eta_2}$	**-**	**0.44534**	**0.475413**	**0.47323**
Ratio $\boldsymbol{M_{test} / M_{p,Rm}}$	$\boldsymbol{y_2}$	**-**	**0.52753**	**0.55364**	**0.55175**
Partial connection factor	η_3	-	0	0	0
Ratio $M_{test} / M_{p,Rm}$	y_3	-	0.11092	0.11092	0.11092

Table 5.4 *INCO70 long span specimens PCM results*

The representation of the interaction PCM curves is depicted in Figure 5.4 for short span specimens and Figure 5.5 for long span specimens. The $\eta_i - (M_{test}/M_{P,Rm})_i$ pairs computed in Tables 5.2 and 5.3 for each laboratory specimen were plotted.

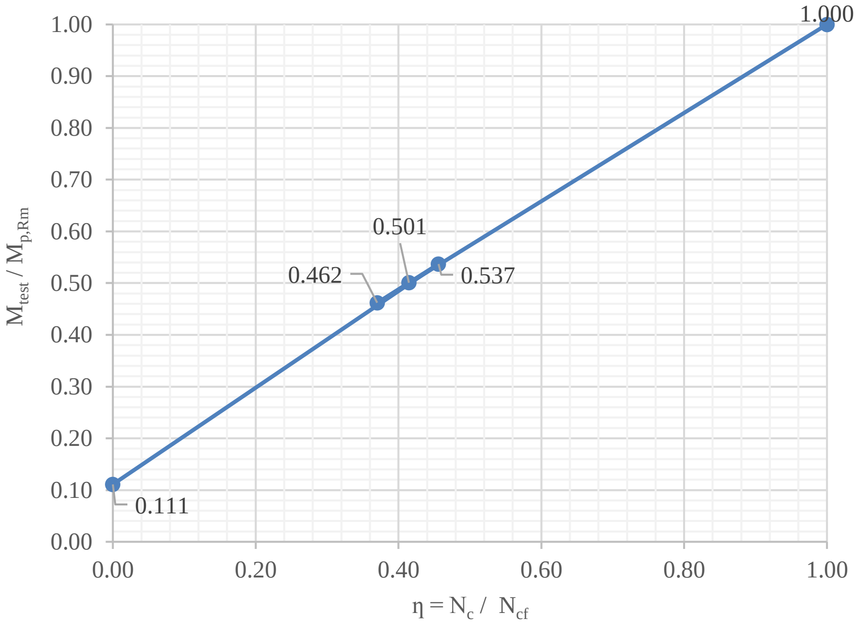

Figure 5.4 *INCO70 short span specimens degree of shear connection from M_{test}*

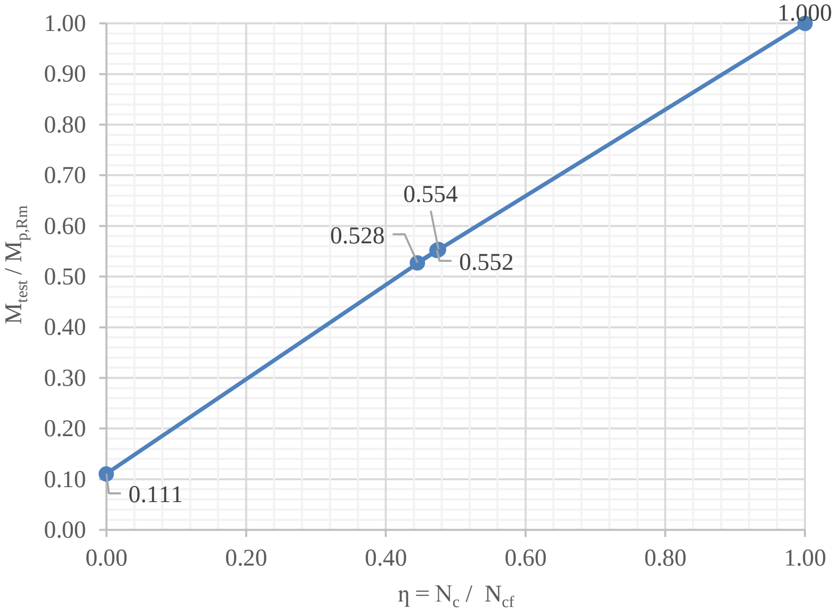

Figure 5.5 *INCO70 long span specimens degree of shear connection from M_{test}*

Table 5.5 shows the final step from the PCM numerical deployment with the computation of the τ_u and $\tau_{u,Rk}$ values. Two different values were reported: first, the value captured in Equation 2.7 that did not include the influence from the support reaction with the parameter $\mu . V_t$; second, with the influence of the shear force as defined in Equation 5.5. Highlighted in bold are the actual results from the PCM design method that would be used for the composite slab characterization.

		Short span slabs specimens			long span slabs specimens		
Equation 2.7	τ_u [N/mm²]	0.21	0.24	0.26	0.13	0.14	0.14
	$\tau_{u,Rk}$ [N/mm²]	0.19	0.22	0.24	0.12	0.13	0.13
	$\tau_{u,Rk}$ [N/mm²]	**0.22**			**0.13**		
Equation 5.5	τ_u [N/mm²]	0.18	0.21	0.23	0.12	0.13	0.13
	$\tau_{u,Rk}$ [N/mm²]	0.17	0.19	0.21	0.11	0.12	0.12
	$\tau_{u,Rk,}$ [N/mm²]	**0.19**			**0.12**		

Table 5.5 *Longitudinal shear strength results PCM*

The difference between the short and long spans longitudinal shear strength was significant. The Eurocode 4 enforces the characterization from the lowest value $\tau_{u,Rk}$ that is always obtained from the long span laboratory specimens group. The short span specimens are hence commonly only used to characterize the laboratory tests either ductile or brittle.

Several authors explored the differences and suggested improvements due to discrepancies observed among specimen lengths. For example, Abdullah suggested that τ_u had a strong relationship with the composite slab geometry. The author developed a variation of the PCM named *p-s method* in which he introduced the slenderness (L_s/d_p) as an inversely proportional element of the longitudinal shear strength τ_u. An interpolation between the τ_u values obtained from the short and long laboratory specimens was suggested, conceptually such as the *m-k* method. The *p-s method* tackled the conservative results from the PCM reported for compact slabs and it is discussed in more detail in chapter 6.

In order to enable the comparison between the different building codes, a common parameter was required that was agnostic on the actual design method calculation processes. The parameter selected was V_t as it represented that maximum shear force that could be compared also with the actual laboratory results. Authors such as Calixto and Abdullah deployed V_t to perform similar comparisons across different building codes. Based on the PCM, Equation 5.12 defines the formula applied to characterize the V_t parameter, based on the method result $\tau_{u,Rk}$.

$$V_t = \frac{\tau_{u,Rk}\cdot b\cdot(L_s+L_0)\cdot z+M_{pr}}{(L_s-\mu\cdot z)} \tag{5.12}$$

where,

$$z = h_c + h_p - 0.5\cdot h_c - e_p + \left(e_p - e\right)\cdot \frac{N_c}{A_p\cdot\frac{f_{yp}}{\gamma_{ap}}} \tag{5.13}$$

$$M_{pr} = 1.25\cdot M_{Rd}\cdot\left(1-\frac{N_c}{N_p}\right) \tag{5.14}$$

$\mu = 0.5$ friction coefficient recommended by Eurocode 4 B.3.6(3)

Table 5.6 shows the computed values for V_t based on PCM and the respective equivalent from the laboratory specimens. It was observed that the largest deviation reported a value close to 30% for one long span specimen. Calixto reported that variations ±15% were frequent based on his research. Collaterally, Abdullah found variations in his studies of ±30% but concluded that variations of ±20%, were more common. The deviations between specimens within a group were more significant for the short span laboratory specimens with values that reached 14%; long span specimens observed variations between them within a 5% range.

	V_t lab. test [kN]	V_t Eurocode 4 PCM [kN]	$V_{t,PCM}$ / $V_{t,lab\ test}$
Short span specimens	31.46	27.02	85.9%
	34.02	26.46	77.8%
	36.41	25.93	71.2%
Long span specimens	18.54	15.67	84.5%
	19.37	15.51	80.1%
	19.31	15.52	80.4%
		Mean	80.0%
		Std deviation	0.0479

Table 5.6 *Comparison Eurocode 4 PCM and laboratory test results*

5.1.3 *m-k* method - Eurocode 4

The Eurocode 4 *m-k* method described in section 2.4.1 was applied to the laboratory results captured initially in Table 5.1. The method is currently leveraged at the vast majority of the composite slab characterization processes based on its simplicity and the presence in multiple building codes with minor variations among them. The method reported the below parameters:

$$m = 114.605\,{}^{N}/_{mm^2}$$
$$k = 0.0578\,{}^{N}/_{mm^2}$$

Figure 5.6 illustrates visually the results from the *m-k* method deployment. The short and long span specimens groups were correlated throughout a linear regression.

Equation 5.15 was applied to compute the V_t values. The formula differed from the Equation 2.3 previously introduced as it disregarded the partial safety factor to enable a direct comparison with other building codes. Table 5.7 compares the V_t values computed and the observed loads at actual laboratory tests.

$$V_l = b \cdot d_p \cdot \left(\frac{m \cdot A_p}{b \cdot L_s} + k\right) \tag{5.15}$$

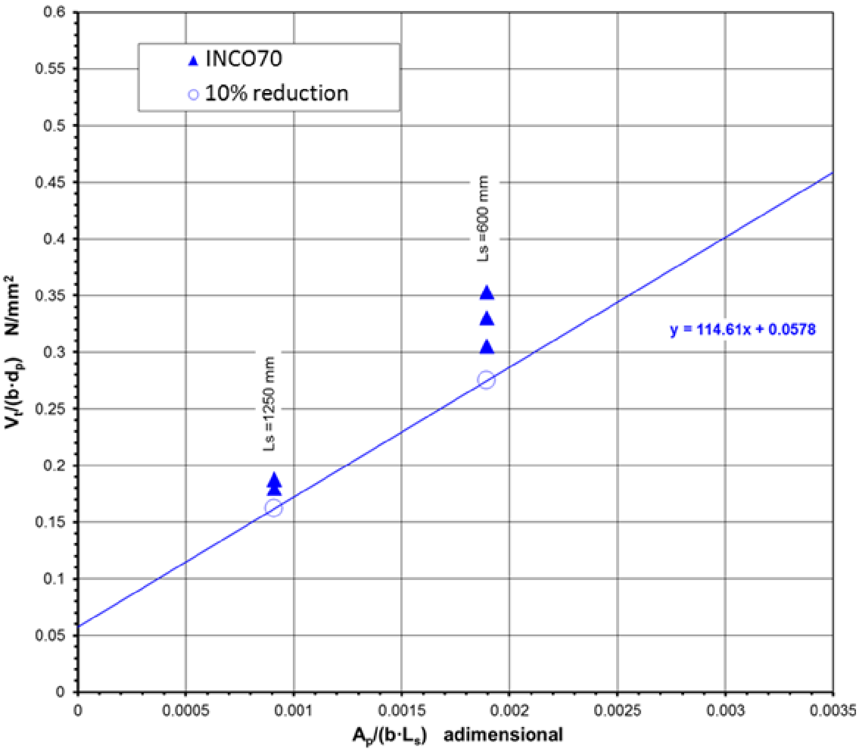

Figure 5.6 *Eurocode 4 m-k method - straight line defining the longitudinal failure mode*

	V_t lab. test [kN]	V_t Eurocode 4 *m-k* [kN]	$V_{t,PCM}$ / $V_{t,\text{lab test}}$
Short span specimens	31.46	28.34	90.1%
	34,02		83.3%
	36.41		77.8%
Long span specimens	18.54	16.70	90.1%
	19.37		86.2%
	19.31		86.5%
		Mean	85.7%
		Std deviation	0.0422

Table 5.7 *Comparison Eurocode 4 m-k method and laboratory test results*

Deviations were observed between the computed values and the laboratory specimens. The largest value was 23% for a short span specimen. Oppositely from the PCM study, the *m-k* method observed similar deviations between the short and long span specimens. The *m-k* calculation leveraged a Eurcode 4 recommended semi-statistical approach to reduce the values 10% from the laboratory results. However, Eurocode 4 also provides another statistical approach, defined in Eurocode 0, in which the lower 5% fractile from the laboratory results can be used. That statistical approach was applied for the PCM calculation and therefore, in order to enable a comparison, it was subsequently also applied for the *m-k* method. Equation 5.16 captures the approach implemented.

$$\left(\frac{V_t}{b\cdot d_p}\right)_{5\%} = \bar{x} - T_{student}\cdot s_{deviation} \tag{5.16}$$

where,

$\bar{x}$	mean value from $\frac{V_t}{b\cdot d_p}$ computed for each group of either short or long span
$T_{student}$	T-Student constant (95%, 3-1 samples)
$s_{deviation}$	standard deviation from laboratory results

The new parameters obtained with the new 5% fractile method were:

$$m = 106.748\,{}^{N}/_{mm^2}$$

$$k = 0.0791\,{}^{N}/_{mm^2}$$

Figure 5.7 draws the two *m-k* straight lines to characterize the composite slab. Based on the new 5% fractile approach, the slope was softer and the *k* initial value higher. Table 5.8 summarizes the results obtained for the new calculation performed for V_t. The values obtained represented more accurately the laboratory tests, specially for the long span laboratory specimens, compared with the previous 10% reduction statistical approach. Furthermore, the new calculation enabled a direct comparison with the PCM results reported at the previous section 5.1.2.

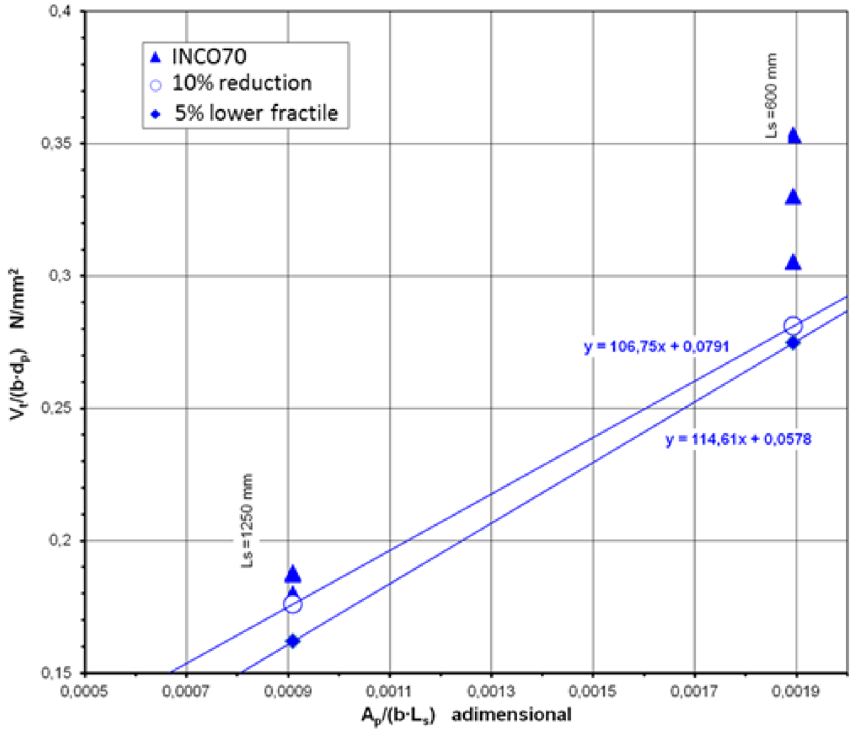

Figure 5.7 *Eurocode 4 m-k method comparison two different statistical treatments*

	V_t lab. test [kN]	V_t Eurocode 4 *m-k* [kN]	$V_{t,PCM}$ / $V_{t,lab\ test}$
Short span specimens	31.46	28.99	92.2%
	34.02		85.2%
	36.41		79.6%
Long span specimens	18.54	18.16	97.9%
	19.37		93.8%
	19.31		94.0%
		Mean	90.5%
		Std deviation	0.0615

Table 5.8 *Comparison Eurocode 4 m-k method with 5% fractile and laboratory test results*

5.1.4 *m-k* method - BS-5950

Besides Eurocode 4, other building codes also include the *m-k* method for composite slab characterization. Prior the introduction of Eurocode 4, BS-5950 was widely used in Europe although today is no longer in use as it was precessed by the Eurocodes. Yet, BS-5950 can be still found in Commonwealth countries. Equation 5.17 captures the solution for V_t characterization.

$$V_s = b \cdot d_p \left(\frac{m_r \cdot A_p}{b \cdot L_s} + k_r \cdot \sqrt{\frac{f_{ck}}{0.8}} \right) \tag{5.17}$$

The most notable difference was the presence of the f_{ck} characteristic concrete compressive strength in the equation. The introduction of the concrete parameter also influenced the k_r measurement unit $[\sqrt{N}/mm]$ that was different from Eurocode 4 *k* unit $[N/mm^2]$. Johson (1994) provided an approach to convert Eurocode 4 *m-k* coefficients to BS-5950 m_r-k_r and vice versa although for this study a complete BS-5950 numerical computation was performed. BS-5950 usually deployed a more conservative approach for the statistical treatment of the results: it proposed a reduction of 15% of the averaged test results for each short and long span groups. Comparatively, Eurocode 4 suggested either a 10% reduction or the 5% lowest fractile for the lowest test result obtained from each short and long span group. The calculated values for BS-5950 were:

$$m_r = 124.76 \, {}^{N}\!/_{mm^2}$$

$$k_r = 0.0076 \, {}^{\sqrt{N}}\!/_{mm}$$

Figure 5.8 illustrates visually the results from each laboratory specimen and the m_r-k_r regression line.

The computation for V_s were performed based on Equation 5.17. Table 5.9 summarizes the results obtained and benchmark them against the actual laboratory test specimens loads. The results deviation was similar to the previously observed in Eurocode 4 *m-k*. Coincidentally, the results also showed more dispersion within the short span specimens.

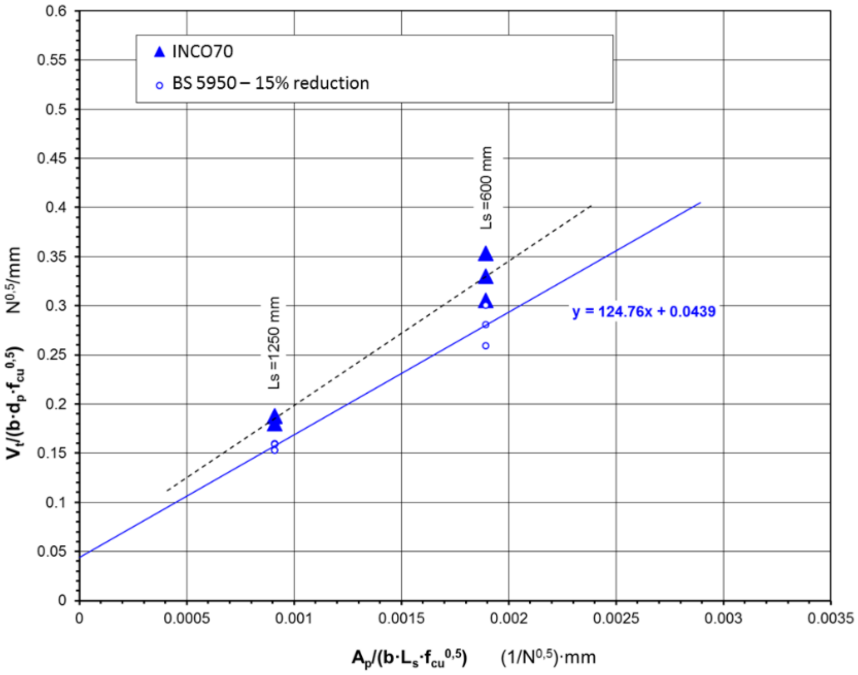

Figure 5.8 *BS-5950 m-k method - straight line defining the longitudinal failure mode*

	V_t lab. test [kN]	V_s BS-5950 *m-k* [kN]	$V_{t,PCM}$ / $V_{t,\text{lab test}}$
Short span specimens	31.46	28.90	91.9%
	34.02		85.0%
	36.41		79.4%
Long span specimens	18.54	16.24	87.6%
	19.37		83.8%
	19.31		84.1%
		Mean	85.3%
		Std deviation	0.0381

Table 5.9 *Comparison BS-5950 m-k method and laboratory test results*

5.1.5 *m-k* method - ANSI/AASCE 3-91

The ANSI/AASCE 3-91 building code also implements the *m-k* method for the characterization of V_e. The building code incorporated the results from the work done by Schuster in 1970 and subsequently by Porter and Ekberg in United States where the composite slabs concept was born. Equation 5.18 captures the V_e formula which also includes f_{ct} as the characteristic value of the cylinder compressive strength of the concrete, similar to BS-5950.

$$\frac{V_e}{b\cdot d_p\cdot\sqrt{f_{ct}}} = \frac{m\cdot A_p\cdot d_p}{L_s\cdot\sqrt{f_{ct}}\cdot b\cdot d_p} + k \tag{5.18}$$

The difference from BS-5950 resided in the safety factors. In order to enable a comparison between the different building codes, they were removed from this study and hence V_e values were equal to the V_s values previously analyzed based on BS-5950. Consequently, both BS-5950 and ANSI/AASCE 3-91 deploy the same equations. Sahin (2009) studied and reported the main differences between building codes and could be a source in case the reader wants to expand in additional differences not only affecting the V_e characterization.

5.1.6 Comparison among design methods

The V_t, V_s, V_e values computed in the previous sections were visually displayed in Figure 5.9. The figure draws the pairs of values ($V_{t,building\_code}$;$V_{t,laboratory\_specimen}$) with the laboratory specimens forces at the Y axis and the computed forces from the simulations at the X axis. The 45-degree line represented an ideal state in which the building codes design methods would perfectly characterize the laboratory specimens results. The additional dotted lines represent a variance of +/- 20% that was proposed by authors Abdullah and Calixto as an acceptable variance.

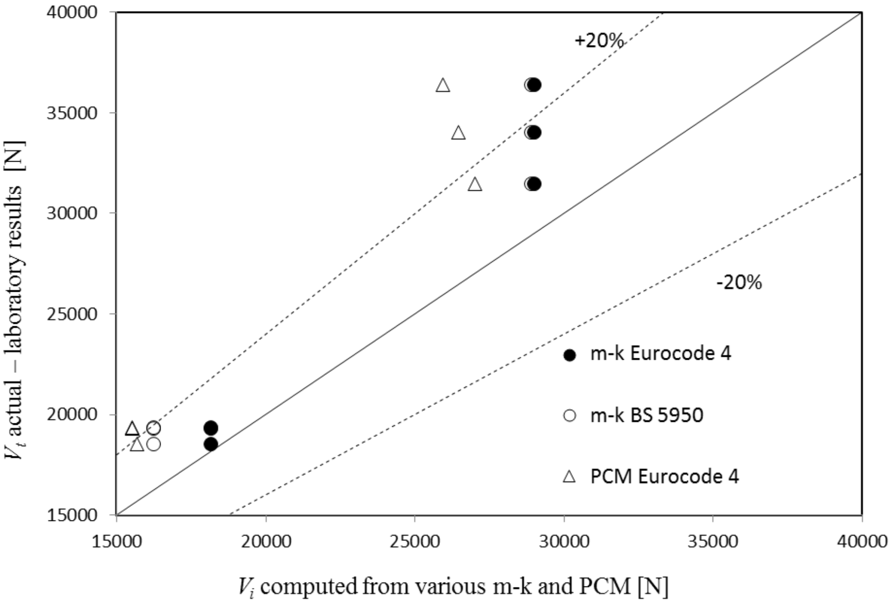

Figure 5.9 *Building code design methods comparison*

All the building codes results were located at the area above the theoretical 45º slope which indicated that none of them generated unsafe characterizations. Furthermore, the results showed how the PCM was the most conservative design method compared with the different *m-k* methods for the INCO70 steel deck analyzed. Eurocode 4 *m-k* presented a strong alignment for the long span with some more notable deviations for short span slabs. BS 5950 and Eurocode reported the same values for short span V_t and V_s calculations with two of the values within the 20% suggested variation range.

Conceptually, the different building code studies showed discrepancies for the composite slab characterization although the inputs for all were the same laboratory test results. The PCM reported the largest variance with the actual values observed and overall, signaled a bias towards a conservative an uneconomical characterization for the laboratory specimens considered. Abdinastir et al (2012) and Abdullah (2015) reached a conclusion that for slender ratios that complied with L_s/d <7 the PCM could report unsafe load values.

The lack of a full understanding of the composite slab micromechanics, that historically resulted in design methods based on approximations, paves an opportunity to continue to develop novel approaches to better characterize the complex behaviour at the composite slabs.

5.1.7 Influence friction parameter in building codes

The Eurocode 9.7.3.(9) equation suggested the implementation of a friction coefficient with a recommended value of $\mu = 0{,}5$ in case that the support reactions were considered for the longitudinal shear strength $\tau_{u,Rd}$ characterization. The formulation was introduced previously in Equation 5.5. Eurocode 4 was the only building code that introduced the friction coefficient at the design method. Due to the uncertainty of the friction coefficient influence in the characterization, a group of additional numerical computations were performed with different values. Table 5.10 summarizes the analyses performed. The $V_{t,Eurocode4}$ / $V_{t,Laboratory}$ results reported a minor influence from the different friction coefficients considered.

	V_t Lab. specimens [kN]	μ=0.0		μ=0.2		μ=0.5		μ=0.7	
		V_t calculated [kN]	$V_t / V_{t,\,lab}$	V_t calculated [kN]	$V_t / V_{t,\,lab}$	V_t calculated [kN]	$V_t / V_{t,\,lab}$	V_t calculated [kN]	$V_t / V_{t,\,lab}$
1^S	31.46	27.10	86.1%	27.07	86.1%	27.02	85.9%	26.99	85.8%
2^S	34.02	26.57	78.1%	26.53	78.0%	26.46	77.8%	26.41	77.6%
3^S	36.41	26.08	71.6%	26.02	71.6%	25.93	71.2%	25.86	71.0%
1^L	18.54	15.75	84.9%	15.72	84.9%	15.67	84.5%	15.64	84.4%
2^L	19.37	15.59	80.5%	15.56	80.4%	15.50	80.1%	15.47	79.9%
3^L	19.31	15.60	80.8%	15.57	80.7%	15.52	80.4%	15.48	80.2%

$^{S,\,L}$ detones either short (S) or Long (L) span

Table 5.10 *Eurocode 4 PCM comparison with different friction coefficients μ*

5.2. Pull-out simulations: numerical analyses

The INCO70 steel deck profile was selected to develop pull-out simulations. Both the simplified and full scale FE models incorporated the modeling approaches deployed at the bending simulations: *SOLID185* and *SHELL281* were deployed as Ansys type elements for concrete and steel materials respectively; high mesh density was implemented at the embossments areas; and, measured dimensions were input.

All the pull-out FE models were developed without the execution of any laboratory test. Two types for simplified and full scale pull-out simulations with the exact same properties were developed. While the simplified version was based on the isolated half pattern introduced in section 4.3.2, the full-scale model captured the actual full geometry of the laboratory specimen, see section 4.3.3. Table 5.11 lists the FE models developed and the main parameters for every simulation. Even though reduced scale tests are currently not accepted by the building codes, they have been extensively used by researchers in composite slabs to characterize the shear bond behavior (Daniels and Crisinel (1993), An (1993), Widjaja (1997), Abdullah (2004) and Ferrer (2006)) and hence a rich literature is available to compare results. The rest of this section introduces these two types of pull-out simulations and discuss parametric design and boundary aspects of the composite slabs.

FE model code	FE model scope	Key Parameter
POS_h1	simplified	Parametric analysis - h_1 variable
POS_h2	simplified	Parametric analysis - h_2 variable
POS_t	simplified	Parametric analysis - t variable
POS_ µ	simplified	Parametric analysis - μ variable
POS_s	simplified	Parametric analysis - s variable
POS_r	simplified	Parametric analysis - r variable
POF_CASE1	full geometry	Corrugated bars position at bottom - Z and X axes impeded
POF_CASE2	full geometry	Corrugated bars position at *cg* - Z and X axes impeded
POF_CASE3	full geometry	Corrugated bars position at top - Z and X axes impeded
POF_CASE4	full geometry	Corrugated bars position at top - Y, Z and X axes impeded

Table 5.11 Pull-out simulations

5.2.1 Parametric analysis – simplified finite element model

Several simplified pull-out models were developed to characterize the shear bond behavior. The geometrical parameters analyzed were the height of the circular embossments h_1, the height of the long embossments h_2, the thickness of the steel sheet t, the coefficient of friction μ, the pattern width s, and the rounding of the edges of the circular embossments r. See Figure 5.10. The force-slip sensitiveness analyses were performed isolating one parameter at a time and hence, the negative cumulative and cross effects from the simultaneous modification of parameters were avoided.

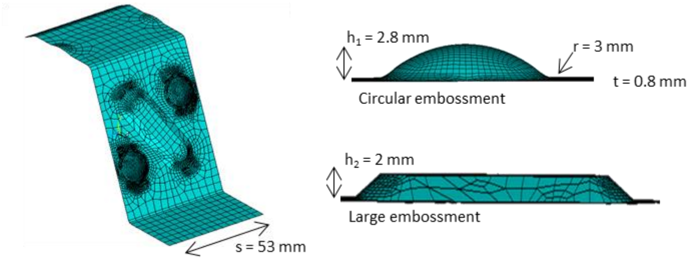

Figure 5.10 *Geometrical parameters under analysis in pull-out simulations. Initial measured dimensions*

Finite Element models validation

The robustness of the pull-out simplified models was analyzed through the review of multiple composite behaviours. The longitudinal and transversal stresses, normal forces and material deformations were investigated to validate the accuracy between the FE models and the pull-out test expected behaviour. The expected behaviours were obtained from the extensive open literature available from pull-out tests.

Steel deck lateral deformation

Figure 5.11 shows two views for the steel deformation, with a 10-time augmented representation. Both the cross-sectional and the three-dimensional views were captured at the maximum load step $F_{u,max}$ of the simulation. The steel deck suffered an inward flexure induced by the slip of the concrete slab over it. The FE model accurately replicated the behaviour expected in the laboratory test. Besides, additional FE models developed subsequently with different steel deck thicknesses and embossment dimensions reported variance in deformations: steel deck profiles with higher thicknesses reported lower deformations and higher maximum loads and shear bond.

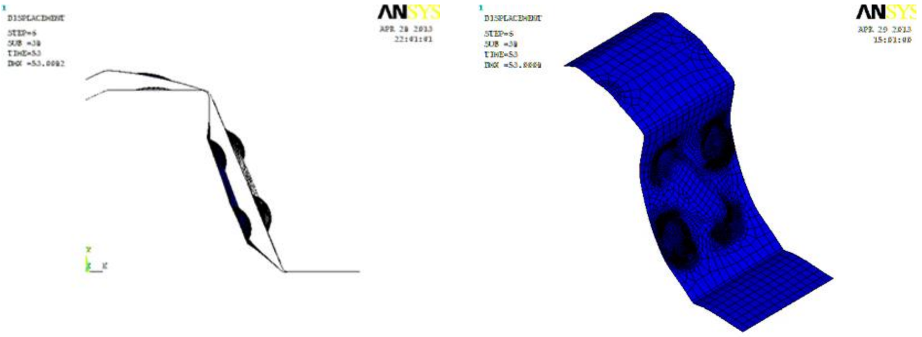

Figure 5.11 *Steel deck deformation at the $F_{u,max}$ maximum load*

Nodal reactions

Figure 5.12 depicts two cases of nodal reactions observed at the long and circular embossments. The distribution among those two types of embossments varied as different dimensions were simulated. Concretely, Figure 5.12(a) depicts a FE model with h_1= 1 mm and h_2 = 2mm. The nodal reactions were mainly concentrated at the long embossments. Oppositely, Figure 5.12(b) depicts a FE model with h_1 = 5 mm and h_2 = 2 mm. The nodal reactions concentrations happened at the circular embossments.

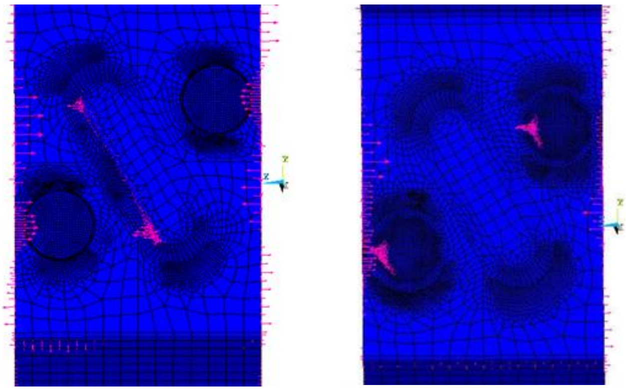

(a) (b)

Figure 5.12 *Nodal forces concentration under different embossment geometries*

Circular embossment deformations

A detailed study was carried out for the deformations at the circular embossment. Figure 5.13 shows two 20-time augmented representations of the von Mises stresses at the base of the embossment. For initial loads, no deformation existed and limited stresses existed. For loads approaching the maximum load $F_{u,max}$, the circular embossment was subjected to local deformations and stresses concentration occurred at the frontal surface most exposed to the concrete slab.

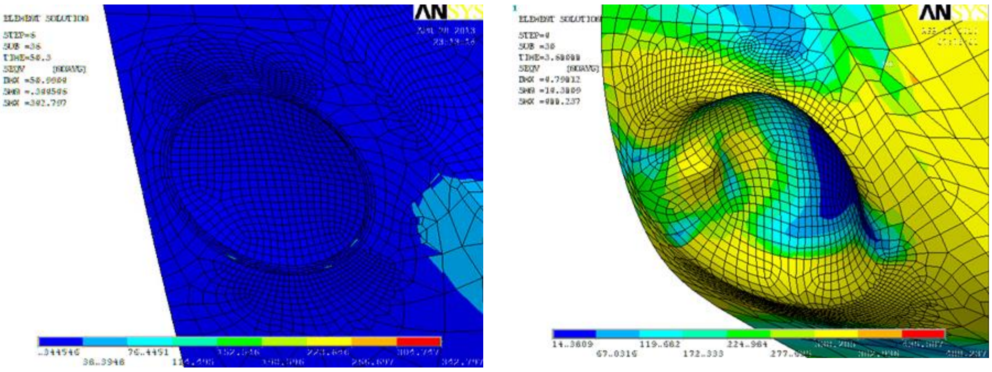

Figure 5.13 *Circular embossment von Mises stress distributions under different loads*

Longitudinal embossment deformations

Similar to the circular embossments, multiple studies were performed to characterize the long embossments geometry influence. Figure 5.14 illustrates four views for the long embossments that captured the initial and end simulation steps at the simplified pull-out FE model. At the early loads captured in blue, the long embossments did not concentrate stresses as the circular embossment captured them. At the maximum shear load $F_{u,max}$, the long embossments concentrated stresses significantly at the shape ends where the interlock with the concrete slab was more relevant. The 20-time augmented representation at the edge of the embossment reported a deformation for the long embossment at the FE models in which h_1 was larger than 3 mm.

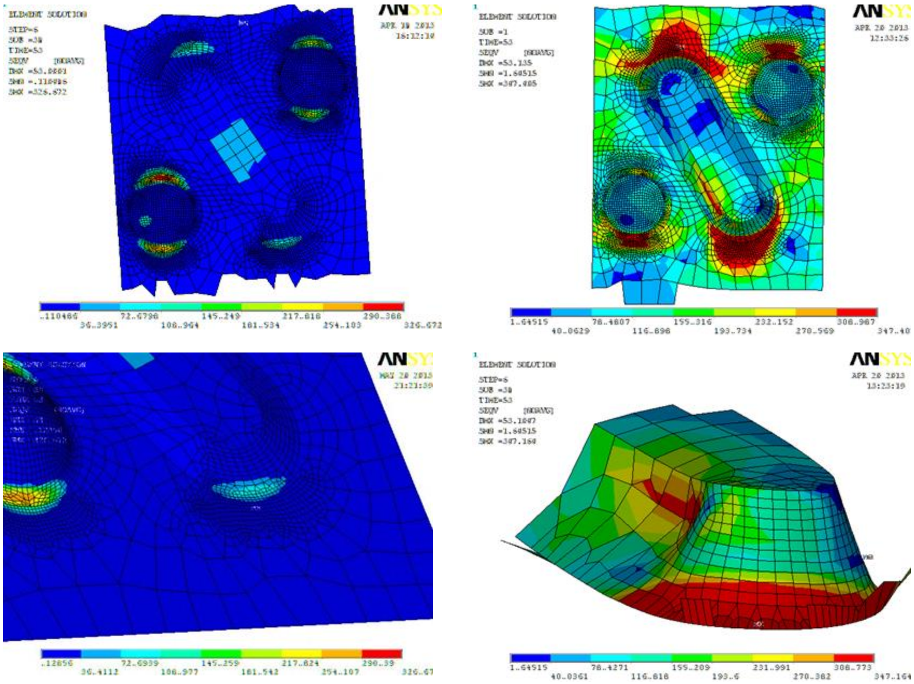

Figure 5.14 *Longitudinal embossment deformations and von Mises stress distributions*

Geometric parameters

The multiple simplified pull-out models developed provided a rich database to compare the sensitiveness of the geometries. Figure 5.15 summarizes in one chart all the studies performed. The studies considered the height of the circular embossments h_1, the height of the long embossments h_2, the thickness of the steel sheet t, the coefficient of friction μ, the pattern width s, and the rounding of the edges of the circular embossments r. As commented previously, the force-slip sensitiveness analyses were performed isolating one parameter at a time and hence the negative cumulative and cross effects from the simultaneous modification of parameters were avoided. The influence of each parameter is commented herein.

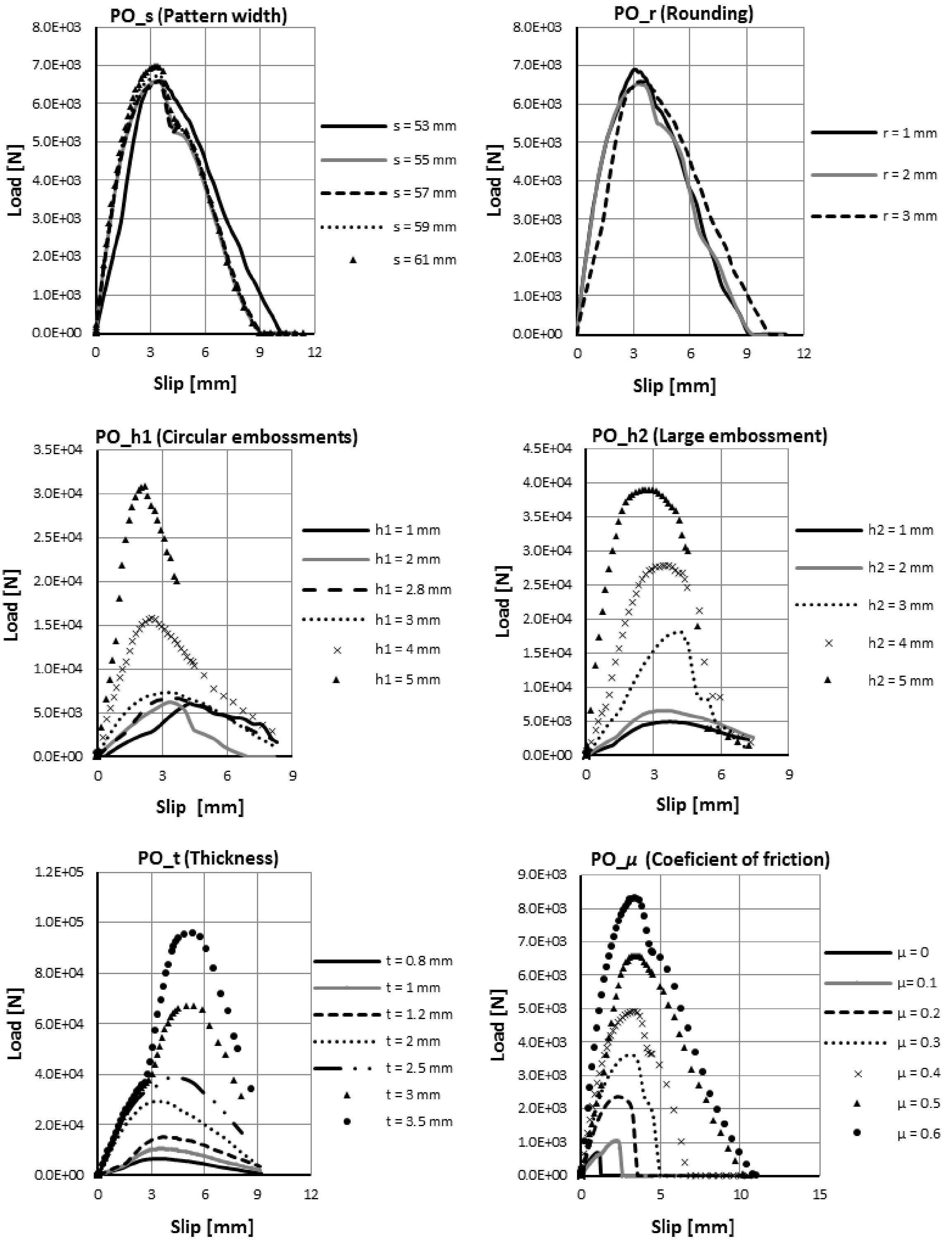

Figure 5.15 *Pull-out parametric analysis for key geometrical parameters*

Measured and nominal dimensions

Prior the study of each parameter, two simplified FE models were created replicating the measured and the nominal steel deck dimensions (see Table 3.1). The differences between the measured and nominal dimensions were detected in all the geometric parameters except for the steel deck thickness t = 0.8 mm. The friction coefficient was input as $\mu = 0.5$ for both FE models. Figure 5.16 illustrates the significant differences observed between the models: the load-slip curves showed a similar slip of 2.2 mm when the maximum load $F_{u,max}$ was achieved, but reported a significant difference in their value 17.80 kN and 6.60 kN. The curves reinforced the strong influence from the use of the measured dimensions in FE modeling as previously identified at the bending simulations.

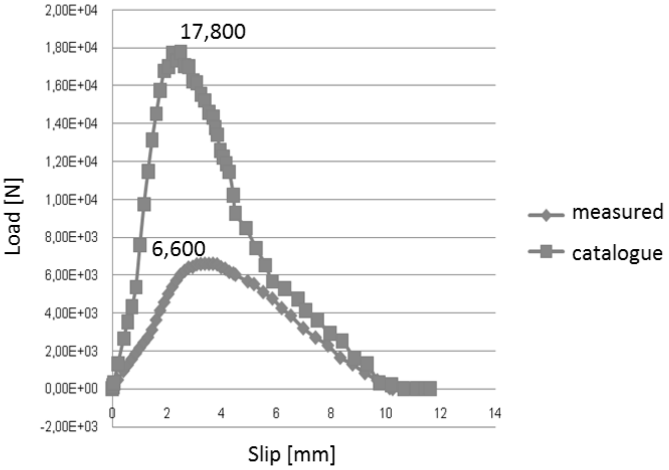

Figure 5.16 *Pull-out models comparison: steel deck measured and nominal geometrical dimensions*

Pattern width (s)

The parameter reported minimal variances for the range of values considered: 53 (measured), 55, 57, 59 and 61 mm. The concrete-steel slips and the maximum loads $F_{u,max}$ observed were similar for all the cases. In order to ensure a solid modeling, the steel deck embossments geometries were constant and located centrally and only the width of the pattern was modified at the edges. See Figure 5.17.

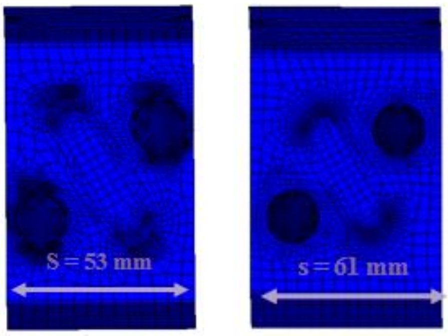

Figure 5.17 *Different steel deck pattern width s investigated*

Ferrer observed some degree of variability for *s* as he investigated a wider range of pattern values between 35 – 100 mm. The INCO70 steel deck profile did not allow to increase the *s* dimensions beyond 61 mm without the need to include additional embossments.

Circular embossment rounding (r)

The parameter reported minimal influence for the range of values considered: 1, 2 (measured) and 3 mm. The concrete-steel slips and loads observed were similar for all the FE models with exactly the same behaviour. Figure 5.18 shows how the different *r* values where implemented: they affected slightly the circular embossment geometry. The von Mises stresses were also investigated and no variance was observed. The results were in line with previous reseach performed by Seres in this parameter.

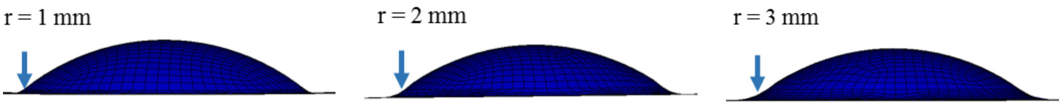

Figure 5.18 *Circular embossment rounding definition at simplified pull-out simulations*

Height circular embossments (h_1)

The parameter reported a significant influence for the range of values considered: 1, 2, 2.8 (measured), 3, 4 and 5 mm. Table 5.12 summarizes the maximum load values $F_{u,max}$ reported for the cases under study. Each linear increase in the h_1 dimension generated an incremental load capacity but with a non-linear behaviour: initial height increases between 1 and 3 mm reported similar load step increases. However, beyond the 3 mm height, the incremental step maximum loads $F_{u,max}$ were more significant. The behaviour observed was aligned with the actual testbed configuration: a higher h_1 at the circular embossment required a significant deformation both at the embossment and the overall steel deck profile for the concrete to override the mechanical interlock.

h_1 [mm]	1	2	2.8	3	4	5
$F_{u,max}$ [kN]	6.04	6.18	6.60	7.28	15.81	30.95

Table 5.12 *Shear bond maximum loads for different h_1 configurations*

Height long embossments (h_2)

The parameter reported a significant influence for the range of values considered: 1, 2, 3, 4 and 5 mm. Table 5.13 summarizes the maximum load $F_{u,max}$ values observed for each case under study. Each step increase in the h_2 dimension generated an incremental load although the overall behaviour was non-linear such as the influence reported from the circular embossment.

h_2 [mm]	1	2	3	4	5
$F_{u,max}$ [kN]	5.01	6.,60	18.14	27.82	38.98

Table 5.13 *Shear bond maximum loads for different h_2 configurations*

Another phenomenon observed was that when h_2 exceeded h_1, the nodal forces were concentrated at the long embossments. Oppositely, when h_1 exceeded h_2 height, a shadow effect from the circular embossment occurred. The long embossment observed less stresses at its base due to the predominance of the circular embossment geometries. Figure 5.19 illustrates the shadow effect between embossments observed in one of the simulations.

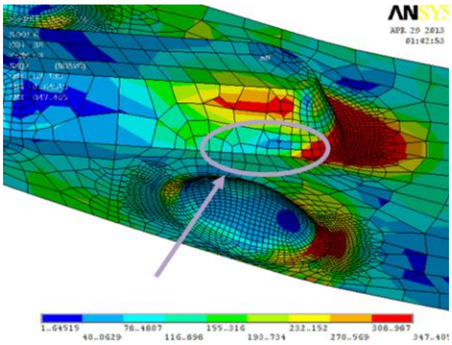

Figure 5.19 *Shadow effect from the circular embossment*

Steel deck thickness (t)

The parameter reported a significant influence for the range of values considered: 0.8, 1, 1.2, 2, 2.5, 3, 3.5 mm. Some of the cases developed were theoretical since the commercial thicknesses range was 0.8 to 1.2 mm due to the limitations from the steel cold-forming process. Table 5.14 summarizes the maximum loads $F_{u,max}$ observed for each case under study. The thickness step increases resulted in significant larger longitudinal shear bond loads as the steel deck inertia and rigidity increased. The steel deck deformations observed at the respective maximum loads $F_{u,max}$ for thicker steel deck profiles were smaller than the ones from the initial $t = 0.8$ and $t = 1$ mm FE models.

t [mm]	0.8	1	1.2	2	2.5	3	3.5
$F_{u,max}$ [kN]	6.59	10.59	15.15	29.08	39.06	67.27	96.05

Table 5.14 *Shear bond maximum loads for different thicknesses t configurations*

Figure 5.20 highlights the von Mises stress distribution at the maximum load $F_{u,max}$ for the 0.8 mm and 3.5 mm FE models. For the lower steel deck thickness, there was a lower concentration of stresses at the lateral sides of the embossments. At the 3.5 mm FE model, some material yielding was observed at the edge of the long embossment.

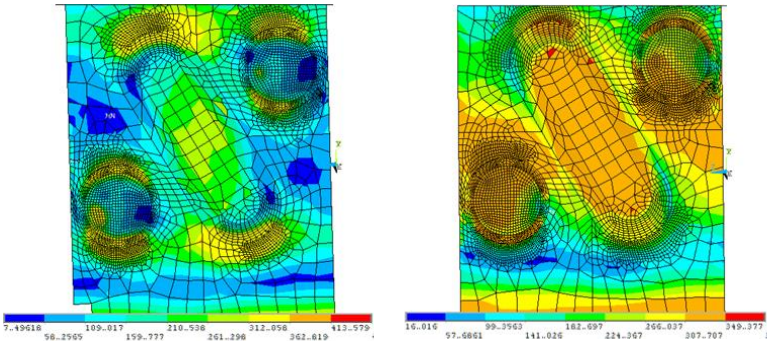

Figure 5.20 *Von Mises stress distribution in $F_{u,max}$ for t=0.8 mm (left) and t=3.5 mm (right)*

Friction coefficient (μ)

The parameter reported a significant influence for the range of values considered: 0.0 to 0.6 in incremental steps of 0.1. Table 5.15 summarizes the maximum load $F_{u,max}$ values observed for each case under study. Each increase in μ generated an incremental load which for this parameter was more linear than the rest of parameters studied. Collaterally, the friction coefficient showed the largest variability for the slip: while the maximum load $F_{u,max}$ was always observed for similar slips, the simulations with higher friction coefficient values reported a more gradual load reduction. See Figure 5.15.

At higher friction coefficients, two singular behaviours were identified. First, the lateral sides of the pattern concentrated more stresses and the yielding areas augmented. Figure 5.21 highlights the von Mises stresses for μ = 0.0 and μ =0.6 observed at the maximum load $F_{u,max}$. Second, larger deformations at the steel deck were observed.

μ [mm]	0.0	0.1	0.2	0.3	0.4	0.5	0.6
$F_{u,max}$ [kN]	0.71	1.06	2.35	3.62	4.91	6.59	8.32

Table 5.15 *Shear bond maximum loads for different friction coefficients*

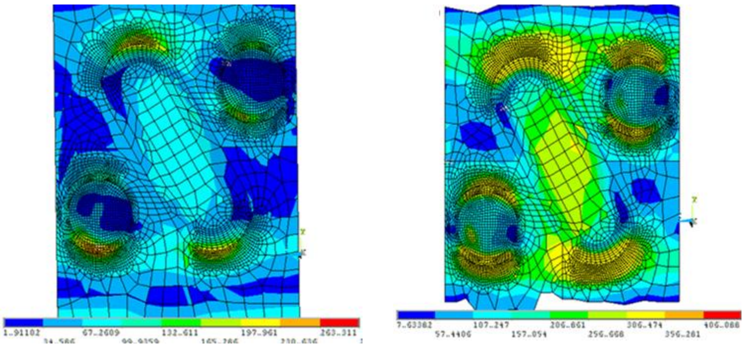

Figure 5.21 *Von Mises stresses for maximum load $F_{u,max}$ in μ = 0.0 (left) and μ = 0.6 (right)*

Results indicate that the parameters with the largest influence in shear resistance for the pull-out specimens were: height of embossments h_1 and h_2; thickness of the steel sheet t; and, the coefficient of friction μ, which was determined to largely depend on the specific geometry of the rib. Oppositely, the shear resistance influences from the width of the pattern *s* and the rounding edges *r* of the circular embossments were less prevalent. These simulation results are consistent with previous parametric studies performed on non-full scale FE models (Ferrer, Seres) and further substantiates the validity of the proposed approach to characterize the longitudinal shear performance for pull-out specimens.

5.2.2 Laboratory testbed – full geometry model

Four full geometry pull-out FE models were developed with different corrugated bars positions and boundary conditions. The corrugated bars were modeled within the concrete block and they were the mechanism to introduce the incremental displacements into the simulations. The actual testbed leveraged the corrugated bars as the mechanism to induce the incremental loads. See Figure 5.22. POF_CASE1 modeled the position of the corrugated bars below the centroidal axis of the steel sheet *cg*. POF_CASE2 modeled the position of the corrugated bars coincident with the *cg* axis. POF_CASE3 and POF_CASE4 assumed the bars above the *cg* axis. In POF_CASE1, POF_CASE2 and POF_CASE3, vertical separation was permitted along the Y axis, while displacements along the Z and X axes were prevented at the four edges of the concrete block. POF_CASE4 assumed corrugated bars above *cg* as POF_CASE3, but vertical separation along the Y axis was prevented. Table 5.11 summarizes the previous key parameters at the simulations.

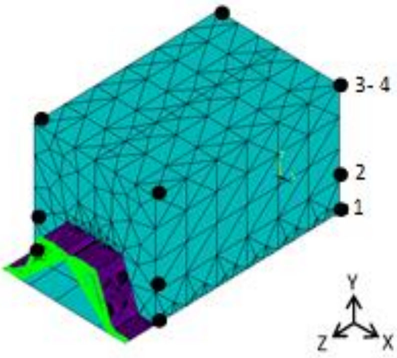

Figure 5.22 *Reinforced bars location for the different pull-out simulations developed*

Initial studies were performed for POF_CASE2 to validate the robustness of the simulation. Figure 5.23(a) to (d) highlight the progression for the nodal reactions as the slip, and consequently the load, increased. The steel deck deformations were augmented 50 times, to ease the visual representation. The initial step with a 0.1 mm slip reported an almost uniform distribution for all the long embossments with a concentration at the bottom side of the rib. The concrete block retained the contact with all the steel deck embossments. As slip increased, such as cases 1 mm and 4.95 mm, the steel deck profile deformation initiated and subsequently the nodal reaction distributions changed with concentration in circular embossments. The concrete block interaction was limited to certain areas of the steel deck rib. At the 9.13 mm slip when the concrete block overrode the steel deck embossments, the nodal reactions were extremely concentrated. Most of the steel deck surface had lost contact already with the concrete block and the contact areas concentrated significant reactions as it was visually noted by the size of the arrows at the representation in Figure 5.23(d).

A similar study was performed at the FE models with a focus on the principal stresses. Figure 5.24(a) to (d) illustrate the 10-time augmented representations observed at the upper fiber of the steel deck. The principal stress vectors representation allowed to identify that the principal concentrations occurred at the surroundings of the circular embossments and in a less degree at the long embossments. A dome effect was observed at the circular embossments: the upper side of the embossment observed compression stresses and the base concentrated tensions.

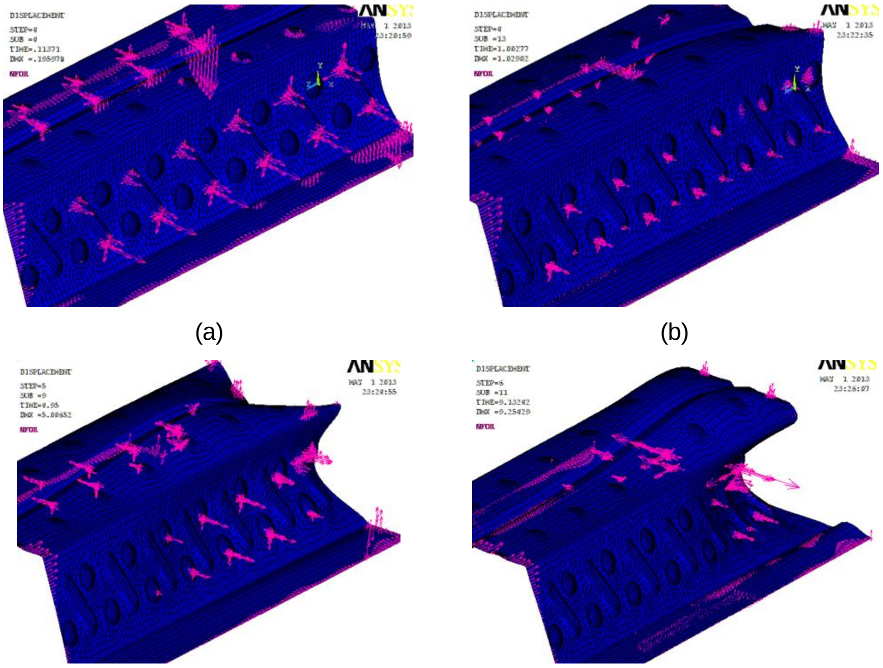

(a) (b)

(c) (d)

Figure 5.23 *Steel deck deformations and nodal reactions for different slips (a) 0.1 mm, (b) 1 mm, (c) 4.95 mm and (d) 9.13 mm*

At the initial 0.1 mm slip, the principal stresses were repetitive in all the embossments. As the slip increased, the concrete block initiated a vertical separation from the steel deck and consequently some embossments decreased the principal stress intensity. At the last simulation slip 9.13 mm, the principal stresses were concentrated at the end of the steel deck where the concrete block rotation occurred. The steel deck was exposed to two different stresses: longitudinal shear and transversal bending from the lateral forces based on the observed principal stresses behaviour.

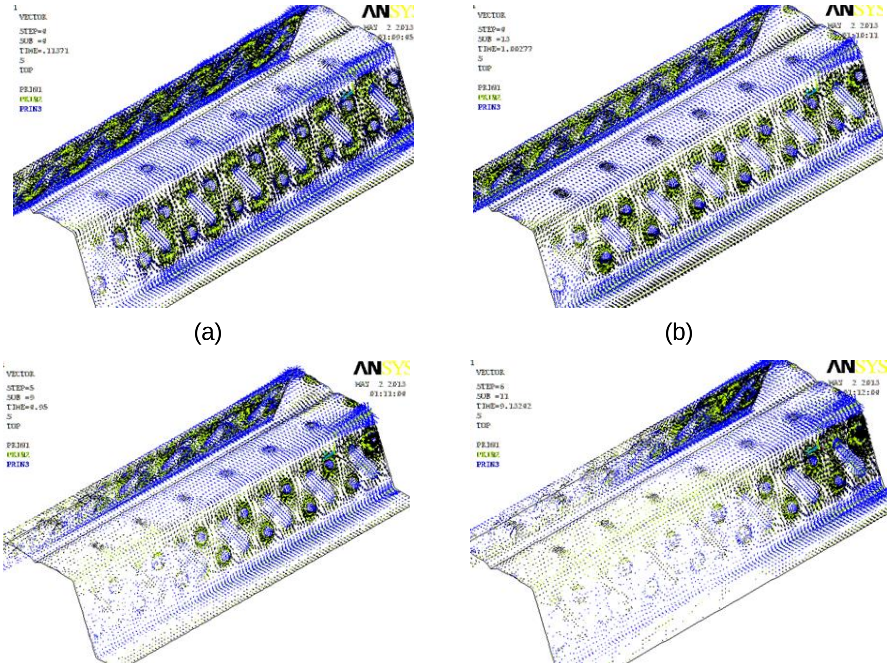

(a) (b)

(c) (d)

Figure 5.24 *Steel deck principal stress vectors for different slips (a) 0.1 mm, (b) 1 mm, (c) 4.95 mm and (d) 9.13 mm*

Subsequently, studies were performed for the rest of the FE models. The results emphasized significant differences in the concrete block behavior. A constant vertical separation was identified in POF_CASE2 when the concrete block slipped over the steel deck and embossments were override. Differently, the concrete block observed a spin in POF_CASE1 and POF_CASE3 in either one or other direction depending on the location of the reinforced bars. In POF_CASE1 the reinforced bars below the *cg* axis generated a tilt towards the front of the specimen. The POF_CASE3 observed an opposite behaviour. See Figure 5.25.

The von Mises stresses were identified for all four pull-out models. Figure 5.26(a) to (d) illustrates the stresses at the maximum load $F_{u,max}$ characterized at the simulations. The steel deck deformations were 20-time augmented to ease the visualization. POF_CASE1 showed a concentration of stresses at the front of the laboratory specimen next to the corrugated bars where the more significant deformations occurred. Oppositely, POF_CASE3 showed a mirrored behaviour with the largest stresses and deformations at the other end of the specimen. Both POF_CASE2 and POF_CASE4 cases reported a more uniform von Mises stress distribution along the rib. Two notable differences were found though in POF_CASE4 in where the restriction on vertical separation introduced a significant uniform deformation along the steel deck, and higher stresses.

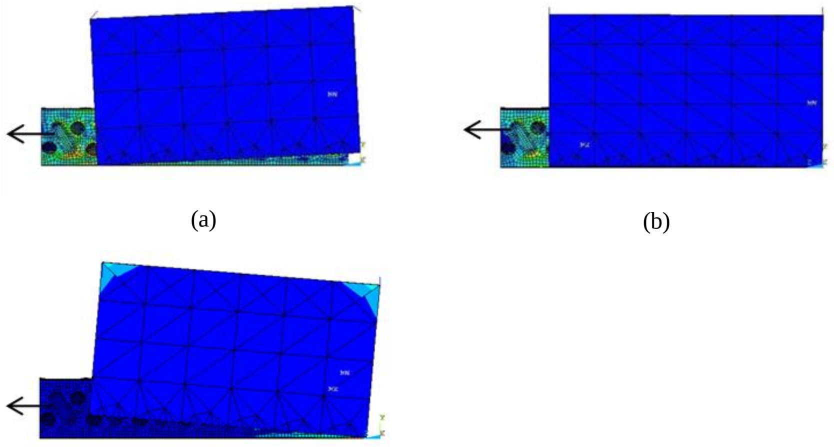

(a) (b)

(c)

Figure 5.25 *Concrete block behavior (a) POF_CASE1, (b) POF_CASE2 and (c) POF_CASE3*

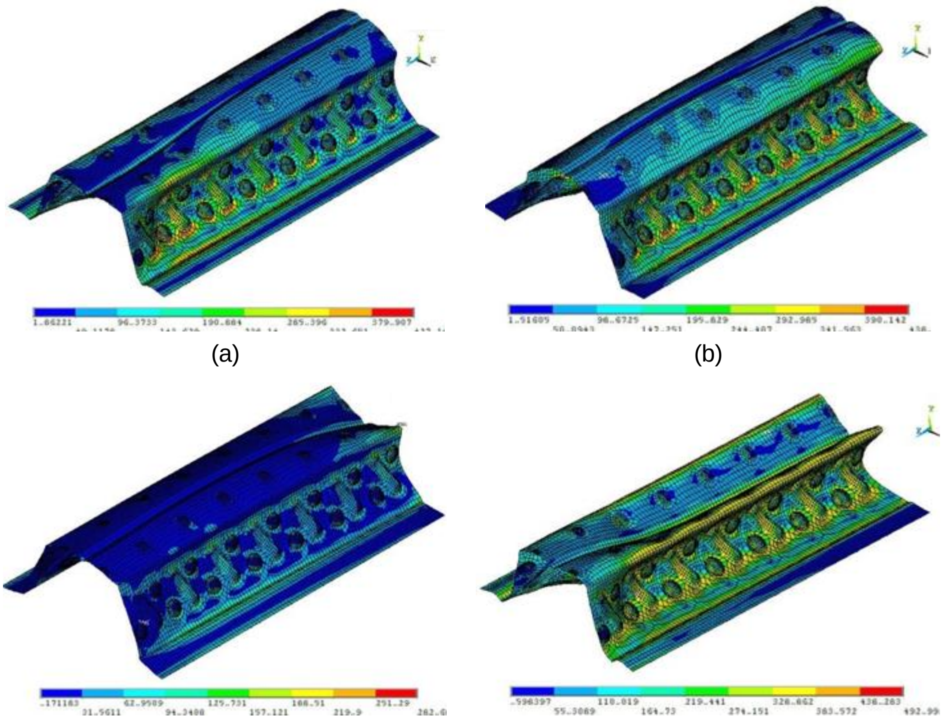

(a) (b)

(c) (d)

Figure 5.26 *Von Mises stresses at maximum load $F_{u,max}$ (a) POF_CASE1, (b) POF_CASE2, (c) POF_CASE3 and (d) POF_CASE4*

The corrugated bars were the mechanism to introduce the displacements at the simulations and significantly affected the longitudinal shear strength. The largest values for end slip and shear bond were characterized under POF_CASE4 due to the concrete block vertical separation prevention. See Figure 5.27. POF_CASE2 and POF_CASE3 reported similar slipping behaviours and maximum shear bond loads while POF_CASE1 showed a different behaviour. Minor variations in the location of the corrugated bars and hence the prescribed displacements produced significant changes in the pull-out simulations behaviours, which were still capable of representing composite slabs micromechanics at any given section with strong convergences.

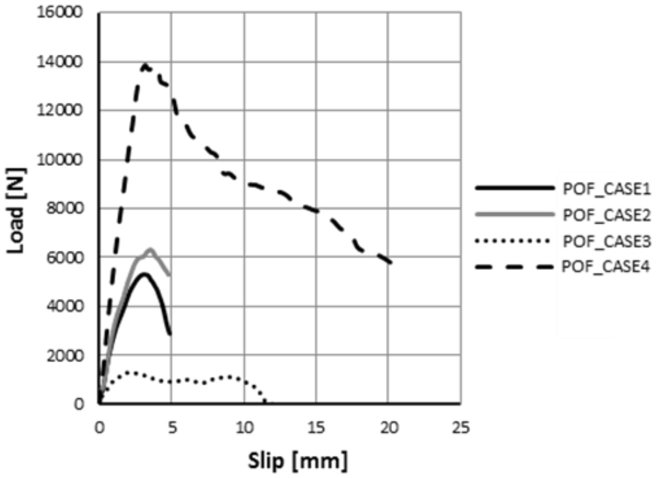

Figure 5.27 *Load-slip curves for full scale pull-out simulations*

The POF_CASE4 simulation was able to simulate large end slips and characterize the behaviour of the steel material beyond a common laboratory test scope. The maximum shear bond load $F_{u,max}$ was observed at the 3.90 mm slip that represented the override of the embossments by the concrete block. Figure 5.28(a) illustrates the shear bond curve recorded from the simulation once it was extended for larger slip values. Figure 5.28(b) illustrates the von Mises stresses for a theoretical slip of 53 mm. It could be observed that steel material yielding appeared at the areas surrounding the long and circular embossment where concentrated nodal forces were previously identified.

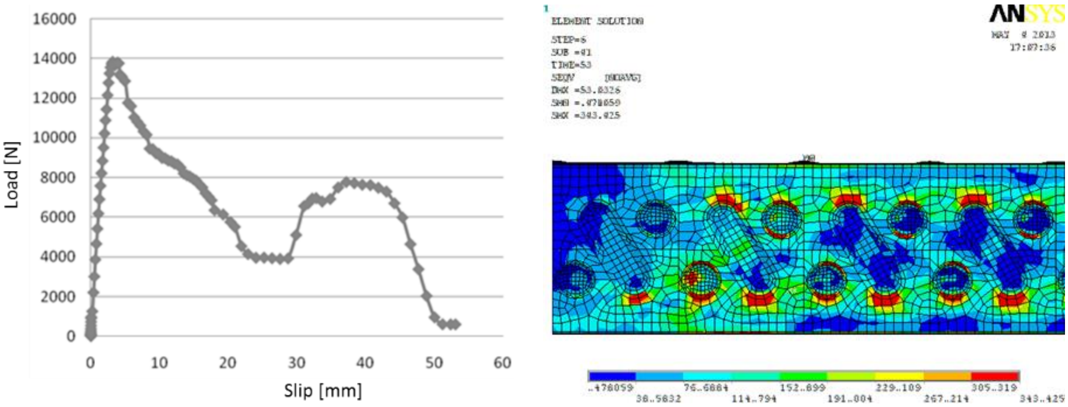

(a) (b)

Figure 5.28 *Load-slip curve and von Mises stresses for extended slip simulation*

Simplified and full-geometry models comparison

The shear resistance characterization differed between the simplified and full-geometry models. Figure 5.29 illustrates the longitudinal shear curves for POF_CASE2, POF_CASE4 and the simplified model that only included one composite slab pattern. The maximum shear bond load $F_{u,max}$ for the POF_CASE4 model reported 13.79 kN while in the simplified model was 6.59 kN and 1.31 kN for the POF_CASE2. The maximum load was achieved at the 3.9 mm, 3.38 mm and 2.04 mm slips respectively.

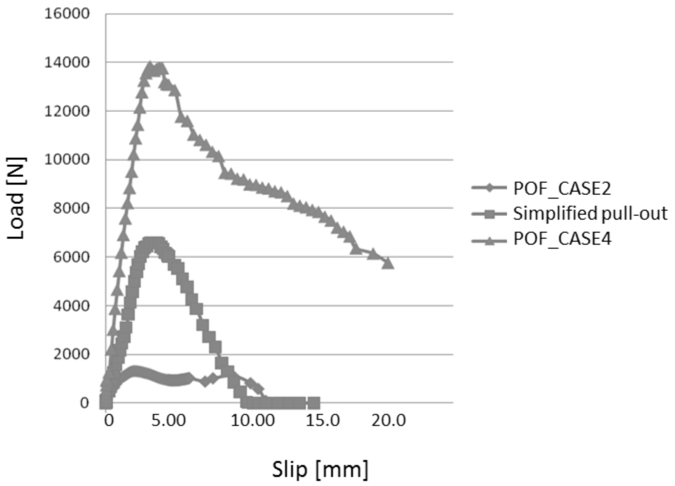

Figure 5.29 *Load-slip curves for full-geometry and simplified pull-out FE models*

Although the simplified FE models were capable to replicate some of the composite behaviours, the full geometry models introduced more complex phenomena such as the concentration of stresses, punctual steel deck deformations, steel deck bending rigidity and concrete block tilt that were not possible to model in one pattern. The full-geometry showed a non-uniform behaviour among the different patterns as it is depicted in Figure 5.30 based on an irregular concrete block vertical separation.

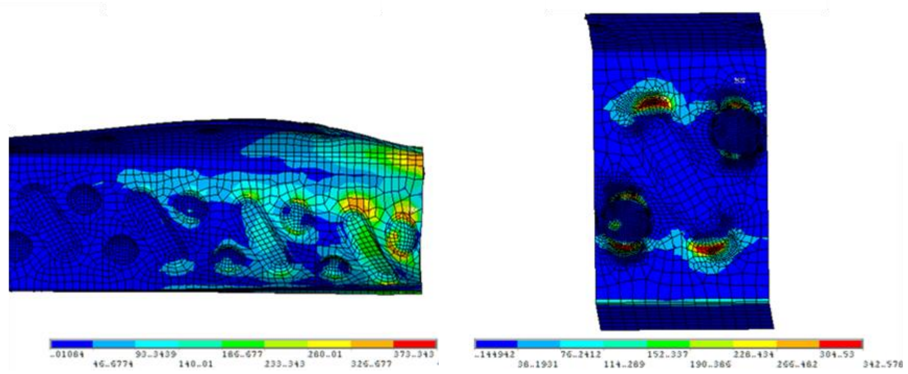

Figure 5.30 *Full-geometry non-uniform stresses distribution along the rib*

Conceptually, the coincidences and discrepancies observed between the simplified and the two full geometry FE models studied can be summarized as:

- The nodal reaction behaviours were similar. At the initial slips without any concrete block vertical separation, the concentration occurred at the longitudinal embossment bases. Subsequently, as the slip increased, the concentration transitioned towards the circular embossments.
- A dome effect was observed in all models for the circular embossments.
- The load-slip curves were influenced by the concrete boundary conditions. At the POF_CASE4 the simulation observed a load recovery after the maximum shear bond load was observed. The POF_CASE2 initiated a sustained decrease in shear bond once the ultime load was achieved. For the simplified models, the simulation computed a complete decrease in shear resistance once the maximum load $F_{u,max}$ was aceived; the concrete separated vertically from the steel deck.

The simulation results, obtained purely from computational modeling and without any laboratory tests, reinforced the deployment of the novel FE accurate modeling as a solid approach to reduce the costs, number and complexity for composite slab laboratory tests. Several studies were performed and pull-out composite shear bond behaviour characterized without the need to test any specimen.

5.3. Bending simulations: numerical analyses

The bending simulations provided more complex models to explore the composite slab micromechanics compared with the pull-out FE models. Once the FE bending models were deemed capable of accurately and reliably replicate the laboratory bending tests, micromechanics phenomena that cannot be observed during such tests were investigated and are described herein. The rest of this chapter discusses the neutral axes behavior under composite action, steel deck and concrete slab vertical disconnection, and the longitudinal shear strength. Since the simulations were based on incremental displacements steps, the different analyses compare midspan deflection cases. The discussions combine displacement cases and load results when appropriate.

5.3.1 Neutral axes steel deck and concrete slab

Composite slab behavior fundamentally depends on the degree of shear η between the steel deck and the concrete slab component. As previously introduced in section 5.1.2, the PCM proposed the definition of a theoretical interaction curve based on laboratory tests. The curve enabled the visualization of the different composite behaviors that could be found in the slab: (i) full shear interaction, which occurred when there was not a relative slip between contact surfaces ($\eta=1$), and resulted in a single neutral axis; (ii) partial interaction, which occurred when there was a slip between the contact surfaces but still with transfer of shear bond stresses ($0<\eta<1$), and resulted in two different neutral axes; (iii) no shear connection, which occurred when the shear stresses were not transferred ($\eta=0$), and resulted in independent behavior of the steel sheet and the concrete slab. Figure 5.31 illustrates the stress distribution at the case that the neutral axis e_n was located within the steel deck height.

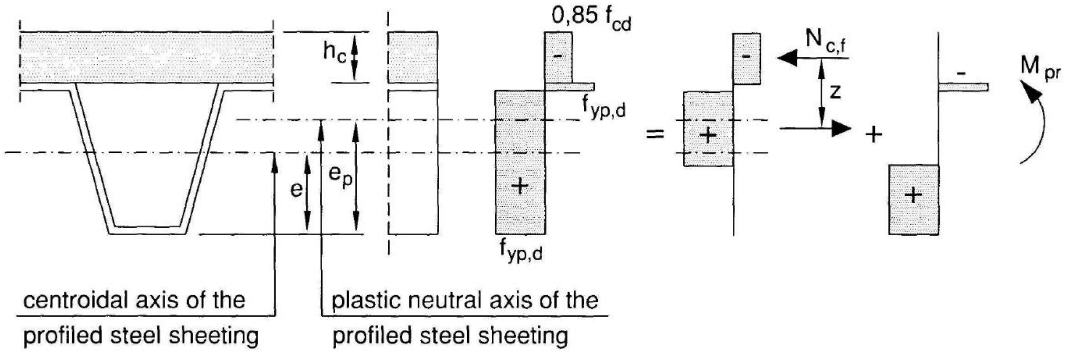

Figure 5.31 *Stress distribution for sagging bending if neutral axis is in steel sheeting, adapted from Eurocode 4*

The steel deck and the concrete slab at the INCO70_S_CI_0.8 model were separately studied and their neutral axes identified along the span for different midspan deflection cases. The process followed required a detailed analysis of the concrete slab and steel deck internal strains in each pattern. Particularly, a vertical section was isolated at the middle of the pattern width *s*. The section reported an area working under tension and another under compression strains. The identification of the different areas, and specially the compression – tension transition area, were the foundations to define the neutral axes. The nodes at the transition area where the strain turned 0.00 kN were isolated; subsequently its distance at the Y axis to the bottom side of steel deck was measured. Figure 5.32 illustrates the strains for a typical concrete slab pattern. Figure 5.33 provides an equivalent visualization for the steel deck strains that captured a different behaviour.

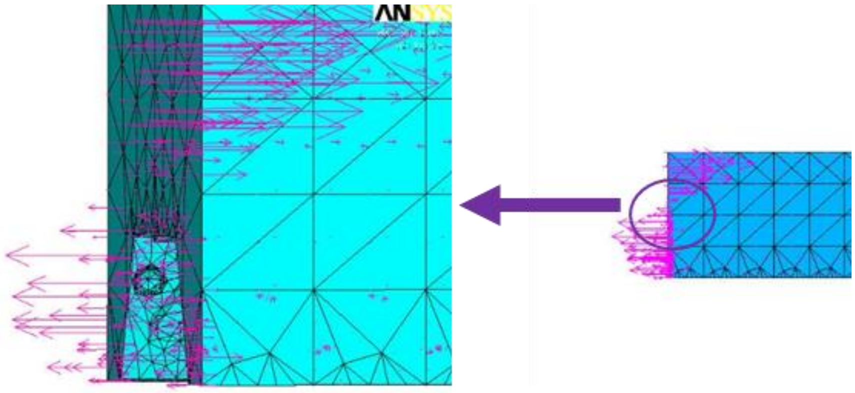

Figure 5.32 *Strain distribution in a typical concrete section*

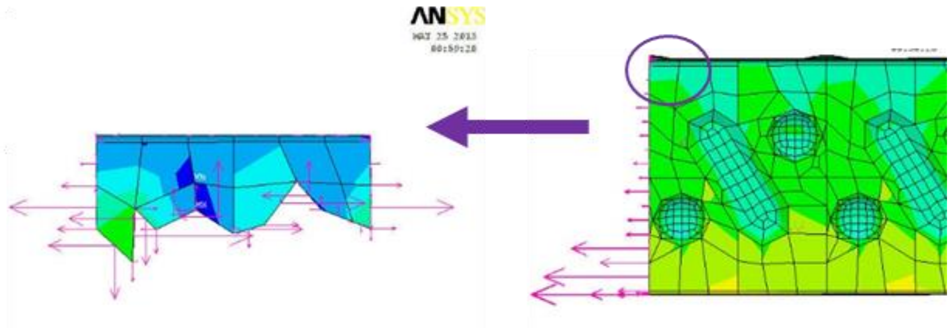

Figure 5.33 *Strain distribution in a typical steel deck section*

First, the neutral axis for the steel deck did not follow a general pattern throughout the rib under the different incremental midspan deflection conditions. See Figure 5.34. However, in the shear span L_s between patterns #14 and #25 the neutral axis vertical location e_n gradually ascended from e_n = 60 mm at the crack inducer pattern #14 to the upper flange of the steel sheet h_p = 70 mm at the support pattern #25. Also, at the bending span $L_{bending}$ between patterns #1 and #14, e_n varied as displacements increased: early stages showed values closer to h_p and decreased as the displacement increased. The observed behavior is consistent with midspan deflections. For early deflections of 1 mm, 5 mm, 7 mm and 14.96 mm, e_n ascended from the crack inducer section in pattern #14 to the end of the span in pattern #1 with a decreasing slope as midspan deflections increased. The midspan deflection of 20 mm showed an almost flat behavior while a negative slope appeared for the 27.47 mm deflection.

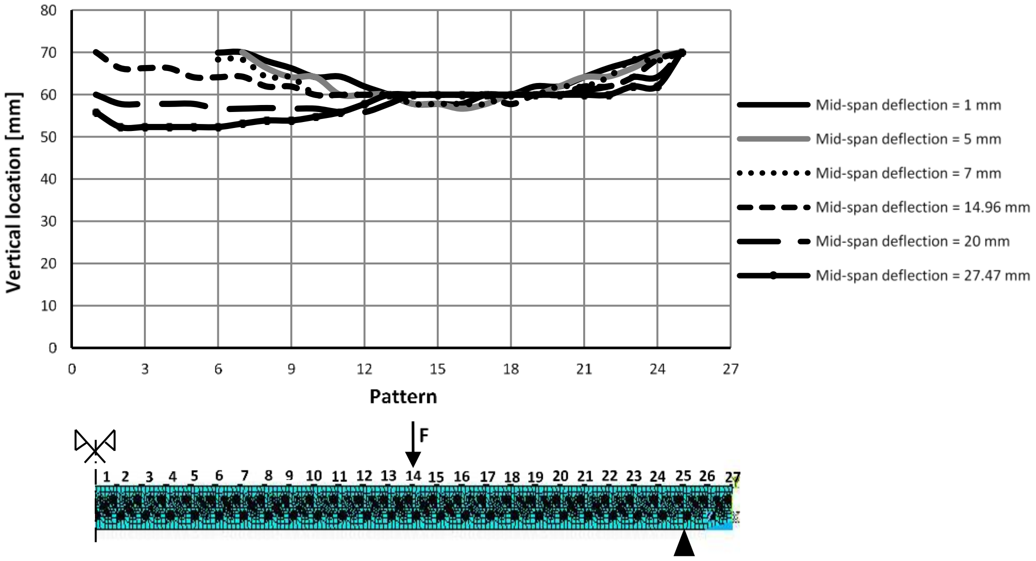

Figure 5.34 *Steel deck neutral axis position* e_n *in different midspan deflection cases*

Second, the concrete slab neutral axis remained unchanged under the different midspan deflections although presented different vertical positions along the rib. See Figure 5.35. The neutral axis position was uniform around 90 mm at the pure bending span between patterns #1 and #14. At the loading and crack inducer section a singularity in the neutral axis position was identified. Between patterns #14 and #25, the neutral axis position of the concrete decreased down to the bottom flange of the steel deck. Figure 5.36 illustrates a three-dimensional view of such condition: grey solid areas represented compression while colored areas represent different levels of tensions. At any given cross section, the boundary between these tension and compression areas defined the neutral axis position for the concrete slab.

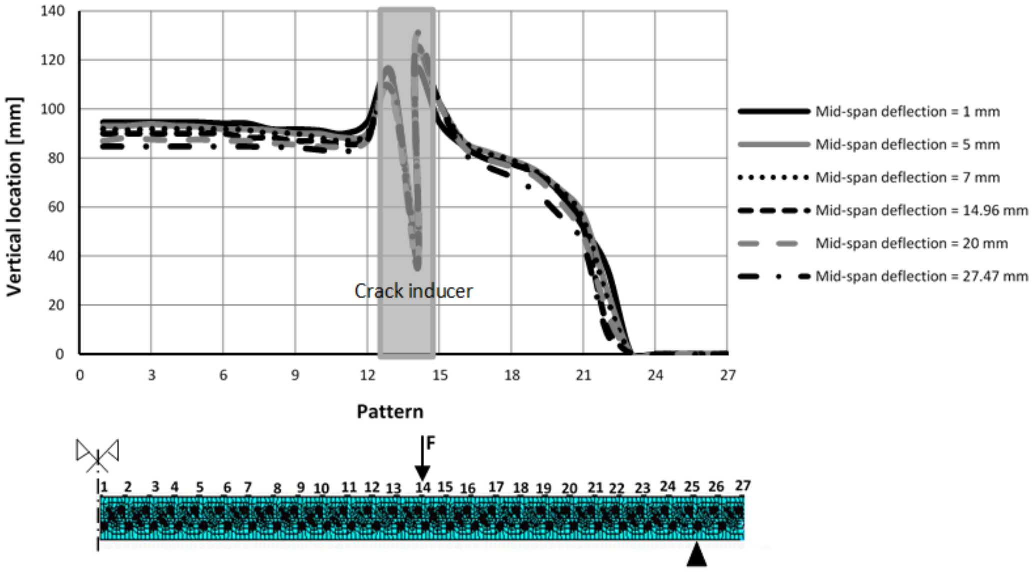

Figure 5.35 *Concrete slab neutral axis position in different midspan deflection cases*

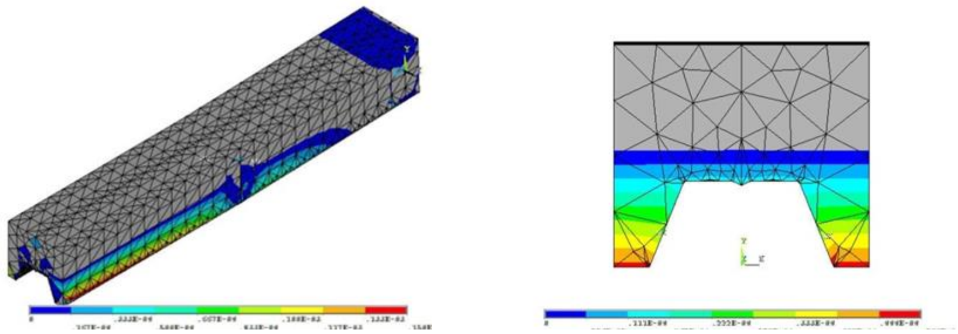

Figure 5.36 *Concrete neutral axis 14.96 mm midspan deflection: tridimensional and cross section views at the bending span*

The FE models facilitated the observation of micromechanics for the different materials under different loading stages, enabling a much more accurate view along the rib of the composite behavior. In particular, the existence of two different neutral axes validated the partial connection behavior in the composite slab and could influence some of the simplifications implemented at the Eurocode 4 PCM such as Equation 5.3 in future research.

5.3.2 Steel deck – concrete slab vertical disconnection

Vertical disconnection between steel deck and concrete slab was another complex phenomenon that occured along the span and could not be observed or measured during laboratory tests. The complexity of this phenomenon increased for open rib steel decks, such as the steel deck profiles INCO70, C60 and T80 studied in this dissertation, since the clamping phenomenon became prevalent. During the laboratory tests, the longitudinal slip between the concrete slab and the steel deck at the point load and support was converted into a local transversal bending moment in the steel deck that had a strong correlation with the amount of shear connection between the materials.

The complex three-dimensional deformations and stress distributions for both materials were captured as part of the simulations for the INCO70 steel deck. Such information could be leveraged to enable improvements in the steel deck designs, for example in thickness, embossments geometry, or tilting angle, among many others. Thus, the vertical disconnection between the steel deck and concrete slab was analyzed along the rib for different midspan deflections. See Figure 5.37. The computed values for vertical disconnection from INCO70_S_CI_0.8 varied under different deflections and pattern locations, except for pattern #14 at the point load and for pattern #25 where the support was located. Variable values were identified at the edge of the rib in pattern #27, at the middle of the shear span in pattern #21, and at the end of the bending span in pattern #1. The largest disconnection was observed at the end of the bending span with a significant difference in comparison with values captured at the edge of the rib and at the middle of the shear span. The FE models accurately represented the limited behaviors that could be directly observed at the laboratory specimens that are depicted in Figure 5.38.

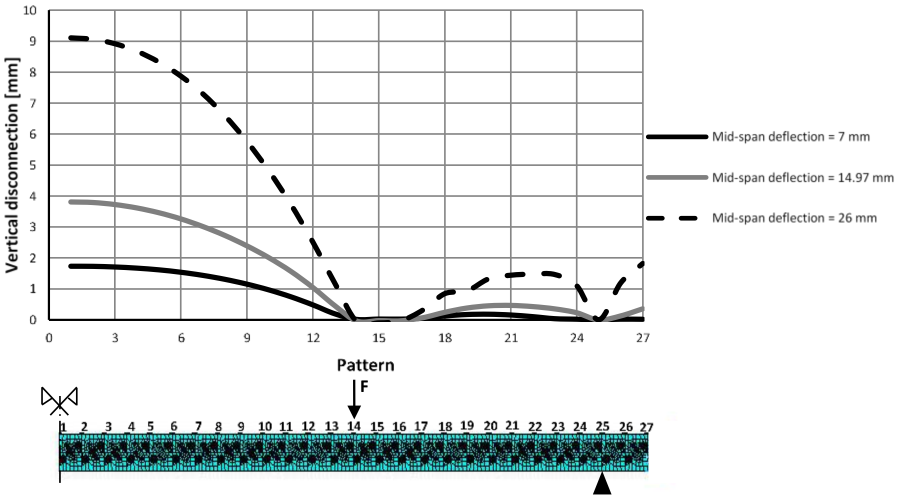

Figure 5.37 *Vertical disconnection between the steel deck and the concrete slab*

Figure 5.38 *Vertical disconnection observed at the laboratory specimen*

5.3.3 Steel deck strains and deformations

The LERMA composite slab database included a set of QL60 long span laboratory specimens with the deployment of gauges for strains monitoring at the shear span. The measures included a detailed record of uni-directional micro-deformations during all the test loads for pre-identified locations at the steel deck. The micro-deformation monitoring and subsequent comparison with the FE model results provided another novel source to characterize composite slabs micromechanics and hence validated the results robustness from the simulations. Figure 5.39(a) illustrates the strains and deformations targeted at the LERMA laboratory tests for the analyses. Figure 5.39(b) depicts the distribution of the strain gauges along the composite slab laboratory specimen. Gauges named *g17* to *g32* collected the micro-deformations from the strains distributions developed at the vertical side of the steel deck.

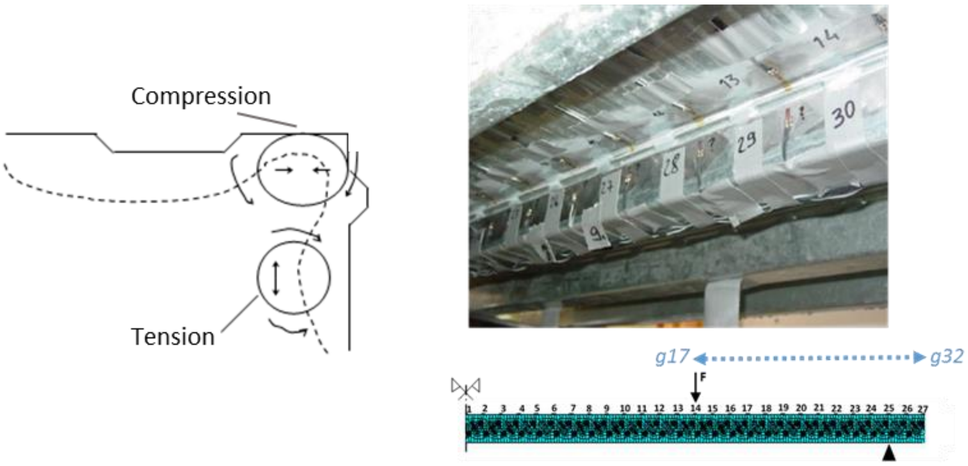

(a) (b)

Figure 5.39 *Strain gauges implemented in laboratory specimen, adapted from Ferrer (2005)*

Figure 5.40 reports the micro-deformations along the rib observed at the gauges for different load conditions captured by Ferrer from the LERMA tests. The author explored different approaches to characterize the shear resistance combining the strain gauges readings with the shear forces and friction coefficients for the steel deck. Figure 5.41 illustrates the equivalent measurements from the FE model. Lectures of strains and micro-deformations were computed at the FE models at the exact same location that the ones from the laboratory specimens.

Qualitatively, a strong correlation was detected at the micro-deformation curves for both the load range 0.0 - 29.6 kN and the different locations *g17* - *g32*. The micro-deformation curves trend and their absolute and partial values observed for both the laboratory results and FE models were similar. Laboratory results observed a constant micro-deformation between the load point where the *g17* gauge was located and the *g32* gauge at the support pattern for each load reported. The FE models reported evolving micro-deformation curves with non-constant values for the same segment of gauges at the shear span L_s. Both test and simulation results reported a sudden micro-deformation decrease at the support section where the *g31* gauge was located. The author hypothesizes that a source to improve the characterization of the micro-deformations could be a new meshing of the FE models. The strain gauge geometry embraced multiple FE type elements and nodes. A new and more granular meshing of the FE models at the gauge area could potentially improve the simulations results.

A few additional studies were performed to compare the results. Although the micro-deformation curves had a different trend, an averaged theoretical *g17* to *g31* micro-deformation value for each load in both the laboratory test and FE model results was computed. The averaged values reported a strong similitude as the inclined curves from the FE model along the span concurred with the flatter behaviour observed at the laboratory readings.

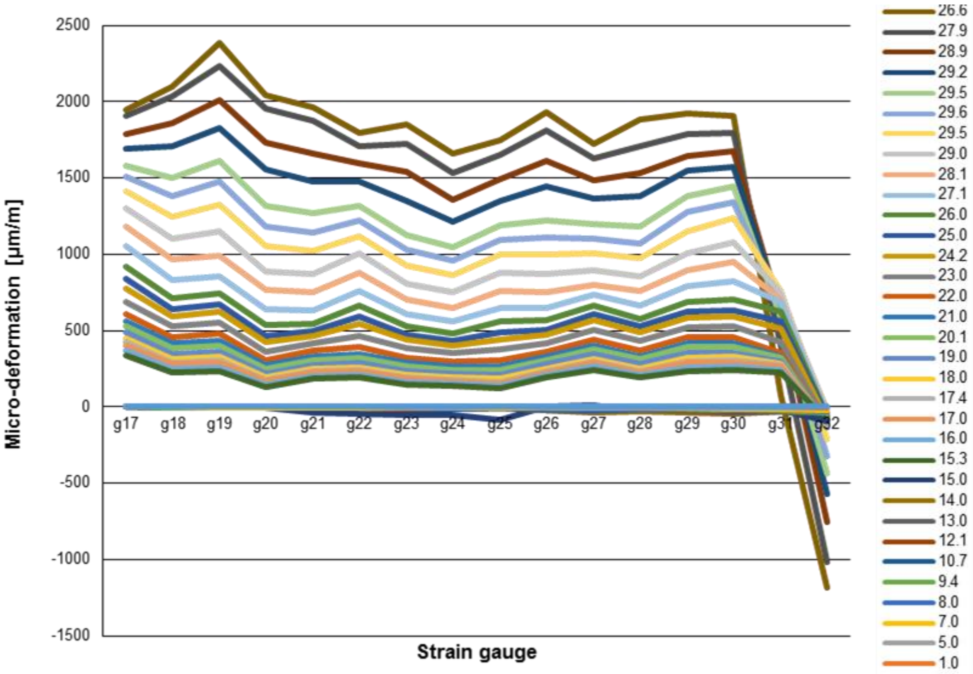

Figure 5.40 *Micro-deformation laboratory, gauges g17 – g32 for loads 0 – 29.6 kN*

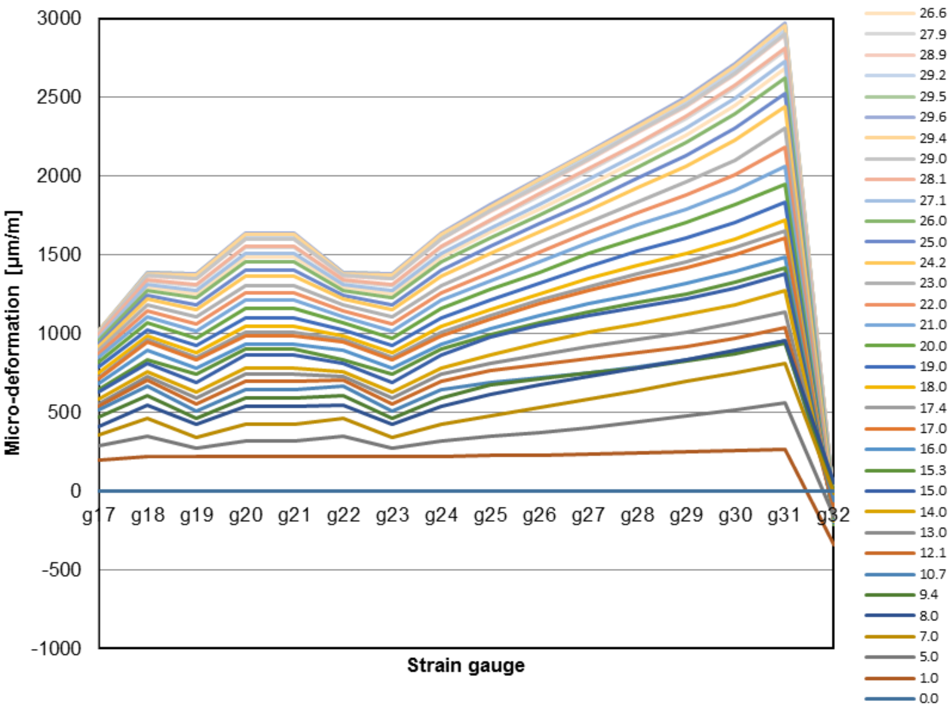

Figure 5.41 *Micro-deformation FE, gauges g17 – g32 for loads 0 – 29.6 kN*

5.3.4 Longitudinal shear strength τ_u

The full-scale FE bending models enabled the analysis of the stresses distribution at any particular section and in any particular simulation step in the composite slab. Similar to the vertical disconnection, neutral axes and the micro-deformations studies performed, the characterization for the longitudinal shear strength τ_u was identified as an important area of focus. The longitudinal failure in composite slab is the most common for open rib profiles and the Eurocode 4 PCM postulates a mechanical model with a constant τ_u at the shear span. Equation 5.5 introduced the PCM formula to characterize the longitudinal shear strength; it is reproduced again as Equation 5.19. Figure 5.42 illustrates conceptually the PCM force distributions and its mechanical model.

$$\tau_\mathrm{u} = \frac{\eta N c f}{b(Ls+Lo)} \tag{5.19}$$

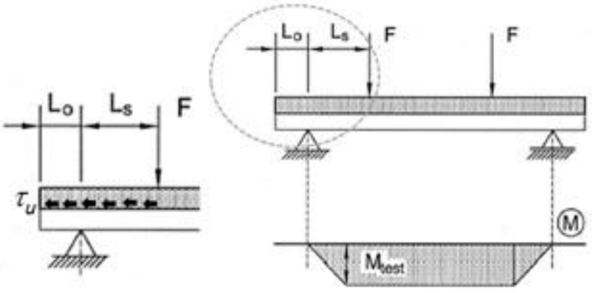

Figure 5.42 *Conceptual visualization longitudinal shear strength* τ_u

Figure 5.43 illustrates a novel representation for the longitudinal shear strength τ_u along the span for the INCO70_S_CI_0.8 model at three different midspan deflection cases: 7 mm; 14.96 mm where the maximum shear load $F_{u,max}$ for the composite slab bearing capacity was observed in laboratory tests; and, 27.47 mm as the last step of the FE simulation. The shear strength distribution was obtained by isolating each composite slab pattern and calculating subsequently its resulting longitudinal shear force divided by the horizontally projected area of the steel deck pattern. The τ_u distribution resembles a "bath-tub" cross section with values varying in correspondence with the external loading conditions. Two maximum values were observed along the distribution for each case: pattern number #14 at the point load section and pattern #24 near the support section. Values at the shear span L_s, outside of the singular patterns for the support and the point load, were almost constant while stresses were zero along the pure bending span $L_{bending}$ between patterns #1 and #14.

The longitudinal shear strength τ_u is a key parameter for the composite slab design since shear bond is the most common failure mode in ductile behavior. The proposed FE simulation methodology results in novel evidence for the τ_u micromechanics behavior. The design method PCM mechanical model assumptions that both the slip is uniform and that the longitudinal shear strength τ_u remains constant at the shear span were validated.

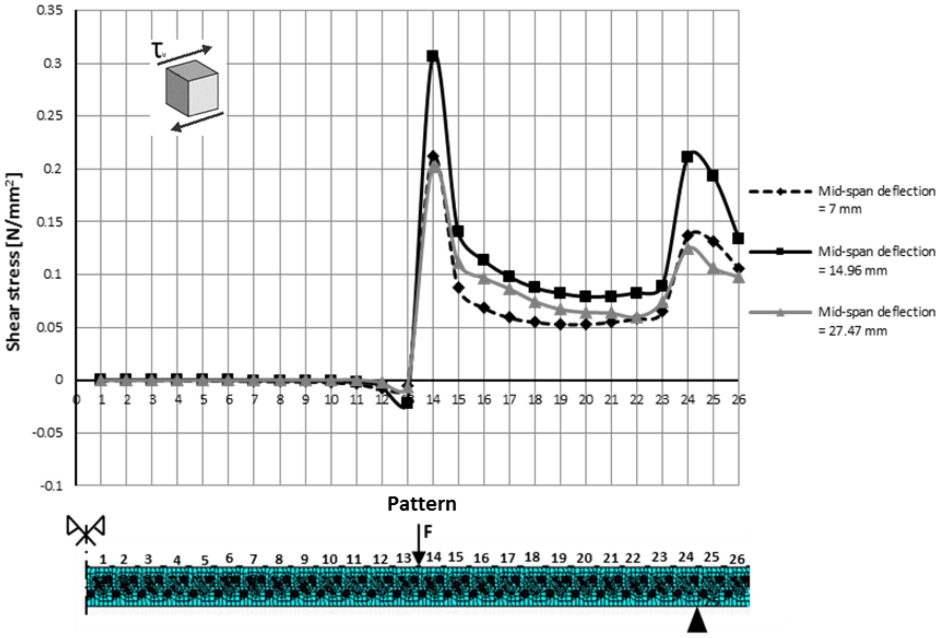

Figure 5.43 *Shear stress distribution τ_u along the span for different midspan deflection cases*

The stresses concentration identified around the point load in pattern #14 and the support in pattern #25 also incentives further research in composite slab characterization as they concentrate higher values due to friction and reactions. The understanding of this micromechanics reinvigorates the path started by other authors with the goal to improve the composite slab design methods beyond the building codes assumptions (Daniels and Crisinel, Patrick and Bridge, Widjaja, Abdullah and Easterling). A detailed discussion of the longitudinal shear strength τ_u interpretation is performed in chapter 6; moreover, a new composite slab characterization parameter is introduced based on the findings from the novel representation introduced.

5.3.5 Normal vertical stress σ_{shear} in composite action

A newly vertical normal σ_{shear} stress was proposed to characterize the interaction between the concrete slab and the steel deck. The new stress was defined as the pattern resultant vertical force divided by the horizontally projected surface of the steel deck pattern. Figure 5.44 illustrates the normal vertical stress curves for two different midspan deflections for the short span FE model INCO70_S_CI_0.8. Similar to the longitudinal shear strength τ_u curves, two stress concentrations were observed at the point load in pattern #13 and at the support pattern #25. Positive values, as reactions from compressive strains at the concrete slab, were observed at the steel deck between patterns #11 and #14 and between patterns #22 and #25. Those reactions represented the efforts from the two different materials against the vertical disconnection at the steel-concrete interface. The clamping phenomenon induced by the longitudinal slip generated a significant concentration of σ_{shear} stresses in those singular areas. The σ_{shear} stress concept is developed in detail in chapter 6.

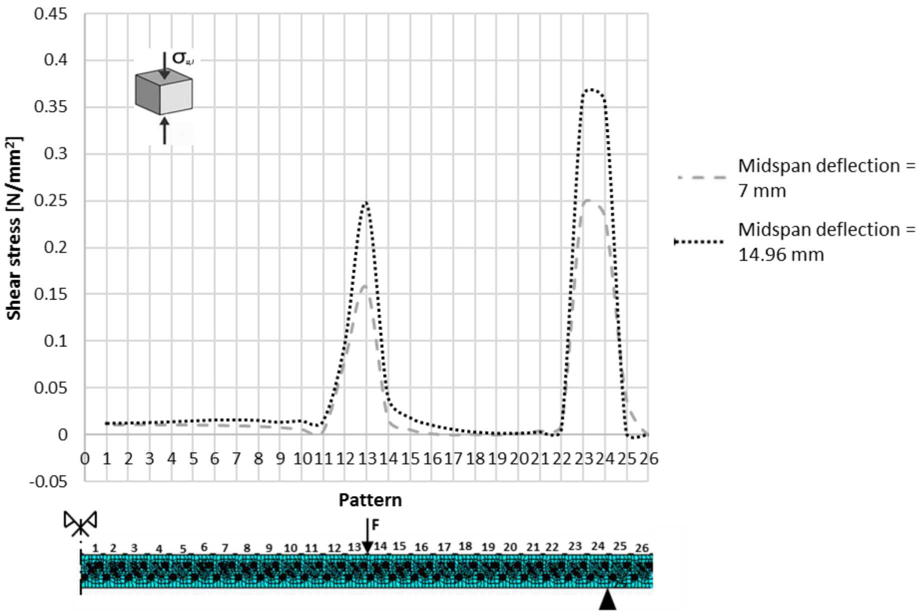

Figure 5.44 *Normal vertical stress distribution σ_{shear} along the span for different midspan deflection cases*

6. Longitudinal shear mechanical strength $\tau_{u,mechanical}$

This chapter develops a new parameter to characterize the shear resistance named longitudinal shear mechanical strength $\tau_{u,mechanical}$. The parameter was developed based on a novel micromechanics interpretation for the shear strength τ_u from the simulations and some subsequent studies performed herein. The studies depicted the influence at the longitudinal shear strength τ_u from the friction coefficient μ, variable loads F_u and composite slab geometries. Prior to the full discussion of the longitudinal shear parameters, an initial review of the vertical normal stress curves σ_{shear} was provided for all the steel decks considered in this dissertation. The σ_{shear} curves allowed the definition of an unclamped segment within the shear span L_s in each FE model that subsequently was leveraged to characterize the new $\tau_{u,mechanical}$ parameter. Finally, a new design process for steel deck profiles was proposed that combined both the novel FE modeling methodology detailed in chapter 4 and the longitudinal shear mechanical strength $\tau_{u,mechanical}$ as a practical contribution in steel deck profile optimization.

The chapter initially considered both long and short span numerical simulations for the studies performed. Gradually, the focus moved towards the short span FE models as their behaviours, and henc composite shear characterization, were more relevant.

6.1. τ_u curve interpretation

The novel representation of the longitudinal shear strength τ_u introduced in section 5.3.4 enabled an in-depth interpretation of the “bathtub” shape. The shape provided a more complex distribution than the previously assumed constant τ_u value by the Eurocode PCM. Figure 6.1 and Figure 6.2 illustrate the σ_{shear} and τ_u curves observed for the C60_S_CI model at the $F_{u,max}$ maximum load as a base case for this discussion. Both curves included the singularities at the point load pattern #16 and support pattern #33. Figure 6.1 moreover introduces a division by segments of the shear span L_s for the different shear behaviours observed at the vertical normal tension curve σ_{shear}.

- “Bathtub” segment: the segment was defined as the window of patterns between the start of the stress increase at the point load pattern and the end of the stress singularity at the support pattern. Conceptually, it included the segment where the longitudinal shear stresses were observed, including the two peaks.
- Unclamped segment: the segment was defined as the window of patterns within the “bathtub” shape where the clamping phenomenon did not exist. The σ_{shear} values observed values close to zero and occasionally negative at the steel – concrete interface.

- Clamped segments: contrary to the unclamped segment, the segments considered the largest stresses at the point load and support patterns were the clamping phenomenon occurred. Conceptually, the segments represented the patterns within the “bathtub” shape outside of the unclamped segment.

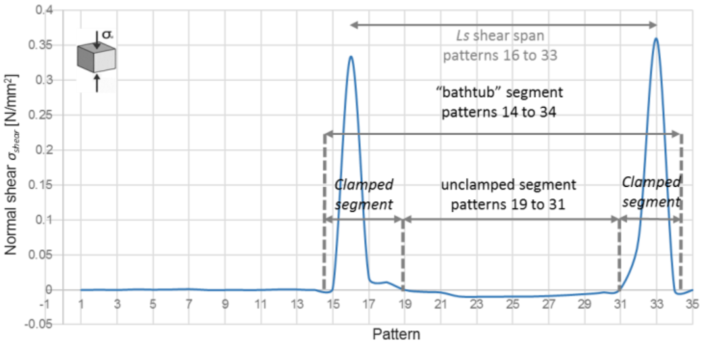

Figure 6.1 *Segmentation of the normal shear stress distribution σ_{shear}, C60 simulation*

The segments defined for the vertical normal stress σ_{shear} were deployed subsequently to characterize different averaged values for the longitudinal shear strength τ_u. The unclamped segment represented conceptually the span where the steel deck clamping phenomenon did not interfere with the concrete slab, enabling a constant slip between the materials. The segment also represented the span in which a constant longitudinal shear strength τ_u existed. Consequently, the longitudinal shear strength τ_u parameters defined were:

- $\tau_{u,bathtub}$: The longitudinal shear strength parameter averaged the τ_u values computed at the “bathtub” segment. The parameter included the influence of the peak values observed at the support and load point patterns.
- $\tau_{u,Ls}$: The longitudinal shear strength parameter averaged the τ_u values computed at the unclamped segment. The new parameter removed the singularities from the peak values observed at the support and load point patterns. Mechanically, the parameter captured a segment with a constant τ_u value and constant slip between the steel deck and concrete. As a concept, the parameter represented the Eurocode 4 PCM definition for the longitudinal shear strength although the PCM design method assumed its presence across all the shear span L_s. See Equation 2.7.
- For the clamped segments, no new averaged longitudinal shear parameter was defined. The segments captured the areas with the largest effect from clamping and therefore were leveraged to characterize the composite behaviour by their shape and stress values, as opposed to any averaged value.

At the C60_S_CI model deployed as base case, the values computed were $\tau_{u,bathtub}$ = 0.0994 N/mm^2 and $\tau_{u,Ls}$ = 0.0985 N/mm^2. Both values were similar for this FE model, as the clamped segments were sharp and concentrated only in some patterns.

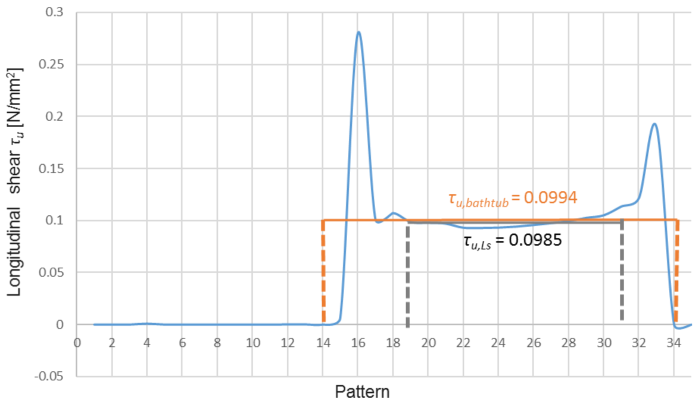

Figure 6.2 *Representation new longitudinal shear stress parameters*

The $\tau_{u,Ls}$ hence was defined as the key parameter from the simulations to characterize the longitudinal shear strength τ_u based on the definition of the unclamped segment from the σ_{shear} curves. It captured the segment within the shear span L_s that observed a constant τ_u value. The unclamped segment length varied for each FE model and consequently an individual computation was required for each composite slab.

6.2. Vertical normal stress σ_{shear} curves

The vertical normal stress σ_{shear} curves were computed for all FE models to define the unclamped segment. Subsequently, the unclamped segment enabled the computation of the $\tau_{u,Ls}$ parameters. Figures 6.3 to 6.10 depict the curves computed for the studied short and long span laboratory specimens; the figures also include the definition of the different segments. The curves were generated for the $F_{u,max}$ maximum load that is described in more detail in section 6.3.

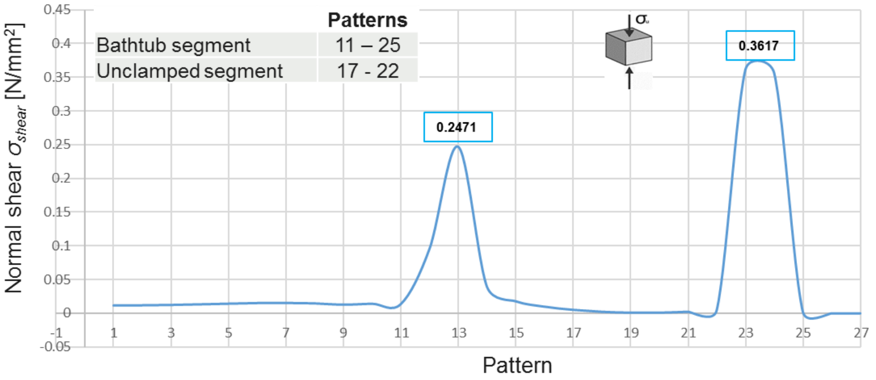

Figure 6.3 *Normal vertical stress distribution σ_{shear} at $F_{u,max}$, INCO70 short span*

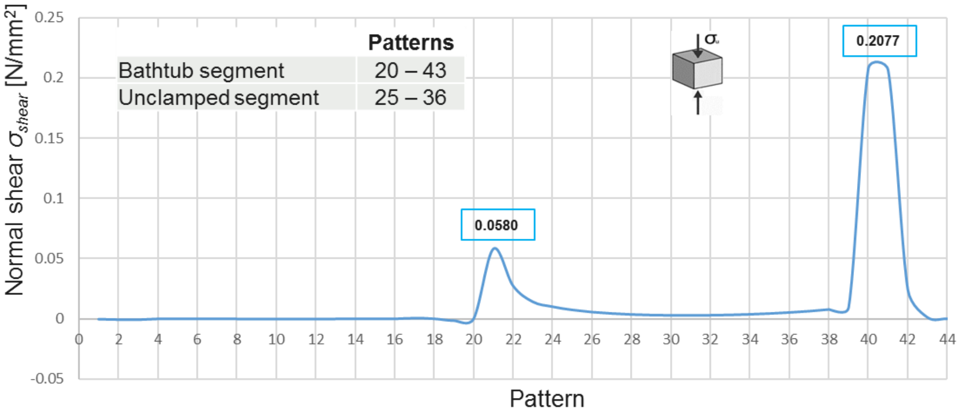

Figure 6.4 *Normal vertical stress distribution σ_{shear} at $F_{u,max}$, INCO70 long span*

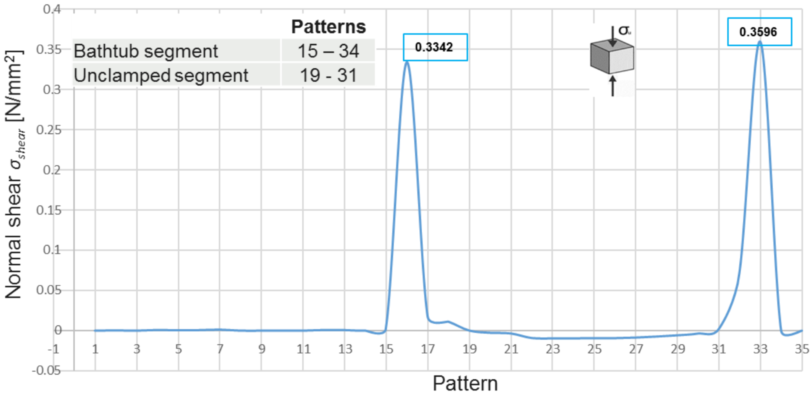

Figure 6.5 *Normal vertical stress distribution σ_{shear} at $F_{u,max}$, C60 short span*

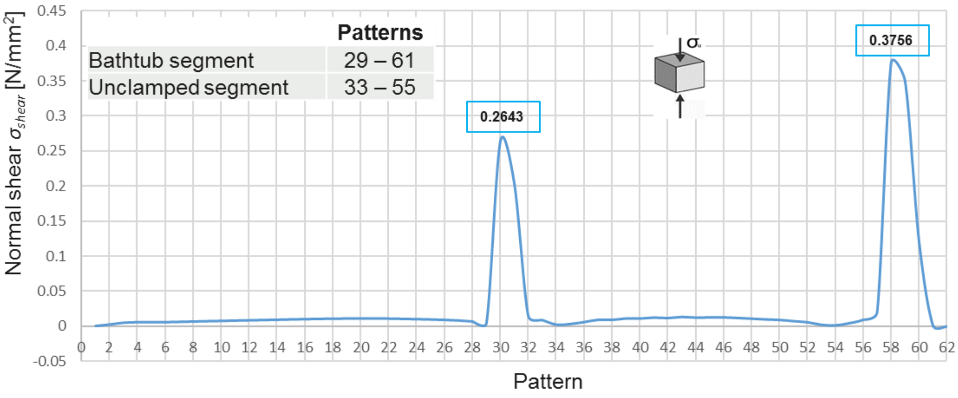

Figure 6.6 *Normal vertical stress distribution σ_{shear} at $F_{u,max}$, C60 long span*

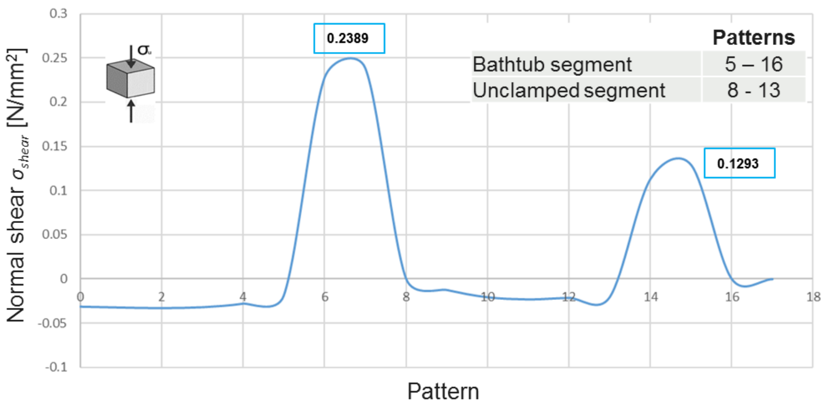

Figure 6.7 *Normal vertical stress distribution σ_{shear} at $F_{u,max}$, QL60 short span*

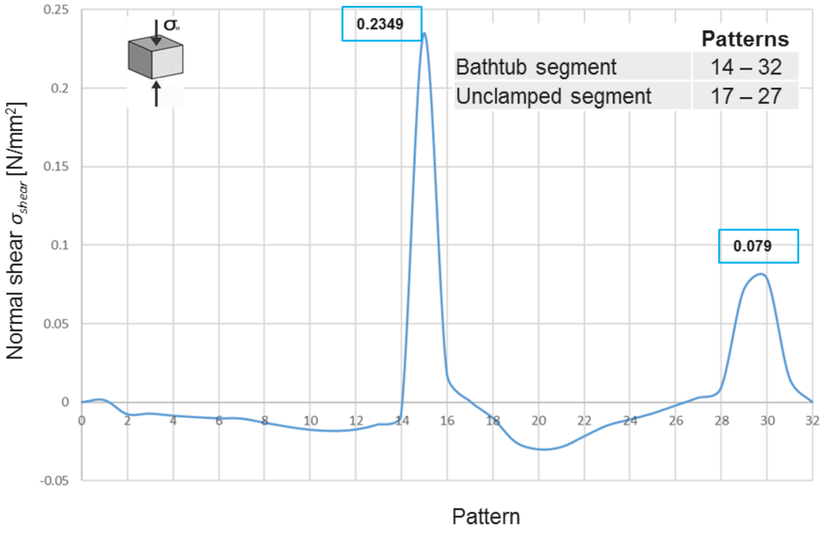

Figure 6.8 *Normal vertical stress distribution σ_{shear} at $F_{u,max}$, QL60 long span*

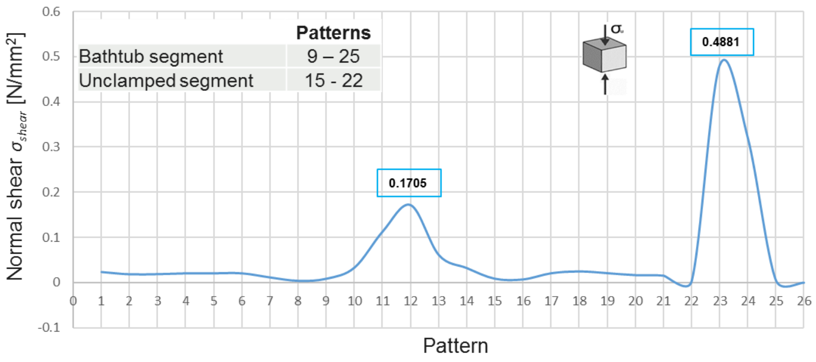

Figure 6.9 *Normal vertical stress distribution σ_{shear} at $F_{u,max}$, T80 short span*

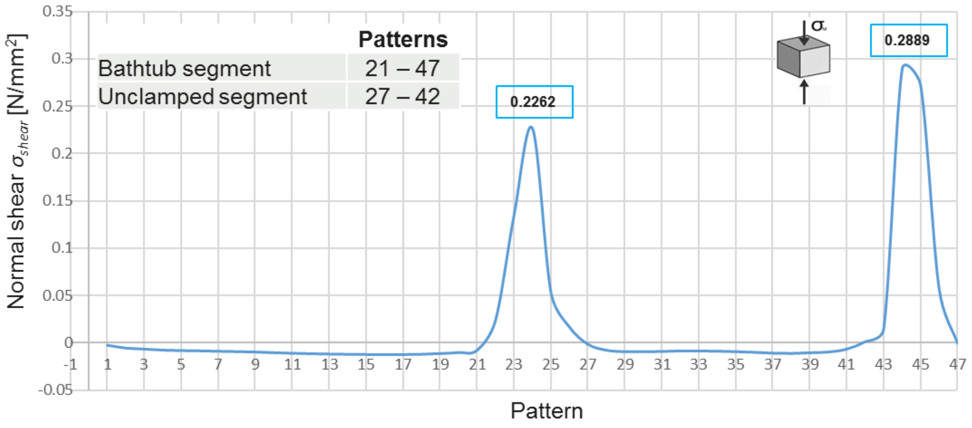

Figure 6.10 *Normal vertical stress distribution σ_{shear} at $F_{u,max}$, T80 long span*

Table 6.1 summarizes the unclamped lengths based on the different σ_{shear} curves computed. The lengths did not correlate among them when compared with their respective shear span length L_s. For some cases, such as the steel deck INCO70, there was a significant difference between the 318 mm computed and the 600 mm for L_s. Oppositely, steel deck QL60 computed a comparable value of 494 mm compared with a L_s of 625 mm.

	FE model span	Unclamped segment [pattern]	Width pattern [mm]	Unclamped segment length [mm]	L_s shear span [mm]
INCO70	short	17 - 22	53	318	600
	long	25 - 36		636	1,250
C60	short	19 - 31	38	494	625
	long	33 - 55		874	1,075
QL60	short	8 - 13	75	450	600
	long	17 - 27		825	1,150
T80	short	15 - 22	50	400	600
	long	27 - 42		800	1,200

Table 6.1 *Length unclamped segments*

Aside of the definition of the different unclamped segments, the σ_{shear} curves also highlighted the different behaviours for open and re-entrant rib steel decks. The C60 profile, with 90-degree vertical sides and with potential to be classified as either open or re-entrant rib, showed a slightly larger concentration of normal stresses at the unclamped segments. See Figures 6.7 and 6.8. The deformation at the steel deck, due to the clamping phenomenon, not only generated the phenomenon of stresses concentration at the point load and support patterns, but it was continued along the rib in some additional patterns at the unclamped segments. The steel deck deformation enhanced the mechanism to constrain the vertical disconnection between the steel deck and the concrete slab.

The σ_{shear} curves also reported different shapes among the open rib steel deck profiles. The INCO70 and C60 curves highlighted a sharp and narrow stress concentrations while at the T80 simulation the clamped segments were wider and with higher stress values. The wider clamped segments observed for the T80 steel deck were in strong agreement with the laboratory specimens shear bond performance: the laboratory test results reported the largest V_t for the T80 specimens, see Table 4.19, once compared with the rest of the steel deck profiles under study.

6.3. τ_u, curves under different loading conditions

The longitudinal shear strength τ_u curves from all the composite slabs studied were computed from the simulations. Figures 6.11 to 6.26 illustrate the τ_u representation for the $F_{u,max}$ maximum load and also for a new $F_{u,max/2}$ load case. The representation of two different loads in each simulation allowed to plot the evolution of the τ_u curves under different external loads. Based on the definition of the unclamped segment from Table 6.1, values for $\tau_{u,Ls}$ were computed and combined with the representation of the stress concentration values at the point load and support patterns. The figures also include the load -midspan deflection representation from each simulation and laboratory test with the values of $F_{u,max}$ and $F_{u,max/2}$ highlighted.

INCO70 numerical simulations

The $\tau_{u,Ls}$ value computed for the $F_{u,max/2}$ load reported a 54% relationship with the $\tau_{u,Ls}$ for the $F_{u,max}$ load at the short span INCO70_S_CI specimen. Thus, a strong alignment was found between the two load cases and the longitudinal shear strength performance. See Figure 6.11.

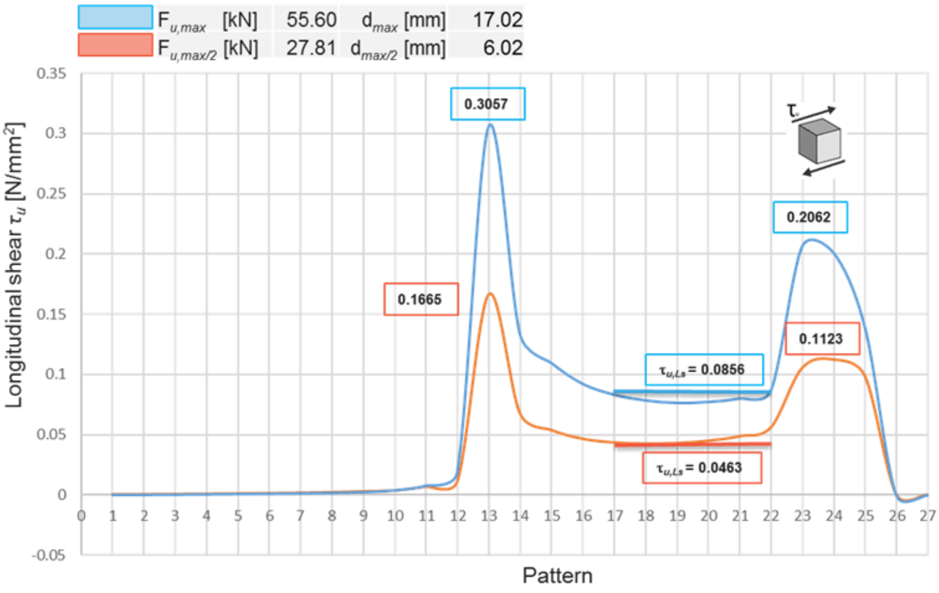

Figure 6.11 *Longitudinal shear strength τ_u, $F_{u,max}$ and $F_{u,max/2}$, INCO70 short span*

The similitude between the relationship and loads was significant for this case. The simulation also presented a strong agreement with the laboratory specimen for the load-midspan deflection curve as it can be inferred from Figure 6.12.

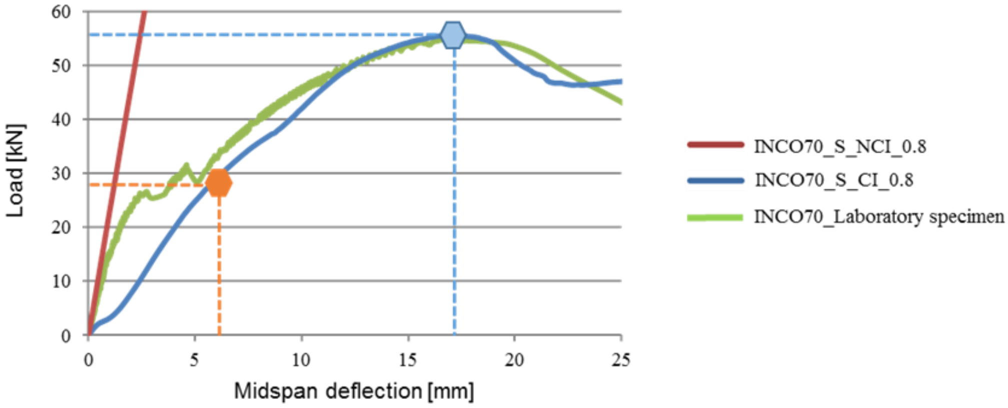

Figure 6.12 *Load-midspan deflection curves for INCO 70, short span*

Figure 6.13 illustrates the τ_u curves computed for the long span FE model INCO70_L_CI. The $\tau_{u,Ls}$ values for $F_{u,max}$ and $F_{u,max/2}$ reported a broader difference once compared with the ones observed at the short span simulations. Concretely, $\tau_{u,Ls}$ value at the $F_{u,max/2}$ load reported a 27.91% relationship when compared with the $\tau_{u,Ls}$ value for $F_{u,max}$. Similar to the short span simulations, the INCO70_L_CI model also presented an strong agreement at the load-midspan deflection between the simulation and the laboratory specimen. See Figure 6.14.

The observation of different relationship for the $\tau_{u,Ls\_Fu,max}$ and $\tau_{u,Ls\_Fu,max/2}$ at the long span simulation provided an intial guidance that the averaged longitudinal shear strength $\tau_{u,Ls}$ parameter alone could not suffice to represent the actual composite slab shear resistance. The computed τ_u curves indicated significant differences at the "bathtub" shape beyond the $\tau_{u,Ls}$ values, especially for the peak stresses at the support and point load patterns as captured in Figure 6.13.

🟦	$F_{u,max}$ [kN]	21.98	d_{max} [mm]	51.40
🟥	$F_{u,max/2}$ [kN]	10.99	$d_{max/2}$ [mm]	16.53

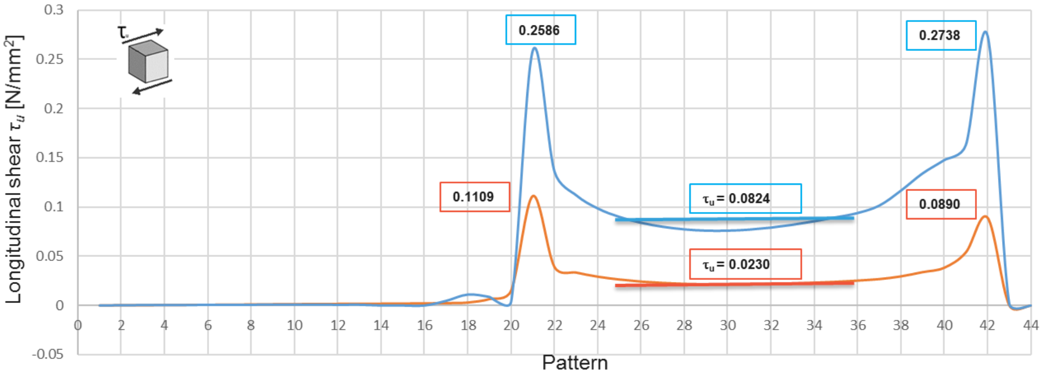

Figure 6.13 *Longitudinal shear strength τ_u, $F_{u,max}$ and $F_{u,max/2}$, INCO70 long span*

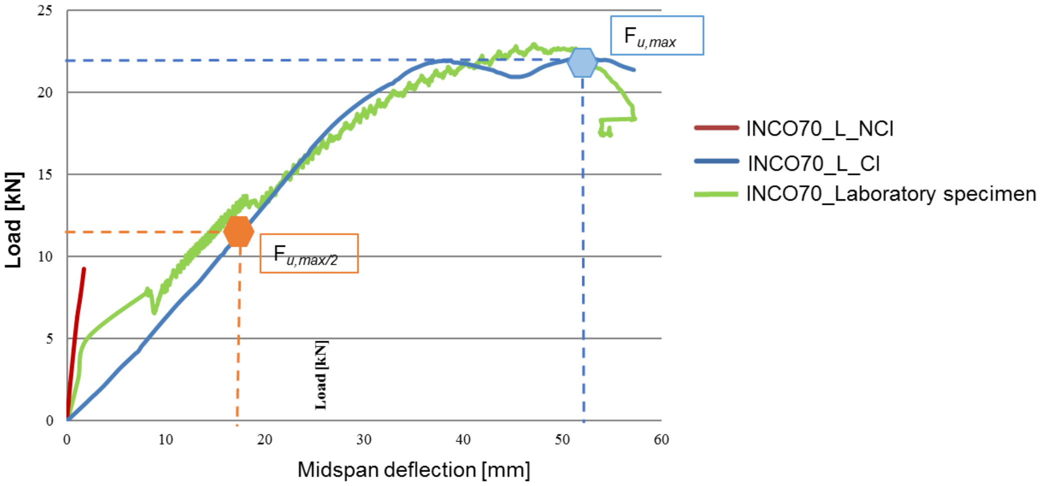

Figure 6.14 *Load-midspan deflection curves for INCO 70, long span*

C60 numerical simulations

Exceptionally, the C60 short span laboratory specimens presented an overall depth h_t = 100 mm for the composite slab while all other specimens, both long and short spans were h_t =180 mm. The process to model and compute the longitudinal shear strength τ_u was common for all the simulations performed. Yet, the concrete slab contribution for the C60 short span laboratory specimens was expected to be different due to the differences in h_t.

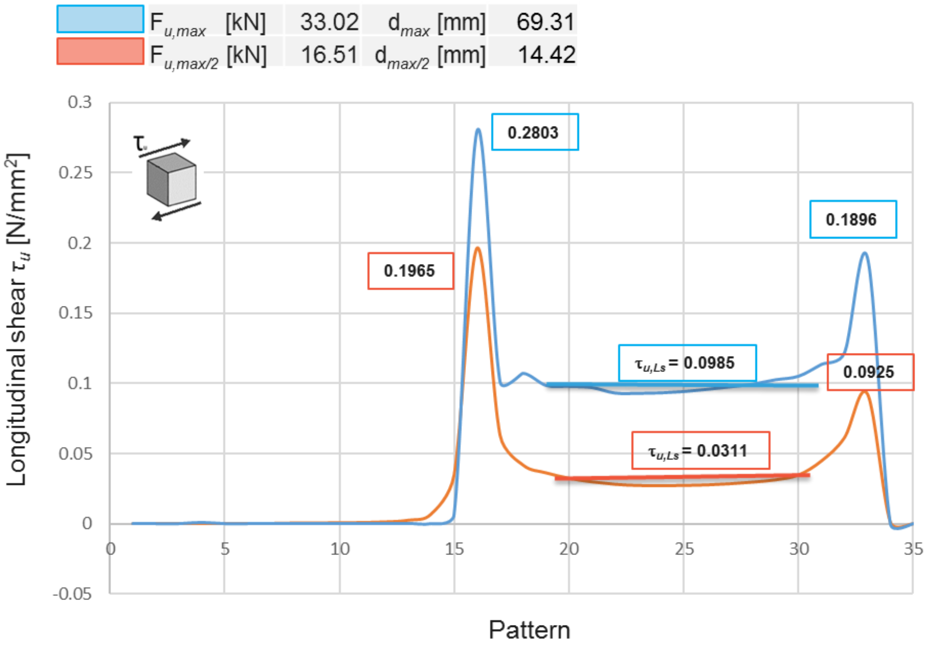

🟦	$F_{u,max}$ [kN]	33.02	d_{max} [mm]	69.31
🟥	$F_{u,max/2}$ [kN]	16.51	$d_{max/2}$ [mm]	14.42

Figure 6.15 *Longitudinal shear strength τ_u,$F_{u,max}$ and $F_{u,max/2}$, C60 short span*

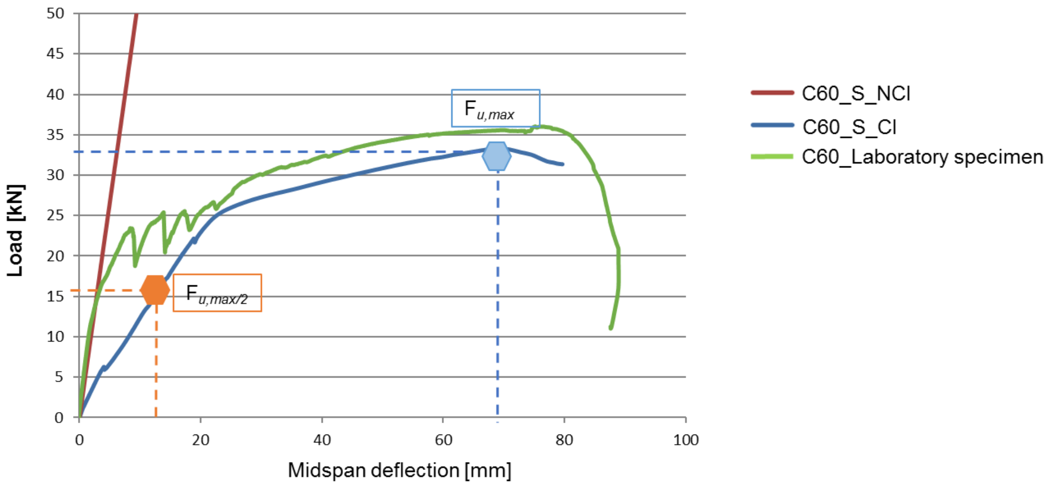

Figure 6.16 *Load-midspan deflection curves for C60, short span*

The $\tau_{u,Ls}$ value computed at the C60 short span simulation for the $F_{u,max/2}$ load reported a 32% relationship with the $\tau_{u,Ls}$ for the $F_{u,max}$ load. Aside of the notion previously introduced that $\tau_{u,Ls}$ did not correlated linearly with the F_u loads due to the "bathtub" shape, the C60 simuation presented an additional factor. The $F_{u,max}$ load was observed at 69.31 mm deflection while the $F_{u,max/2}$ load reported a value of 14.42 mm. See Figure 6.16. The representation indicated that not only the load but also the midspan deflection affected the computation of $\tau_{u,Ls}$ and the overall shear bond characterization. Oppositely, the C60 long span studies reported a 50% relationship between $F_{u,max}$ and $F_{u,max/2}$ for $\tau_{u,Ls}$. The midspan deflections also reported a rough 50% difference as can be observed in Figure 6.17.

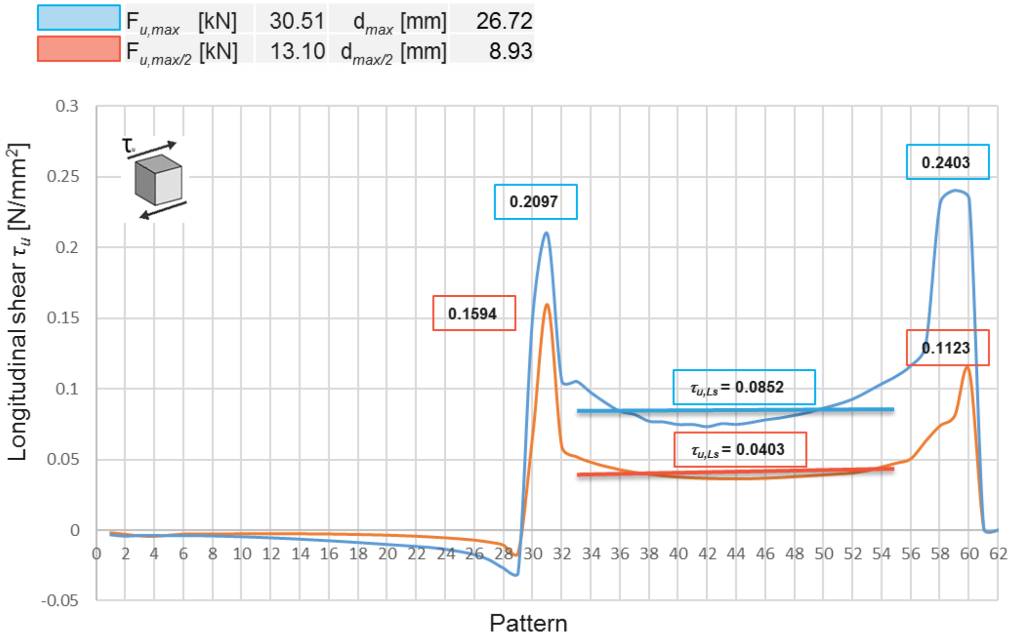

🟦	$F_{u,max}$ [kN]	30.51	d_{max} [mm]	26.72
🟥	$F_{u,max/2}$ [kN]	13.10	$d_{max/2}$ [mm]	8.93

Figure 6.17 *Longitudinal shear strength τ_u,$F_{u,max}$ and $F_{u,max/2}$, C60 long span*

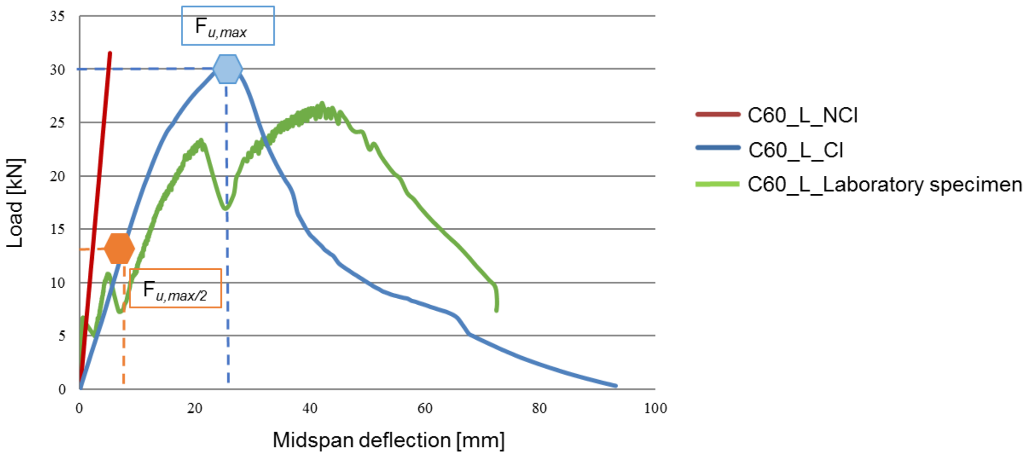

Figure 6.18 *Load-midspan deflection curves for C60, long span*

QL60 numerical simulations

The $\tau_{u,Ls}$ value computed for the QL60 simulations mirrored some of the behaviours previously observed. The $\tau_{u,Ls}$ relationship computed for both short and long spans were close to 40% with midspan deflections really close to a 50% relationship for $F_{u,max}$ and $F_{u,max/2}$. The τ_u curves observed a wider clamped segment at the $F_{u,max}$ load, in alignment with the σ_{shear} curve previously introduced in Figures 6.7 and 6.8.

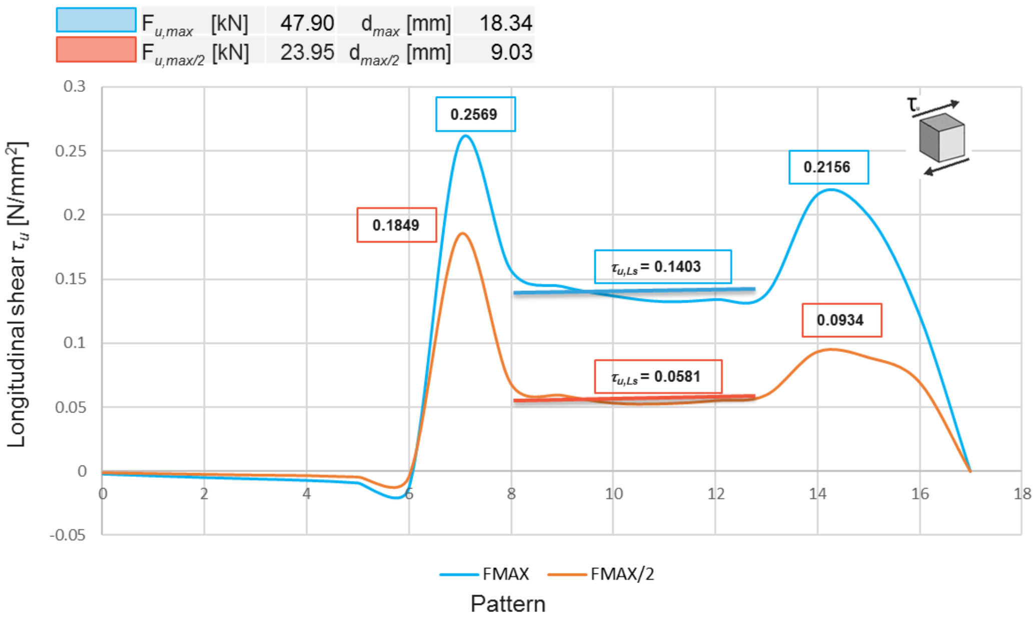

Figure 6.19 *Longitudinal shear strength* τ_u,$F_{u,max}$ *and* $F_{u,max/2}$, *QL60 short span*

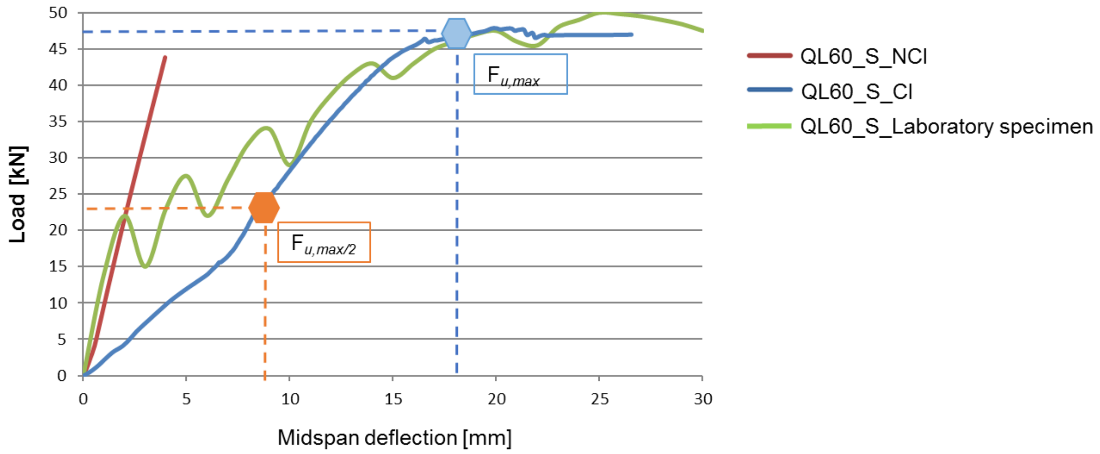

Figure 6.20 *Load-midspan deflection curves for QL60, short span*

The load- midspan deflection curve computed for the QL60_L_CI model presented a strong agreement with the laboratory specimen results for $F_{u,max}$. However, a noticeable difference was observed at the midspan deflection where $F_{u,max}$ was achieved. The simulation reported a value of 26.72 mm while the laboratory specimen was 41.25 mm. See Figure 6.22.

🟦	$F_{u,max}$ [kN]	26.19	d_{max} [mm]	28.42
🟥	$F_{u,max/2}$ [kN]	13.10	$d_{max/2}$ [mm]	14.44

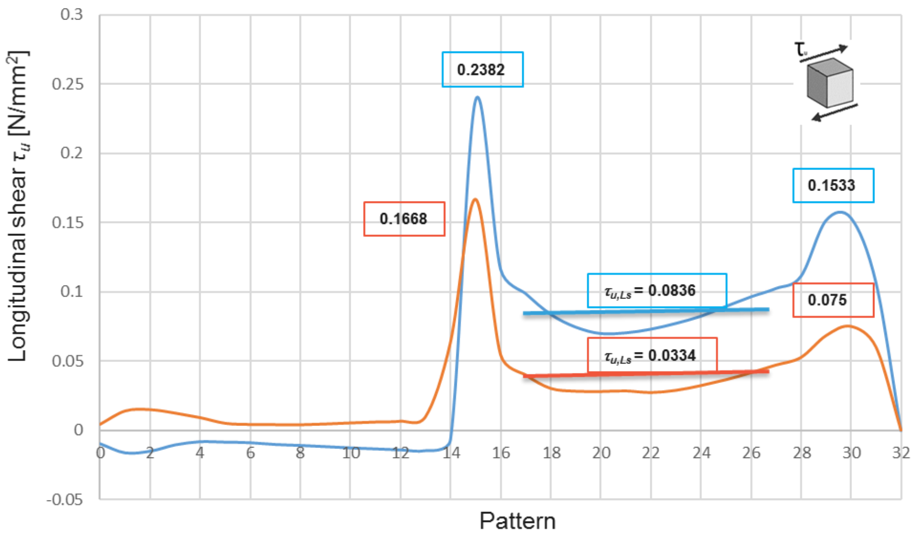

Figure 6.21 *Longitudinal shear strength* τ_u*,* $F_{u,max}$ *and* $F_{u,max/2}$*, QL60 long span*

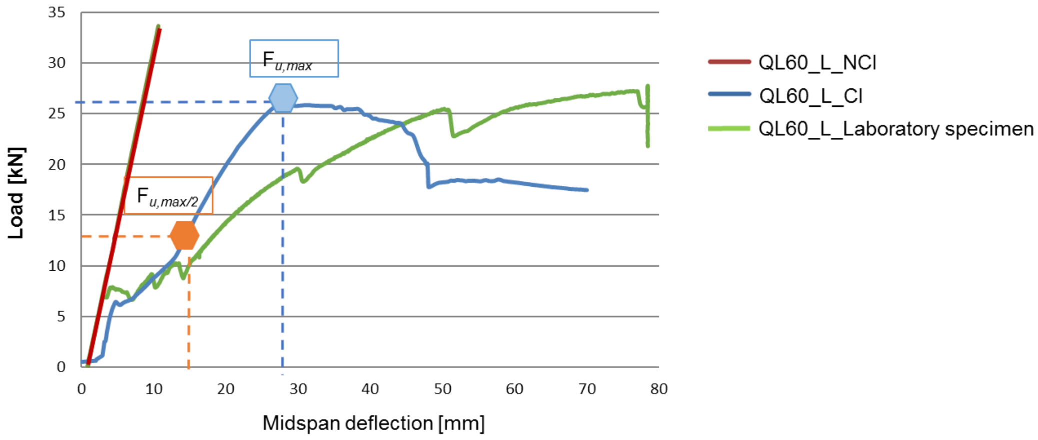

Figure 6.22 *Load-midspan deflection curves for QL60, long span*

T80 numerical simulations

The relationship among $F_{u,max}$ and $F_{u,max/2}$ computed for the $\tau_{u,Ls}$ parameter at the T80 simulations reported 54.87% and 45.73% for the short and long spans respectively. The τ_u curves at the long span simulation observed significant larger peak values at the clamped segments in comparison with previsou simulations. Also, the width at the clamped segments for the short span was noticiable as embraced four patterns with high stress values.

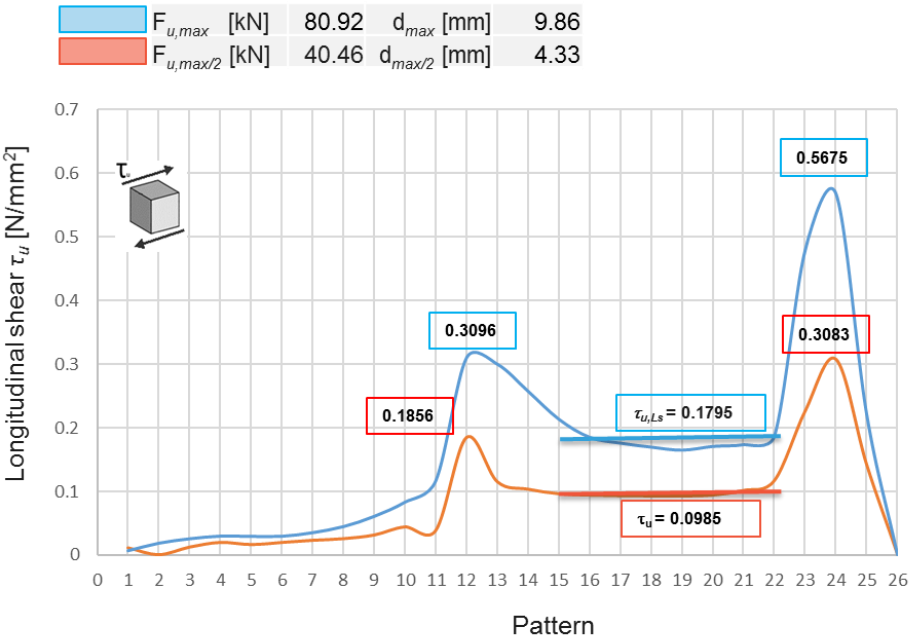

Figure 6.23 *Longitudinal shear strength τ_u, $F_{u,max}$ and $F_{u,max/2}$, T80 short span*

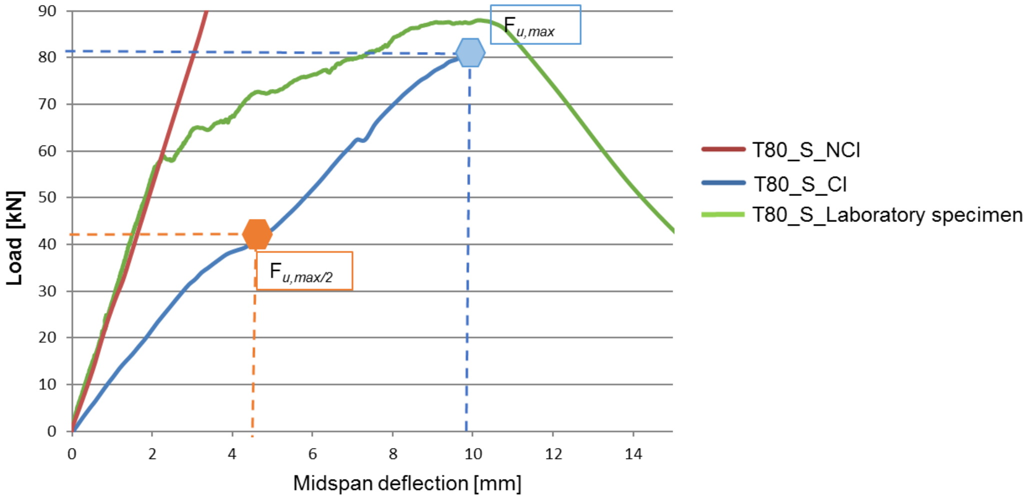

Figure 6.24 *Load-midspan deflection curves for T80, short span*

🟦	$F_{u,max}$ [kN]	44.56	d_{max} [mm]	87.53
🟥	$F_{u,max/2}$ [kN]	22.28	$d_{max/2}$ [mm]	20.41

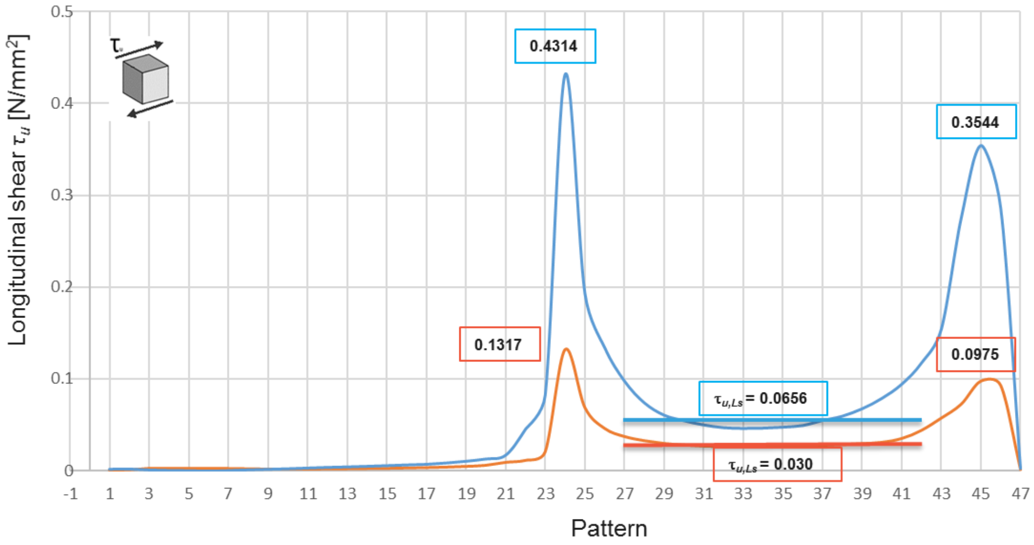

Figure 6.25 *Longitudinal shear strength τ_u, $F_{u,max}$ and $F_{u,max/2}$, T80 long span*

The T80 long span laboratory specimen $F_{u,max}$ was characterized based on the observation a maximum midspan deflection of *L/50* as the rupture load was not observed previously.

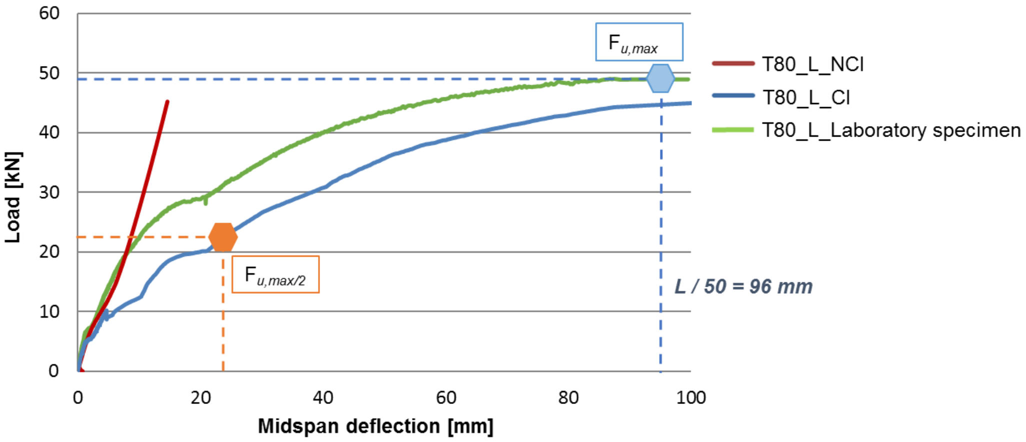

Figure 6.26 *Load-midspan deflection curves for T80, long span*

Composite performance characterization

Tables 6.2 and 6.3 summarize the values computed for $\tau_{u,Ls}$ for all the numerical simulations developed. The stress values computed at the point load and support patterns were also included, in combination with the maximum loads observed both at the FE model $F_{u,max}$ and at the laboratory tests $V_{t.}$ The largest value in each column is highlighted in bold. The T80 simulation for the short span reported the highest value for the $\tau_{u,Ls}$ parameter, *stress at point load, stress at support* and $F_{u,max}$ indicating the best longitudinal shear performance among all the steel deck profiles studied. The performance was in strong agreement with the V_t reported from the laboratory results and in which the building codes *m-k* and PCM based their implementation. Hence, the T80 steel deck profile was the most efficient composite slab which was also captured from the computation of the $\tau_{u,Ls}$ parameter at the numerical simulations for the short span specimens.

Yet, the $\tau_{u,Ls}$ values computed for the rest of the short span simulations did not align completely with the actual V_t laboratory test results. The failure load V_t reported INCO70, QL60 and lastly C60 as the sequence for the best-to-worst composite slab performance. On the contrary, the $\tau_{u,Ls}$ values provided the sequence QL60, C60 and INCO70 when considering longitudinal shear performance. The C60 short span results were not compared as the overall depth from the laboratory specimen and the FE model was h_t = 100 mm, as opposed to h_t = 180 mm from all the rest of simulations and specimens.

A similar behaviour was observed at the long span simulations, in which the $\tau_{u,Ls}$ values did not sequence equally the longitudinal shear performance from the composite slabs once compated with the V_t labotatory results. The numerical simulations reported QL60, INCO70, C60 and lastly T80 as the sequence for the best-to-worst composite slab performance.

Short span specimens	$\tau_{u,Ls}$ [N/mm^2]	Stress at point load [N/mm^2]	Stress at support [N/mm^2]	$F_{u,max}$ FE model [kN]	$F_{u,max}$ (V_t) lab. specimen [kN]
INCO70	0.0856	0.3057	0.2062	55.60	55.13
C60	0.0985	0.2803	0.1896	32.02	33.06
T80	**0.1795**	**0.3096**	**0.5675**	**80.92**	**88.10**
QL60	0.1403	0.2569	0.2156	47.9	50.01

Table 6.2 *Computed $\tau_{u,Ls}$ for all short span laboratory specimens*

Long span specimens	$\tau_{u,Ls}$ [N/mm^2]	Stress at point load [N/mm^2]	Stress at support [N/mm^2]	$F_{u,max}$ FE model [kN]	$F_{u,max}$ (V_t) lab. specimen [kN]
INCO70	0.0824	0.2586	0.2738	21.98	23.05
C60	0.0730	0.2655	0.1830	30.51	26.14
T80	0.0656	**0.4314**	**0.3544**	**44.56**	**49.50**
QL60	**0.0836**	0.2382	0.1533	26.19	27.55

Table 6.3 *Computed $\tau_{u,Ls}$ for all long span laboratory specimens*

In a similar framework, the T80 steel deck also observed the largest difference at the $\tau_{u,Ls}$ values between the short and long specimen with a 21.78% relationship. See Table 6.4. On the contrary, a 59.59% relationship was computed for the QL60 profile as the value with the closest agreement.

	$\tau_{u,Ls}$ short span [N/mm^2]	$\tau_{u,Ls}$ long span [N/mm^2]	$\tau_{u,Ls}$ $\frac{\text{long span}}{\text{short span}}$ %
INCO70	0.0856	0.0824	96.26%
C60	0.0985	0.0730	-
T80	0.1795	0.0656	36.54%
QL60	0.1403	0.0836	59.59%

Table 6.4 *Comparison between Zu,L short and long span simulations*

The results indicated two novel shear bond findings: first, a constant longitudinal shear strength $\tau_{u,Ls}$ computed for each simulation was not capable to characterize alone the shear bond performance observed at the laboratory tests. The influence from the stresses at the clamped areas was significant and must be considered. Second, it was not possible to define a universal relationship for $\tau_{u,Ls}$ between the short and long span groups as the composite performance showed significant variability among the different composite slab studied.

Consequently, the development of numerical simulations must consider different lengths, mirroring the different building codes requirements. Eurocode 4 requires the testing of at least two different lengths and multiple specimens for each length to subsequently deploy the design methods *m-k* and PCM. See sections 2.4.1 and 2.4.2. Additionally, the shear resistance characterization required not only the computation of $\tau_{u,Ls}$ but also a complete understanding of the "bathtub" curve. Both requirements are addressable through FE modeling with almost no cost and without the need to perform laboratory tests.

$\tau_{u,Ls}$ and $\tau_{u,Eurocode4\_PCM}$ discussion

The perfect bond behaviour in composite slab is achieved when full connection η = 1 exist between the steel deck and the concrete slab at the $F_{u,max}$ maximum load. The perfect bond represented the theoretical maximum shear capacity for the composite slab as the steel deck reached the ultimate yield strength f_{yp}. The comparison of any longitudinal shear strength parameter with the perfect bond provides a quantitatively metric of the shear resistance performance for the composite slab. Figure 6.27 illustrates conceptually the perfect bond distribution and Equations 6.1 and 6.2 capture the key parameters.

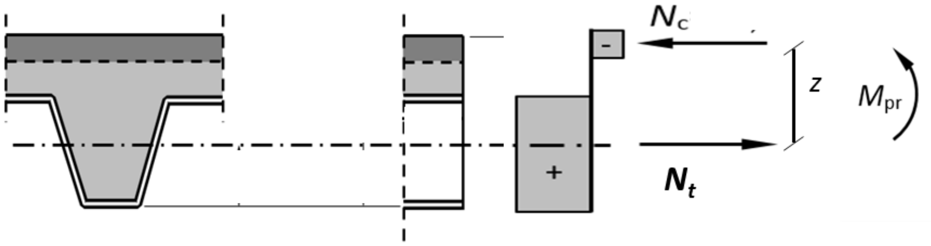

Figure 6.27 *Perfect bond strain distribution*

$$N_c = \frac{A_c \cdot f_{c,k}}{\gamma_c} \tag{6.1}$$

$$N_t = \frac{A_{pe} \cdot f_y}{\gamma_s} \tag{6.2}$$

The perfect bond equilibrium assumed $N_t = N_c$, and subsequently the partial factors were removed to define the perfect bond longitudinal shear strength formula captured in Equation 6.3.

$$\tau_{perfect\ bond} = \frac{N_t}{b \cdot L_s} = \frac{A_{pe} \cdot f_y}{b \cdot L_s} \tag{6.3}$$

where,

A_{pe} effective cross-sectional area of the steel deck profile

The Eurocode 4 PCM design method and the perfect bond longitudinal shear strengths were computed for the C60 laboratory specimens, in addition to the INCO70 case previously presented in section 5.1.2. Equation 5.5 was deployed to characterize the PCM design method, as it removed from the τ_u the effect from the friction at the support, similar to the concept of $\tau_{u,Ls}$. Tables 6.5 and 6.6 capture the results computed for both cases and introduce the relationships between $\tau_{u,Ls}$, $\tau_{u,PCM}$ and $\tau_{perfect\_bond}$.

	$\tau_{u,Ls}$ [N/mm^2]	$\tau_{u,EC4\_PCM}$ [N/mm^2]	$\tau_{perfect\ bond}$ [N/mm^2]	$\frac{\tau u,Ls}{\tau u,EC4\_PCM}$ %	$\frac{\tau u,Ls}{\tau u\ perfect\ bond}$ %	L_s [mm]
INCO70	0.0856	0.2120	0.5410	40.37%	15.82%	600
C60	0.0985	0.2350	0.4685	41.91%	21.02%	625

Tale 6.5 *Comparison longitudinal shear strengths at $F_{u,max}$, short span slabs*

	$\tau_{u,Ls}$ [N/mm^2]	$\tau_{u,EC4\_PCM}$ [N/mm^2]	$\tau_{perfect\ bond}$ [N/mm^2]	$\frac{\tau u,Ls}{\tau u,EC4\_PCM}$ %	$\frac{\tau u,Ls}{\tau u\ perfect\ bond}$ %	L_s [mm]
INCO70	0.0824	0.1367	0.2596	26.65%	14.56%	1,250
C60	0.0730	0.1340	0.2724	54.47%	7.30%	1,075

Tale 6.6 *Comparison longitudinal shear strengths at $F_{u,max}$, long span slabs*

The $\tau_{u,Ls}$ computed from the simulations at the unclamped segments reported always values below the $\tau_{u,PCM}$ from the Eurocode 4 PCM. The relationship varied depending on the laboratory specimen but results reported a window of 26.65 % to 54.47%. Similarly, comparisons were performed with the longitudinal shear strength from the perfect bond $\tau_{perfect\_bond}$ that reported even lower values as expected. Figures 6.28, 6.29 and 6.30 capture visually the different longitudinal shear strength τ_u parameters computed for the INCO70 laboratory specimens and simulations.

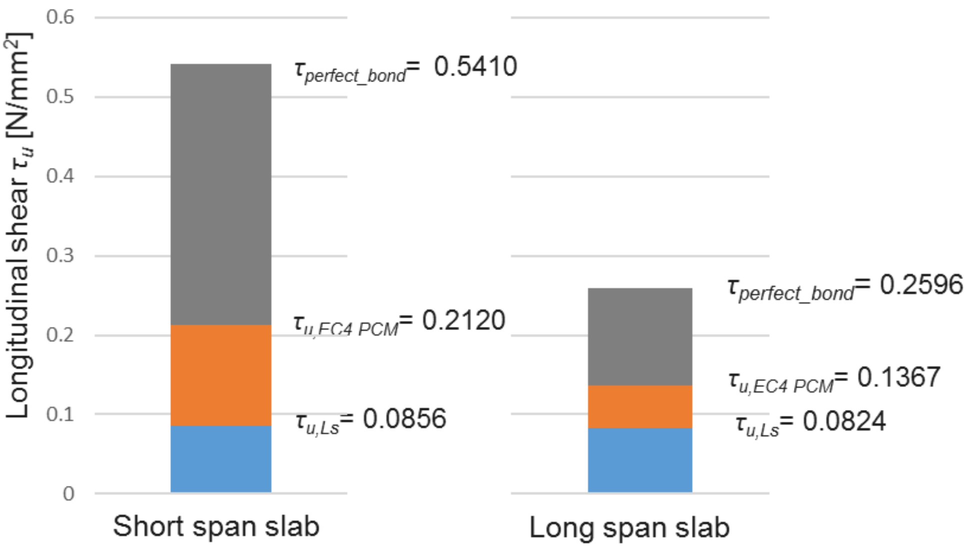

Figure 6.28 *Comparison different longitudinal shear strength τ_u parameters,*

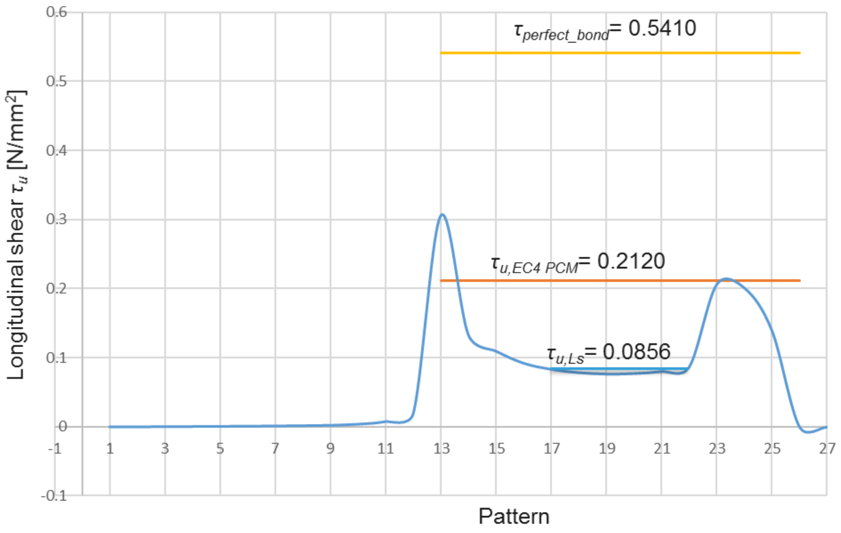

Figure 6.29 *Representation* $\tau_{u,Ls}$, $\tau_{u,\ EC4\_PCM}$ *and* $\tau_{perfect\_bond}$, *INCO70 short span*

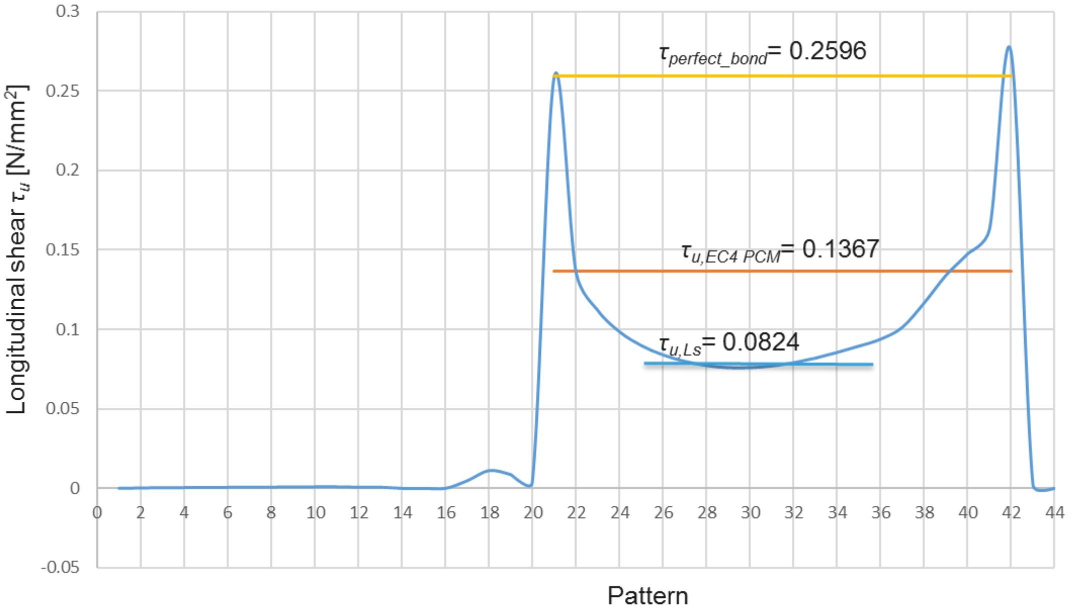

Figure 6.30 *Representation* $\tau_{u,Ls}$, $\tau_{u,\ EC4\_PCM}$ *and* $\tau_{perfect\_bond}$, *INCO70 long span*

Similarly, Figures 6.31, 6.32 and 6.33 capture visually the different longitudinal shear strength τ_u parameters computed for the C60 laboratory specimens and simulations. Both INCO70 and C60 computed curves reported similar behaviours:

- $\tau_{u,Ls}$ was in all the simulations the lowest longitudinal shear strength characterization parameter. The values observed, based on the unclamped segments, represented the span at the composite slab where both a constant longitudinal stress and slip existed.

- $\tau_{u,EC4\_PCM}$ computed values were always higher than $\tau_{u,Ls}$ and conceptually had presence at the full L_s shear span. The values did not exceed the highest stress peak values observed at the τ_u representation from the simulations.
- $\tau_{perfect\_bond}$ was modeled such as a theoretical stress behaviour that is not commonly achieved at the composite slabs. The longitudinal shear stress representation though highlighted the significant differences in τ_u values due to the partial connection as opposed to a full connection.

Eurocode 4 PCM shortcomings

Based on the observation of the different τ_u representations, some limitations from the Eurocode 4 PCM design method are discussed.

- The τ_u curve computed from the simulations highlighted the relevance of the longitudinal shear stress concentrations that occurred at the support and the load point patterns at the segments previously defined as “clamped”. A preliminary conclusion can be reached for the composite characterization: the longitudinal shear strength τ_u needs to consider not only the segment with a constant value, but also the other clamped segments at the shear span. The values for $\tau_{u,Ls}$ and $\tau_{u,EC4\_PCM}$ were computed a very similar $F_{u,max}$ but reported a significant different value. See Tables 6.2 and 6.3.
- The mechanical model at the PCM did not accurately represent the actual composite behaviour for the longitudinal shear strength, but conceptually provided a reasonable approximation: the computed value $\tau_{u,EC4\_PCM}$ ignored any concentration at the support and load point, but the value resided in between $\tau_{u,Ls}$ and the stress peaks observed. Conceptually though, the PCM focus only in one unique $\tau_{u,EC4\_PCM}$ from the laboratory test did not factor the clamping phenomenon originated in some areas, that resulted in important contribution for the shear resistance at the simulations.
- The PCM assumption that the steel and concrete materials reached the ultimate yield capacity f_y and f_{cm} in some areas was inaccurate. Although it supported the simple engineered model to compute $\tau_{u,EC4\_PCM}$, the detailed von Mises representations from the FE models reported only the ultimate yield for the steel deck in some punctual embossment areas. Concretely, at the steel deck embossments with deep frontal contact with the concrete slab.
- The τ_u representation from the simulations suggested a characterization formula for the longitudinal shear strength with two components: one must characterize the constant slip

and stress segment; $\tau_{u,Ls}$ captured that behaviour. The other must characterize the shapes observed at the clamped segments. Equation 6.4 provides an initial attempt to scope a more universal approach to characterize the longitudinal shear strength.

$$\tau_{u,i} = \tau_{u,Ls} + \tau_{u,campling,i} \tag{6.4}$$

where,

$\tau_{u.i}$	longitudinal shear strength at point *i*
$\tau_{u.Ls}$	constant longitudinal shear strength at the unclamped segment
$\tau_{u.campling,i}$	longitudinal shear strength contribution from the clamped segment at point *i* minus $\tau_{u.Ls}$

Equation 6.4 did not provide a practical design formula for composite slab. The characterization for the $\tau_{u,clamping}$ would require the deployment of either complex measurement systems at the laboratory testbeds or the development of the FE modeling. In one hand, new measurements in testbeds would increase the costs and complexity of the already tedious laboratory test and hence were discouraged. On the other hand, the development on numerical simulations provide a much richer characterization of the longitudinal shear strength τ_u and hence provided little incentive to develop a formulation.

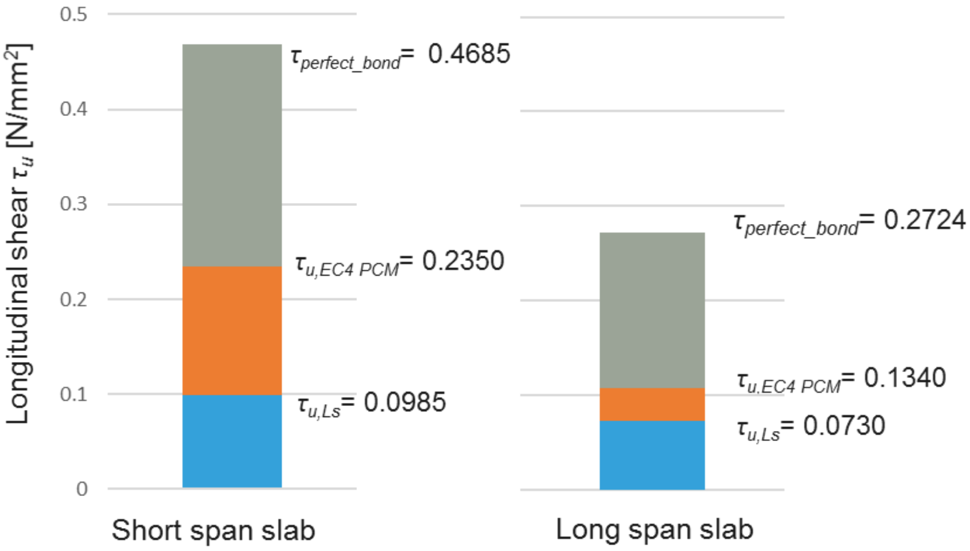

Figure 6.31 *Comparison different longitudinal shear strength τ_u parameters, C60*

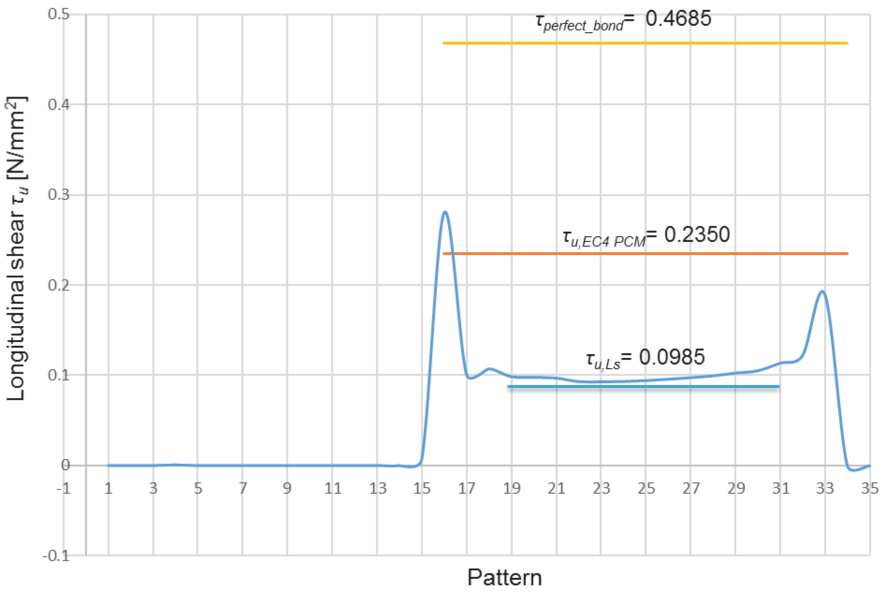

Figure 6.32 *Representation* $\tau_{u,Ls}$, $\tau_{u,\ EC4\_PCM}$ *and* $\tau_{perfect\_bond}$, *C60 short span*

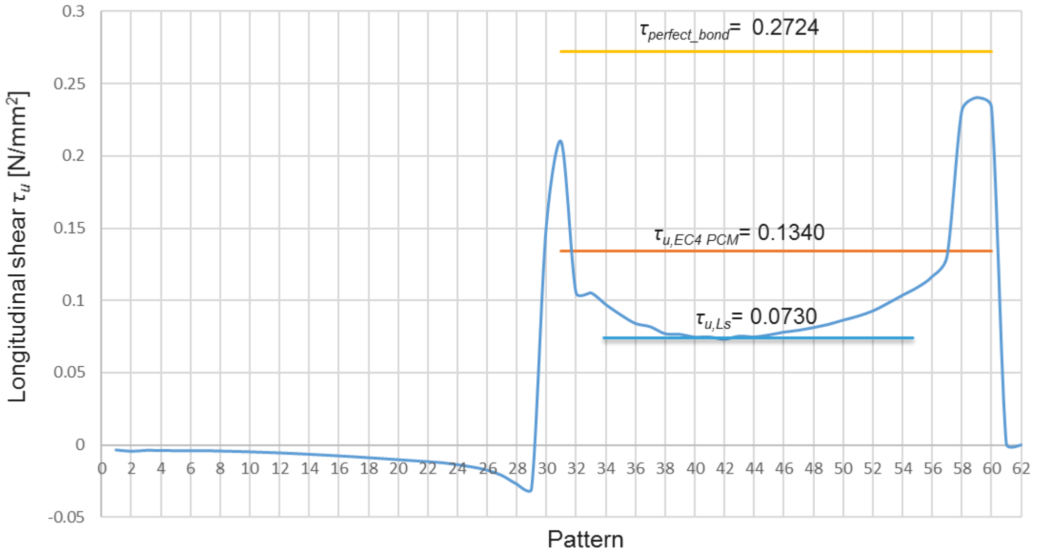

Figure 6.33 *Representation* $\tau_{u,Ls}$, $\tau_{u,\ EC4\_PCM}$ *and* $\tau_{perfect\_bond}$, *C60 long span*

6.4. τ_u curves under different friction coefficients

The definition and development of the different τ_u parameters in previous sections indicated the relevance of the clamped segments for the shear bond characterization. A coefficient friction $\mu = 0.5$ was defined for all the simulations as it reported the most accuracy in modeling the actual laboratory specimens. See section 4.4. This section introduces several simulations performed for different friction coefficients as a vehicle to characterize the clamped segments. The studies focused in the short span laboratory specimens and simulations as their characterization reported more influence for the overall shear bond.

Figure 6.34 illustrates the τ_u curves, $F_{u,max}$ value and the maximum midspan deflections at the INCO70 simulations for $\mu = 0.0$ and $\mu = 0.5$. Both τ_u curves depicted a similar "bathtub" shape, but with significant lower stress values for the $\mu = 0.0$ case: the $\tau_{u,Ls}$ computed was 0.0216 N/mm^2 or 26.68% of the value observed for $\mu = 0.5$. Similarly, the stress peaks values at the support and point load patterns were lower. The $F_{u,max}$ observed for the newly developed $\mu = 0.0$ simulation was 13.07 kN which was lower than the 55.60 kN observed for $\mu = 0.5$.

The plotted curves highlighted two different phenomena: first, the coefficient friction influenced significantly the $\tau_{u,Ls}$ and $F_{u,max}$ values. The same steel deck, under the same boundary conditions, reported lower values for both parameters. Second, the shape and values for the stress peaks at the clamped segments were influenced significantly by the friction coefficient parameter.

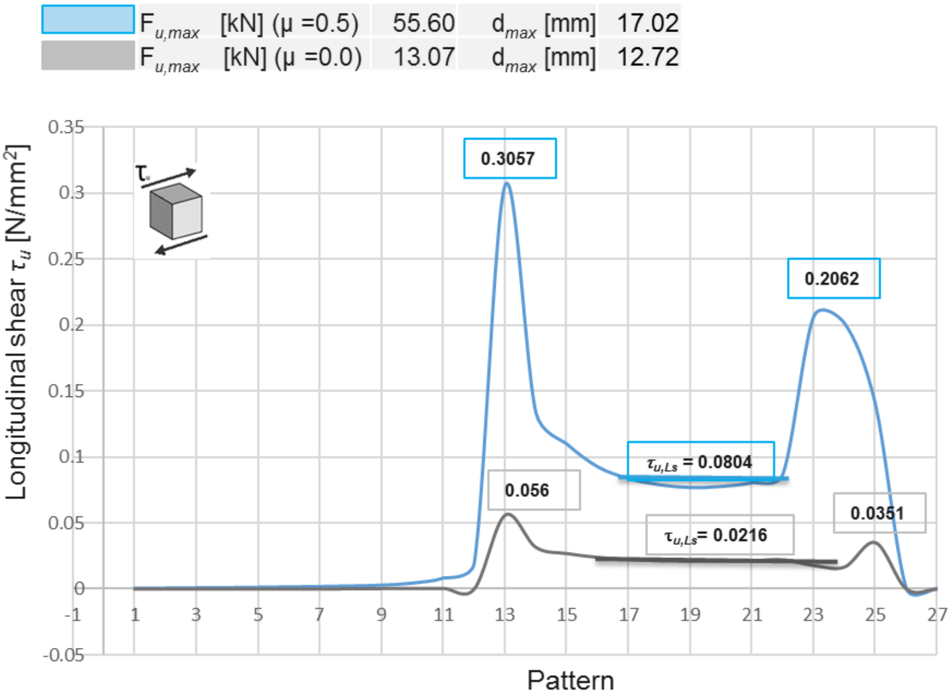

Figure 6.34 *Longitudinal shear strength, INCO70 short span, μ = 0.5 and μ = 0.0*

Figures 6.35, 6.36 and 6.37 illustrate the τ_u curves, the $F_{u,max}$ values and the maximum midspan deflections for the C60, QL60 and T80 simulations for $\mu = 0.0$ and $\mu = 0.5$. Similar to the INCO70 simulations, all the τ_u curves depicted a similar "bathtub" shape, but with significant lower stress values for the μ = 0.0 case: at the QL60 simulation, the $\tau_{u,Ls}$ computed was 0.0421 N/mm^2 or 30.02% of the value observed for μ = 0.5. The T80 simulation reported a $\tau_{u,Ls}$ of 0.0437 N/mm^2 or 24.25% of the value observed for μ = 0.5. A more extreme comparison was observed at the C60 profile, as the $\tau_{u,Ls}$ comparison values computed reported a 8.73% for the FE model with a friction coefficient μ = 0.0. Similarly, the stress peaks values at the support and point load patterns were significantly lower.

The results for $F_{u,max}$ and τ_u from different friction coefficients at the laboratory specimens are difficult to obtain as the steel deck profiles are produced throughout an industrialized process. The numerical simulations for μ = 0.0 were therefore theoretical representations to characterize the shear bond for an extreme case.

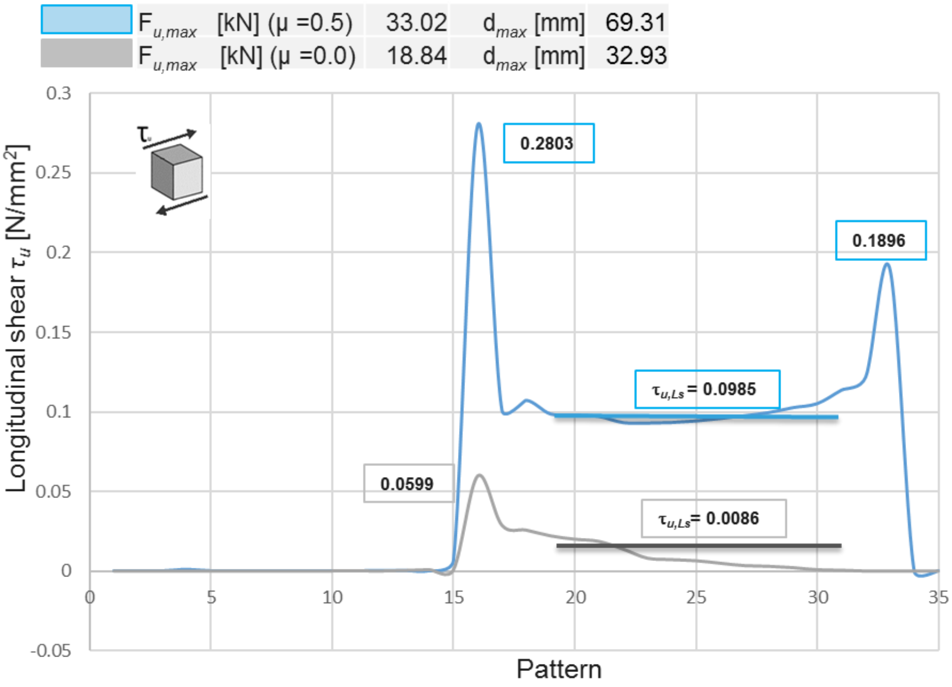

Figure 6.35 *Longitudinal shear strength, C60 short span, μ = 0.5 and μ = 0.0*

🟦	$F_{u,max}$ [kN] (μ =0.5)	47.90	d_{max} [mm]	18.34
▨	$F_{u,max}$ [kN] (μ =0.0)	18.84	d_{max} [mm]	14.12

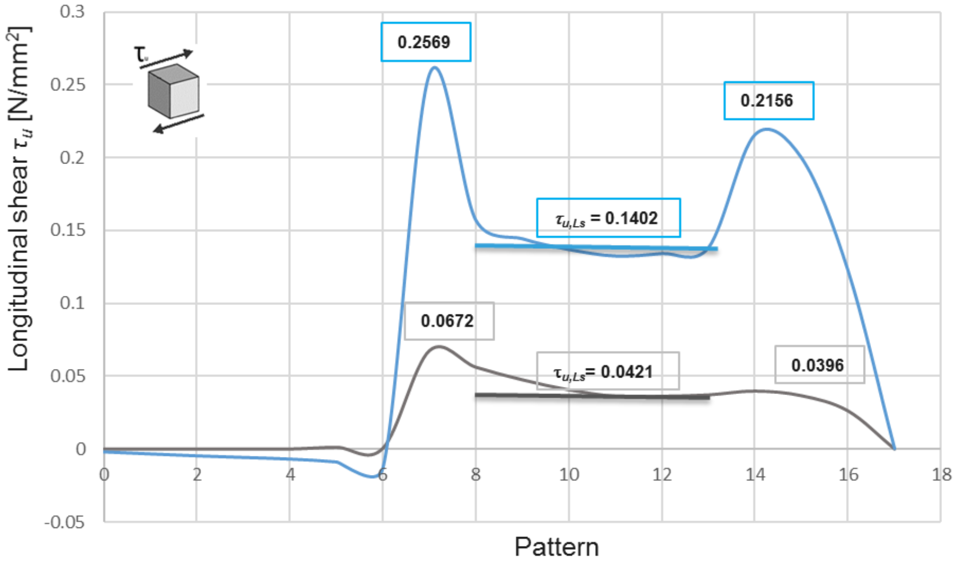

Figure 6.36 *Longitudinal shear strength, QL60 short span, μ = 0.5 and μ = 0.0*

🟦	$F_{u,max}$ [kN] (μ =0.5)	80.92	d_{max} [mm]	9.86
▨	$F_{u,max}$ [kN] (μ =0.0)	23.46	d_{max} [mm]	6.02

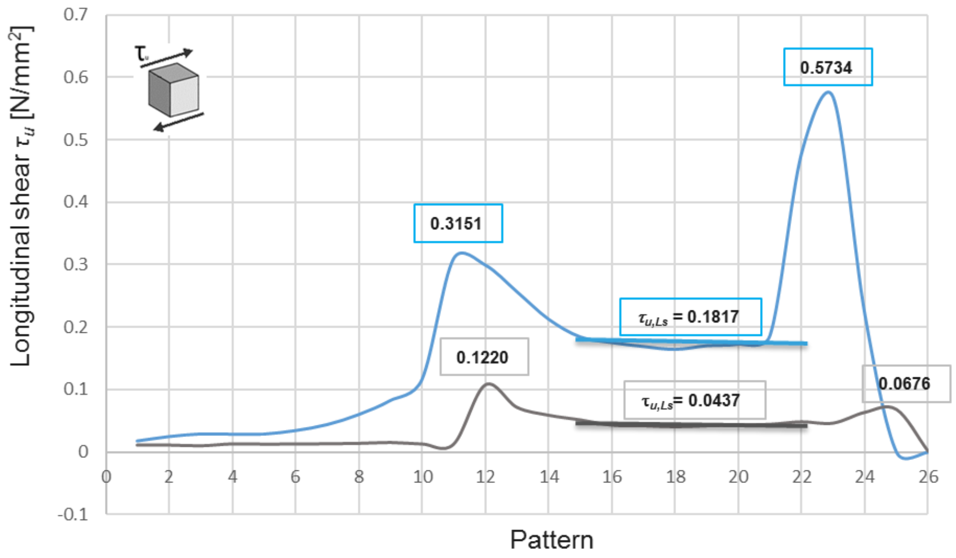

Figure 6.37 *Longitudinal shear strength, T80 short span, μ = 0.5 and μ = 0.0*

6.5. Comparison τ_u curves performance $F_{u,max}$ (μ=0,0)

The simulations developed with the $\mu = 0.0$ friction coefficient enabled a first approach to characterize the composite behaviour at the clamped areas. It was observed that the lower friction coefficients reported lower longitudinal shear strength $\tau_{u,Ls}$ but also lower $F_{u,max}$ and midspan deflections between simulations sharing the same steel deck profile. As the maximum loads $F_{u,max}$ were not equal among each pair of $\mu = 0.0$ - $\mu = 0.5$ simulations, the influence from the friction coefficient was not comparable as it included different loads. This section develops a new group of simulations for the laboratory specimens: first, new FE models were developed with friction coefficients $\mu = 0.3$ and $\mu = 0.8$. In combination with previous FE models developed for $\mu = 0.5$ and $\mu = 0.0$, the simulations provided a broader spectrum of sensitiveness for the friction coefficient. Second, all the $\tau_{u,Ls}$ curves for the simulations were computed for the same F_u load. In particular, the F_u selected was the $F_{u,max}$ for the $\mu = 0.0$ model which could be achieved in all the simulations as it reported the lower load value within the same group of simulations. The $F_{u,max}(\mu = 0.0)$ ensured a comparison of the longitudinal shear strength τ_u under the same load condition for all the models.

Figure 6.38 illustrates the load-midspan deflection behaviours for the different INCO70 short span simulations. The only difference between the models was the definition of the friction coefficient factor μ. As previously observed in Figure 6.34 for $\mu = 0.0$ and $\mu = 0.5$, the new friction coefficient curves also behaved in correspondence with the value of the friction coefficients. The $\mu = 0.8$ simulation reported a $F_{u,max} = 64.16$ kN which was the largest for the group. The $\mu = 0.3$ reported a $F_{u,max} = 29.31$ kN which was characterized in between $\mu = 0.0$ and $\mu = 0.5$ cases. The slope for the load-midspan deflection curves highlighted an important characterization parameter in shear resistance: higher friction coefficients reported a stiffer slope which indicated a larger shear bond for early midspan deflections.

🟩	$F_{u,max}$	[kN] (μ =0.8)	64.16	d	[mm]	13.16
🟦	$F_{u,max}$	[kN] (μ =0.5)	55.64	d	[mm]	17.02
🟨	$F_{u,max}$	[kN] (μ =0.3)	29.31	d	[mm]	20.95
⬜	$F_{u,max}$	[kN] (μ =0.0)	13.07	d_{max}	[mm]	12.72

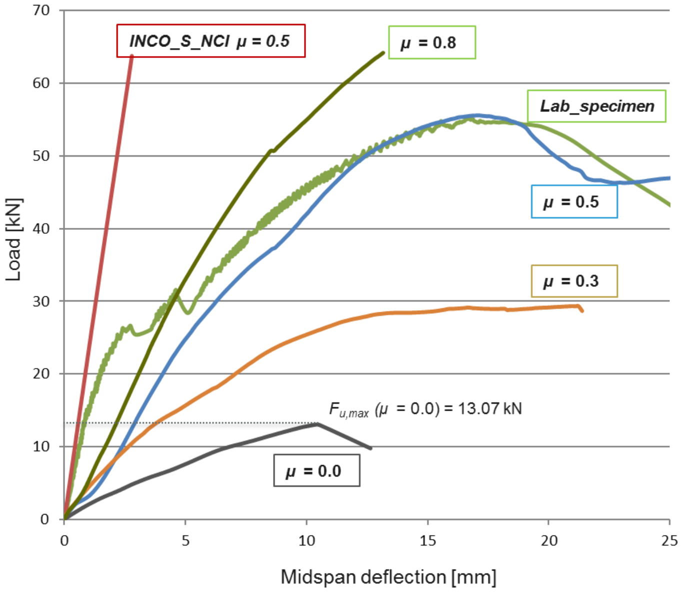

Figure 6.38 *Load-midspan displacements different friction coefficients, INCO70*

Figure 6.39 introduces another novel view for the τ_u representations at the INCO70 short span simulations under the same F_u = 13.07 kN but different friction coefficients. The τ_u “bathtub” shape was observed in all the cases, but the computed $\tau_{u,Ls}$ and peak values at the support and point load were significantly different. The simulation with μ = 0.0 reported the lower $\tau_{u,Ls}$ value at 0.0216 N/mm^2. The rest of the $\tau_{u,Ls}$ values increased as the friction coefficient did. However, the increase among each friction coefficient increase was minimal except for the μ = 0.0 initial case. Another phenomenon observed was the width and peak stress values variation at the clamped areas: higher friction coefficients reported higher peak values at both the support and point load patterns for the INCO70 simulations.

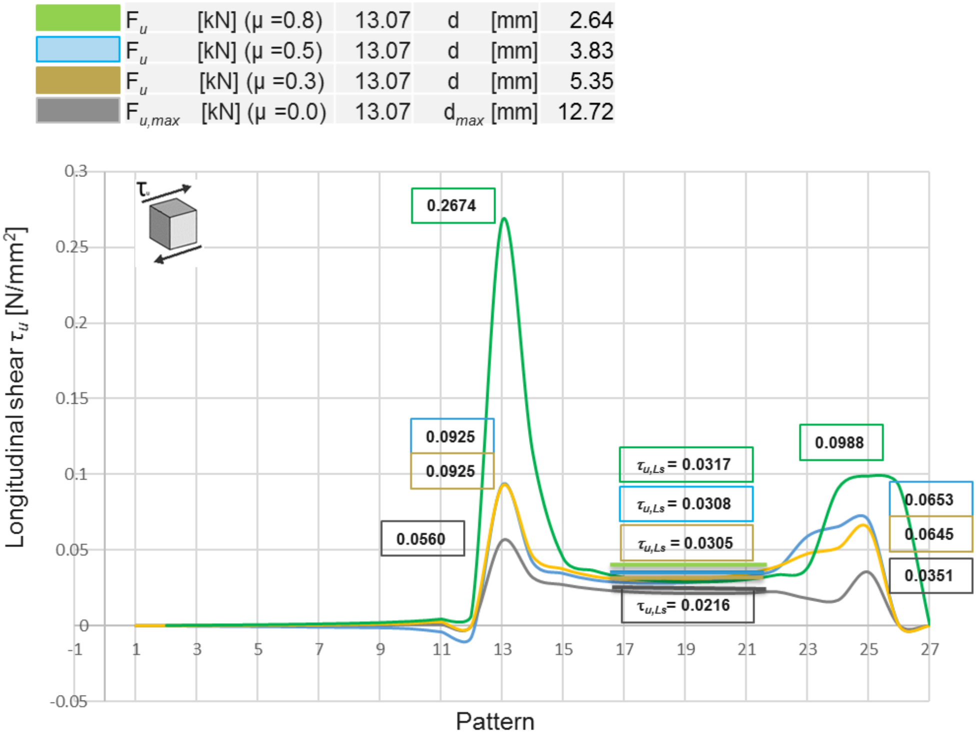

Figure 6.39 *Representation INCO70 short span τ_u curves μ = 0.0, 0.3, 0.5, 0.8 for F_u = $F_{u,max}$(μ=0.0)*

The same study performed for the INCO70 short span laboratory specimens and simulations was performed for the C60, QL60 and T80 FE models. Figures 6.40, 6.42 and 6.44 illustrate the load-midspan deflections curves for the different simulations with friction coefficients μ = 0.0, μ = 0.3, μ = 0.5 and μ = 0.8 and F_u equalized to the respective $F_{u,max}(\mu = 0.0)$. The curves mirrored the behaviours observed at the initial INCO70 simulations in which the increased friction coefficients were translated into stiffer slopes and larger $F_{u,max}$ values. Figures 6.41, 6.43 and 6.44 drawn the computed τ_u representations for each composite slab group and for each friction coefficient. The τ_u “bathtub” shape was observed in all the steel decks and friction coefficient simulations with μ = 0.0 always reported the lower $\tau_{u,Ls}$ value. The sensitiveness of the different FE model in front of the friction coefficient was similar: all the simulations reported an increased $\tau_{u,Ls}$ value as the μ coefficient friction increased. Similarly, the width and peak values at the clamped segments increase as the friction coefficient did.

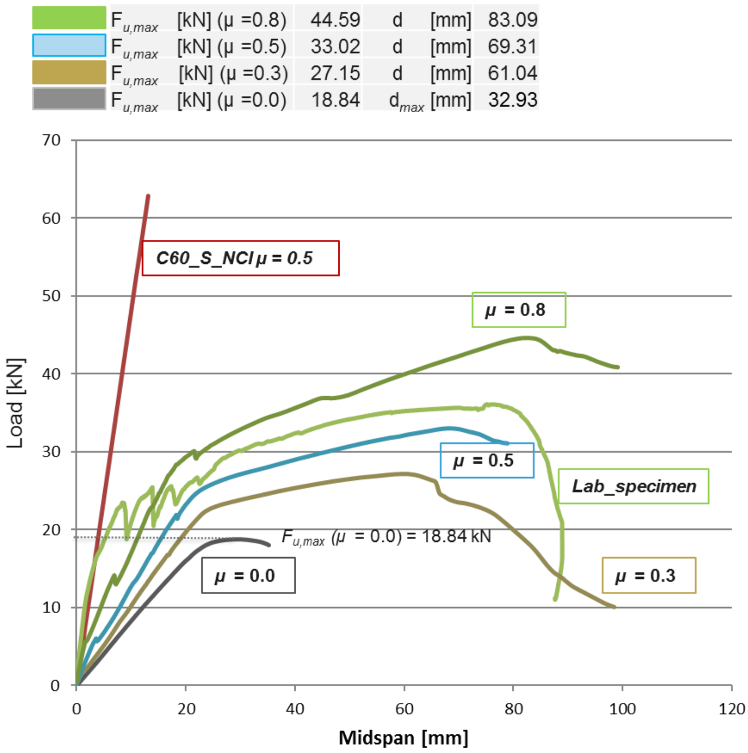

Figure 6.40 *Load-midspan displacements different friction coefficients, C60*

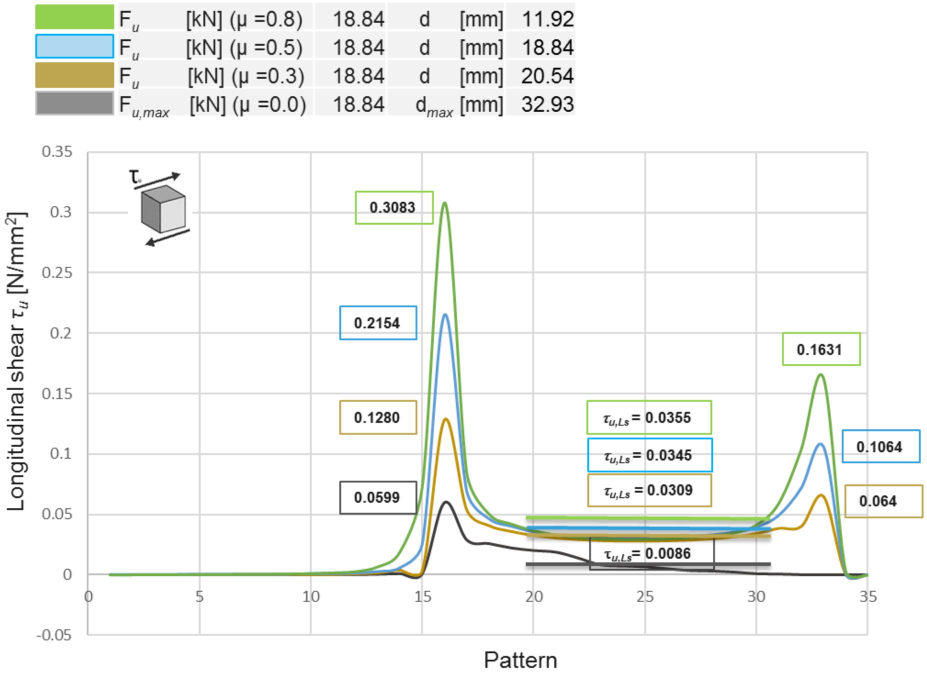

Figure 6.41 *Representation C60 short span τ_u curves μ = 0.0, 0.3, 0.5, 0.8 for F_u = $F_{u,max}$(μ=0.0)*

🟩	$F_{u,max}$	[kN] (μ =0.8)	76.18	d	[mm]	18.48
🟦	$F_{u,max}$	[kN] (μ =0.5)	47.9	d	[mm]	13.67
🟨	$F_{u,max}$	[kN] (μ =0.3)	33.73	d	[mm]	13.22
▨	$F_{u,max}$	[kN] (μ =0.0)	18.86	d_{max}	[mm]	14.13

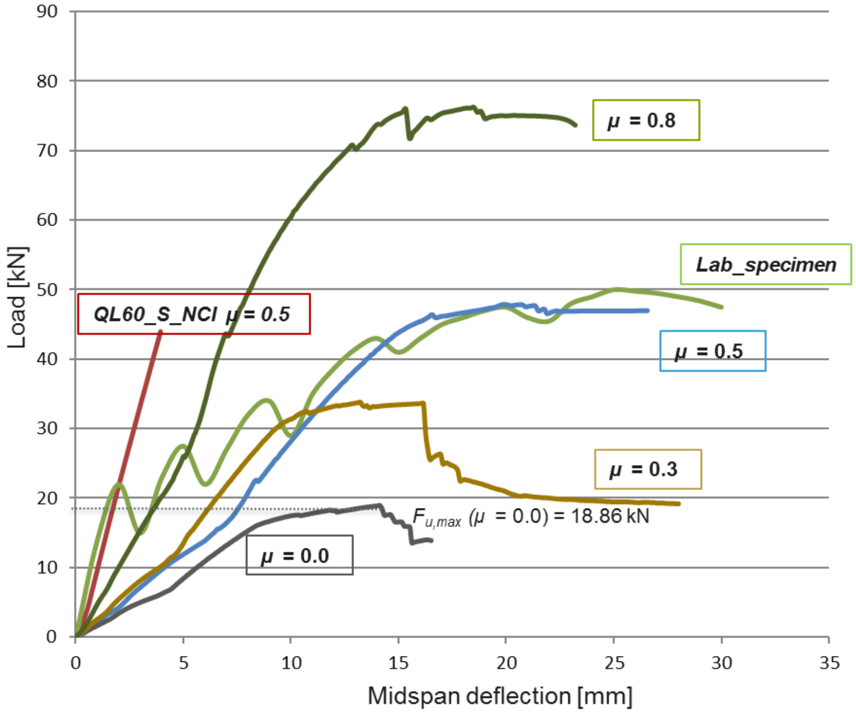

Figure 6.42 *Load-midspan displacements different friction coefficients, QL60*

🟩	F_u	[kN] (μ =0.8)	18.86	d	[mm]	3.72
🟦	F_u	[kN] (μ =0.5)	18.86	d	[mm]	4.86
🟫	F_u	[kN] (μ =0.3)	18.86	d	[mm]	6.25
▨	$F_{u,max}$	[kN] (μ =0.0)	18.86	d_{max}	[mm]	14.12

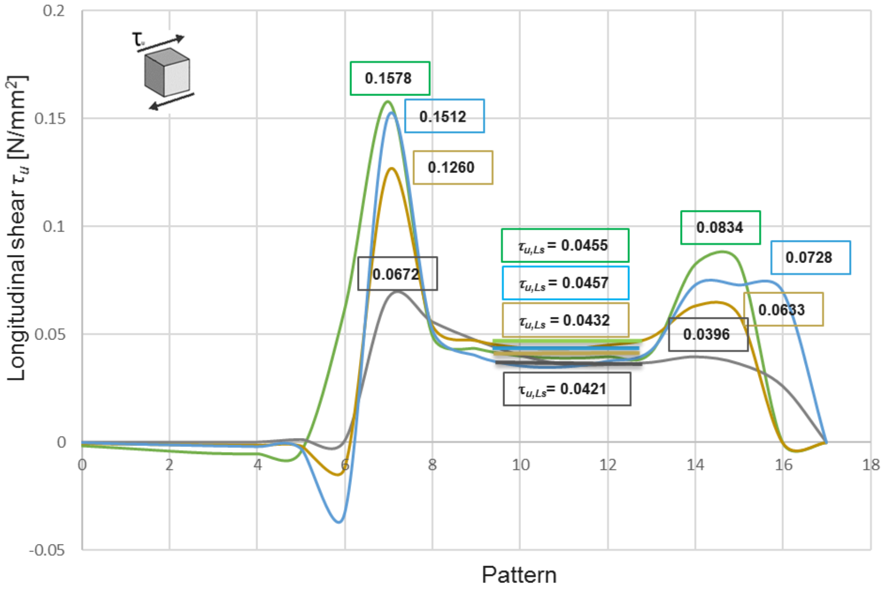

Figure 6.43 *Representation QL60 short span τ_u curves μ = 0.0, 0.3, 0.5, 0.8 for F_u = $F_{u,max}$(μ=0.0)*

🟩	$F_{u,max}$	[kN] (μ =0.8)	82.03	d	[mm]	8.04
🟦	$F_{u,max}$	[kN] (μ =0.5)	80.92	d	[mm]	9.86
🟨	$F_{u,max}$	[kN] (μ =0.3)	49.78	d	[mm]	6.02
⬜	$F_{u,max}$	[kN] (μ =0.0)	23.46	d_{max}	[mm]	6.00

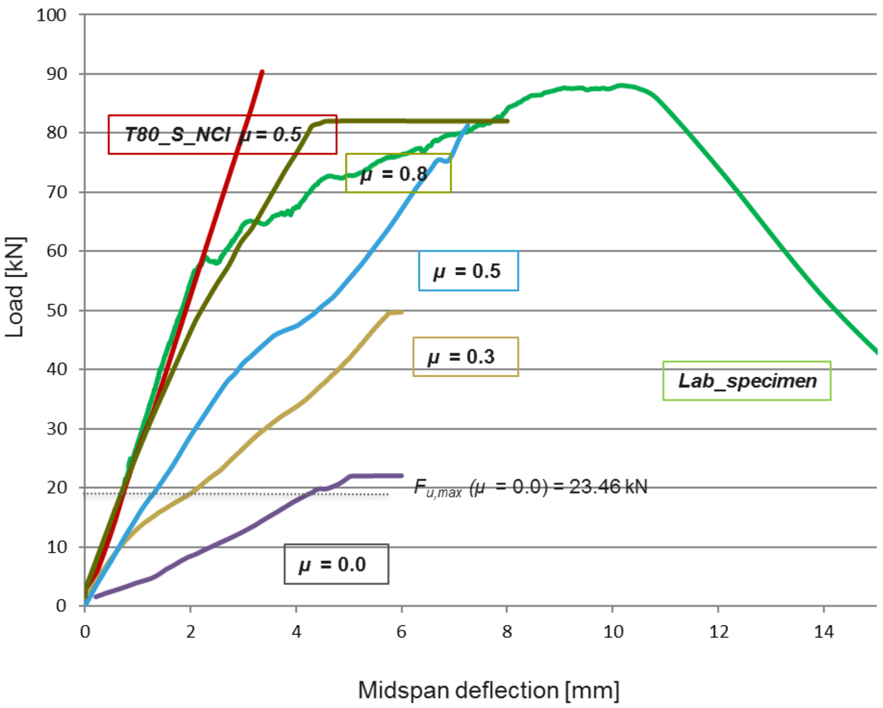

Figure 6.44 *Load-midspan displacements different friction coefficients, QL60*

🟩	F_u	[kN] (μ =0.8)	23.46	d	[mm]	0.84
🟦	F_u	[kN] (μ =0.5)	23.46	d	[mm]	1.51
🟨	F_u	[kN] (μ =0.3)	23.46	d	[mm]	2.39
⬜	$F_{u,max}$	[kN] (μ =0.0)	23.46	d_{max}	[mm]	6.05

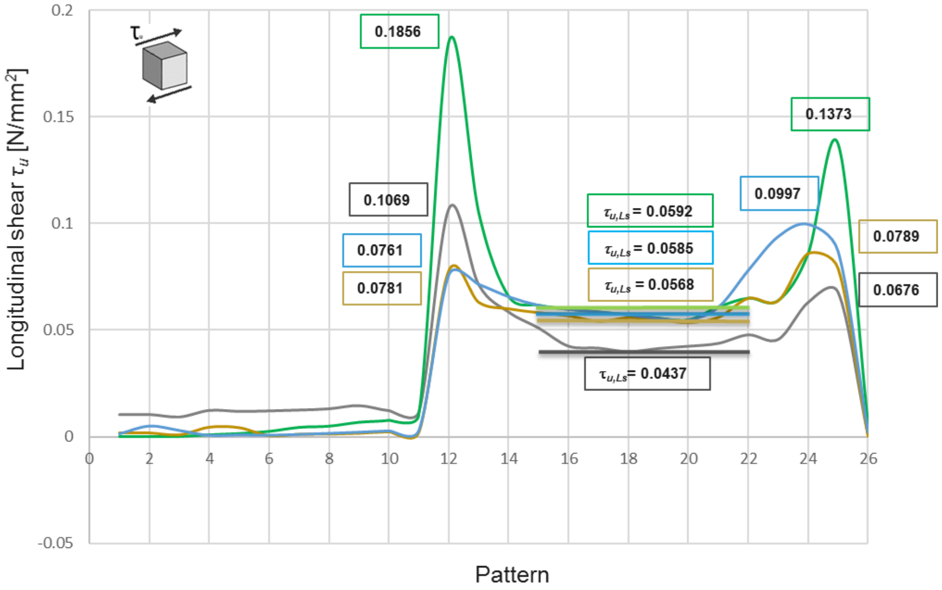

Figure 6.45 *Representation T80 short span τ_u curves μ = 0.0, 0.3, 0.5, 0.8 for F_u = $F_{u,max}$(μ=0.0)*

Figure 6.46 draws the longitudinal shear strength $\tau_{u,Ls}$ values at the Y-axis and the friction coefficients at the X- axis for all the different simulations computed. The figure highlighted that the $\tau_{u,Ls}$ value for μ = 0,0 was the lowest value from each steel deck profile group studied. The trend can be also observed at Table 6.7 that summarizes numerically the $\tau_{u,Ls}$ values plotted. Furthermore, another behaviour observed was the rapid increased in $\tau_{u,Ls}$ values for the μ = 0.3 simulations once compared with the initial μ = 0,0 simulations. Subsequently, $\tau_{u,Ls}$ values observed minor increases for the μ = 0.5 and μ = 0.8 simulations in the friction coefficient for all the composite slabs studied.

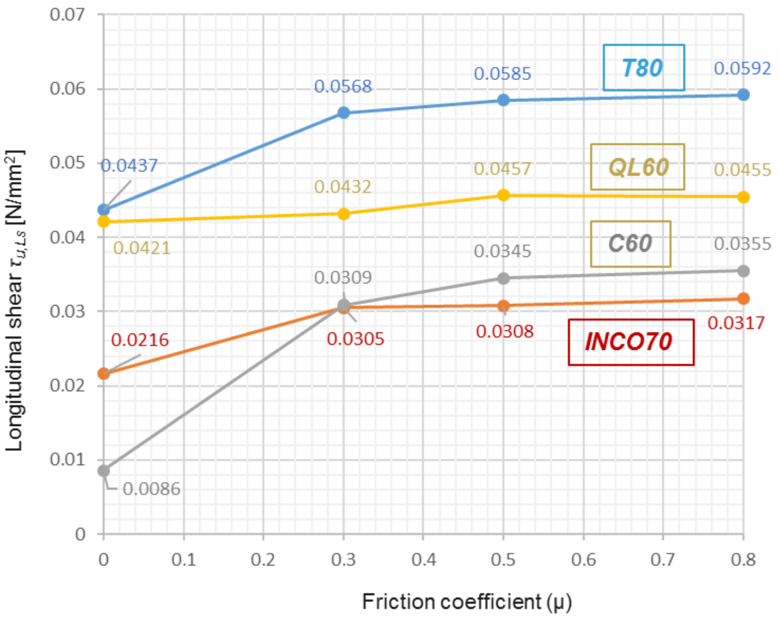

Figure 6.46 *All composite slabs $\tau_{u,Ls}$ representation for μ = 0.0, 0.3, 0.5, 0.8 simulations*

Short span	μ	INCO70	C60$^{(*)}$	QL60	T80
F_u [kN]	-	13.07	18.84	18.86	23.46
$\tau_{u,Ls}$ [N/mm^2]	0.8	0.0317	0.0355	0.0455	0.0592
	0.5	0.0308	0.0345	0.0457	0.0585
	0.3	0.0305	0.0309	0.0432	0.0568
	0.0	0.0216	0.0086	0.0421	0.0437

$^{(*)}$ C60 short span models presented a h_t = 100 mm

Table 6.7 *Longitudinal shear strength $\tau_{u,Ls}$, $F_u = F_{u,max}(\mu=0,0)$*

The studies performed indicate that the friction coefficient influenced significantly the longitudinal shear characterization of the composite slab. Higher values for the friction coefficient reported the larger $\tau_{u,Ls}$ values and the larger concentration of stresses at the clamped segments. The friction coefficient is a parameter that can not be influenced at the design of the composite slab as it is dictated from the cold-forming production process. However, the influence observed suggested to continue the path started by the Eurocode 4 building code to include a friction coefficient parameter at the formulation of the design method, see Equation 5.5. The stress concentrations observed at the clamped areas contribute significantly at the overall shear bond and the friction coefficient is a key parameter.

Figures 6.47 and 6.48 introduce a new representation for the values from Table 6.7. The different $\tau_{u,Ls}$ for each friction coefficient were combined in every composite slab. The columns represented a cumulative sum of the $\tau_{u,Ls}$ values from $\mu = 0.0$ to $\mu = 0.8$. The ultimate column height represented the values observed for $\mu = 0.8$ and provided a break down from each friction coefficient computed. The visualizations reinforced the previous highlighted trend of a rapid increase of $\tau_{u,Ls}$ values once friction coefficient was larger than $\mu = 0.0$ or in another words, when the friction was enabled at the FE models.

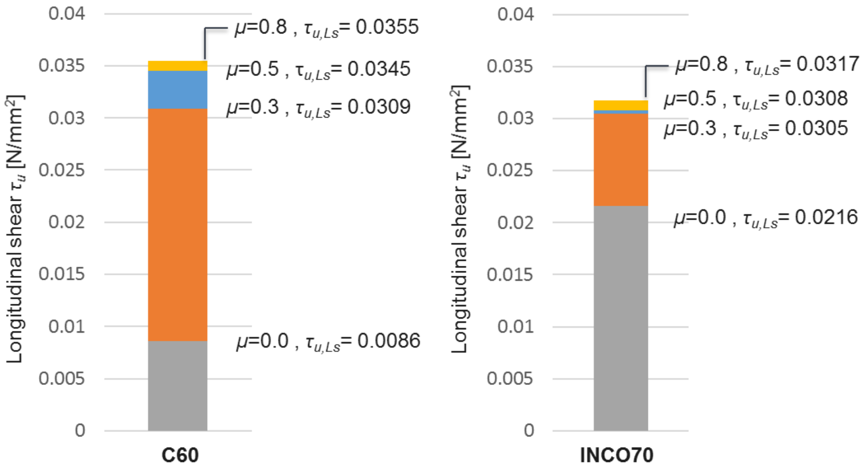

Figure 6.47 *Longitudinal shear strength for different friction coefficients, C60 and INCO70*

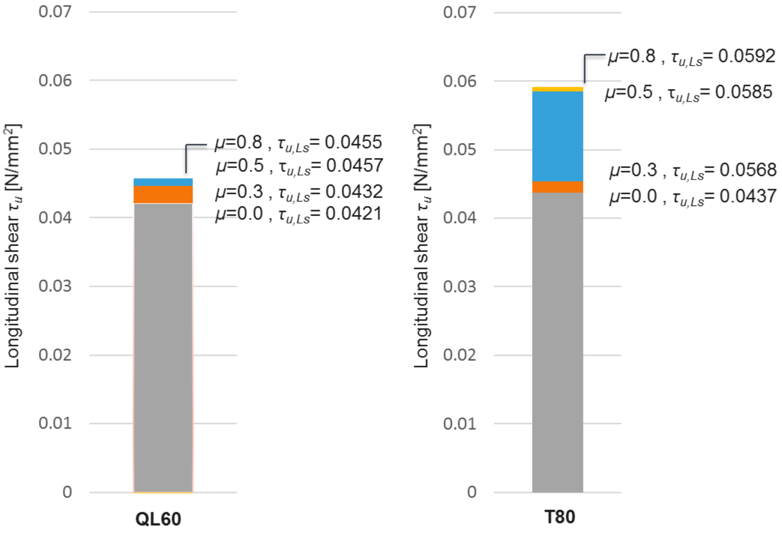

Figure 6.48 *Longitudinal shear strength, different friction coefficients, QL60 and T80*

6.6. New composite slab characterization parameter $\tau_{u,mechanical}$

The observation of the FE models behaviour for different loads, different friction coefficients, different load-midspan displacements and the novel "bathtub" longitudinal shear strength representation enabled the definition of a new longitudinal shear characterization parameter named $\tau_{u,mechanical}$.

The foundations for the new parameter resided in the observation that the longitudinal shear strength $\tau_{u,Ls}$ value for the friction coefficient $\mu = 0.0$ always reported the lowest shear bond value. The $\mu = 0.0$ characterization removed the influence from any frictional resistance at the support and the point load segments, previously defined as clamped segments. Similarly, it also removed the intrinsic forces developed at the embossments and steel deck sides based on friction. Figure 6.49 schematically represents the influence from the friction $\mu = 0.0$ in one steel deck profile rib.

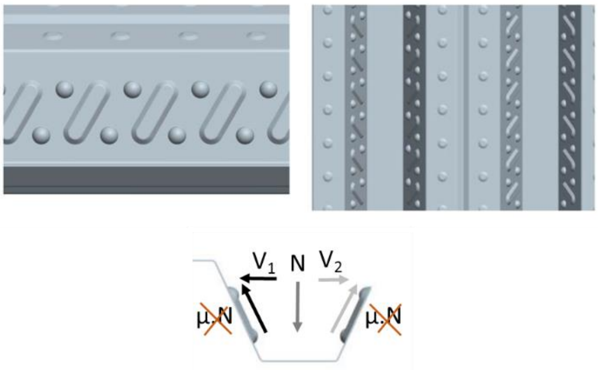

Figure 6.49 *Influence μ = 0.0 at the steel deck force distribtuions*

Once the friction influence is removed from the three-dimensional models, the reported $\tau_{u,Ls}$ (μ=0.0) only features the geometrical and material properties from the steel deck and concrete slab. As such, the $\tau_{u,mechanical}$, defined as the $\tau_{u,Ls}$ for a null friction $\mu = 0.0$, reported a shear resistance efficiency and geometry design quality parameter for the steel deck profile and enabled the comparison between FE models with the same shear span L_s and overall depth h_t. The development of the parameter and the supporting details are discussed herein.

Tables 6.8 and 6.9 summarize the $\tau_{u,Ls}$, $F_{u,max}$ and *stress reactions at the support* and *point load* for the long and short span simulations developed in this dissertation for a friction coefficient $\mu = 0.5$. The measured failure load W_t was also included at the table to enable comparisons. The largest values for each column are highlighted in bold to ease the reading. A few discussions points follow based on the behaviours observed at the numerical analyses.

First, the results indicate that the $\tau_{u,Ls}$ values computed for the coefficient friction $\mu = 0.5$ simulations at the short span accurately modeled the best performing steel deck profile. See Table 6.9. The

T80 values for the longitudinal shear strength 0.1795 N/mm^2 for the short span was the largest value among the different steel decks. The $\tau_{u,Ls}$ largest value was in concordance with the W_t largest value 88.15 kN reported from the laboratory tests. The tables also highlighted that the T80 simulations captured the largest concentrations values at the clamped segments, both for long and short spans. However, the second largest $\tau_{u,Ls}$ value 55.13 kN at the short span simulations was computed for the QL60 composite slab and did not coincide with the second largest W_t value observed at the INCO70 laboratory specimen. The short span C60 models were based on an overall composite slab depth of h_t = 100 mm and consequently could not be directly compared.

	Long span				
$\mu=0.5$	$\tau_{u,Ls}$ $\mu=0.5$ [N/mm^2]	$F_{u,max}$ FE model [kN]	Concentration at point load [N/mm^2]	Concentration at support [N/mm^2]	Actual lab. specimen W_t [kN]
INCO70	0.0824	21.98	0.2586	0.2738	23.05
C60	**0.0852**	30.51	0.2097	0.2403	31.63
T80	0.0656	**44.56**	**0.4314**	**0.3544**	**49.50**
QL60	0.0836	26.19	0.2382	0.1533	31.015

Table 6.8 *Comparison $\tau_{u,Ls}$, long span specimens*

	Short span				
$\mu=0.5$	$\tau_{u,Ls}$ $\mu=0.5$ [N/mm^2]	$F_{u,max}$ FE model [kN]	Concentration at point load [N/mm^2]	Concentration at support [N/mm^2]	Actual lab. specimen W_t [kN]
INCO70	0.0856	55.6	0.3057	0.2062	55.13
C60$^{(*)}$	0.0985	33.03	0.2803	0.1896	33.06
T80	**0.1795**	**80.92**	**0.3096**	**0.5675**	**88.15**
QL60	0.1403	47.90	0.2569	0.2156	50.01

$^{(*)}$ C60 short span models presented a h_t = 100 mm

Table 6.9 *Comparison $\tau_{u,Ls}$, short span specimens*

Second, the steel deck profile C60 was categorized as the best performing design based on computation of the $\tau_{u,Ls}$ values for the long span simulations in close proximity to the values computed for INCO70 and QL60. The W_t laboratory results for the INCO70, C60, and QL60 long spans were similar (27.08 kN, 31.63 kN, 31.015 kN). See Table 6.8. Oppositely, the $\tau_{u,Ls}$ value computed for the T80 simulation reported the lowest characterization although the T80 laboratory specimens reported the largest W_t value with 49.50 kN. The T80 computed τ_u curve reported the highest stress values at the support and point load patterns, with values being significantly larger than the rest of the composite slabs studied.

The concentration of stress values, and more concretely the "bathtub" shape of the longitudinal shear strength τ_u, indicated that the shear resistance characterization must consider the influence from the clamped areas to define the composite behaviour. The consideration of an unique $\tau_{u,Ls}$ value isolated to characterize the shear bond was not possible as the τ_u representations indicated different degrees of stress concentrations.

Third, based on the influence of the clamped segments to characterize the shear bond, Table 6.10 summarizes the longitudinal shear mechanical strength $\tau_{u,mechanical}$ parameter computed for the short span models. The $\tau_{u,mechanical}$ represented the $\tau_{u,Ls}$ for friction coefficient μ = 0.0. The removal of the friction resistance from the multiple phenomena that occur at the three-dimensional deformation and stress distribution enabled a characterization based on the efficiency of the steel deck design. Hence, $\tau_{u,mechanical}$ was proposed as a new characterization parameter for composite slab performance in longitudinal shear failure.

All the laboratory specimens had similar shear span L_s lengths and equal overall depths h_t which enabled the comparison among them, except the short span C60. The steel deck C60 was listed as a reference although it could not be directly compared within the group due to its different h_t=100 mm. The $\tau_{u,mechanical}$ values suggested a best-to-worst sequence T80, QL60 and INCO70 for the steel deck profiles performance. The W_t failure loads for the long span specimens reported a largest-to-smallest sequence T80, QL60 and INCO70 matching the $\tau_{u,mechanical}$ classification.

μ=0.0	$\tau_{u,mechanical}$ short span [N/mm^2]	$F_{u,max}$ (µ =0,0) FE model [kN]	Actual lab. long span W_t [kN]
INCO70	0.0216	13.07	23.05
C60$^{(*)}$	0.0086	18.84	-
T80	**0.0437**	**23.46**	**49.50**
QL60	0.0421	18.86	31.01

$^{(*)}$ C60 short span models presented a h_t = 100 mm

Table 6.10 *Comparison* $\tau_{u,mechanical}$

The computation of the $\tau_{u,mechanical}$ for the short span optimized the computational cost and represented more accurately the shear bond performance once compared with the respective long span simulation. The new $\tau_{u,mechanical}$ parameter provided a shear resistance metric that represented the longitudinal shear performance for the long span laboratory specimens. The importance to characterize the long span laboratory specimens resided in the fact that current design methods, such as *m-k* and PCM, input the lowest W_t, and consequently the $F_{u,max}$ computed from the simulations, to compute the composite slab resistance behaviour.

6.7. Steel deck design process

The combination of the novel FE modeling approach introduced in chapter 4 and the new $\tau_{u.mechanical}$ characterization parameter were the foundations for a new process to design and optimize steel deck profiles. The numerical simulations enabled a complete understanding of the composite slab micromechanics and provide a platform to test multiple concrete slab and steel deck configurations with almost no cost. In parallel, the $\tau_{u.mechanical}$ defined an unique composite slab performance parameter that enabled a direct comparison between different steel deck profile designs. The design methodology is illustrated in Figure 6.50 and consisted in 7 sequential steps.

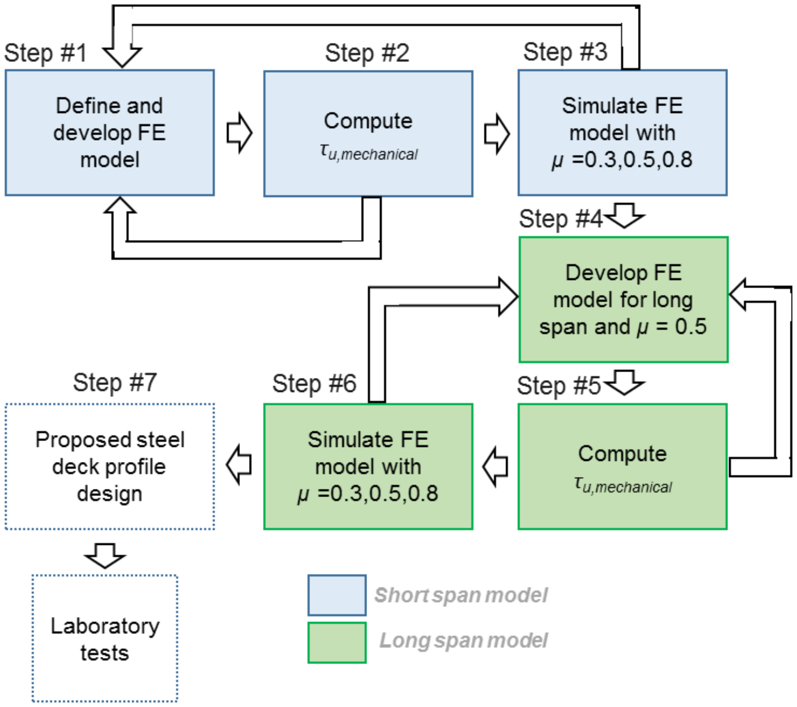

Figure 6.50 *Schematic representation new design process for steel deck profile design*

Step 1: Define and develop FE model

In this initial step, the FE model needs to be created. Table 6.13 captures the required parameters to define the composite slab geometry. It is recommended to define some constant geometry parameters along the design process and focus the optimization on a set reduced variables. Equally, the material definition is input in this first step and recommended to be kept constant for the subsequent steps. Once the geometry is completed, the numerical simulation is performed and an iterative process to optimize the FE computational parameters and density of the meshing performed.

Geometry *Constant parameters*	h_p, h_t, t, b, L_{total}, L_s, rim length, friction coefficient μ=0.0
Geometry *Variable parameters*	Top /bottom/lateral circular embossment diameter Top/bottom/lateral circular embossment depth Top/bottom/lateral circular embossment slope Top/bottom/lateral longitudinal embossment Top/bottom/lateral longitudinal embossment slope Separation between patterns Steel deck profiled angle/s
Material definition *Constant parameters*	f_{yp}, f_{ck}

Table 6.11 *Definition initial parameters for composite slab design*

A basic understanding of the steel deck cold-forming process is strongly recommended. The industrialized process introduces some boundaries at most of the geometrical parameters of the steel deck profile such as the distance between embossments, embossments depths and the steel deck width.

Step 2: Compute $\tau_{u, mechanical}$

The τ_u and σ_{shear} curves are computed from the initial simulation results. The σ_{shear} curve provides the required information to define the clamped and unclamped segments, see Figure 6.1. Once the unclamped segment length is characterized within the longitudinal shear span, the longitudinal shear strength averaged value $\tau_{u,Ls}$ can be calculated. As the model did input a friction coefficient μ = 0.0, the values calculated represent $\tau_{u.mechanical}$.

Based on the initial result from $\tau_{u.mechanical}$, the sensitiveness of the variable geometry parameters defined in Table 6.13 are explored. The process recommends to modify only one geometrical parameter per iteration to avoid a cross-effect influence. Thus, multiple simulations are performed and subsequently the $\tau_{u.mechanical}$ parameter computed for each of them. The focus of the optimization process is to maximize the $\tau_{u.mechanical.}$ value and also identify the most influential geometry parameters affecting the composite slab performance for $F_{u,max}$, load-midspan deflection and load-end slip.

Step 3: Simulate FE models with different friction coefficients (μ)

The optimization process for the $\tau_{u.mechanical}$ parameter minimizes the influence of the clamped areas near the support and point load patterns. The design process continues with the simulation of the steel deck profile from *Step* 2 for friction coefficients μ = 0.3, 0.5 and 0.8. The increase in friction introduces at the simulation the composite slab capacity in front of the clamping phenomenon, a key element for the longitudinal shear failure. The design process requires the observation and evaluation of the following behaviours from the simulations:

- Computation of the τ_u and load-midspan deflection curves for each simulation and characterization of the $\tau_{u,Ls}$ and $F_{u.max}$ parameters.
- Review the shape and maximum stress values at the τ_u curve for the clamped segments as indicator of concertation stresses capacity of the composite slab
- (optional) Computation of the neutral axes for the steel deck and composite slab as indicator of the partial connection

Conceptually, the simulations with higher friction coefficients μ need to report higher values across the different composite parameters computed, especially at the unclamped segments. Otherwise, the steel deck profile design needs to increase the performance in front of the clamping phenomenon. Common tactics to improve it are the increase of the rib profiled angle, steel thickness t, separation among lateral embossments and the geometry of the top embossments.

Step 4: Develop FE model for long span and μ = 0.5

The FE model is modified in L_{total} and L_s to expand the simulation for the long span composite slabs. The optimization process performed in *Step 1* for the meshing and geometries of the FE model does not need to be repeated. The building codes require the testing of different lengths of specimens and thus the requirement is mirrored at the simulations as a friction coefficient $\mu = 0.5$ is deployed.

The τ_u and σ_{shear} curves are computed from the simulation results. The σ_{shear} curve provides the required information to define the new clamped and unclamped segments for the long span simulations. Once the unclamped segment length is characterized, the longitudinal shear strength averaged value $\tau_{u,Ls}$ can be computed. The goal of this step is to review the τ_u curve and verify that no singularities are found at the “bathtub” shape. It is recommended to perform an additional simulation with a variance in the most significant geometrical parameter identified in *Step 3* to characterize how the $\tau_{u.Ls}$ value fluctuates.

Step 5: Compute $\tau_{u, mechanical}$

A new simulation is performed for a coefficient friction $\mu = 0.0$ for the long span FE model. The τ_u curve is computed and the $\tau_{u,mechanical}$ characterized. Based on the research performed, this value should not be compared among different designs as it does not have a direct correlation in maximum longitudinal shear performance. However, the $\tau_{u,mechanical}$ and τ_u curve provide a strong understanding of the steel deck profile performance in front of the clamping phenomenon for the long span configuration. The τ_u curves computed in previous *Step 4* can be compared and the stress concentration at the clamped segments studied.

Step 6: Simulate FE models with different friction coefficients (μ)

Similar to *Step 3*, multiple simulations are performed introducing the friction coefficients μ = 0.3 and 0.8 for the long span FE model. The simulations are subsequently compared with the models with $\mu = 0.5$ and $\mu = 0.0$ developed in *Steps 4* and *5* respectively. The computed values for the τ_u curve are compared with the focus on the composite slab capability in front of the clamping. The simulations with higher friction coefficients need to report higher values computed across the different composite parameters computed, specially at the unclamped segments. Otherwise, the steel deck profile design need to focus to increase the performance in front of the clamping phenomenon as described in *Step 3*.

Step 7: Proposed steel deck profile design

The last step captures the results from all the simulations performed and recommended a steel deck profile design.

Throughout a sequential process, the design optimizes the shear bond based on the most influential geometry parameters. The optimization process might not be possible for each isolated step: as example, some enhancements to improve the short span $\tau_{u,mechanical}$ might reduce simultaneously the performance in $\tau_{u,Ls}$ for the long span $\mu = 0.5$ simulation. Consequently, the design process is envisioned as set of dynamic loops between *Steps* as opposed to a fixed linear and sequential approach. Yet, the proposed linear approach weights the most important geometrical design parameters towards early steps for the design process.

7. Conclusions and recommendations

This dissertation contributes to the body of knowledge in composite slabs with novel insights in the longitudinal shear strength characterization through advanced computing modeling and simulation techniques. First, the study provides evidence that the full-scale, three-dimensional and accurate geometry modeling and simulation methodology developed provides a strong platform for the advancement in composite slab characterization. Second, the innovative modeling and simulation approach was leveraged to produce a novel understanding on composite slabs structural micromechanics. Finally, such ability to predict composite macro- and micro-composite performance ahead of costly and time-consuming physical tests was leveraged to define a new composite slab characterization parameter named $\tau_{u,mechanical}$ and a design process for steel deck profiles.

7.1. Advanced finite element modelling

The proposed modeling and simulation methodology in the finite element software tool Ansys consistently replicated maximum loads $F_{u,max}$, midspan deflections and end slip composite performances for the Eurocode 4 bending laboratory tests in addition to other composite behaviors. Common limitations and simplifications related to steel-concrete contact, adhesion, and cohesion factors in previous research efforts were addressed. The initial FE models developed required an intense optimization process as the computational costs and sizes associated with them were significant. The *SOLID185* type element was selected to model the concrete slab; other concrete type elements were tested but reported an increased level of complexity with limited influence at the simulations results. *SHELL281* was selected as the steel deck FE type element, with a mesh densification at the critical surfaces for the longitudinal shear failure. Similarly, an iterative process was implemented to optimize the characterization of the material properties, crack inducer and chemical bond (initial friction) at the simulations.

Based on the robustness of the bending simulations, pull-out tests were subsequently modeled and a parametric study performed in consideration of multiple steel deck geometrical parameters. The height of the short and long embossments h_1 and h_2, the thickness t and the coefficient of friction μ reported a significant influence for the shear resistance behavior while the width of the pattern s and the rounding edges r were less influential.

Composite slab macro behaviours were observed both at the bending and pull-out simulations: end slip, crack inducer separation, concrete peeling and stressed zones, concrete nodal forces traces and steel deck deformation at point load. Furthermore, novel insights in stresses concentration at the embossments, strains distributions along the rib and the clamping phenomenon were identified at the FE models.

The combination of the accurate modeling methodology and the strong agreement with the laboratory results enables two significant benefits: first, it postulates the FE modeling and numerical analyses as a reliable vehicle to characterize composite slabs with less dependency in laboratory tests. For example, the simulations could reduce significantly the number of mandatory laboratory specimens required as defined today by building codes. Second, based on the increased computational footprint available at engineering and design firms, it can pave a new approach to export the actual composite slab FE model into larger structural analysis models. Today, several structural analysis software packages deploy FE elements for the engineering of building designs. The composite slab FE model could become an additional structural input, similar to concrete/steel beams, columns or foundations. Consequently, the composite slab could become a part of the complete structural solution and consider membrane effects, local loads and the connection with the superstructure, beyond today isolated characterization of its failure at the laboratory testbed.

7.2. Composite slabs micromechanics

The FE models enabled the possibility to perform in-deep studies for the steel deck and concrete slab at any given step of the simulation. Neutral axes for the steel deck and concrete slab and vertical disconnection representations were characterized and subsequently proved the existence of partial connection between the materials. Micro-deformation laboratory results from strain gauges were also compared with simulation micro-deformations with strong agreement for one group of composite slabs.

A new normal vertical tension parameter σ_{shear} was introduced to describe the vertical stresses between the steel deck and the concrete slab at the bending simulations. The new parameter was leveraged subsequently to define the different segments that characterize the shear resistance along the rib within the shear span L_s.

Similarly, the longitudinal shear strength τ_u was computed from the bending simulations for different midspan deflections, loads and friction coefficients. The observation of a constant value at the shear span unclamped segment defined as $\tau_{u,Ls}$ was novel and supported the Eurocode 4 *Partial Connection Method* mechanical model assumption for composite slab design. Results also supported other subsequent design methods developed by multiple authors based on a constant shear strength distribution τ_u at the shear span.

A better understanding of the composite slab micromechanics throughout the numerical models might generate multiple implications for the current building codes. Both *m-k* and PCM design methods were developed 30 years ago based on the observation of hundreds of laboratory tests and the adoption of some formulae from other composite structures. The capability to isolate principal stresses, strains and deformations at the FE models introduces the option to amplify the laboratory testbed configurations and to develop novel solutions with the certainty of a safe characterization.

7.3. New composite slab characterization parameter: $\tau_{u,mechanical}$

The Eurocode 4 *Partial Connection Method* mechanical model assumption provided an approximation for the longitudinal shear strength τ_u but was not capable to describe the complex shape observed at the simulations. The values computed for $\tau_{u,EC4\_PCM}$ were higher than $\tau_{u,Ls}$ from the simulations but smaller than the concentrated stresses found at the support and point load areas. It was proved that the friction coefficient influenced significantly the concentration of longitudinal shear stresses and hence, the overall shear resistance.

A new characterization parameter $\tau_{u,mechanical}$ was proposed to measure the steel deck profile design. The parameter was defined as the longitudinal shear strength $\tau_{u,Ls}$ computed from the simulations for a friction coefficient $\mu = 0.0$. The deployment of a null friction removed the multiple contributions from the friction at the complex three-dimensional behaviors from the composite slab. The $\tau_{u,mechanical}$ hence characterized quantitatively the design efficiency for a composite slab. The new parameter proved to accurately classify the different composite slabs analyzed in this dissertation when compared with the maximum loads $F_{u,max}$ observed at the long span laboratory tests.

Finally, a practical application from the research findings was discussed. A new design process was proposed that combined the new FE model methodology and the $\tau_{u,mechanical}$ parameter. Based on a sequential and iterative process, the method proposed a computer-focused approach to design efficient steel deck profiles and reduce the reliance in the costly and tedious laboratory tests.

8. Future research developments

The studies performed proved that the new modeling methodology provides an opportunity to ease and accelerate the concrete slab and steel deck design parameters, such as thickness, embossments geometries, or tilting angle prior to the actual production of the steel deck profile. Such ability to compute and predict composite behavior is fundamental to optimize composite slab behavior ahead of physical tests. Collaterally, the results of this dissertation imply an opportunity to enhance composite design with the consideration of micromechanics. The detailed understanding of micromechanics has the potential to introduce more elaborated testbeds to characterize composite slab performance. A few areas of future development are introduced herein, categorized by the three major areas of focus of the dissertation.

8.1. Advanced finite element modelling

The natural advancement in computational capabilities over time, even at the domestic levels, are expected to incentive the computation of more complex FE models. The author envisions the below new areas as firm candidates to be implemented:

- *Inclusion of cracking and crushing phenomena at the concrete slab*: the cracking and crushing of the concrete might influence some of the behaviours observed at critical contact surfaces for maximum loads $F_{u,max}$ that today are mainly focused on the understanding of the steel deck performance. The concrete behaviour might be more relevant for re-entrant rib profiles, in which the concrete slab is enclosed within the steel ribs.
- *Inclusion of the steel rebaring:* the steel mesh and the reinforcing bars main functionality is not structural, although they might introduce indirect enhancements. Eurocode 4 suggests that the resistance for longitudinal shear from those elements might be taken into account, although it not provides a method and suggests the realization of three additional test specimens. Johnson and Shepherd (2013) developed a new design method based on PCM that included the contribution of the reinforcing bars that could be investigated through simulations.
- *Deployment of dynamic friction models to characterize the initial chemical bond*: the initial shear resistance is not linked to any geometrical parameter and yet, it is an important component of the experimental tests. The existence of a large database of bending test results in open literature and the availability of complex friction models at the commercial FE software packages encourages a gradual improvement in the modeling of the initial behaviour.

- *Definition of new laboratory testing configurations:* the study performed focused in the Eurocode 4 testbed for two symmetric loads; today other laboratory arrangements exist such as distributed loads or even multi-span configurations that include different load distributions.
- *Inclusion of end anchorages:* end anchorages are also a common element in composite structures design that enhance the shear resistance performance at the composite slab and could be included at the simulations.
- *Expand composite slab characterization under fire actions*: most commercial FE software packages include specific modules for material definition under fire that characterize yields, temperatures and strains among other parameters. New FE models could include the testing arrangements for composite slab characterization under fire actions.

The influence from some of the parameters was investigated but the limited influence observed, in combination with a higher order of magnitude for the numerical analyses required, discouraged their implementation within this research.

8.2. Composite slabs micromechanics

The access to rich and large pools of data from the simulations enables the possibility to explore and define new micromechanics at the composite slab. The author envisions the below new areas as firm candidates to be studied:

- *Rotational deformation* of the steel deck middle section at the bending specimens
- *Shear failure* at the concrete slab for compact composite slabs
- *Punching shear* failure from punctual loads

Additionally, the development of new FE visualization from the simulations based on von Mises stresses, principal stresses, nodal reactions, and material deformations for singulars areas such as the crack inducer, point load, support or rim, can further enrich the understanding of the composite behaviour.

8.3. New composite slab characterization parameters

The Eurocode 4 PCM mechanical model provided a rough approximation for the actual longitudinal shear behaviour observed at the simulation, but only for a reduced segment within the shear span L_s. A constant slip and longitudinal shear strength was observed at the simulations, but the computed values by the building code $\tau_{u,EC4\_PCM}$ and the simulation $\tau_{u,Ls}$ values differed. The clamping influence observed at the support and point load areas, defined as clamped segments, was discussed and reported to be key contributor to the longitudinal shear resistance. Future research can explore an enhanced universal characterization for the clamping phenomenon, that in combination with the proposed longitudinal shear strength $\tau_{u,Ls}$ from the simulations, can provide a more complete and accurate longitudinal shear characterization.

The composite slab design method *m-k* and PCM have been repeatedly classified as conservative and inaccurate by different authors. Yet, the complexity of the phenomena that occur at the composite slab makes difficult to find alternative universal design methods. The definition of parameters such as $\tau_{u,mechanical}$ is an initial attempt to enhance the methods to characterize composite slab based on computing models which over time should significantly reduce the reliance in laboratory tests.

9. Bibliography

[1] Abdullah, R., Experimental evaluation and analytical modeling of shear bond in composite slabs, PhD dissertation, Virginia Polytechnic Institute and State University, Blacksburg, VA, 2004.

[2] Abdullah, R., Easterling, W., New modeling and evaluation procedures for horizontal shear bond in composite slabs, *Journal of Constructional Steel Research*, 65(4), 891-899, 2009.

[3] Alvarez-Rabal, F.P., Guerrero-Muñoz, J., Alonso-Martinez, M., Martinez-Martinez, J.E., Bending and shear experimental tests and numerical analysis of composite slabs made up of lightweight concrete, *Journal of Engineering*, Hindawi Publishing Corporation, ID 6819190, 1-10, 2016.

[4] An, L., Load bearing capacity and behaviour of composite slabs with profiled steel sheet, PhD dissertation, Chalmers University of Technology, Sweden, 1993.

[5] Ansys Inc., “Ansys 13 documentation“, Canonsburg, PA, 2013.

[6] American Society of Civil Engineers (ASCE), Standard for the Structural Design of Composite Slabs, *ANSI/AASCE 3-91*, New York, NY, 1992.

[7] Bode, H., Sauerborn, I., Modern design concept for composite slabs with ductile behaviour, *Proc., Eng. Foundation Conf. on Composite Construction in Steel and Concrete II*, American Society of Civil Engineers, 125-141, 1992.

[8] Bode, H., Minas, F., Sauerborn, I., Partial connection design of composite slabs, *Journal of Structural Engineering*, 6(1), 41-46, 1996.

[9] Bode, H., Dauwel, T., Steel-concrete composite slabs – design based on partial connection, *Proc., Int. Conf. on Steel and Composite Struct.*, Delft, The Netherlands, 2.1-2.10, 1999.

[10] British Standard Institution (BSI), Structural use of steelwork in building – part 4: Code of Practice for design of composite slabs with profiled steel sheeting, *BS-5950*, London, UK, 1994.

[11] Burnet, J., Oehkers, D., Rib shear connectors in composite profiled slabs, *Journal of Construction Steel Research*, 57(12), 1267-1287, 2001.

[12] Calixto, J. M., Lavall, A. C., Melo, C. B., Pimenta, R. J., Monteiro, R. C., Behaviour and strength of composite slabs with ribbed decking.”, *Journal of Construction Steel Research*, 46(1), 211-212, 1998.

[13] CEN (European Committee for Standardization), Design of composite steel and concrete structures - Part 1-1: General rules and rules for buildings, *Eurocode 4*, Brussels, 1994.

[14] M. Crisinel, F. Marimon, A new simplified method for the design of composite slabs, *Journal of Constructional Steel Research*, 60 (3-5), 481-491, 2003.

[15] Chen, S., Shi, X., Shear bond mechanism of composite slabs – A universal FE approach, *Journal of Construction Steel Research*, 67(10), 1475-1484, 2011.

[16] Canadian Sheet Steel Building Institute CSSBI, Standard for Composite steel deck, *12M-96*, 1996.

[17] Daniels, B. J., Crisinel, M., Composite slab behavior and strength analysis. Part II: comparisons with test results and parametric analysis, *Journal of Structural Engineering*, 119(1-4), 36-49, 1993.

[18] Ferrer, M., Estudio numérico y experimental de la interacción entre la chapa de acero y el hormigón: para la mejora resistente de las losas mixtas frente al deslizamiento longitudinal, PhD dissertation, Universitat Politècnica de Catalunya. Barcelona, Espanya, 2005.

[19] Ferrer, M., Marimon, F., Crisinel, M., Designing cold-formed steel sheets for composite slabs: an experimentally validated FEM approach to slip failure mechanics., *Thin-Walled Structures Journal*, 44(12), 1261-1271, 2006.

[20] Gholamhoseini, A., Gilbert, R. I., Bradford, M. A., Chang, Z.T., Longitudinal shear stress and bond-slip relationships in composite concrete slabs, *Journal of Structural Engineering*, 69, 37-48, 2014.

[21] Hickks, S., EN 1994 - Eurocode 4: Design of composite steel and concrete structures. Composite slabs, *Ascot, The Steel Construction Institute*, p. 24, 2008.

[22] Johnson, R. P., Anderson, D., “Designers' guide to EN-1994-1-1 Eurocode 4: design of composite steel and concrete structures. Part 1.1: General rules and rules for buildings”, Thomas Telford. London, 2004.

[23] Johnson, R.P., Shepherd, A.J., (2013). Resistance to longitudinal shear of composite slabs with longitudinal reinforcement, *Journal of Constructional Steel Research*, 82, 190-194

[24] Laboratori d’Elasticitat i Resistència de Materials (LERMA), “Ensayo paramétrico de losas mixtas con el perfil QL-60 de British Robertson S.L.”, Escola Tècnica Superior d’Enginyeria Industrial de Barcelona (Universistat Politècnica de Catalunya). Barcelona, 2004.

[25] Laboratori d’Elasticitat i Resistència de Materials (LERMA), “Ensayo de losas mixtas con la chapa nervada colaborante T80. Metalperfil S.A.”, Escola Tècnica Superior d’Enginyeria Industrial de Barcelona (Universistat Politècnica de Catalunya). Barcelona, 2005.

[26] Laboratori d’Elasticitat i Resistència de Materials (LERMA), “Ensayo de losas mixtas con el perfil INCO 70.4 COLABORANTE de la empresa Ingeniería y Construcción del Perfil S.A., espesor nominal 0,8mm, según la normativa Eurocódigo-4 EN 1994 Parte 1-1:2004”, Escola Tècnica Superior d’Enginyeria Industrial de Barcelona (Universistat Politècnica de Catalunya). Barcelona, 2006.

[27] López, M., Larrúa, R., Recarey, C., A new system for designing embossments in steel sheets to increase composite slabs shear resistance, *Revista Ingeniería de Construcción*, 22, 145-156, 2007.

[28] Majdi, Y., Hsu, C.T., Zarei, M., Finite element analysis of new composite floors having cold-formed steel and concrete slab, *Engineering Structures*, 77(15), 65-83, 2014.

[29] Nagy, Z.V., Szatmari, I., Composite Slab Design, *2nd International Symposium in Civil Engineering*, Budapest. Technical University of Budapest, Budapest.1998.

[30] Palerm, A., Análisis numérico del comportamiento resistente de la patente UPC P200801846, Universitat Politècnica de Catalunya, Barcelona, 2011.

[31] Patrick, M., Bridge, R., Q., Partial shear connection design of composite slabs, *Engineering Structures*, 16(5), 348-362, 1994.

[32] Porter, M. L., Ekberg, C. E., Investigation of cold formed steel deck reinforced concrete floor slabs, *Proc., 1st Int. Specialty Conf. on Cold-Formed Steel Structures*, Rolla, Missouri, 79-185, 1971.

[33] Porter, M. L., Ekberg, C. E., Design recommendations for steel deck floor slabs, *Proc., 3rd Int. Specialty Conf. on Cold-Formed Steel Structures*, St. Louis, Missouri, 761-785, 1975a.

[34] Porter, M. L., Ekberg, C. E., Design vs. Test results for steel deck floor slabs, *Proc., 3rd Int. Specialty Conf. on Cold-Formed Steel Structures*, St. Louis, Missouri, 793-809, 1975b

[35] Şahin, S., A comparative study of AISC-360 and Eurocode 3 strength limit states, The Graduate School of Natural and Applied Sciences of Middle East Technical University, Ankara, Turkey, 2009.

[36] Seleim, S. S., Schuster, R. M., Shear-bond resistance of composite deck–slabs, *Canadian Journal of Civil Engineering*, Vol. 12, 316-323, 1985.

[37] Schuster. R.M., Strength and behaviour of cold-rolled steel-deck-reinforced concrete floor slabs, PhD dissertation, Iowa State University, Iowa, USA, 1970.

[38] Seres, N., Behaviour and resistance of concrete encased embossments in composite slabs, PhD dissertation, Budapest University of Technology and Economics, Budapest, Hungary, 2012.

[39] Stark, J., Design of composite floors with profiled steel sheet, *Proc. 4th Int. Specialty Conf. on Cold-Formed Steel Structures*, St Louis, Missouri, 893-992, 1978.

[40] Stark, J., Brekelmans, J. W., Plastic design of continuous composite slabs, *Journal of Construction Steel Research*, 15(1-2), 23-47, 1990.

[41] Structural Applications of Ferritic Stainless (SAFSS), “Work package 3: Structural and thermal performance of steel-concrete composite floor systems. Research Fund for Coal & Steel”, Departament de Resistència de Materials i Estructures a l’Enginyeria, Universitat Politècnica de Catalunya. Barcelona, 2013.

[42] Tsalkatidis, T., Avdelas, A., The unilateral contact problema in composite slabs: experimental study and numerical threatment, *Journal Construction Steel Research*, 66 (3), 480-486, 2010.

[43] Tzaros, K. A., Mistakidis, E. S., Perdikaris, P. C., A numerical model based on nonconvex-nonsmooth optimization for the simulation of bending tests on composite slabs with profiled steel sheeting, *Engineernig Structures*, Vol. 32, Pàg. 843-853, 2010.

[44] Vainiunas, P., Valivonis, J., Marciukaitis, G., Jonaitis, B., Analysis of longitudinal shear behaviour for composite steel and concrete slabs, *Journal of Constructional Steel Research*, 62, 1264–1269, 2006.

[45] Veljkovic, M., Behavior and resistance of composite slabs, PhD dissertation, Lulea University of Technology, Lulea, Sweden, 1996a.

[46] Veljkovic, M., An improved partial connection method for composite slab design", *Proc., Eng. Foundation Conference on Composite Construction in Steel and Concrete III*, American Society of Civil Engineers, 644-659, 1996b.

[47] Veljkovic, M., Influence of load arrangement on composite slab behavior and recommendations for design, *Journal of Construction Steel Research*, 45 (2), 149-178, 1998.

[48] Veljkovic, M., Behavior and design of shallow composite slabs. *Engineering Foundation Conference - Composite Construction,* Alberta, Canada, 2000.

[49] Widjaja, B. R., Analysis and design of steel deck-concrete composite slabs, PhD dissertation, Virginia Polytechnic Institute and State University, Blacksburg, VA, 1997.

Papers from the dissertation

[50] Plans, A., Gras, A., Ferrer, M. Marimon, F., Andreu, A., 3D non-linear realistic simulations of composite slabs bending test, *Proc. 7th European Conference on Steel and Composite Structures Eurosteel*, Naples, Italy, 523-524, 2014.

[51] Plans, A., Alamillo, D., Ferrer, M., Marimon, F., Caracterización micromecánica de la interacción acero-hormigón en las losas mixtas mediante el uso de modelos de elementos finitos, *Revista Internacional de Métodos Numéricos para Cálculo y Diseño en Ingeniería*, (enviado 16/01/2016, pendiente aceptación)

[52] Plans, A., Grau, D., Ferrer, M., Marimon, F., Andreu, A., Three-dimensional finite element modeling for bending and pull-out composite slab tests, *Journal of Structural Engineering*, (enviado 20/04/2016, pendiente aceptación)

Additional bibliography

[53] Abadal, I., Abadal, S., Análisis del comportamiento de las chapas nervadas de acero para losas mixtes, Master thesis, Universitat Politècnica de Catalunya, 2003.

[54] An, L., Cederwall, K., The theoretical and experimental study of composite slabs. Etude théorique et expérimentale de dalles mixtes, *Nordic concrete research*, 8, 159-175, 1989.

[55] An, L., Cederwall, K., Push test on stud connectors in normal and high strength concrete, *Journal of Constructional Steel Research*, 36 (1), 15-29, 1996.

[56] Armstrong, S.E., Proyecto "SSEDTA-2": Eurocódigo para las estructuras de acero y mixtas-desarrollo de una propuesta transnacional, [trad.] Miguel Ángel Serrano López. Universidad de Oviedo, Oviedo, 2001.

[57] Abdullah, R., Composite slab design using partial shear connection (PSC) method according to Eurocode 4, Johor Bahru, University Teknologi Malaysia. Malaysia, 2004.

[58] Bode, H., Minas, F., Sauerborn, I., Composite slabs with and without end anchorage under static and dynamic loading, *Proc., Engineering Conference Composite Construction*, 265-270, Innsbruck, Austria, 1997.

[59] Bradford, M. A., Ductility and strength of composite T-beams with trapezoidal slabs, *Proc., International Symposium, Advances in Steel and Composite Structures,* Hong Kong Institute of Steel Construction, 1-17, 2005.

[60] Bradford, M. A., Filonov, A., Hogan, T. J., Ranzi, G., Uy, B., Strength and ductility of shear connection in composite T-beams, *Proc., 8th International Conference, Steel, Space and Composite Structures*, 15-26, Kuala Lumpur, 2006.

[61] Calixto, J. M., Comparative study of longitudinal shear design criteria for composite slabs, *Minas Gerais: Revista Ibracon de estruturas e materiais*, 124-141, 2009.

[62] Cándido-Martins, J. P. S., Costa-Neves, L. F., Vellasco, L., Experimental evaluation of the structural response of Perfobond shear connectors, *Engineering Structures*, 32(8), 1976-1985, 2010.

[63] Cederwall, K., Engstrom, B., Effects an the shear capacity of floor slabs due to support fixations, *Institutionen för Konstruktionsteknik*, 77(5), Göteborg,1977.

[64] Chen, S., Load carrying capacity of composite slabs with various end constraints, *Journal of Constructional Steel Research*, 59(3), 385-403, 2003.

[65] Crisinel, M., Partial-Interaction Analysis of Composite Beams with Profiled Sheeting and Non-welded shear connectors, *Journal of Constructional Steel Research*, 15/1-2), 65-98, 1990.

[66] Daniels, B. J., Comportament et capacite portante des dalles mixtes: modelisation mathematique et etude experimentale, PhD dissertation N. 895, Ecole plytechnique Federale de Lausanne (EPFL), Switzerland,1990.

[67] Daniels, B. J., “Shear bond pull-out tests for cold-formed-steel composite slabs”, Rapport d’essais, ICOM-194, EPFL, Lausanne, Switzerland, 1988.

[68] Daniels, B. J., Crisinel, M., Composite slab behavior and strength analysis. Part I: Calculation procedure, *Journal of Structural Engineering*, 119(1), 16-35, 1993.

[69] Elloboy, E., Young, B., Performance of shear connection in composite beams with profiled steel sheeting, *Journal of Constructional Steel Research*, 62, 682-694, 2006.

[70] Faella, C., Martinelli, E., Nigro, E., Steel and concrete composite beams with flexible shear connection: “exact” analytical expression of the stiffness matrix and applications, *Computer & Structures*, 80(11), 1001-1009, 2002.

[71] Guerrero, A., Medina, P., Diseño de un perfil de acero para losa mixta y realización de ensayos pull-out para estudio de un nuevo sistema de conexión mecánica entre acero y hormigón, Master thesis, Universitat Politècnica de Catalunya (UPC), Barcelona, Spain, 2009.

[72] Guerreo, J., Análisis y optimización del comportamiento térmico y estructural de forjados mixtos en homigón ligero, PhD dissertation, Universidad de Oviedo, Oviedo, Spain, 2016.

[73] Hicks, S. J., Strength and ductility of headed stud connectors welded in modern profiled steel sheeting, *The Structural Engineer*, 85(22), 32-38, 2007.

[74] Hicks, S.J., Resistance and ductility of shear connection: full-scale beam and push tests, *Proc., 6th International Conference, Steel and Aluminum Structures*, Oxford Brookes University, 613-620, 2007.

[75] Hicks, S.J., McConnell, R.E., The shear resistance of headed studs used with profiled steel sheeting, *Composite Construction in Steel and Concrete III*, ASCE, 325-338, 1997.

[76] Holomek, J., Karásek, R., Bajer, M., Barnat, J., Thin-walled steel sheets with indentations in composite steel-concrete structure under different types of loading, *International Conference on Energy, Environment, Economics, Devices, Systems, Communications, Computers*, IAASAT Press, Iasi, 2011.

[77] Jayas, B. S., Hosain, M. U., Behaviour of headed studs in composite beams: push-out tests, *Canadian Journal of Civil Engineering*, 15, 240-253, 1988.

[78] Jeong, Y.-J., Kim, H.-Y., Koo, H.-B., Longitudinal shear resistance of steel–concrete composite slabs with perfobond shear connectors**,** *Journal of Constructional Steel Research*, 65(1), 81-88, 2009.

[79] Johnson, R. P., Prediction of shear resistance of headed studs in troughs of profiled sheeting, *International Conference on Composite Construction in Steel and Concrete*, Tabernash, Colorado, United States, 2008.

[80] Johnson, R. P., Yuan, H., Models and design rules for stud shear connectors in troughs of profiled sheeting. *Proc., Institution of Civil Engineers. Structures and Buildings,* 128(3), 252-263, 1998a.

[81] Johnson, R. P., Yuan, H., Existing rules and new tests for stud shear connectors in troughs of profiled sheeting. *Proc., Institution of Civil Engineers. Structures and Buildings,* 128, 244-51, 1998b.

[82] Jolly, C. K., Lawson, R. M., End anchorage in composite slabs: an increased load carrying capacity, *The Structural Engineer*, 70(11/2), 202-205. 1992.

[83] Kim, B., Wright, H. D., Cairns, R., The behaviour of through-deck welded shear connectors: an experimental and numerical study, *Journal of Construction Steel Research*, 57, 1359-1380, 2001.

[84] Lam, D., Elloboy, E. Behavior of headed stud shear connectors in composite beams, *Journal of Structural Engineering*, 131(1), 96-107, 2005.

[85] Lam, D., Qureshi, J., Prediction of longitudinal shear resistance of composite slabs with profile sheeting to Eurocode 4, *The Regency Steel Asia International Symposium on innovations in structural steel*, Singapore, 2008.

[86] Lloyd, R. M., Wright, H. D., Shear connection between composite slabs and steel beams, *Journal of Constructional Steel Research*, 15, 255-85. 1990.

[87] Lyons, J. C., Easterling, W., Murray, T. M., *Strength of welded shear studs. Vols I and II, Report CE/VPI-St 94/07*, 130-496, Virginia Polytechnic Institute, 1994.

[88] Lutrel, L. D., Davidson, J. H., Composite slabs with steel deck panels, *Proc., 2nd International Speciality Conference on Cold-Formed steel Structures*, St. Louis, Missouri, 573-603, 1973.

[89] Lutrell, L. D., Prasannan, L., Strength formulations for composite slabs, *Proc., 7th International Speciality Conference on Cold-Formed steel Structures*, St. Louis, Missouri, 307-324, 1984.

[90] Lutrell, L.D., Methods for predicting strength in composite slabs, *Proc., 8th International Speciality Conference on Cold-Formed steel Structures,* St. Louis, Missouri, 419-431, 1986.

[91] Lutrell, L.D., Flexural strength of composite slabs, *Composite Steel Structures - Advances, Design and Construction*, 106-115, 1987.

[92] Marciukaitis, G., Jonaitis, B., Valivonis, J,. Analysis of deflections of composite slabs with profiled sheeting up to the ultimate moment, *Journal of Constructional Steel Research*, 62, 820–830, 2006.

[93] Marimon, F., “Recomendaciones para el proyecto y construcción de forjados mixtos de chapa nervada (F.M.C.N.)”, ACHE, 14-15. Barcelona, Spain, 2008.

[94] Marimuthu, V., Seetharaman, S., Jayachandran, S., Chellappan, A., Bandyopadhyay, T. K, Dutta, D., Experimental studies on composite deck slabs to determine the shear-bond characteristic (m-k) values of the embossed profiled sheet. *Journal of Constructional Steel Research*, 63, 791-803, 2007.

[95] Mistakidis, E., Dimitriadis, K., Bending resistance of composite slabs made with thin-walled steel sheeting with indentations or embossments, *Thin-Walled Structures Journal*, 46(2), 192-206, 2008.

[96] Mottram, J. T., Johnson, R.P., Push tests on studs welded through profiled steel sheeting, *The Structural Engineer*, 68(10), 187-93, 1990.

[97] Nguyen, H.T., Kim, S. E., Finite element modeling of push-out tests for large stud shear connectors. *Journal of Constructional Steel Research*, 65, 1909-1920, 2009.

[98] O'Leary, D., Ei-Dharat, A., Duffy, C., Composite reinforced end-anchoraged concrete floors. *Composite Steel Structures*, 117-126, 1987.

[99] Patrick, M., Shear connection performance of profiled steel sheeting in composite slabs, PhD dissertation, University of Sydney, Australia, 1993.

[100] Porter, M., Greiman, L. F., Shear bond strength of studded steel deck slabs, *Proc., 7th Internationally Specialty conference on Cold-formed steel structures*, 285-306, 1984.

[101] Queiroz, F. D., Vellasco, P. C. G. S., Neyherco, D. A., Finite element modelling of composite beams with full and partial shear connection, *Journal of Constructional Steel Research*, 63(4), 505-521, 2006.

[102] Schurman, R. G., Stark. W. B., Longitudinal shear resistance of composite slabs—A new model, Composite Construction in Steel and Concrete IV, *Proc., 4th International Conference on Composite Construction in Steel and Concrete*, Alberta, Canada, 2000.

[103] Shanmugam, H. E., Kumar, H. Ghanshyam, E., Thevendranm V., Finite element modelling of double skin composite slabs, *Finite Elements in Analysis and Design*, 38(7), 579-599, 2002.

[104] Stark, W. B., Design of composite floors with profiled steel sheet, *Proc., 4th International Specialty Conference on Cold Formed Steel Structures*, University of Missouri. Rolla, 1978.

[105] Stark, W. B., Brekelmans, J., "Annex E to Eurocode 4", 3rd Revised draft, 1991.

[106] Stark, W. B., Brekelmans, J., Plastic design of continuous composite slabs, *Journal of Constructional Steel Research*, 15, 23-47, 1990.

[107] Steel Construction Institute, "Composite slabs and beams using steel decking: best practices for design and construction", MCRMA, Technical paper No 13, SCI P300, Revised Edition. 2009.

[108] Schuurman, R.G., The physical behaviour of shear connections in composite slabs, PhD dissertation, Delft University of Technology, The Netherlands, 2001.

[109] Valente, I., Cruz, P. J. S, Experimental analysis of perfobond shear connection between steel and lightweight concrete, *Journal of Constructional Steel Research*, 60, 465-479, 2004.

[110] Veljkovic, M., Longitudinal shear capacity of composite slabs, Swedish Institute of Steel Construction, *Proc., Nordic Steel Construction Conference 1995,* 2, 547-554, 1995.

[111] Vicente, R. Redistribución de esfuerzos en forjados de chapa nervada y hormigón continuos. Master thesis, Universidad Politécnica de Madrid (UPM), Madrid, Spain, 2004.

[112] Widjaja, B. R., Easterling, W. S., Strength and stiffness calculation procedures for composite slabs, *Proc., 13th International Specialty Conference on cold-formed steel structures,* St. Louis Missouri, US, 389-401, 1996.

Appendices

Appendix A: Ansys macro definition, composite slab INCO70

The appendix provides a complete description of the instructions to model the INCO70 composite slab in ANSYS.

```
finish
/clear
pi=acos(-1)
/view,1,1,1,1
/prep7
*ask,r,radi de curvatura,3
*ask,h1,alçada embotició circular,2.3
*ask,d1,diàmetre base emboticó circular,15
*ask,h2,alçada embotició lateral,1.8
*ask,d3,diàmetre emtodició superior,14
*ask,h3,alçada embotició superior,1
*ask,freg,coeficient de fricció, 0.5
*ask,s,longitud del patró,53
*ask,t,gruix xapa,0.8

!*
!*Type1 real1 (no té real constant, es defineix constant ficticia) mat1: placa acer
!*Material 2: coeficient de fricció
!*Type2 real2 Ressort transversal mat3 (acer) LINK11
!*Type3 (SOLID185_formigó) real3 (no té real constant, es defineix constant ficticia) mat4: Formigó

!**********Acer



ET,1,SHELL281
MP,EX,1,2.1E5
MP,NUXY,1,0.28
TB,BISO,1,1,1
TBTEMP,0
TBDATA,1,342,21
SECTYPE,1,SHELL
SECDATA,t,,5

!*
!**********Contactes acer-formigo
```

```
!*
!*Constants real 1 i 3 buides

R,1,,,
R,3,,,

ET,2,LINK11
R,2,1.875e-3,-.2, ,
MP,EX,3,2.0E5   !*material 3_ la molla


!*
MP,MU,2,freg

!*******************Formigó
ET,3,SOLID185
!*
!*
MPTEMP,,,,,,,,
MPTEMP,1,0
MPDATA,EX,4,,20000
MPDATA,PRXY,4,,0.2
MPTEMP,,,,,,,,
MPTEMP,1,0
MPDATA,DENS,4,,2.5e-9

!*
!**********Generació del perfil
!*
K,1 ,0,70-3.7677,0,
K,2 ,7.5353,70,0,
K,3 ,7.5353+39.7016,70,0,
K,4 ,75.9665,0,0,
K,5 ,210/2,0,0,
K,6 ,7.5353+18.3674,70,0

L,1,2
L,2,6
L,6,3
L,3,4
```

```
L,4,5

LFILLT,1,2,3.7677, ,
LFILLT,3,4,2.8257, ,
LFILLT,4,5,1.8838
K,13,,70-3.7677,s
L,1,13
FLST,2,8,4,ORDE,2
FITEM,2,1
FITEM,2,-8
ADRAG,P51X, , , , , ,9

NUMM,kp
numc,kp
numc,line
numc,area

!*
!************Generació emboticio lateral
!*
WPCSYS,-1,0
wpoff,0,0,s/2
ASBW,      6
wpoff,0,70/2,0
wprot,0,90
FLST,2,2,5,ORDE,2
FITEM,2,9
FITEM,2,-10
ASBW,P51X
KWPLAN,-1,     25,     23,     26
wprot,240
RECTNG,-17/2,17/2,-48/2,48/2,
wpoff,0,0,-h2
RECTNG,-8.5/2,8.5/2,-39/2,39/2,
LFILLT,39,40,4, ,
LFILLT,40,41,4, ,
LFILLT,38,39,4, ,
LFILLT,38,41,4, ,
LFILLT,28,37,17/2, ,
LFILLT,28,20,17/2, ,
```

```
LFILLT,4,20,17/2, ,
LFILLT,4,37,17/2, ,
FLST,3,4,4,ORDE,4
FITEM,3,42
FITEM,3,45
FITEM,3,48
FITEM,3,51
ASBL,      10,P51X
FLST,3,4,4,ORDE,4
FITEM,3,54
FITEM,3,57
FITEM,3,59
FITEM,3,62
ASBL,      9,P51X
APLO
FLST,2,8,5,ORDE,5
FITEM,2,10
FITEM,2,19
FITEM,2,-21
FITEM,2,14
FITEM,2,-17
ADELE,P51X, , ,1

!*
!*****************Generació emboticions circulars

!*1ª embotició

wpoff,0,0,h2
wprot,-240
wpoff,-(13.42),-16.96,
CSYS, 4
K,49, 0,0,0
wpoff,0,0,-h1
K,50, 0,0,0
L,49,50
wpoff,0,0,h1
CYL4,0,0,d1/2
LARC,27,29,50
LARC,28,30,50
```

```
wpoff,0,-((s/2)-16.96),0
k,51,0,0,0
L,30,51
wpoff,0,s/2,0
k,52,0,0,0
l,28,52

kwplan,-1,10,24,22
wpoff,0,((s/2)-16.96),0
k,53,0,0,0
l,53,29
kwplan,-1,24,25,11
wpoff,((s/2)-16.96),0,0
k,54,0,0,0
l,54,27
LDIV,49,0.5,,,0
LDIV,47,0.5,,,0
NUMM,KP
LFILLT,58,53,r,,
LFILLT,49,52,r,,
LFILLT,47,55,r,,
LFILLT,56,50,r,,
circle,49,,31,33,,
kcenter,kp,34,55,57,,,
circle,63,,31,34,,
ADELE,9, , ,1
FLST,2,4,4
FITEM,2,65
FITEM,2,68
FITEM,2,67
FITEM,2,66
AL,P51X
ASBA,6,9
NUMM,KP
FLST,2,4,4
FITEM,2,65
FITEM,2,72
FITEM,2,60
```

```
FITEM,2,61
AL,P51X
FLST,2,4,4
FITEM,2,63
FITEM,2,70
FITEM,2,67
FITEM,2,64
AL,P51X
FLST,2,4,4
FITEM,2,64
FITEM,2,71
FITEM,2,68
FITEM,2,60
AL,P51X
FLST,2,4,4
FITEM,2,61
FITEM,2,66
FITEM,2,63
FITEM,2,69
AL,P51X
FLST,2,3,4
FITEM,2,49
FITEM,2,72
FITEM,2,58
AL,P51X
FLST,2,3,4
FITEM,2,49
FITEM,2,69
FITEM,2,47
AL,P51X
FLST,2,3,4
FITEM,2,47
FITEM,2,70
FITEM,2,56
AL,P51X
FLST,2,3,4
FITEM,2,56
FITEM,2,58
FITEM,2,71
AL,P51X
```

```
!*2ª embotició

wpoff,33.92,13.42,
NUMMC,KP
NUMC,KP
K,56, 0,0,0
wpoff,0,0,h1
K,57, 0,0,0
L,56,57
wpoff,0,0,-h1
CYL4,0,0,d1/2
LARC,61,59,57
LARC,58,60,57
wpoff,((s/2)-16.96),0,0
k,62,0,0,0
L,58,62
wpoff,-(s/2),0,0
k,63,0,0,0
l,63,60
kwplan,-1,19,23,26
wpoff,((s/2)-16.96),0,0
k,64,0,0,0
l,59,64
kwplan,-1,25,26,23
wpoff,16.96,0,0
k,65,0,0,0
l,65,61
LDIV,74,0.5,,,0
LDIV,75,0.5,,,0
NUMM,KP
LFILLT,79,74,r,,
LFILLT,76,75,r,,
LFILLT,80,78,r,,
LFILLT,81,77,r,,
circle,56,,57,71,,
kcenter,kp,70,72,67,
circle,78,,57,72,,
ADELE,21, , ,1
FLST,2,4,4
```

```
FITEM,2,88
FITEM,2,89
FITEM,2,86
FITEM,2,87
AL,P51X
ASBA,13,21
NUMM,KP
FLST,2,4,4
FITEM,2,88
FITEM,2,83
FITEM,2,91
FITEM,2,82
AL,P51X
FLST,2,4,4
FITEM,2,83
FITEM,2,89
FITEM,2,84
FITEM,2,92
AL,P51X
FLST,2,4,4
FITEM,2,84
FITEM,2,86
FITEM,2,85
FITEM,2,93
AL,P51X
FLST,2,4,4
FITEM,2,85
FITEM,2,87
FITEM,2,90
FITEM,2,82
AL,P51X
FLST,2,3,4
FITEM,2,91
FITEM,2,75
FITEM,2,74
AL,P51X
FLST,2,3,4
FITEM,2,75
FITEM,2,92
FITEM,2,80
```

```
AL,P51X
FLST,2,3,4
FITEM,2,80
FITEM,2,93
FITEM,2,81
AL,P51X
FLST,2,3,4
FITEM,2,81
FITEM,2,90
FITEM,2,74
AL,P51X
NUMC,KP
NUMM,KP



!*
!****************Generació emboticicons superiors
!*
WPCSYS,-1,0
wpoff,7.5353+18.3674,70,0
wprot,0,90
CSYS, 4
K,71, 0,0,0
wpoff,0,0,-h3
K,72, 0,0,0
wpoff,0,0,h3
CYL4, 0,0,d3/2
CSYS, 0
wpoff, 0,s,0
CSYS, 4
K,77, 0,0,0
wpoff,0,0,-h3
K,78, 0,0,0
wpoff,0,0,h3
CYL4, 0,0,d3/2
CSYS, 0
WPCSYS,-1,0
```

```
ASBW,30
wpoff,0,0,s
ASBW,31
FLST,2,2,5,ORDE,2
FITEM,2,33
FITEM,2,30
ADELE,P51X, , ,1
!*
!**************FINALITZACIÓ EMBOTICIÓ LATERAL (FORAT + ÀREES LATERALS)
!*
FLST,2,4,5,
FITEM,2,12
FITEM,2,11
FITEM,2,23
FITEM,2,10
ASBA,P51X,22
FLST,2,2,5
FITEM,2,3
FITEM,2,4
FLST,3,2,5,ORDE,2
FITEM,3,34
FITEM,3,32
ASBA,P51X,P51X
L,42,37
L,42,35
L,44,38
L,43,36
L,83,36
L,41,31
L,39,32
L,39,33
L,40,34
L,76,34
FLST,2,4,4
FITEM,2,62
FITEM,2,2
FITEM,2,51
FITEM,2,14
AL,P51X
FLST,2,5,4
```

```
FITEM,2,14
FITEM,2,103
FITEM,2,41
FITEM,2,105
FITEM,2,107
AL,P51X
FLST,2,3,4
FITEM,2,107
FITEM,2,106
FITEM,2,94
AL,P51X
FLST,2,4,4
FITEM,2,106
FITEM,2,45
FITEM,2,99
FITEM,2,54
AL,P51X
FLST,2,3,4
FITEM,2,40
FITEM,2,99
FITEM,2,98
AL,P51X
FLST,2,4,4
FITEM,2,98
FITEM,2,42
FITEM,2,37
FITEM,2,57
AL,P51X
FLST,2,5,4
FITEM,2,37
FITEM,2,95
FITEM,2,104
FITEM,2,16
FITEM,2,39
AL,P51X
FLST,2,3,4
FITEM,2,16
FITEM,2,102
FITEM,2,15
AL,P51X
```

```
FLST,2,4,4
FITEM,2,15
FITEM,2,59
FITEM,2,48
FITEM,2,3
AL,P51X
FLST,2,3,4
FITEM,2,38
FITEM,2,2
FITEM,2,3
AL,P51X
NUMC,KP
NUMM,KP

!* ÀREA EMBOTICIONS SUPERIORS

K,82,7.5353+18.3674,70,s+d3/2
L,74,75
L,74,76
L,74,78
L,74,79
LARC,79,82,75
LARC,76,78,75
LDIV,112,0.5,,,0
LDIV,113,0.5,,,0
LDELE,114,,,1
NUMM,KP
FLST,2,3,4
FITEM,2,115
FITEM,2,112
FITEM,2,96
AL,P51X
FLST,2,3,4
FITEM,2,112
FITEM,2,113
FITEM,2,97
AL,P51X
K,82,7.5353+18.3674,70,0-d3/2
L,68,69
L,68,72
```

```
L,68,70
L,68,71
LARC,72,70,69
LARC,82,71,69
LDIV,119,0.5,,,0
LDIV,120,0.5,,,0
LDELE,120,,,1
NUMM,KP
FLST,2,3,4
FITEM,2,44
FITEM,2,122
FITEM,2,119
AL,P51X
FLST,2,3,4
FITEM,2,122
FITEM,2,121
FITEM,2,43
AL,P51X
WPCSYS,-1,0
APLO

!*********Correcció triangles emboticions
FLST,2,8,5
FITEM,2,3
FITEM,2,38
FITEM,2,37
FITEM,2,36
FITEM,2,12
FITEM,2,22
FITEM,2,23
FITEM,2,32
ADELE,P51X
FLST,2,6,4
FITEM,2,2
FITEM,2,3
FITEM,2,15
FITEM,2,99
FITEM,2,98
FITEM,2,106
LDELE,P51X
```

```
FLST,2,3,4,ORDE,3
FITEM,2,62
FITEM,2,59
FITEM,2,102
LCOMB,P51X,,0
FLST,2,3,4,ORDE,3
FITEM,2,51
FITEM,2,38
FITEM,2,48
LCOMB,P51X,,0
FLST,2,3,4,ORDE,3
FITEM,2,94
FITEM,2,54
FITEM,2,57
LCOMB,P51X,,0
FLST,2,3,4,ORDE,3
FITEM,2,45
FITEM,2,40
FITEM,2,42
LCOMB,P51X,,0
FLST,2,4,4
FITEM,2,37
FITEM,2,40
FITEM,2,107
FITEM,2,54
AL,P51X
FLST,2,4,4
FITEM,2,59
FITEM,2,14
FITEM,2,38
FITEM,2,16
AL,P51X

NUMM,ALL
NUMC,ALL
csys,0

!****************Generacio de la malla
!*
ASEL,S,AREA,,1,36
```

```
TYPE,1
REAL,1
MAT,1

ESIZE,10,0
MSHAPE,0,2D
MSHKEY,1
FLST,5,4,5,
FITEM,5,33
FITEM,5,34
FITEM,5,35
FITEM,5,36
ASEL,,,,P51X
AMESH,ALL


ASEL,S,AREA,,1,36
ESIZE,10,0
MSHKEY,0
FLST,5,4,5
FITEM,5,1
FITEM,5,10
FITEM,5,11
FITEM,5,8
ASEL,,,,p51X
AMESH,ALL


ASEL,S,AREA,,1,36
ESIZE,10,0
MSHKEY,0
FLST,5,4,5
FITEM,5,29
FITEM,5,32
FITEM,5,28
FITEM,5,30
ASEL,,,,p51X
AMESH,ALL

ASEL,S,AREA,,1,36
```

```
ESIZE,10,0
MSHKEY,1
LCCAT,23,26
LCCAT,27,24
lsla
lsel,s,line,,5
lsel,a,line,,6
lsel,a,line,,15
lsel,a,line,,19
LESIZE,ALL,,,2,,,,,0
AMESH,2
AMESH,5
AMESH,7
ASEL,S,AREA,,1,36

ESIZE,5,0
MSHKEY,0
lsla
LCCAT,90,92
LCCAT,91,85
FLST,5,4,5
FITEM,5,12
FITEM,5,4
FITEM,5,31
FITEM,5,3
ASEL,,,,P51X
AMESH,ALL
ASEL,S,AREA,,1,36

ESIZE,10,0
AMESH,18
ASEL,S,AREA,,1,36


ESIZE,3,0
FLST,5,4,5
FITEM,5,16
FITEM,5,20
FITEM,5,19
FITEM,5,17
```

```
ASEL,,,,P51X
AMESH,ALL
ASEL,S,AREA,,1,36

FLST,5,4,5
FITEM,5,24
FITEM,5,26
FITEM,5,27
FITEM,5,25
ASEL,,,,P51X
AMESH,ALL
ASEL,S,AREA,,1,36

ESIZE,3,0
FLST,5,4,5
FITEM,5,13
FITEM,5,23
FITEM,5,22
FITEM,5,21
ASEL,,,,P51X
AMESH,ALL
ASEL,S,AREA,,1,36

ESIZE,3,0
FLST,5,4,5
FITEM,5,6
FITEM,5,14
FITEM,5,9
FITEM,5,15
ASEL,,,,P51X
AMESH,ALL
ASEL,S,AREA,,1,36


FLST,5,15,5,
FITEM,5,6
FITEM,5,14
FITEM,5,9
FITEM,5,15
FITEM,5,36
```

```
FITEM,5,34
FITEM,5,16
FITEM,5,20
FITEM,5,13
FITEM,5,23
FITEM,5,22
FITEM,5,24
FITEM,5,27
FITEM,5,26
FITEM,5,3
CM,_Y,AREA
ASEL, , , ,P51X
CM,_Y1,AREA
CMSEL,S,_Y
CMDELE,_Y
AREVERSE,_Y1,0
CMDELE,_Y1
CM,_Y,AREA


FLST,3,36,5,ORDE,2
FITEM,3,1
FITEM,3,-36
AGEN,44,P51X, , , , ,s, ,0


!****La malla és coincident en les línies de contacte (excepte uns nodes que cauen molt aprop)


FLST,3,1584,5,ORDE,2
FITEM,3,1
FITEM,3,-1584
ARSYM,Z,P51X, , , ,0,0

ASEL,S,AREA,,1585,3168


FLST,3,1584,5,ORDE,2
FITEM,3,1585
FITEM,3,-3168
```

```
ARSYM,X,P51X, , , ,0,1



FLST,3,1584,5,ORDE,2
FITEM,3,1585
FITEM,3,-3168
AGEN, ,P51X, , , , ,44*s, , ,1

!***Comprovació de nodes coincidents

!***Ok són coincidents en el pla mig

!***Fusió dels nodes i keypoints

NUMMRG,NODE
NUMCMP,NODE
NUMMRG,KP
NUMCMP,KP

!****Creació dels blocs de formigó



!*************GENERACIÓ SUPERFÍCIES DE CONTATCE******************
!*
!*Acer:1-36*n*2
!*Formigó:(36*n*2+1)-(36*n*2+36)
!*
ASEL,S,AREA,,37,72
AGEN,2,all,,,,,,,1
ASEL,S,AREA,,3169,3204
LSLA
KSLL

!******Gir de les normals del formigó

!***No fa falta, ja están ben orientades



k,3925,105,180,s
k,3926,0,180,s
```

```
L,    3925,    3926
L,    3896,    3925
L,    3869,    3926



FLST,2,14,4
FITEM,2,112
FITEM,2,141
FITEM,2,403
FITEM,2,821
FITEM,2,824
FITEM,2,459
FITEM,2,230
FITEM,2,759
FITEM,2,719
FITEM,2,305
FITEM,2,363
FITEM,2,828
FITEM,2,839
FITEM,2,848
AL,P51X

NUMMRG,KP
NUMCMP,KP


K,3927,0,180,2*S


L,   3926,   3927
L,   3927,   3872

FLST,2,4,4
FITEM,2,860
FITEM,2,136
FITEM,2,848
FITEM,2,853
```

```
AL,P51X



WPOFF,O,O,1.5*S
ASBW,3206,SEPO
ASBW,3169
ADELE,    3208, , ,1



NUMMRG,KP
NUMCMP,KP
NUMCMP,LINE
NUMCMP,AREA



ET,4,MESH200
!*
KEYOPT,4,1,5
KEYOPT,4,2,0
!*


TYPE,4
MAT,4
ESIZE,45,0
AMESH,3204

TYPE,4
MAT,4
ESIZE,45,0
AMESH,3206

ESEL,TYPE,4

FLST,3,1,5,ORDE,1
FITEM,3,3206
ARSYM,Z,P51X, , , ,0,0
```

```
FLST,3,1,5,ORDE,1
FITEM,3,3208
AGEN, ,P51X, , , , ,3*S, , ,1


FLST,3,1,5,ORDE,1
FITEM,3,3204
AGEN,2,P51X, , , , ,S, ,0

ESEL,TYPE,4
NSLE
NUMMRG,NODE
NUMCMP,NODE
NUMMRG,KP
NUMCMP,KP

ASEL,S,AREA,,3169,3203
ASEL,A,AREA,,3205
ASEL,A,AREA,,3207

TYPE,4
MAT,4
ESIZE,10,0
AMESH,3207
AMESH,3205
AMESH,3177
AMESH,3178
AMESH,3195
AMESH,3196
AMESH,3198
AMESH,3185
AMESH,3171
AMESH,3175
AMESH,3197
AMESH,3199

ASEL,a,AREA,,3204
Asel,a,area,,3206
```

```
Asel,a,area,,3208
Asel,a,area,,3209
LSLA
KSLL


L,    3931, 3925


FLST,2,5,4
FITEM,2,826
FITEM,2,900
FITEM,2,6964
FITEM,2,6978
FITEM,2,6962
AL,P51X
FLST,2,4,4
FITEM,2,6962
FITEM,2,837
FITEM,2,6977
FITEM,2,368
AL,P51X




FLST,2,43,5,ORDE,2
FITEM,2,3169
FITEM,2,-3211
VA,P51X


Type,3
!**Solid 185 no té real constant
MAT,4
VSEL,s,volu,,1
MSHAPE,1,3D
ESIZE,45
SMRTSIZE,10,1,1,2,3,28,1.5,1,1,4,0
VMESH,ALL
```

```
FLST,3,1,6,ORDE,1
FITEM,3,1
VSYMM,Z,P51X, , , ,0,0

FLST,3,1,6,ORDE,1
FITEM,3,2
VSYMM,X,P51X, , , ,0,1



FLST,3,1,6,ORDE,1
FITEM,3,2
VGEN, ,P51X, , , , ,3*S, , ,1


ESEL,TYPE,4
EPLOT
NSLE
NSEL,R,LOC,X,0
NPLOT

!**OK NODES DEL PLA MIG COINCIDENTS

ESEL,TYPE,3
EPLOT
NSLE
NSEL,R,LOC,X,0
NPLOT
!**OK ELS NODES DE FORMIGÓ COINCIDEIXEN

!***S'uneixen nodes del pla mig

esel,type,3
nsle
NUMMRG,NODE
NUMCMP,NODE

!**ok, nodes de formigó del pla mig s'han fusionat
```

```
esel,type,4
nsle
NUMMRG,NODE
NUMCMP,NODE

!**ok, nodes del pla mig de l'element mesh200 fusionats
!**Fusó dels dos volums

vsel,all
vplot
aslv
lsla
ksll
NUMMRG,kp
NUMCMP,kp


!***Repetició dels volums

FLST,3,2,6,ORDE,2
FITEM,3,1
FITEM,3,-2
VGEN,43,P51X, , , , ,s, ,0


!*****Creació de l'inductor de fissura

esel,type,3
eplot
nsle
nplot
eplot
NSEL,R,LOC,Z,0,22.5*s
nplot
NUMMRG,NODE
NUMCMP,NODE

!****Ok, nodes fusionats
```

```
esel,type,3
nsle
nsel,r,loc,z,23.5*s,44*s
nplot
NUMMRG,NODE
NUMCMP,NODE


alls
esel,type,3
nsle
nsel,r,loc,z,23*s
nplot
nsel,r,loc,y,180
nplot

!****Nodes de la línia d'adalt sense fusionar
!*els fusionem
NUMMRG,NODE
NUMCMP,NODE

!**Fusionem ara les línies on están els nodes (Línies d'adalt)

alls
lsel,s,loc,z,23*s
lsel,r,loc,y,180
lplot
KSLL
NUMMRG,kp
NUMCMP,kp

!***Fusió dels dos volums, dins Ls i la propia Ls

ALLS
Vsel,S,loc,z,0,23*s
vplot
ASLV
APLOT
LSLA
KSLL
```

```
NUMMRG,kp
NUMCMP,kp



ALLS
Vsel,S,loc,z,23*S,44*s
vplot
ASLV
APLOT
LSLA
KSLL
NUMMRG,kp
NUMCMP,kp

alls



!**gir de les normals de l'acer

ASEL,S,TYPE,,1
areverse,all

!************Definició del 1r contacte

!**Superfícies de l'acer en contacte:

alls
ASEL,S,TYPE,,1
ASEL,R,LOC,Z,S,23*S

!***Superfícies de contacte del formigó

alls
ASEL,S,LOC,Z,S,23*S
ASEL,U,LOC,Y,100,200
asel,U,loc,x,105
asel,U,loc,x,-105
ASEL,U,TYPE,,1
```

```
FLST,5,48,5,ORDE,48
FITEM,5,3204
FITEM,5,3209
FITEM,5,3247
FITEM,5,3252
FITEM,5,3293
FITEM,5,3331
FITEM,5,3377
FITEM,5,3415
FITEM,5,3461
FITEM,5,3499
FITEM,5,3545
FITEM,5,3583
FITEM,5,3629
FITEM,5,3667
FITEM,5,3713
FITEM,5,3751
FITEM,5,3797
FITEM,5,3835
FITEM,5,3881
FITEM,5,3919
FITEM,5,3965
FITEM,5,4003
FITEM,5,4049
FITEM,5,4087
FITEM,5,4133
FITEM,5,4171
FITEM,5,4217
FITEM,5,4255
FITEM,5,4301
FITEM,5,4339
FITEM,5,4385
FITEM,5,4423
FITEM,5,4469
FITEM,5,4507
FITEM,5,4553
FITEM,5,4591
FITEM,5,4637
FITEM,5,4675
FITEM,5,4721
```

```
FITEM,5,4759
FITEM,5,4805
FITEM,5,4843
FITEM,5,4889
FITEM,5,4927
FITEM,5,4973
FITEM,5,5011
FITEM,5,5052
FITEM,5,5098
ASEL,u, , ,P51X

ALLS

!*
/COM, CONTACT PAIR CREATION - START
CM,_NODECM,NODE
CM,_ELEMCM,ELEM
CM,_KPCM,KP
CM,_LINECM,LINE
CM,_AREACM,AREA
CM,_VOLUCM,VOLU
/GSAV,cwz,gsav,,temp
!MP,MU,2,freg
MAT,2
MP,EMIS,2,7.88860905221e-031
R,3
REAL,3
ET,5,170

!*
KEYOPT,5,1,1
KEYOPT,5,2,0
KEYOPT,5,3,0
!*
KEYOPT,5,4,0
KEYOPT,5,5,0
!*


ET,6,174
```

```
R,3,,,0.01,0.2,0,
RMORE,,,1.0E20,0.0,1.0,
RMORE,0.0,0,1.0,,1.0,0.5
RMORE,0,1.0,1.0,0.0,,1.0
KEYOPT,6,4,0
KEYOPT,6,5,0
KEYOPT,6,7,0
KEYOPT,6,8,0
KEYOPT,6,9,0
KEYOPT,6,10,2
KEYOPT,6,11,0
KEYOPT,6,12,0
KEYOPT,6,2,0
KEYOPT,5,5,0
! Generate the target surface

alls
ASEL,S,LOC,Z,S,23*S
ASEL,U,LOC,Y,100,200
asel,U,loc,x,105
asel,U,loc,x,-105
ASEL,U,TYPE,,1


FLST,5,48,5,ORDE,48
FITEM,5,3204
FITEM,5,3209
FITEM,5,3247
FITEM,5,3252
FITEM,5,3293
FITEM,5,3331
FITEM,5,3377
FITEM,5,3415
FITEM,5,3461
FITEM,5,3499
FITEM,5,3545
FITEM,5,3583
FITEM,5,3629
FITEM,5,3667
FITEM,5,3713
```

```
FITEM,5,3751
FITEM,5,3797
FITEM,5,3835
FITEM,5,3881
FITEM,5,3919
FITEM,5,3965
FITEM,5,4003
FITEM,5,4049
FITEM,5,4087
FITEM,5,4133
FITEM,5,4171
FITEM,5,4217
FITEM,5,4255
FITEM,5,4301
FITEM,5,4339
FITEM,5,4385
FITEM,5,4423
FITEM,5,4469
FITEM,5,4507
FITEM,5,4553
FITEM,5,4591
FITEM,5,4637
FITEM,5,4675
FITEM,5,4721
FITEM,5,4759
FITEM,5,4805
FITEM,5,4843
FITEM,5,4889
FITEM,5,4927
FITEM,5,4973
FITEM,5,5011
FITEM,5,5052
FITEM,5,5098
ASEL,u, , ,P51X

CM,_TARGET,AREA
TYPE,5
NSLA,S,1
ESLN,S,0
ESLL,U
```

```
ESEL,U,ENAME,,188,189
NSLE,A,CT2
ESURF
CMSEL,S,_ELEMCM



! Generate the contact surface

alls

ASEL,S,TYPE,,1
ASEL,U,LOC,Z,0,S
ASEL,U,LOC,Z,23*S,44*S



CM,_CONTACT,AREA
TYPE,6
NSLA,S,1
ESLN,S,0
NSLE,A,CT2 ! CZMESH patch (fsk qt-40109 8/2008)
ESURF
ALLSEL
ESEL,ALL
ESEL,S,TYPE,,5
ESEL,A,TYPE,,6
ESEL,R,REAL,,3
/PSYMB,ESYS,1
/PNUM,TYPE,1
/NUM,1
EPLOT
ESEL,ALL
ESEL,S,TYPE,,5
ESEL,A,TYPE,,6
ESEL,R,REAL,,3
CMSEL,A,_NODECM
CMDEL,_NODECM
CMSEL,A,_ELEMCM
CMDEL,_ELEMCM
CMSEL,S,_KPCM
CMDEL,_KPCM
```

```
CMSEL,S,_LINECM
CMDEL,_LINECM
CMSEL,S,_AREACM
CMDEL,_AREACM
CMSEL,S,_VOLUCM
CMDEL,_VOLUCM
/GRES,cwz,gsav
CMDEL,_TARGET
CMDEL,_CONTACT
/COM, CONTACT PAIR CREATION - END
*CREATE,cwzplot,mac
/COM,
/COM,PLOT CONTACT PAIR(S)
~eui,'::apdl::noprint 1'
~eui,'::apdl::nooutput 1'
!*
CM,_CWZ_EL,ELEM
CM,_CWZ_ND,NODE
CM,_CWZ_KP,KP
CM,_CWZ_LN,LINE
CM,_CWZ_AR,AREA
CM,_CWZ_VL,VOLU
ESEL,NONE
ESEL,A,REAL,,3
ESEL,R,ENAME,,171,177
NSLE
*GET,_z1,ELEM,,NUM,MAX
KSLN,S
LSLK,S,1
ASLL,S,1
/PNUM,REAL,1
/NUM,1
/PSYMB,ESYS,0
EPLOT
CMSEL,S,_CWZ_EL
CMDEL,_CWZ_EL
CMSEL,S,_CWZ_ND
CMDEL,_CWZ_ND
CMSEL,S,_CWZ_KP
CMDEL,_CWZ_KP
```

```
CMSEL,S,_CWZ_LN
CMDEL,_CWZ_LN
CMSEL,S,_CWZ_AR
CMDEL,_CWZ_AR
CMSEL,S,_CWZ_VL
CMDEL,_CWZ_VL
!*
/PSYMB,ESYS,0
/NUM,0
/PNUM,TYPE,0
/PNUM,REAL,0
/mrep,cwzplot
~eui,'::apdl::nooutput 0'
~eui,'::apdl::noprint 0'
*END
cwzplot
!*
CM,_CWZ_EL,ELEM
CM,_CWZ_ND,NODE
CM,_CWZ_KP,KP
CM,_CWZ_LN,LINE
CM,_CWZ_AR,AREA
CM,_CWZ_VL,VOLU
ESEL,NONE
ESEL,A,REAL,,3
ESEL,R,ENAME,,171,177
NSLE
*GET,_z1,ELEM,,NUM,MAX
KSLN,S
LSLK,S,1
ASLL,S,1
*CREATE,cwzplot,mac
/COM,
/COM,PLOT CONTACT PAIR(S)
~eui,'::apdl::noprint 1'
~eui,'::apdl::nooutput 1'
/PNUM,REAL,1
/NUM,1
/PSYMB,ESYS,1
EPLOT
```

```
/PSYMB,ESYS,0
/NUM,0
/PNUM,TYPE,0
/PNUM,REAL,0
/mrep,cwzplot
~eui,'::apdl::nooutput 0'
~eui,'::apdl::noprint 0'
*END
cwzplot
*SET,_REALID,3
CMSEL,S,_CWZ_EL
CMDEL,_CWZ_EL
CMSEL,S,_CWZ_ND
CMDEL,_CWZ_ND
CMSEL,S,_CWZ_KP
CMDEL,_CWZ_KP
CMSEL,S,_CWZ_LN
CMDEL,_CWZ_LN
CMSEL,S,_CWZ_AR
CMDEL,_CWZ_AR
CMSEL,S,_CWZ_VL
CMDEL,_CWZ_VL
!*
*CREATE,cwzplot,mac
/COM,
/COM,PLOT CONTACT PAIR(S)
~eui,'::apdl::noprint 1'
~eui,'::apdl::nooutput 1'
!*
CM,_CWZ_EL,ELEM
CM,_CWZ_ND,NODE
CM,_CWZ_KP,KP
CM,_CWZ_LN,LINE
CM,_CWZ_AR,AREA
CM,_CWZ_VL,VOLU
ESEL,NONE
ESEL,A,REAL,,3
ESEL,R,ENAME,,169,170
NSLE
*GET,_z1,ELEM,,NUM,MAX
```

```
KSLN,S
LSLK,S,1
ASLL,S,1
/PNUM,REAL,1
/NUM,1
/PSYMB,ESYS,1
EPLOT
CMSEL,S,_CWZ_EL
CMDEL,_CWZ_EL
CMSEL,S,_CWZ_ND
CMDEL,_CWZ_ND
CMSEL,S,_CWZ_KP
CMDEL,_CWZ_KP
CMSEL,S,_CWZ_LN
CMDEL,_CWZ_LN
CMSEL,S,_CWZ_AR
CMDEL,_CWZ_AR
CMSEL,S,_CWZ_VL
CMDEL,_CWZ_VL
!*
/PSYMB,ESYS,0
/NUM,0
/PNUM,TYPE,0
/PNUM,REAL,0
/mrep,cwzplot
~eui,'::apdl::nooutput 0'
~eui,'::apdl::noprint 0'
*END
cwzplot
/MREP,EPLOT
/DIST,1,1.08222638492,1
/REP,FAST


!******Definició segon contacte

alls

ASEL,S,TYPE,,1
ASEL,R,LOC,Z,23*s,44*S
```

```
!****

alls
ASEL,S,LOC,Z,23*S,44*S
ASEL,U,TYPE,,1
asel,u,loc,y,100,200
asel,u,loc,x,105
asel,u,loc,x,-105
asel,U,loc,x,0

FLST,5,46,5,ORDE,46
FITEM,5,4973
FITEM,5,5011
FITEM,5,5052
FITEM,5,5057
FITEM,5,5095
FITEM,5,5098
FITEM,5,5141
FITEM,5,5179
FITEM,5,5225
FITEM,5,5263
FITEM,5,5309
FITEM,5,5347
FITEM,5,5393
FITEM,5,5431
FITEM,5,5477
FITEM,5,5515
FITEM,5,5561
FITEM,5,5599
FITEM,5,5645
FITEM,5,5683
FITEM,5,5729
FITEM,5,5767
FITEM,5,5813
FITEM,5,5851
FITEM,5,5897
FITEM,5,5935
FITEM,5,5981
```

```
FITEM,5,6019
FITEM,5,6065
FITEM,5,6103
FITEM,5,6149
FITEM,5,6187
FITEM,5,6233
FITEM,5,6271
FITEM,5,6317
FITEM,5,6355
FITEM,5,6401
FITEM,5,6439
FITEM,5,6485
FITEM,5,6523
FITEM,5,6569
FITEM,5,6607
FITEM,5,6653
FITEM,5,6691
FITEM,5,6737
FITEM,5,6775

ASEL,U, , ,P51X

ALLS

!*
/COM, CONTACT PAIR CREATION - START
CM_NODECM,NODE
CM,_ELEMCM,ELEM
CM,_KPCM,KP
CM,_LINECM,LINE
CM,_AREACM,AREA
CM,_VOLUCM,VOLU
/GSAV,cwz,gsav,,temp
MP,MU,2,freg
MAT,2
MP,EMIS,2,7.88860905221e-031
R,4
REAL,4
ET,7,170
```

```
!*
KEYOPT,7,1,1
KEYOPT,7,2,0
KEYOPT,7,3,0
!*
KEYOPT,7,4,0
KEYOPT,7,5,0
!*

ET,8,174
R,4,,,0.01,0.2,0,
RMORE,,,1.0E20,0.0,1.0,
RMORE,0.0,0,1.0,,1.0,0.5
RMORE,0,1.0,1.0,0.0,,1.0
KEYOPT,8,4,0
KEYOPT,8,5,0
KEYOPT,8,7,0
KEYOPT,8,8,0
KEYOPT,8,9,0
KEYOPT,8,10,2
KEYOPT,8,11,0
KEYOPT,8,12,0
KEYOPT,8,2,0
KEYOPT,7,5,0
! Generate the target surface


alls
ASEL,S,LOC,Z,23*S,44*S
ASEL,U,TYPE,,1
asel,u,loc,y,100,200
asel,u,loc,x,105
asel,u,loc,x,-105
asel,U,loc,x,0

FLST,5,46,5,ORDE,46
FITEM,5,4973
FITEM,5,5011
FITEM,5,5052
FITEM,5,5057
```

```
FITEM,5,5095
FITEM,5,5098
FITEM,5,5141
FITEM,5,5179
FITEM,5,5225
FITEM,5,5263
FITEM,5,5309
FITEM,5,5347
FITEM,5,5393
FITEM,5,5431
FITEM,5,5477
FITEM,5,5515
FITEM,5,5561
FITEM,5,5599
FITEM,5,5645
FITEM,5,5683
FITEM,5,5729
FITEM,5,5767
FITEM,5,5813
FITEM,5,5851
FITEM,5,5897
FITEM,5,5935
FITEM,5,5981
FITEM,5,6019
FITEM,5,6065
FITEM,5,6103
FITEM,5,6149
FITEM,5,6187
FITEM,5,6233
FITEM,5,6271
FITEM,5,6317
FITEM,5,6355
FITEM,5,6401
FITEM,5,6439
FITEM,5,6485
FITEM,5,6523
FITEM,5,6569
FITEM,5,6607
FITEM,5,6653
FITEM,5,6691
```

```
FITEM,5,6737
FITEM,5,6775

ASEL,U, , ,P51X

CM,_TARGET,AREA
TYPE,7
NSLA,S,1
ESLN,S,0
ESLL,U
ESEL,U,ENAME,,188,189
NSLE,A,CT2
ESURF
CMSEL,S,_ELEMCM
! Generate the contact surface

alls

ASEL,S,TYPE,,1
ASEL,R,LOC,Z,23*s,44*S

CM,_CONTACT,AREA
TYPE,8
NSLA,S,1
ESLN,S,0
NSLE,A,CT2 ! CZMESH patch (fsk qt-40109 8/2008)
ESURF
ALLSEL
ESEL,ALL
ESEL,S,TYPE,,7
ESEL,A,TYPE,,8
ESEL,R,REAL,,4
/PSYMB,ESYS,1
/PNUM,TYPE,1
/NUM,1
EPLOT
ESEL,ALL
ESEL,S,TYPE,,7
ESEL,A,TYPE,,8
ESEL,R,REAL,,4
```

```
CMSEL,A,_NODECM
CMDEL,_NODECM
CMSEL,A,_ELEMCM
CMDEL,_ELEMCM
CMSEL,S,_KPCM
CMDEL,_KPCM
CMSEL,S,_LINECM
CMDEL,_LINECM
CMSEL,S,_AREACM
CMDEL,_AREACM
CMSEL,S,_VOLUCM
CMDEL,_VOLUCM
/GRES,cwz,gsav
CMDEL,_TARGET
CMDEL,_CONTACT
/COM, CONTACT PAIR CREATION - END
*CREATE,cwzplot,mac
/COM,
/COM,PLOT CONTACT PAIR(S)
~eui,'::apdl::noprint 1'
~eui,'::apdl::nooutput 1'
!*
CM,_CWZ_EL,ELEM
CM,_CWZ_ND,NODE
CM,_CWZ_KP,KP
CM,_CWZ_LN,LINE
CM,_CWZ_AR,AREA
CM,_CWZ_VL,VOLU
ESEL,NONE
ESEL,A,REAL,,4
ESEL,R,ENAME,,171,177
NSLE
*GET,_z1,ELEM,,NUM,MAX
KSLN,S
LSLK,S,1
ASLL,S,1
/PNUM,REAL,1
/NUM,1
/PSYMB,ESYS,0
EPLOT
```

```
CMSEL,S,_CWZ_EL
CMDEL,_CWZ_EL
CMSEL,S,_CWZ_ND
CMDEL,_CWZ_ND
CMSEL,S,_CWZ_KP
CMDEL,_CWZ_KP
CMSEL,S,_CWZ_LN
CMDEL,_CWZ_LN
CMSEL,S,_CWZ_AR
CMDEL,_CWZ_AR
CMSEL,S,_CWZ_VL
CMDEL,_CWZ_VL
!*
/PSYMB,ESYS,0
/NUM,0
/PNUM,TYPE,0
/PNUM,REAL,0
/mrep,cwzplot
~eui,'::apdl::nooutput 0'
~eui,'::apdl::noprint 0'
*END
cwzplot
!*
CM,_CWZ_EL,ELEM
CM,_CWZ_ND,NODE
CM,_CWZ_KP,KP
CM,_CWZ_LN,LINE
CM,_CWZ_AR,AREA
CM,_CWZ_VL,VOLU
ESEL,NONE
ESEL,A,REAL,,4
ESEL,R,ENAME,,171,177
NSLE
*GET,_z1,ELEM,,NUM,MAX
KSLN,S
LSLK,S,1
ASLL,S,1
*CREATE,cwzplot,mac
/COM,
/COM,PLOT CONTACT PAIR(S)
```

```
~eui,'::apdl::noprint 1'
~eui,'::apdl::nooutput 1'
/PNUM,REAL,1
/NUM,1
/PSYMB,ESYS,1
EPLOT
/PSYMB,ESYS,0
/NUM,0
/PNUM,TYPE,0
/PNUM,REAL,0
/mrep,cwzplot
~eui,'::apdl::nooutput 0'
~eui,'::apdl::noprint 0'
*END
cwzplot
*SET,_REALID,4
CMSEL,S,_CWZ_EL
CMDEL,_CWZ_EL
CMSEL,S,_CWZ_ND
CMDEL,_CWZ_ND
CMSEL,S,_CWZ_KP
CMDEL,_CWZ_KP
CMSEL,S,_CWZ_LN
CMDEL,_CWZ_LN
CMSEL,S,_CWZ_AR
CMDEL,_CWZ_AR
CMSEL,S,_CWZ_VL
CMDEL,_CWZ_VL
!*
*CREATE,cwzplot,mac
/COM,
/COM,PLOT CONTACT PAIR(S)
~eui,'::apdl::noprint 1'
~eui,'::apdl::nooutput 1'
!*
CM,_CWZ_EL,ELEM
CM,_CWZ_ND,NODE
CM,_CWZ_KP,KP
CM,_CWZ_LN,LINE
CM,_CWZ_AR,AREA
```

```
CM,_CWZ_VL,VOLU
ESEL,NONE
ESEL,A,REAL,,4
ESEL,R,ENAME,,169,170
NSLE
*GET,_z1,ELEM,,NUM,MAX
KSLN,S
LSLK,S,1
ASLL,S,1
/PNUM,REAL,1
/NUM,1
/PSYMB,ESYS,1
EPLOT
CMSEL,S,_CWZ_EL
CMDEL,_CWZ_EL
CMSEL,S,_CWZ_ND
CMDEL,_CWZ_ND
CMSEL,S,_CWZ_KP
CMDEL,_CWZ_KP
CMSEL,S,_CWZ_LN
CMDEL,_CWZ_LN
CMSEL,S,_CWZ_AR
CMDEL,_CWZ_AR
CMSEL,S,_CWZ_VL
CMDEL,_CWZ_VL
!*
/PSYMB,ESYS,0
/NUM,0
/PNUM,TYPE,0
/PNUM,REAL,0
/mrep,cwzplot
~eui,'::apdl::nooutput 0'
~eui,'::apdl::noprint 0'
*END
cwzplot
/MREP,EPLOT
/DIST,1,1.08222638492,1
/REP,FAST

alls
```

```
!******Tercer contacte
alls
vsel,all
aslv
aplot
asel,r,loc,z,23*S

alls
asel,s,area,,3118
asel,a,area,,3072


alls
asel,s,area,,3031
asel,a,area,,2993



/COM, CONTACT PAIR CREATION - START
CM,_NODECM,NODE
CM,_ELEMCM,ELEM
CM,_KPCM,KP
CM,_LINECM,LINE
CM,_AREACM,AREA
CM,_VOLUCM,VOLU
/GSAV,cwz,gsav,,temp
MP,MU,2,freg
MAT,2
MP,EMIS,2,7.88860905221e-031
R,5
REAL,5
ET,9,170
ET,10,174
KEYOPT,10,9,0
KEYOPT,10,10,2
R,5,
RMORE,
RMORE,,0
RMORE,0
```

```
! Generate the target surface
ASEL,S,,,3072
ASEL,A,,,3118
CM,_TARGET,AREA
TYPE,9
NSLA,S,1
ESLN,S,0
ESLL,U
ESEL,U,ENAME,,188,189
NSLE,A,CT2
ESURF
CMSEL,S,_ELEMCM
! Generate the contact surface
ASEL,S,,,2993
ASEL,A,,,3031
CM,_CONTACT,AREA
TYPE,10
NSLA,S,1
ESLN,S,0
NSLE,A,CT2 ! CZMESH patch (fsk qt-40109 8/2008)
ESURF
ALLSEL
ESEL,ALL
ESEL,S,TYPE,,9
ESEL,A,TYPE,,10
ESEL,R,REAL,,5
/PSYMB,ESYS,1
/PNUM,TYPE,1
/NUM,1
EPLOT
ESEL,ALL
ESEL,S,TYPE,,9
ESEL,A,TYPE,,10
ESEL,R,REAL,,5
CMSEL,A,_NODECM
CMDEL,_NODECM
CMSEL,A,_ELEMCM
CMDEL,_ELEMCM
CMSEL,S,_KPCM
CMDEL,_KPCM
```

```
CMSEL,S,_LINECM
CMDEL,_LINECM
CMSEL,S,_AREACM
CMDEL,_AREACM
CMSEL,S,_VOLUCM
CMDEL,_VOLUCM
/GRES,cwz,gsav
CMDEL,_TARGET
CMDEL,_CONTACT
/COM, CONTACT PAIR CREATION - END


!*
!***********CONDICIONS DE CONTORN.DESPLAÇAMENTS***********
!*
!*


!********************CONDICIONS DE CONTORN SOBRE L'ACER

!****Recolzaments a l'extrem de la llosa
alls

ASEL,S,TYPE,,1
LSLA
LSEL,R,LOC,z,3*s
Lsel,r,loc,y,0

FLST,2,2,4,ORDE,2
FITEM,2,230
FITEM,2,6679
!*
DL,P51X, ,UY,
ALLS




!**Condicions de simetria
```

```
!***Simetria de l'acer

!*SIMETRIA ACER

ESEL,TYPE,1
NSLE
NSEL,R,LOC,X,-105
DSYM,SYMM,X,0,

ESEL,TYPE,1
NSLE
NSEL,R,LOC,X,105
DSYM,SYMM,X,0,

ESEL,TYPE,1
NSLE
NSEL,R,LOC,Z,44*S
DSYM,SYMM,Z,0,

ALLS

!*
!***SIMETRIA FORMIGÓ

ESEL,TYPE,3
NSLE
NSEL,R,LOC,X,-105
DSYM,SYMM,X,0,
ALLS

ESEL,TYPE,3
NSLE
NSEL,R,LOC,X,105
DSYM,SYMM,X,0,
ALLS

ESEL,TYPE,3
NSLE
NSEL,R,LOC,Z,44*S
```

```
DSYM,SYMM,Z,0,


!*

ALLS
FINISH
/SOLU
CSYS,0
ALLS
SAVE

!*
!********************càlcul**************
!*
!*
ESEL,TYPE,3
NSLE
NSEL,R,LOC,Z,23*s
NSEL,R,LOC,Y,180
NPLOT
CM,acer,node
*GET,NM2,NODE,,num,min
CP,NEXT,UY,ALL
alls
save

/solu



!******************Opcions de càlcul******************

!**Desplaçament imposat
!*
ACEL,,9810,
ANTYPE,STAT,NEW
SOLCONTROL,ON!,ON
RESCONTROL,DEFINE,NONE
NLGEOM,ON
```

```
NROPT,UNSY, ,OFF
PRED,ON
NEQIT,100
!*
!*******Pas 1: interacció inicial
TIME,1e-8
NSUBST,1
AUTOTS,OFF
NEQIT,100
D,NM2,UY,-0
OUTRES,basic,-30
SOLVE
!*
!*******Pas 2: tracció petita
D,NM2,UY,-1e-4
TIME,1e-4
DELTIM,.0001
SOLVE
!*******Pas 3: 0.05mm només salva últim substep (pas automàtic)
NEQIT,100
AUTOTS,ON
DELTIM,.005,.00000001,.05,ON
D,NM2,UY,-0.05
TIME,.05
SOLVE

!*******Pas 4: 4.5mm salva 19 substeps equidistants
OUTRES,basic,-30
D,NM2,UY,-3*1.5
NSUBST,30,2000,30,ON
TIME,3*1.5
SOLVE

!*******Pas 5: 6mm salva 60 substeps equidistants
OUTRES,basic,-30
D,NM2,UY,-6
TIME,6
!**error
SOLVE
```

```
!*******Pas 6: 10mm salva 19 substeps equidistants
OUTRES,basic,-50
D,NM2,UY,-10
NSUBST,50,2000,50,ON
TIME,10
SOLVE


!*******Pas 7: 15mm salva 19 substeps equidistants
OUTRES,basic,-50
D,NM2,UY,-15
NSUBST,50,2000,50,ON
TIME,15
SOLVE


!*******Pas 8: 20mm salva 19 substeps equidistants
OUTRES,basic,-50
D,NM2,UY,-20
NSUBST,50,2000,50,ON
TIME,20
SOLVE


!*******Pas 9: 25mm salva 19 substeps equidistants
OUTRES,basic,-40
D,NM2,UY,-28
NSUBST,40,2000,40,ON
TIME,28
SOLVE

!*******Pas 10: 50mm salva 19 substeps equidistants
OUTRES,basic,-40
D,NM2,UY,-60
NSUBST,40,2000,40,ON
TIME,60
SOLVE
```